Development of a Novel Additive Manufacturing Process using Material Extrusion for the Production of Porous Titanium Orthopaedic Implant Material

Forber, Timothy

This dissertation is submitted for the degree of Doctor of Philosophy

August 2023

School of Engineering

Lancaster University

United Kingdom

Declaration

This thesis has not been submitted in support of an application for another degree at this or any other university. It is the result of my own work and includes nothing that is the outcome of work done in collaboration except where specifically indicated. Many of the ideas in this thesis were the product of discussion with my supervisor Professor Andrew Kennedy.

Abstract

There is an increasing demand for the development of artificial orthopaedic implant material that can aid the bone recovery process due to the complications associated with harvesting bone from other parts of the body (autograft), and the limited supply of donor material (allograft) as well as the risk of immune rejection or transmission of disease. Titanium and its alloys, and particularly Ti-6Al-4V, have become popular materials for orthopaedic implants because of their mechanical strength, biocompatibility and corrosion resistance. It is crucial that artificial implant material mimics the porous structure of human bone in order to ensure sufficient fusion between the implant and surrounding bone through bone in-growth, as well as allow fluid transportation throughout the implant. Also, the ability to produce implants with bespoke geometries for patient-specific applications is required.

This research focuses on the development of a novel manufacturing method for producing porous titanium scaffolds for the application of orthopaedic implant material, through the combination of foam gel casting and additive manufacturing (AM) by material extrusion. Foam gel casting offers the ability to control the level of porosity and pore sizes of the resulting material, and despite its successful implementation with a wide range of ceramics as well as even with stainless steel, remains almost entirely unexplored for Ti-6Al-4V. AM offers the capability to easily produce bespoke geometries that can be tailored to specific applications. As such, the combination of these two processes offers a unique novel method of manufacturing which presents the capability to address the complex requirements of artificial implant material. In this work the foam gel casting process has been developed for Ti-6Al-4V and optimised to produce material with optimal porosity in terms of size, shape and interconnected structure of the pores, for the replacement of human trabecular bone. In addition, it has been demonstrated that this process can be combined with AM, using a standard desktop 3D printer with a paste extrusion toolhead attachment, in order to produce bespoke 3D structures through the deposition of single tracks and building up successive layers, whilst still maintaining the optimised porous structure of the material.

This research demonstrates the feasibility of this novel manufacturing method which offers the capability of producing artificial implant material with both optimal porosity for biocompatibility, as well as the potential to readily produce patient-specific implants with bespoke geometry.

Acknowledgements

I would like to express my gratitude to my primary supervisor, Professor Andrew Kennedy, for his continual guidance and support throughout my PhD studies, and in particular for his patience and valuable input during the final months whilst I was working full-time and writing my thesis. I would also like to thank my secondary supervisor, Professor Allan Rennie, for his ongoing support and input, as well as his professional guidance during my time working as a member of the Lancaster Product Development Unit. I am extremely grateful to the rest of the LPDU team for their moral and practical support throughout this process, and for sharing their valuable knowledge. In particular, I would like to honour the memory of Mary Mason, who provided much encouragement during my time in the LPDU team. Her smile and enthusiasm for life will be remembered fondly by all who were fortunate enough to work with her. I would like to thank all the technical and support staff within the School of Engineering for sharing their expertise, as well as all the other postgraduate research students I have shared this journey with. I would like to express my gratitude to my wider family, for their ongoing practical and emotional support throughout all the ups and downs of this process, and in particular for providing much-needed childcare which has enabled me to spend time completing my thesis. Finally, I would like to thank my son Asher, for always giving me a reason to smile and teaching me how to enjoy every moment.

List of Abbreviations and Acronyms

SS 316L	Stainless Steel 316L
Co-Cr	Cobalt-Chromium
Ti	Titanium
Ti64	Titanium Alloy Ti-6Al-4V
AM	Additive Manufacturing
CAD	Computer Aided Design
SLS	Selective Laser Sintering
DMLS	Direct Metal Laser Sintering
SLM	Selective Laser Melting
SLA	Stereolithography
FDM	Fused Deposition Modelling
DLP	Digital Light Processing
EBM	Electron Beam Melting
RPDs	Removable Partial Dentures
UV	Ultraviolet light
PLA	Polylactic Acid
PEEK	Polyetheretherketone
CpTi	Commercially Pure Titanium
PVA	Polyvinyl Alcohol
CT	Computerised Tomography
MRI	Magnetic Resonance Imaging
API	Active Pharmaceutical Ingredient
EVA	Ethylene-Vinyl Acetate
TDD	Transdermal Drug Delivery
CLIP	Continuous Liquid Interface Production
PET	Polyethylene Terephthalate
PM	Powder Metallurgy
NaCl	Sodium Chloride
TMPS	Triply Periodic Minimal Surfaces
TiH_2	Titanium Hydride
MC	Methylcellulose
HEMC	Hydroxyethyl Methylcellulose

HPMC	Hydroxypropyl Methylcellulose
HA	Hydroxyapatite
PF	Packing Fraction
VF	Volume Fraction
CFD	Computational Fluid Dynamics
DXF	Drawing Exchange Format

Contents

List of Figures

List of Tables

1 Chapter 1: Introduction

1.1 Background Information

1.1.1 Properties of Human Bone and Orthopaedic Implants

Bone tissue is known to have impressive self-healing abilities, however large defects ($> 2\ mm$) [1, 2] sometimes cannot be healed entirely by the body and therefore the use of bone implant material to bridge the gap is necessary to assist the healing process [3, 4]. This tissue can be grafted from another part of the body (autografts) or can be taken from a donor (allografts) [5]. Grafted bone tissue has many clear advantages as implant material, including ideal structural and compatibility properties for osseointegration, as well as avoiding any complications as a result of immune rejection that can occur with allografts or artificial implants [6]. Autograft material is most commonly harvested from the posterior iliac crest, however this bone material is a limited resource and a number of complications can arise as a result of the surgical procedure, and it is also restricted by the age and health of the patient [4, 7]. The side effects of the surgery can be long lasting, with some patients reported to still experience pain up to 2 years afterwards [8]. Allografts are generally the second surgical choice following autografts, with an increasing availability of allograft tissue. However, this process presents even more complications, including the risk of disease transmission and potential rejection of the implanted bone tissue by the body [4]. Both autografts and allografts require processing and shaping during the surgical procedure in order to produce implants with personalised geometry. Therefore, there is an increasing demand for the development of artificial bone implant materials that can aid the bone recovery process [7], as well as fabrication techniques that can produce implants with patient-customised geometry. Artificial bone implants have to be designed to either decompose in the long term and be replaced by new bone, or allow for the surrounding tissue to be incorporated into the implant material [3].

In order to ensure bio-compatibility, implants must present a number of specific characteristics. Since human bone grafting is the primary choice material for implants, it is vital that artificial implant material is comparable in its properties to human bone [4]. Ideally implants should be manufactured from biocompatible materials and demonstrate porosity and mechanical properties that mimic those of human bone [7]. A summary of these properties is presented in Table 1.

	Coritcal Bone	Trabecular Bone	Ti-6Al-4V
Porosity (%)	<10 [9]	$50-90$ [9]	-
Pore Sizes (μm)	$10-50$ [10]	$300-600$ [10]	-
Young's Modulus (GPa)	$10-30$ [11]	$<$ 0.5 [10]	$110-120$ [11]

Table 1: Summary of human bone material properties compared against cast Ti64.

Interconnected porosity within implants is essential, particularly in non-degradable implants, in order to allow transportation of fluids and create a scaffold that promotes bone in-growth [7, 9, 12]. Implant-loosening due to weak bone-implant bonding is a common problem which is minimised by using porous implants which have been shown to promote a more stable fixation [13]. Figure 1 shows an example of new bone growing within a porous implant scaffold. Several studies have investigated the ideal implant pore geometries that promote bone growth and bone-implant fusion [14–16]. Pore shape as well as size have been found to impact bone growth within implant scaffolds [17]. In particular, curvature of pores has received specific attention and it has been shown that concave surfaces promote higher levels of bone growth than flat or convex surfaces [18]. In studies investigating the effect of pore size, bone growth has been observed within scaffolds with pore sizes ranging from $100-1200$ μm, however the optimal pore sizes have been identified in most cases to be $300-600$ μm [14–16, 19–21]. Also, the optimum porosity for implant scaffolds is suggested to be $60-65$ % [22]. Limited research has attempted to quantify the optimal interconnectivity between pores, however a study by Lu et al. showed the most favourable size of connections to be over 40 μm when investigating porous ceramics with mean interconnections ranging from $30-100$ μm [23]. Other work has shown that, in general, a higher level of interconnectivity and permeability between pores results in greater osseointegration [21].

Bone tissue is made up of two structures; cortical and trabecular (cancellous) bone. Trabecular bone makes up the inner spongy part of bone which has a porosity of $50-90$ % with pore sizes ranging from $300-600$ μm, whereas the denser cortical bone that creates an outer layer has a porosity of less than 10 % with pore sizes $10-50$ μm [9–11]. However, as high levels of interconnected porosity are vital for the incorporation of the implant material within the body, the primary aim when developing artificial implant material should be to mimic the structure and porosity of trabecular bone as it is known that stem cells involved in bone regeneration respond

to these porosity characteristics [1]. The porous structure of trabecular bone, as seen in Figure 2, is largely stochastic and isotropic (non-directionally dependant), which should also be aimed for when producing artificial implant scaffolds [24]. This helps to ensure that optimal fluid transport and bone in-growth can occur in any direction through the implant.

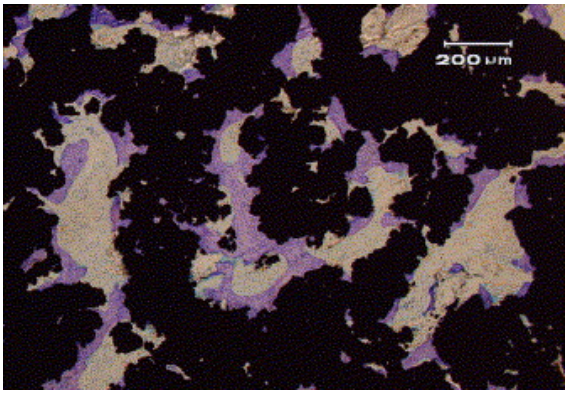

Figure 1: Optical micrograph showing bone in-growth (purple stain) within a porous scaffold of pore sizes between $300 - 500\ \mu m$ and porosity $40 - 60\ \%$. Adapted from [25]

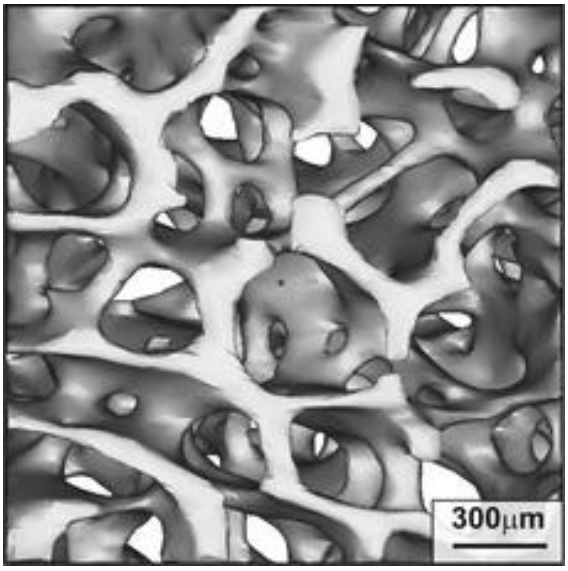

Figure 2: CT scan of human trabecular bone. Adapted from [24]

The material used to produce an implant must itself be biocompatible. Implant scaffolds have been manufactured successfully from a wide variety of biocompatible ceramic materials however the major limitation with these materials is low mechanical strength and therefore the implants are restricted to non-load bearing applications [9, 21]. To overcome this issue, metals such as stainless

steel 316L (SS 316L) and cobalt-chromium (Co-Cr) alloys have been used as implant materials [26–28], however titanium (Ti) and its alloys have become the most popular material of choice due to their high mechanical strength and superior biocompatibility and corrosion resistance [29, 30]. The high corrosion resistance of Ti and its alloys results from the formation of an oxide layer on the surface of the metal within milliseconds of exposure within a range of corrosive environments, which acts as a protective barrier [31]. In particular Ti alloy Ti-6Al-4V (Ti64) has become a commonly used alloy for the production of orthopaedic implants [32]. The mechanical properties of implants are an important characteristic for ensuring biocompatibility, in particular the Young's modulus [33]. Cortical bone has a modulus of $10-30\ GPa$ and trabecular bone $<\ 0.5\ GPa$ [29, 34, 35]. The disadvantage of using metals as implant material is that often the Young's modulus of the metal is significantly higher than the surrounding bone, as in the case of Ti64 where $E \approx 110\ GPa$ [29, 30]. Where the Young's modulus of the implant is significantly higher than that of the surrounding bone, it has been known to result in a failure known as 'stress shielding' which requires painful revision surgery [34]. This phenomenon occurs as a result of the high modulus of implant material causing a stress concentration at the bone/implant interface. It is therefore important that implant scaffolds exhibit similar mechanical properties to those of human bone. It has been shown that introducing porosity to implant materials such as Ti alloys reduces the Young's modulus, and so modulus can be altered by carefully controlling the porosity [30, 36]. Therefore, there is a clear demand for the development of manufacturing techniques that are able to produce Ti64 implant material with specifically tailored levels of porosity that more closely matches both the porosity and mechanical properties of human bone.

1.1.2 Additive Manufacturing

Additive Manufacturing (AM) has become an increasingly popular manufacturing technique since first emerging in 1981 [37] due to the material flexibility, geometrical freedom and customisation it offers [38]. In contrast to conventional subtractive manufacturing processes, AM fabricates 3D products from a digital file (typically CAD file) through additive layer-by-layer techniques, making it inherently less wasteful in terms of material. AM encompasses a wide range of technologies including selective laser sintering (SLS), selective laser melting (SLM), direct metal laser sintering (DMLS), stereolithography (SLA), fused deposition modelling (FDM), digital light processing

(DLP), electron beam melting (EBM), material jetting and binder jetting, and can fabricate products from materials including polymers, metals, ceramics and composites [39, 40]. The geometrical flexibility that AM offers provides the capability of producing more lightweight components that reduce material consumption and both energy consumption and CO_2 throughout manufacturing, transportation and overall product life cycle [39, 40], as well as the ability to produce complex geometries that would not be achievable using conventional manufacturing processes. As such, it has been suggested that AM could provide the way forward for manufacturing reproducible porous Ti-based implants with specifically tailored porosity and mechanical properties which meet the optimal requirements for orthopaedic implants as outlined later in Section 2.9 [41]. Also, the ease of customisation that AM offers makes it ideal for the production of implant scaffolds where the geometry of the implant has to be tailored to each individual application.

1.2 Aim and Objectives

This project aims to develop, understand and optimise a novel method of manufacture which utilises AM technology, capable of producing orthopaedic implant material with optimised porous structure as well as bespoke geometries. The key objectives of this work are as follows:

- To conduct an in-depth review of the current applications of AM in the medical sector and understand how this technology is being applied to solve the complex issues presented in this field.
- To research the existing methods of manufacture that have been applied to produce porous Ti implant material, and critically assess the properties of the material produced using each method against the requirements outlined in Section 1.1.
- To identify the limitations of the existing methods of manufacturing for this application, and highlight the knowledge gaps that require addressing.
- To pioneer and optimise a novel method of manufacture which is able to produce porous Ti64 structures that mimic the structure of human trabecular bone and meet all the outlined criteria highlighted from previous research as being optimal for orthopedic implants.
- Through a combination of systematic experimental work and mathematical modelling, to develop a detailed understanding of this manufacturing process and how to optimise the process parameters in order to produce scaffold material with optimal properties.
- To understand the limitations of this process and highlight a route for further development.

1.3 Thesis Structure

This thesis follows a traditional structure of 'Introduction, Literature Review, Experimental Procedures, Results/Discussion and Conclusions'. The results/discussion part of this work is divided into four chapters which represent the four key subdivisions of the work completed.

Chapter 2 provides a detailed review of the literature covering existing research relevant to this area of work. This includes the various applications of AM in the medical sector, the existing methods of manufacture that have been used to produce porous Ti for orthopaedic implants including their strengths and limitations, thin-layer drying models and their applications, and the knowledge gaps from the existing research that this project aims to address. Chapter 3 outlines the experimental procedures followed in this work including the materials and equipment used, as well as details of the processes that were followed.

Chapter 4 presents the development of the foam gel casting procedure using AM grade Ti64 powder, and how the parameters can be controlled to optimise the porosity of the resulting material to meet the criteria of orthopaedic implants. This chapter also demonstrates the stability of the optimised powder-based slurry, and the ability to extrude this foamed slurry from a syringe whilst still maintaining the optimal porous structure of the resulting material. Chapter 5 addresses the challenges around controlling the viscosity of foamed metal powder-based slurries, and investigates various methods of reducing viscosity in order to make the slurries suitable for material extrusion, whilst maintaining the slurry stability and the green strength of the dried material.

Chapter 6 presents the development of the 3D material extrusion process using foamed metal powder-based slurries, from the extrusion of single individual tracks through to the deposition of multi-layer 3D structures. In particular, this chapter highlights how the viscosity of the slurry has a significant impact on the quality of the extruded tracks, layers and full 3D structures. Chapter 7 investigates the drying behavior of Ti powder-based slurry when deposited on a heated platform, and demonstrates how this understanding is vital when designing the process parameters for 3D material extrusion. This includes the application and development of thin-layer mathematical drying models for this process, and assessing the suitability of these models for this application.

Finally, Chapter 8 summarises the key conclusions from this work and presents recommendations for further development within this area.

2 Chapter 2: Literature Review

2.1 Introduction

This review provides a broad summary of how AM technologies have been, and continue to be applied within the medical sector. Titanium alloy Ti64 is highlighted as a popular choice for orthopaedic implant material due to its mechanical strength, biocompatability and corrosion resistance. Existing manufacturing techniques used to produce porous titanium implants are reviewed, and their limitations are highlighted. Additive manufacturing is proposed as a way forward for producing porous titanium implants with specific mechanical and structural properties. The development of gel casting as a manufacturing technique is reviewed, with a focus on how it has been adapted to produce highly porous ceramic and, in more recent years, metal components. It is suggested that this technique could be adapted to produce porous Ti64, and combined with AM technology in order to capitalise on the benefits that it offers, particularly with regard to flexibility over the geometries that can be produced.

2.2 AM and Medical Applications

With the rapid adoption and development of AM technologies in recent decades across multiple sectors, it is unsurprising that there is an increasing interest in the development of AM for applications within the medical sector. The AM Platform Roadmap [42] highlights *Health* as one of the seven key sectors in which AM technologies have been adopted and is predicted to expand, along with *Aerospace*, *Automotive*, *Consumer Goods and Electronics*, *Industrial Equipment and Tooling*, *Construction* and *Energy*, and finally *Defense*, which has been added to the roadmap since its publication. Sections 2.2.1 - 2.2.5 provide a summary of how AM technologies have been utilised across various applications within the *Health* sector, and Section 2.2.7 highlights the barriers that must be overcome in order for widespread adoption of AM in this sector to be achieved.

2.2.1 Dental Applications

Out of all the medical fields the dental market represents the largest share of AM applications, with the technology currently being developed for the manufacture a range of implants and devices

including crowns, bridges, drill guides, dental aligners, dentures and maxillofacial implants, using a range of AM technologies including SLM, DMLS, SLS, SLA and FDM [28, 42–45].

Dentures provide a replacement for teeth and their connecting tissue for patients who have lost some or all of their teeth, which are designed to be removable for daily cleaning. Dentures can be full or partial depending on the clinical requirements of the patient. Removable partial dentures (RPDs) consist of a metal wire frame that connects the artificial teeth which are manufactured from acrylic, nylon or Co-Cr [46]. The wire frame is conventionally manufactured from Ti alloys or Co-Cr by producing a wax mould and then casting [47, 48]. Research has shown that metal powder sintering AM processes including SLM and DMLS can be utilised to manufacture these RPD metal frames from SS 316L and Co-Cr [49, 50], and also that this manufacturing technique can be combined with 3D scanning in order to produce a frame geometry that closely matches that of the patient's anatomy [51]. In addition to these developments, the orthodontic company Dentca (California, USA) received FDA approval in 2015 for their acrylic based UV curable resins which can be used to produce 3D-printed full and partial dentures using 3D scanning and SLA technology, with the aim to provide dentists with the ability to manufacture patient-tailored dentures on-site [52]. Further to these FDA approved acrylic resins, there has also been research conducted into the development of antimicrobial resins that can be used to produce dentures using SLA [53]. There has also been more recent interest in the application of FDM in producing complete trial dentures from polylactic acid (PLA) [54, 55], as well as the development of removable partial dentures (RPDs) produced from polyetheretherketone (PEEK) using FDM [56]. However, the approval of Dentca's SLA resins offer the most promising route to widespread application of AM technology to the manufacture of dentures.

Orthodontic implants provide an alternative to traditional dentures, whereby individual teeth are replaced by inserting implants directly into the jaw bone which provide a mount for a ceramic or metal crown to be fixed to. The implants themselves are conventionally manufactured from a rod of comercially pure titanium (CpTi) or Ti64 by machining, with further post-processing and surface treatments applied to produce rough/porous surfaces which promote osseointegration within the jawbone [57]. Over the last decade however there has been an expanding body of research in conjunction with clinical studies around the application of AM, specifically powder bed fusion methods such as SLM, SLS and DLMS, for producing titanium dental implants [58–

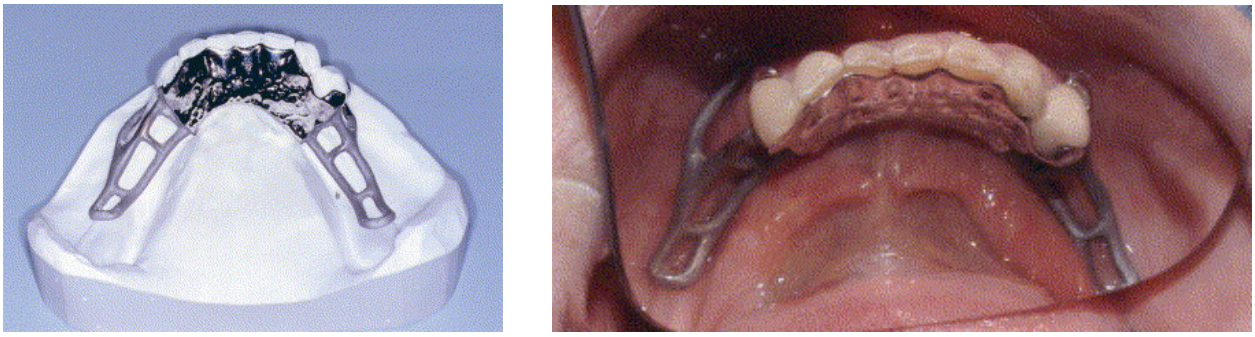

(a) (b)

Figure 3: SLM produced Co-Cr RPD frame fitted to a cast of the patient's anatomy (a) and fitted within the patient's mouth (b). Taken from [49].

61]. In general it has been concluded that AM technologies provide a superior alternative for the production of custom implants, with controlled porosity levels and surface roughness that improve the osseointegration process [62]. Ti64 dental implants have been produced using SLS with a porous outer surface and dense core have been clinically evaluated and shown to have a 94.3 % success rate after 3 years [63]. Other clinical studies have been conducted using implants manufactured in the same way with even higher success rates, but with shorter follow-up durations [64, 65]. In addition to being attached to implants as a direct replacement for lost teeth, dental crowns can also be fitted over a damaged tooth to provide protection against further damage as well as improving appearance [44]. Crowns are typically fabricated from ceramics or inert metals. The development of ceramic powder suspended photosensitive resins has opened up the potential for dental crowns to be 3D printed using SLA, which has been explored in various experimental studies [66, 67]. SLA fabricated alumina has been shown to have comparable mechanical properties to milled zirconia as well as alumina fabricated using conventional subtractive techniques, and superior to dry pressed alumina [66, 68, 69]. The main complication with SLA fabricated ceramic crowns is the post-processing required to burn out photosensitive polymer binder, as well as the subsequent sintering of the ceramic powder. These processes cause anisotropic shrinkage of SLA fabricated ceramic components which raises an issue with dental crowns where high geometric accuracy is required, and therefore further process/material development is required in order to overcome these challenges [66]. In addition to SLA, there is also some emerging research around FDM 3D printing of dental crowns from polyvinyl alcohol (PVA) filament [70], however this is still in its infancy and only the geometrical accuracy of crowns fabricated in this way has been assessed.

In some clinical cases, patients who suffer from a fractured chin or jaw or damage to the bone tissue as a result of cancer may require maxillofacial (specifically mandibular) implants to provide partial or full replacement of the jawbone [12]. Currently, autologous bone grafting is the gold standard technique for the fabrication of these implants [71], however the drawbacks of this process have already been discussed in Section 1.1.1. AM techniques have been used to assist in the fabrication of these types of implant, such as using SLA to produce a casting mould from patient CT scan geometry data into which molten titanium was cast [72]. The cast titanium formed a tray which was filled with harvested trabecular bone, and covered with harvested cortical bone which was then shaped to provide the desired geometry. The tray was fabricated in this way in order to provide an implant shape that accurately restored the patient's jaw line. Whilst this method reduces the amount of bone material that needs to be harvested compared with conventional autograft techniques, it is still quite a complex multi-step fabrication process and does still require bone material to be harvested from the patient. Therefore there is clearly still demand for the development of AM methods that can directly fabricate complete maxillofacial implants that remove the requirement for bone material harvesting. There have been news reports of an elderly patient in 2012 who became the first person to undergo a full titanium jawbone transplant that was manufactured using SLM [73, 74], however very little information is available regarding the design and fabrication processes, and no details regarding the properties of the implant and its long-term success are provided. Despite the lack of provided information, this example once again demonstrates how AM technology continues to provide unique solutions to modern-day medical challenges.

Binder jetting 3D printing has been used to produce hydroxyapatite maxillofacial implants which have been successfully clinically tested in-vivo (Figure 4) [75]. Custom implants were fabricated from CT scans of ten patients using a Z406 3D printer (Z-Corporation, USA) which uses an inkjet printhead to deposit binder upon successive layers of powder. The 3D models were modified to design internal porous structures to allow osseointegration. The powder material used was α-tricalcium phosphate, which was selected because with the addition of water it forms hydroxyapatite, which also solidifies without the need for sintering. The binder/curing agent that was deposited was a solution mixed using sodium chondroitin sulfate, disodium succinate and distilled water. Previous attempts to produce implants using this method had resulted in insufficient

mechanical strength for surgical handling, meaning the implants had to be sintered which impacts dimensional compatibility because of shrinkage as well as potentially compromising biodegradability [76]. Sufficient mechanical strength for surgical handling was achieved within this work by optimising the powder particle size and the viscosity and pH of the curing solution. Osseointegration of the host bone within the implants was observed within all patients after 6 to 12 months. This work presents promising suitability of implants fabricated by binder jetting 3D printing for maxillofacial implants, however it should be acknowledge that this artificial hydroxyapatite bone material would not be suitable for load bearing applications due to insufficient mechanical strength. There has been recent research and in-vivo clinical testing of 3D printed PEEK mandibular implants [6]. The specific AM technology used to fabricate the implants is not stated in the study, but is assumed to be FDM. The clinical testing presented a number of positive outcomes including no observed local infection or inflammatory responses. However, the bio-inert nature of PEEK means that it cannot provide osseointegration and so the implants were instead fixed to the surrounding bone using titanium screws, increasing the risk of implant failure in the long-term. Therefore, further development of the material is required before these implants can be reliably implemented.

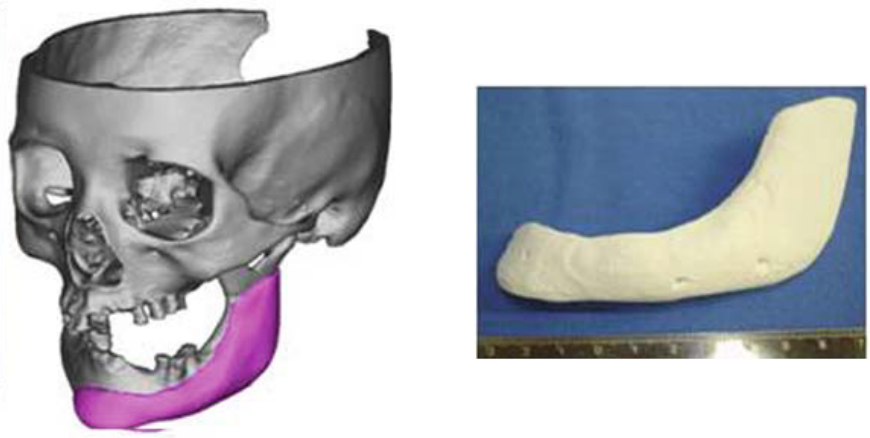

Figure 4: Images showing 3D CAD model generated from CT scan data (a) and hydroxyapatite binder jetting 3D printed maxillofacial implant (b). Taken from [75].

2.2.2 Surgical Guides and Models

AM combined with 3D imaging (predominantly MRI and CT scanning) provides the ability to produce models of a patient's anatomical structure which can be used by surgeons as a guide, and

also for training purposes [28, 45]. Providing surgeons with highly accurate 3D models of a patient's anatomy can improve surgical results and reduce medical errors, and studies have demonstrated the benefits of implementing these methods for educational purposes and surgical planning [77, 78]. Surgical models have been manufactured using these methods to assist with liver transplants, renal malignancy surgery, laparoscopic pyeloplasty surgery and cardiovascular surgery, by producing accurate 3D models of patients' livers, tumors, blood vessels, organ contours, nephrons, ureter, renal pelvis, kidneys and cardiovascular systems [79–84]. In addition to the dimensional and geometric accuracy of 3D models produced using 3D imaging and AM, technology including binder jetting and material jetting can produce full-colour models allowing the components of a patient's anatomy to be clearly distinguished [12]. Also, the use of translucent materials, or printing mesh structures rather than solid bodies, can improve visibility of the anatomy being modelled, thus providing surgeons with a clearer view [77].

2.2.3 Bioprinting

Bioprinting refers to the guided deposition of living cells to produce artificial living tissue, through the application of AM technologies including SLA, material jetting and material extrusion [45]. Whilst these methods have been successfully implemented to develop soft-structure implants for tissue reconstruction, significant development is still required in order to be able to produce fully-functioning anatomical models and artificial organs [12]. Bioprinting typically involves the creation of a solution containing biomaterials which forms a hydrogel that is then extruded, cured or sprayed in a layer-by-layer manner to produce full 3D artificial tissue structures [28]. Hydrogels are made up of crosslinked hydrophilic polymers that are capable of absorbing large quantities of water without dissolving, which creates an ideal environment for encapsulating cells [85]. Materials that have been used in studies to create hydrogels for bioprinting include alginate, fibrin, nano-hydroxyapatite, collagen and hyaluronic acid [45]. Alginate presents a number of properties that make it effective for use as a hydrogel, which when combined with its high availability and non-immunogenicity make it a popular choice of biomaterial [86]. Various studies have combined alginate with living tissues including collagen and other human stem cells to produce bioinks or hydrogels for bioprinting 3D tissue structures [85, 87, 88], some of which have shown promising results from in-vitro testing, however further detailed in-vivo testing is still required for these artificial tissue structures before

they can be adopted.

2.2.4 Pharmaceutical Applications

The first extended drug release formulation was released seventy years ago [89], and since then there has been an increasing interest in the development of new techniques that allow release formulation to be personalised to the patient needs [90], however currently still around 70 % of oral medicines are immediate release formulations [91]. AM technology offers obvious advantages regarding dosage forms and formulation for pharmaceutical drug delivery, and whilst these techniques are in their infancy there has been an increasing research interest in the application of AM within the production of both oral and transdermal drugs [12], using techniques including FDM, binder jetting, SLA, DLM and SLS [86, 90]. These methods can be used to produce oral drugs with various shapes and internal structures, which can be altered to tailor the drug release or even combine multiple active pharmaceutical ingredients (APIs) with different release rates, resulting in better dispersion throughout the gastrointestinal tract as well as improving dose accuracy when compared with manual dose splitting [12, 90]. The various AM techniques for producing oral pharmaceutical drugs that have been explored all involve combining the API(s) (typically in powder form) with a biocompatible/bioabsorbable material and producing a structure that enables them to be released through dissolution whilst within the digestive system [90]. There is limited availability of biocompatible FDM polymers, however traditional FDM polymers such as PLA, PVA and EVA (ethylene-vinyl acetate) are all non-toxic and have been applied to the development of formulations for drug delivery [92–95]. PVA is already used within oral drug formulations [96], and EVA is used within transdermal drug delivery systems [97], therefore these polymers show promising signs of being suitable for the production of oral drug formulations using FDM. The methods for loading the API within the polymer filament that have been explored are soaking the filament and printed tablets in API powder dissolved within a solution, and melting the polymer and combining with powder API prior to extruding into a filament. The drug loading level achieved through soaking of the filament and tablets is fairly limited ($<$ 2 %) [98–101], whereas higher loadings of up to 70 % were achieved through melting and mixing prior to extruding the filament, although the addition of plasticisers was required at higher loadings [94, 102, 103].

In addition to oral drug delivery, the use of AM technologies is also being applied to the

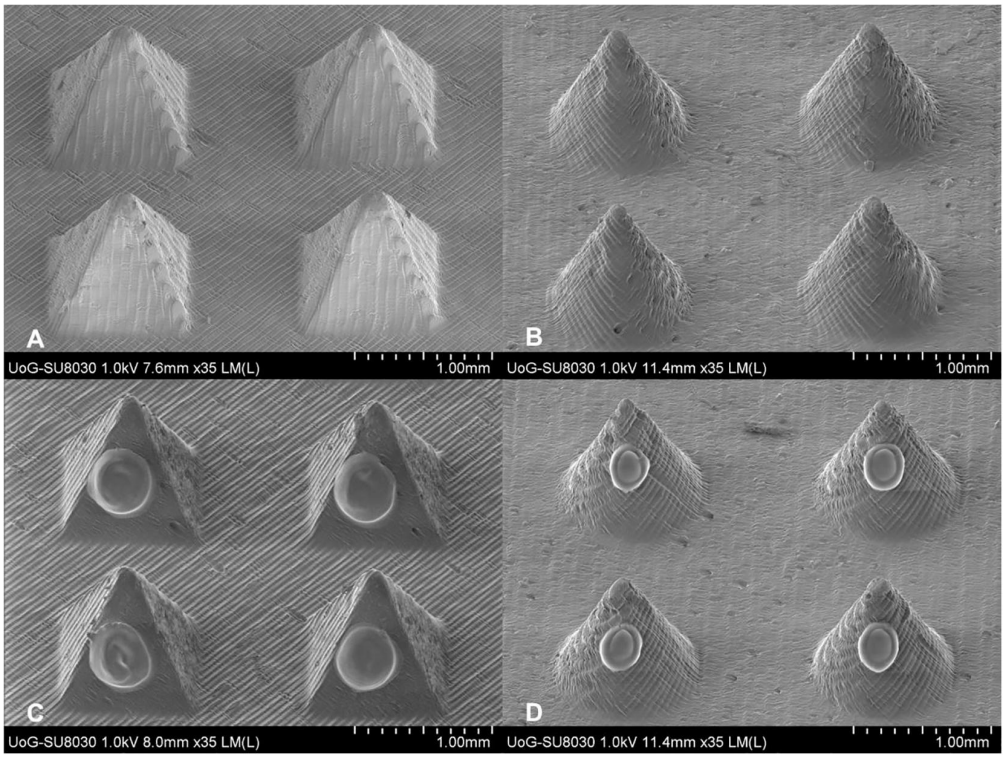

Figure 5: SEM images of micro-SLA fabricated microneedles for TDD showing different needle geometries and insulin dose loaded onto individual needles using material jetting. Taken from [104].

development of transdermal drug delivery (TDD). TDD refers to a pain-free method of drug delivery where the formulation is applied to the patient's intact skin, and passes through to the dermal layer where it becomes available for systematic absorption, predominantly through absorption or the use of micro-needles [105, 106]. In order for drug molecules to pass through the outer layers of skin through absorption, they must possess a strict set of properties, which is unfortunately not the case for many pharmaceutical drugs [107]. The most effective way to overcome this barrier is the use of microneedle arrays which penetrate the outer skin barriers allowing the drug formulation to pass directly through to the dermal layer. Microneedles are minimally invasive devices which contain needles that are long enough to pass through to the dermis ($300 - 750\mu m$ [108, 109]), but also narrow enough to avoid stimulating the nerves. Delivery of the drug formulation is typically achieved in one of two ways; the use of hollow-bore microneedles which allow the drug to flow directly through the centre of the needles, or polymeric drug-containing microneedles which release the formulation as they biodegrade within the dermis [106]. Microneedles have been manufactured from a range of materials including silicon, metals and polymers, using a variety of microfabrication

techniques such as etching, electrodeposition and micromoulding [107]. Due to the ability of some AM technologies to produce components with micrometer scale precision, there has naturally been interest in applying AM to the production of TDD microneedle arrays [12]. Processes including SLA, DLP and material jetting have been used to manufacture microneedle arrays, either directly or by producing micromoulds which were then used to fabricate the needles [104, 110–114]. In some of these studies the microneedle structures were fabricated using AM technologies such as FDM or CLIP (continuous liquid interface production - similar to DLP), and then loaded with an API either by soaking the arrays within a solution [113, 114]. Pere et al. fabricated the microneedle arrays using micro-SLA technology in conjunction with a biocompatible resin, and then applied an insulin coating to the needles using material jetting [104]. The results from their in-vitro tests using porcine skin show that this method of delivery produced rapid insulin release rates. In addition to this, they highlight that the use of material jetting in coating the microneedle arrays allows a highly accurate specific dosing of API to be applied. The microneedle structures produced in this study are presented in Figure 5, which also shows the insulin loaded onto the individual needles.

2.2.5 Patient Customisable Devices

The ability of AM technologies to easily fabricate complex geometries, alongside the use of 3D scanning technology that can accurately acquire and generate 3D models of physical objects or anatomy, lends itself naturally to the application of patient customisable medical devices, and as such there have been a range of developments in this area. AM has been applied to fabricate a wide range of patient-specific medical devices including prosthetics, splints, insoles and hearing aids [12, 28, 43, 73]. Zuniga et al. fabricated a prosthetic wrist-driven hand from PLA and acrylonitrile butadiene styrene using various FDM machines [115]. The devices were tested by children with congenital upper-limb deficiencies for 6 months, and it was reported that the children used the prosthetic devices for a range of activities during this duration including school activities, sport and playing. Paterson et al. compared a range of AM technologies for fabricating customised wrist splints, and concluded that SLS, SLA and material jetting showed promising results, but that further research into the materials, processes and splint optimisation is required in order to realise the full potential of AM within this application [116]. Images of some of the splints fabricated in this work are presented in Figure 6.

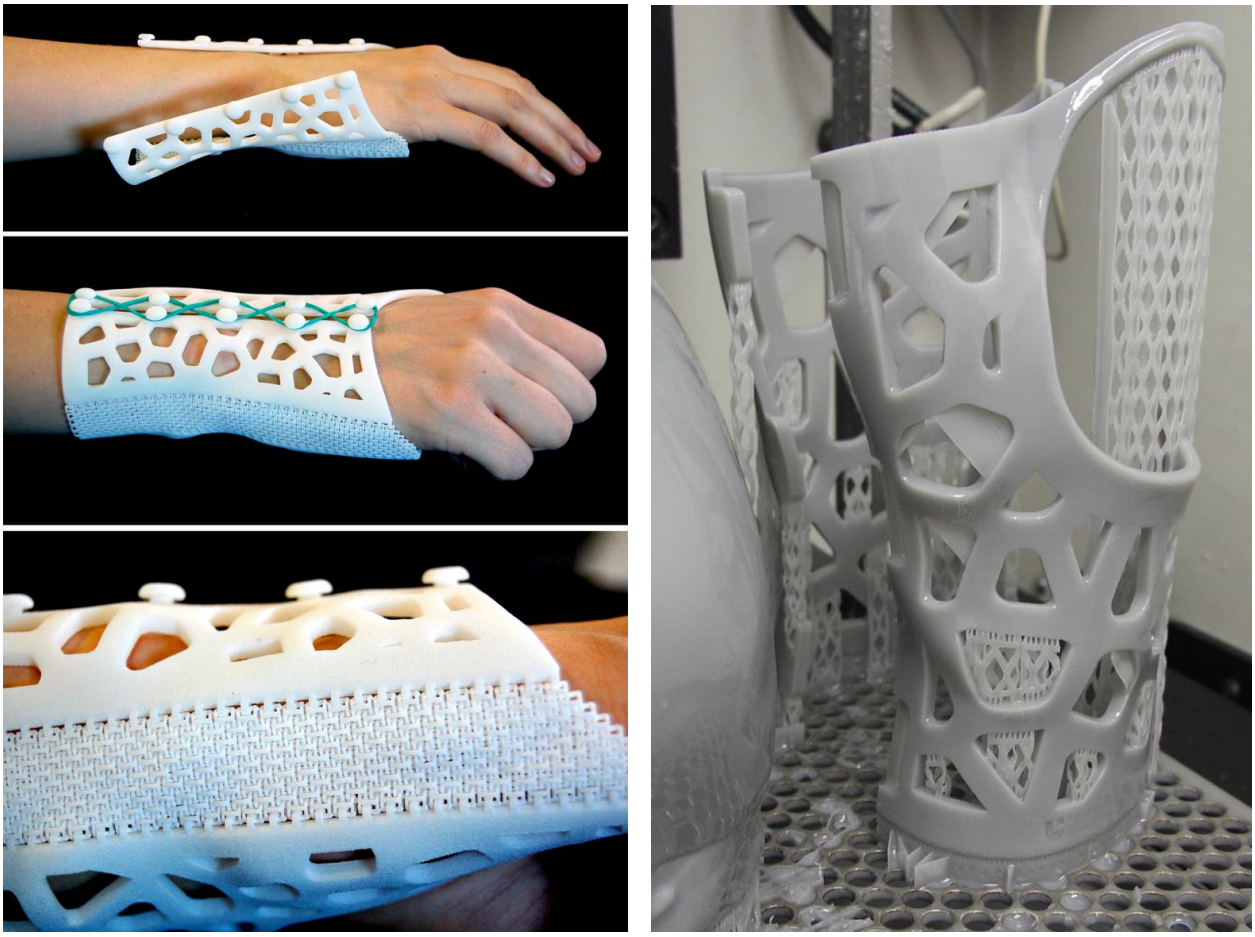

(a) (b)

Figure 6: Custom wrist splints fabricated using SLS (a) from nylon powder (PA2200) and SLA (b) technology using a tough and durable resin (Accura Xtreme, 3D Systems). Taken from [116].

AM has been applied to the development of patient-specific insoles for the treatment of plantar fasciitis and diabetic foot [117, 118]. Flexible TPU insoles with porous inner structures were fabricated using FDM with gradient modulus which was achieved by varying the porosity throughout [118]. The insoles were not tested by users, however the work clearly demonstrated the feasibility of the process and highlighted that such AM fabricated insoles can provide optimal support through the careful control of the inner porosity. Xu et al. performed an extensive study with 60 patients suffering from bilateral plantar fasciitis in order to compare traditional pre-manufactured support insoles with custom 3D printed insoles [117]. 3D gait scanning technology was used to obtain the geometry and dynamic foot pressure of the patients, which was then used to produce CAD designs of the custom insoles. The insoles were fabricated from EVA by a commercial orthosis manufac-

turer, however the specific AM technology that was used is not stated. The scanning equipment was used to obtain pressure, strength and contact area data of the patients' feet over 8 weeks of use for both the pre-manufactured and custom insoles, and also feedback was gathered from the patients throughout the duration of the study. The results show that the custom 3D printed insoles provided more effective support and that the patients reported greater comfort compared to the pre-manufactured insoles.

Figure 7: Images showing a face mask fabricated using SLS technology from nylon in response to the demand for PPE during the COVID-19 pandemic. Taken from [119].

The use of AM technology in the fabrication of patient specific hearing aids is potentially the most widely adopted use of AM in the medical sector. Various hearing aid manufacturers use technologies including SLS and SLA combined with 3D scanning to fabricate hearing aids with geometries tailored to the patient [28, 120]. Hearing aid manufacturer Sonova (Sonova Group,

Switzerland) have been producing hearing aids using AM technology for over 20 years. Their fabrication process involves creating a silicone impression of the ear canal, then using 3D scanning technology to create a 3D model which is then used to fabricate the hearing aid shell using SLA [121].

In response to the unprecedented demand for face masks during the COVID-19 pandemic there was a rapid rise in the use of AM technologies to fabricate face mask and shield components [122–124]. Components were fabricated from a range of materials including nylon, PET, PLA, and even biodegradable materials, using AM technologies such as SLS and FDM [119, 125, 126]. The use of AM in conjunction with 3D scanning technology allowed masks to be custom-fabricated to fit individuals, and this unique situation also demonstrates how AM technology is able to provide a rapid response to demand for specific components, which continues to be an issue faced in many sectors today. Figure 7 shows a face mask fabricated using SLS that was custom-designed to fit a specific individual using 3D scanning.

2.2.6 Acetabluar Cups

Total hip arthroplasty, also known as total hip replacement, is a surgical procedure in which a damaged or worn-out hip joint is replaced with an artificial implant. During the surgery, the damaged portions of the hip joint, including the ball-shaped head of the femur and the hip socket (acetabulum), are removed and replaced with prosthetic components. The artificial hip components can be made of metal, ceramic, or plastic materials and are designed to mimic the natural movement of the hip joint. The replacement acetabular cups have historically been manufactured from Ti64 using traditional methods, however a range of clinically approved artificial acetabular cups that have been manufactured using EBM are now available for this procedure. It is estimated that at least 10 % of the replacement acetabular cups used for this procedure in the UK in 2017 were manufactured using AM, and it is likely that this figure has significantly significantly increased since then [127]. Conventionally manufactured acetabular cups present issues around poor fixation with the host bone, despite being widely clinically implemented [128]. Cups produced using AM have been designed with a highly porous surface in an attempt to provide enhanced fixation with bone compared to conventionally manufactured cups. Figure 8 presents examples of Ti64 acetabular cups produced using EBM which have been developed for this procedure.

Figure 8: Images showing Delta TT (Lima Corporate, Italy) and Mpact 3D Metal (Medacta, Switzerland) acetabular cups with porous surfaces manufactured using EBM. Adapted from [127].

Whilst these artificial acetabular cups have undergone benchmark testing in order to obtain the required certification for clinical use, the only clinical testing that has been performed has been short-term due to the fact that this process is still relatively new [127, 128]. The short-term studies have demonstrated promising clinical results regarding the revision rates of cups produced using AM [129, 130], however there is a clear demand for long-term clinical testing in order for the success of these newly developed cups to be assessed against those manufactured using traditional methods.

2.2.7 Barriers to Adoption of AM in Medical Applications

These developments in the application of AM in the medical sector clearly demonstrate that this technology offers the capability to tackle many complex medical issues faced in society, however significant further development is required before widespread adoption of these methods can be implemented. Multiple barriers remain that must be addressed including a lack of clinical design interfaces for AM systems or standardised geometry generation processes (particularity for patient customisable devices), uneconomic material and processing costs, limitations regarding material properties, limited selection of biomaterials suitable for AM, challenges regarding sterility and packaging and the strict requirements that have to be met in order to receive FDA approval [12, 86, 131].

2.3 Methods of Manufacturing Dense and Porous Ti

2.3.1 Ti64 Sintering and Properties

Ti64 is an alpha-beta titanium alloy containing aluminium (at $5.5 - 6.75$ $wt\%$) and vanadium (at $3.5 - 4.5$ $wt\%$) [132], which presents impressive mechanical properties despite its relatively low density (4.5 g/cc) [133]. The mechanical properties of Ti64 can vary depending on heat treatment processes. Table 2 presents typical property value ranges for 'well-processed' Ti64. Different heat treatment processes alter the microstructure of the alloy, specifically the levels of both the alpha and beta grain structures [134].

	Melting Point (K)	***Young's Modulus (GPa)***	***Shear Modulus (GPa)***	***Bulk Modulus (GPa)***	***Poisson's Ratio***	***Yield Stress (Tensile, MPa)***	***Ultimate Tensile Stress (MPa)***	***Hardness, Rockwell C***	***Uniform Elongation (%)***
Min	1878	104	40	96.8	0.31	880	900	36	5
Max	1933	113	45	153	0.37	920	950	36	18

Table 2: Summary of mechanical properties of Ti64 alloy. Data gathered from [135–137].

Powder Metallurgy (PM) is an extremely popular manufacturing technique used across a wide range of industries that produces metal components from powders. The process typically involves mixing the metal powder with additive or lubricants, compacting the mixture using a die into preform green compacts, sintering in a controlled atmosphere in order to metallurgically bond the particles, and finally any post-processing that is required [138]. PM provides a comparatively low-cost, low-energy and material-efficient manufacturing route that offers high workability and near-net-shaping of components [139, 140]. The high melting point of the alloy means that a high sintering temperature is required when fabricating Ti64 by PM. Due to the high cost of the material, PM is one of the preferred fabrication techniques because of its near-net-shape capabilities

which help to reduce wastage [141, 142]. However, PM fabrication typically produces material with unwanted residual porosity which compromises its mechanical properties, therefore there is been significant interest in developing PM conditions which are able to produce highly dense Ti64 with mechanical properties comparable to that of the wrought material [141]. Numerous studies have explored various sintering techniques for Ti64 in order to achieve the highest possible final density, including powder compaction techniques prior to sintering such as die pressing and ultrasonic compaction [30, 142–144], as well as optimising sintering pressure, temperature and duration [30, 142, 145], reporting achieved sintered relative densities as high as $99.6 - 99.7$ % [143, 144]. It has been demonstrated that for various sintering temperatures, increasing sintering time up to a certain point results in higher final relative densities, but that the rate of increase then plateaus and further increase in time results in no further improvement in final density [144, 145].

The residual porosity that occurs as a result of PM fabrication techniques has actually been exploited as a method of producing porous Titanium for the purpose of orthopaedic implant material, which is discussed further in Section 2.3.3.

2.3.2 Historical Development of Orthopaedic Implant Manufacture and Fixation

The clinical methods for implant fixation have evolved dramatically over the past century. Historically, fixation was achieved through impaction of the implant within the medullary cavity of bone (the hollow part of bone that contains bone marrow) or by means of mechanical fixation such as screws [146]. Implants secured by impaction rely on compressive stress for fixation, but often resulted in failure due to stress concentrations developing or motion between the implant and surrounding bone resulting in reduced bone in-growth and a loss of fixation [147]. In the 1950s an acrylic cement was developed by John Charnley [148] to overcome the issues highlighted with the alternative methods of implant fixation. The cement consisted of a powder component and a fluid component which were mixed together prior to application, and then self-cured after a certain duration allowing for the surgical procedure to be completed prior to curing. This method of fixation presented the benefit of ensuring a larger contact surface area between the implant and surrounding bone, which reduced concentrations of stress and as such decreased implant failure rates due to implant loosening and stress-shielding. The success of this fixation method compared with the traditional methods led to it becoming adopted as the standard procedure, however over

time concerns were raised regarding the long-term reliability of this implant fixation method with delayed failures occurring as a result of relative motion between the acrylic cement and bone as well as cracking due to the presence of voids [147]. As a result of these concerns, in the early 1970s there emerged an interest in the development of porous-coated implant systems that achieve stable fixation by bone in-growth within the porous surfaces [149].

Early methods of producing Ti64 with a porous coating included sintering of powder or wire mesh onto the dense titanium surface, and more recently have included plasma-spraying of Ti powder on the surface [150–153]. Successful bone in-growth within the porous coating of Ti64 implants has been observed in various clinical trials [147], with enhanced initial bone growth being achieved with the application of a thin hydroxyapatite or polymeric layer upon the porous coating [154, 155]. Whilst the development of these porous coated implants provided a suitable alternative to cement based fixation of implants, the issue of mismatch in mechanical properties between implant material and that of the adjacent bone, and the complications this presents (as discussed in Section 1.1.1) still remain. In addition to this, as previously discussed, interconnected porosity is vital for vessel growth and fluid transportation throughout the implant. Also, studies have observed reduced fatigue strength of Ti64 with a porous coating produced by sintering of powder onto the surface due to crack initiation close to particle/substrate contact interfaces [156]. As a result of these complications, in the early 2000s attention shifted with the suggestion that entirely porous Ti structures could be created which could achieve mechanical properties comparable to that of human bone whilst also stimulating bone growth by providing an interconnected porous structure for osseointegration as well as fluid transportation and vessel growth [157]. Since this point the primary focus of research in this field has been on developing open-cell porous Ti scaffolds, and as a result various methods of producing such implant material have been developed including a range of powder metallurgy techniques, gel casting and additive manufacturing. The methods are all explored in detail within this section.

2.3.3 Powder Metallurgy and Porous Ti

As previously discussed in Section 2.3.1, the unfortunate drawback of PM is that the relative density of the final material after compaction and sintering of the powder is unable to match that of the wrought material (typically < 95 %) [142], which in turn has a detrimental impact on the

mechanical properties [158]. The residual porosity that is experienced is a result of gaps within the compacted particle arrangement which causes incomplete densification during sintering, or due to phase and structural changes that occur during the sintering process [142, 159]. Whilst the residual porosity phenomenon is undesirable when manufacturing dense materials using PM, for the application of bone implant material it is something that has been exploited in attempts to produce porous Ti scaffolds.

2.3.3.1 Loose Sintering

The PM route can provide a cost effective and flexible way of producing porous materials, where porosity can be controlled by altering the compaction pressure, sintering temperature of the powder and particle size of the powder [158, 160]. As discussed in Section 2.3.1, increasing powder compaction pressure prior to sintering has been shown to help produce almost fully dense material. In contrast, loose powder sintering is the extreme case where the powder is sintered without prior compaction which creates the maximum porosity achievable through the PM route. However, as the porosity is simply a result of the gaps between powder particles due to lack of compaction, this process is fairly limited in terms of the level of porosity that can be achieved, although controlling sintering temperature and increasing the particle size of the powder can provide some scope [160, 161]. Figure 9 shows the effect of sintering temperature on porosity of Ti and Ti64 manufactured by loose sintering. The higher porosities observed for Ti64 within the overlapping temperature range is explained by the greater particle size of the Ti64 powder than the Ti powder, with mean diameters of 107 μm and 74 μm respectively.

Similarly, Oh et al. explored fabricating porous CpTi structures using PM by controlling sintering conditions including particle size range, temperature and pressure [30] with just a low compaction pressure of 70 MPa applied to the powder prior to sintering. The powder compacts were sintered at a range of temperatures between $1173 - 1373$ K and under various pressures of $0 - 10$ MPa, which resulted in final samples with a range of porosity between $5 - 37.1$ %. The maximum porosity of 37.1 % was achieved at a sintering temperature of 1173 K with no pressure applied, which is similar porosity to the values achieved by Esen et al. using the same technique [161]. The Young's modulus of the sample produced with this porosity was reported to be 9 GPa, which is comparable to that of human cortical bone, however the yield strength reported was lower

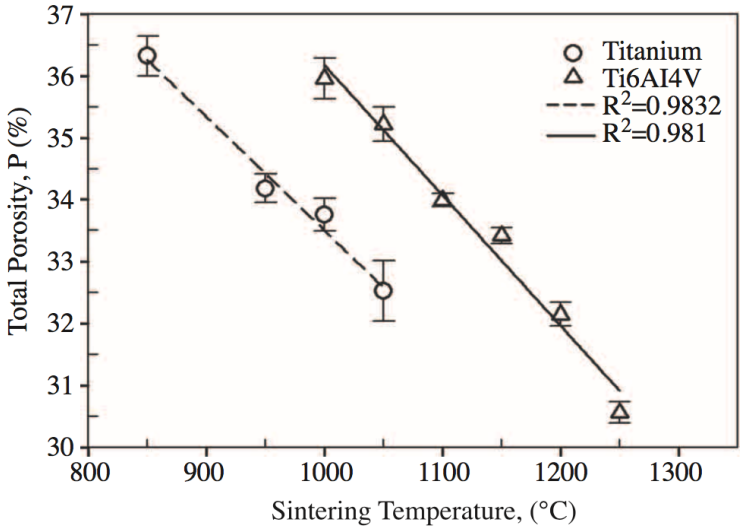

Figure 9: Graph showing effect of sintering temperature on porosity of Ti and Ti64 manufactured using loose powder sintering. Taken from [161].

than that of cortical bone which is explained by the lower initial yield strength of bulk CpTi. As discussed in Section 2.3.1, it has been demonstrated that greater average powder size produces higher levels of porosity in samples produced using PM [158]. This work confirms this observation, but also interestingly highlights that powder size has a greater influence on porosity when sintering is performed under pressure than in ambient pressure conditions. When sintering at 1173 K with no pressure applied, samples produced from average powder size of 374 μm resulted in porosity that was only $<$ 3 % greater than those produced from powder with an average size of 64 μm, however at 10 MPa pressure the difference in porosity was 14 %.

In addition to being restricted by the levels of achievable porosity, the diameter of the pores produced via loose sintering are extremely limited. Mean pore sizes achieved are typically <50 μm which is well below the optimal range for bone in-growth [160, 161]. Unfortunately, Oh et al. provide no analysis of the pore sizes produced by sintering different powder sizes, so it is not possible to confirm whether increasing the powder particle size can result in the creation of larger pores [30]. Increasing sintering temperature has been observed to cause a slight reduction in pore sizes [161]. Hence, whilst loose sintering is a relatively straight forward way of producing porous Ti components which can produce Ti samples with mechanical properties close to that of cortical bone, by itself it is unable to achieve the necessary levels of porosity and pore sizes required for orthopaedic implants.

2.3.3.2 Space-holder

A common adaptation of the PM route used to increase porosity and pore sizes is the space-holder technique [29]. This method involves mixing Ti powder with a space-holder material of a larger particle size and the mixture is then compacted by applying pressure. The space-holder particles are removed either by dissolution or by burnout prior to sintering the Ti powder [157]. Several materials have been used as space-holders in order to control the size and shape of the pores produced including urea, starch, magnesium, polypropylene carbonate, copper, stearin, steel, sodium chloride and sodium aluminate [29, 162–165]. In a direct comparison between loose powder sintering and the space-holder technique, Torres et al. demonstrated that the pore sizes and porosity that can be obtained via loose sintering are limited in comparison with what can be obtained via the space-holder technique [166]. CpTi powder with a mean particle size of 23.3 μm was sintered without compaction at $1000°C$ and $1100°C$, whilst NaCl space-holder particles of mean diameter 384 μm were mixed with the Ti powder at volume fractions of $40 - 70$ % before compaction, dissolution of NaCl particles and sintering of the Ti powder. The highest porosity and mean pore diameters obtained by loose sintering were 41.5 % and 18 μm respectively compared 65.9 % and 92 μm using the space-holder. This study also showed that the space-holder technique offers significantly more control over both porosity and pore size by varying the volume fraction and particle size of space-holder material in comparison with loose sintering.

Carbamide (or urea) has been a popular choice of space-holder material for creating porous Ti structures due to its low decomposition temperature making removal easy prior to sintering [167] and its range of available particle shapes which allow control over pore geometry [168]. Kotan and Bor were able to produce Ti64 structures with porosity of $60 - 75$ % and a mean pore size of ~ 400 μm using spherical carbamide space-holders of diameters $200 - 600$ μm, however the mechanical properties of the samples were insufficient due to the sintering temperature [167].

Spherical sugar pellets made of sucrose and starch, that are widely used in pharmaceutical applications, have been investigated as a highly bio-compatible space-holder material [169]. Porous CpTi was produced with various levels of porosity by mixing different volumetric quantities of sugar pellets ($30-70$ %) followed by compaction of the mixture, dissolution of the sugar in distilled water at $70 - 80°C$ and sintering the Ti powder. The resulting structures had porosities ranging from

$20 - 55$ % in relation to the quantity of space-holder used, showing that porosity can be easily controlled. The samples with low levels of porosity had very limited interconnectivity (as low as 10 %) due to the pores being isolated, whereas those produced using a 70 % volumetric quantity of space-holder had extremely good interconnectivity (up to 98 %). An example of the porous structure produced as well as the pore interconnections is shown in Figure 11b. The overall porosities of the structures were around 10 % lower than the volumetric quantity of sugar pellets within each initial mixture, which is suggested to be a result of shrinkage during sintering. No measurements of the pore sizes are provided so it is difficult to analyse against the ideal values for human bone implants, however, the initial sugar pellet sizes were in the range of $212 - 500$ μm which would have likely resulted in pore sizes in the optimal region for this application.

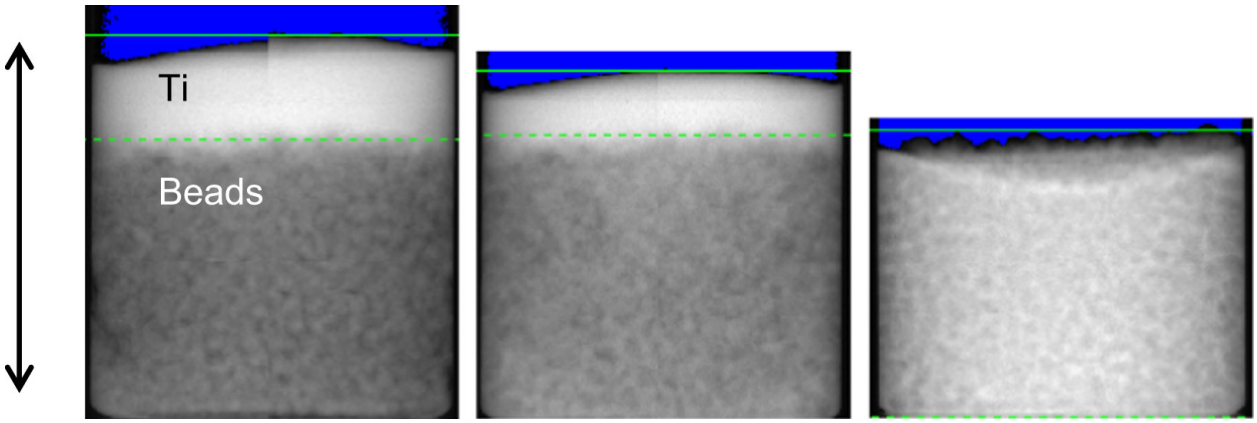

Figure 10: X-ray radiographs showing progression of Ti being tapped into a NaCl particle network after 0, 50 and 100 taps (left to right). Taken from [170].

A novel method for mixing Ti powder and space-holder particles was developed by Jia et al., whereby rather than employing the conventional dry mixing technique CpTi powder was mechanically tapped into a pre-existing NaCl particle network [170]. Near-spherical NaCl beads of four different size ranges ($0.5 - 1, 1 - 1.4, 1.4 - 2$ and $3 - 2.5$ mm) were packed into a cylindrical die and CpTi powder (mean diameter of 39 μm) was placed on top before being mechanically tapped for an optimised number of cycles to ensure complete progression of Ti powder within the salt particles. The mixture was then compacted, before the NaCl being removed by dissolution in water, followed by drying and sintering of the Ti parts. Figure 10 shows the progression of Ti powder being tapped into the NaCl network. The final porosities of the resulting structures were 79, 75, 74 and 71 % for samples produced using $0.5 - 1$ mm through to $2 - 2.4$ mm. Pore geometry and interconnectivity

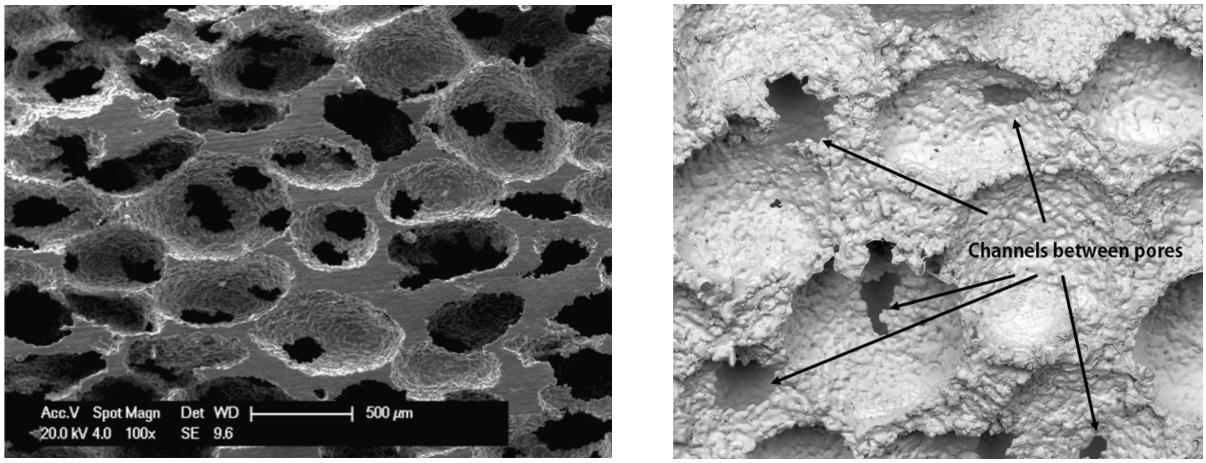

(a) (b)

Figure 11: SEM images showing interconnected porous structure of Ti scaffolds produced by mechanically tapping Ti powder into a NaCl network using $0.5 - 1$ mm space-holder particles (a). Taken from [170]. Interconnected porous structure of CpTi produced by space-holder sintering using sugar pellets (b). Adapted from [169].

was analysed for the Ti parts made using $0.5 - 1$ mm salt particles, the structure of which is shown in Figure 11a. The mean pore size was measured at 375 μm with mean interconnecting window size of 190 μm and the connectivity density of the pores was measured to be higher than that of human bone. The impressive interconnectivity is due to the tapping process which pre-establishes contacts between the NaCl particles during initial compaction before incorporating the Ti powder into the available spaces. These properties make the porous Ti parts produced using this method very suited to the application of bone implant material, and show that this method is able to obtain higher levels of porosity and interconnectivity than conventional dry powder mixing and compaction. The Young's modulus of the sample produced using $0.5 - 1$ mm salt particles was found to be 0.86 GPa, which is stated to be a close match to that of trabecular bone. Whilst this is true, this value is significantly below that of cortical bone, and as such if this was used as an implants it may not be able to provide sufficient support for load bearing applications.

Whilst the space-holder technique has been shown to be capable of producing Ti scaffolds with promising levels of porosity and pore sizes for implant application, it does suffer from a number of drawbacks. Issues can be caused by irregular mixing of Ti and space-holder powder which creates unpredictable distribution of pores. Also, a lack of contact between space-holders results in poor interconnectivity between pores which is absolutely essential within bone implants, as outlined in

Section 1.1.1. Finally, the geometry of implants produced using this method is restricted by the use of a mould. Ideally implant geometry needs to be tailored to specific applications, which would mean that a new mould would have to be produced each time. Using a tapping technique to incorporate Ti powder within a network of NaCl beads has been shown to overcome the drawbacks associated with irregular distribution of pores and poor interconnectivity [170], however still suffers from the same geometric constraints.

2.3.3.3 Hollow Particle Sintering

Porous metals can be produced by packing and sintering hollow particles or sacrificial spheres coated in metal powder-binder slurry that create hollow particles when sintered. Hollow particle sphere sintering was originally developed for the production of ceramic structures, but has since been adapted to metals [171]. Hollow spheres are created by injecting powder based slurries through the outer jet of a coaxial nozzle, with gas being blown through the inner jet to form bubbles [172]. The slurry forms a film around the gas bubbles, which when dried creates hollow spheres that have sufficient strength for handling and further treatment without significant breakage or deformation. These spheres are then sintered either individually or as a packed structure, burning out the materials involved in creating the slurry, and causing coalescing or 'sintering necks' between adjacent particles resulting in an interconnected porous structure.

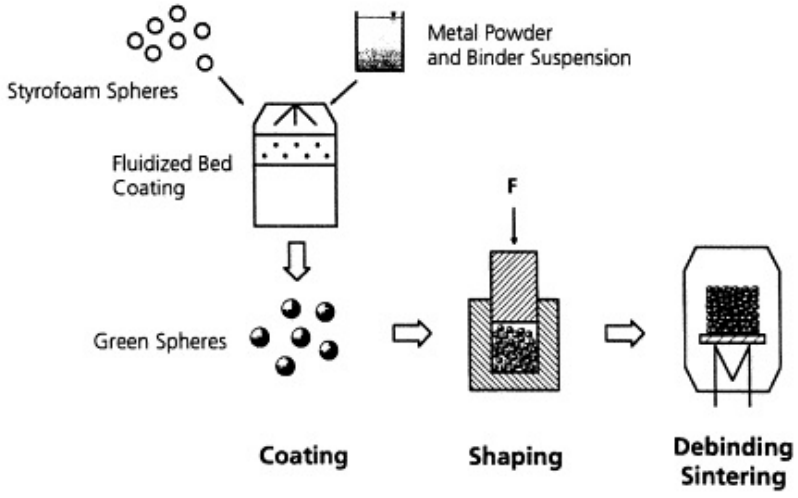

Figure 12: Schematic showing the coating process for making hollow Ti and SS sphere structures using sacrificial styrofoam spheres. Taken from [173].

Coated sacrificial spheres are produced by spray coating of a metal slurry (Figure 12), followed by a similar sintering process to as described for hollow spheres, which removes the sacrificial material leaving hollow interconnected metal spheres [174]. These highly porous structures have gathered interest for a variety of applications due to their energy absorption under compression, sound and thermal insulation properties, and low weight. To date, however, this technique has not been used to produce porous implants. This may be explained by the level of porosity and large pore sizes that are produced being greater than what is required for this application. Typically the hollow sphere diameters range from $0.8 - 8\ mm$ [157], and can result in porosities as high as 97 % [174].

2.3.4 Selective Laser Melting and Porous Ti

Selective Laser Melting (SLM) is an AM technology that was first developed in 1998 as a way of manufacturing metal parts directly from powders [175]. Other AM methods for producing metal components from a powder have been developed, such as Selective Laser Sintering and Electron Beam Melting, however SLM technology has progressed to become the most popular AM process for the production of metal components due to the versatility of materials that can be processed, the high surface quality of components and good repeatability [32, 38].

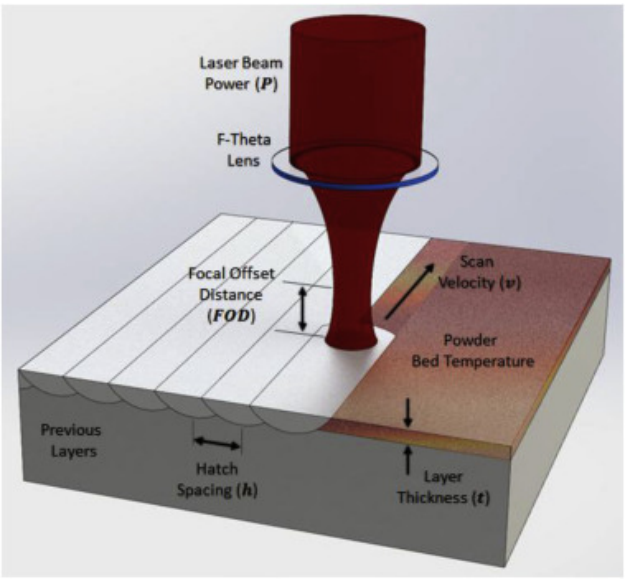

Figure 13: Schematic showing the main SLM Process Parameters. Taken from [38].

Almost fully dense parts with mechanical properties comparable to wrought metals can be

produced using SLM if the appropriate process parameters are applied (laser power, spot size, scanning speed, hatch distance, hatch angle/strategy and layer thickness), without requiring any post-processing [176–178]. During the SLM process, CAD data is divided into several thin slices ($\sim 50\mu m$), and a part is built by selectively melting thin layers of metal powder using a high energy density laser. Once each layer has been melted, the build platform drops, and a fresh layer of powder is swept over the top and the process is repeated to build a 3D object. In order to build parts with structural integrity there must be sufficient fusion between adjacent laser scan tracks and also between each successive layer of powder. Balling is a well-known defect that can occur when instability of the molten metal pool causes splashing of droplets [177], as shown in Figure 14a. Balling creates an irregular surface which causes improper deposition of the subsequent layer, which can lead to cracking and failure of the process [38, 179]. Keyhole-mode melting describes when melt pool depth increases beyond the width [180], as displayed in Figure 14b. Pores formed by keyhole melting are reported to be much larger than pores formed in normal (conduction-mode) melting [179]. Also, the collapse of a keyhole cavity can leave behind large voids [181]. Keyhole melting occurs when the melt pool is heated to a high enough temperature, and this temperature has been suggested to be the boiling point of the metal [181]. Contrastingly, if the temperature is not high enough, incomplete melting of the metal powder occurs, causing a lack of fusion between tracks and layers [182]. These defects are affected by a number of different process parameters, and as such can be reduced if the parameters can be optimised for specific materials [179, 183].

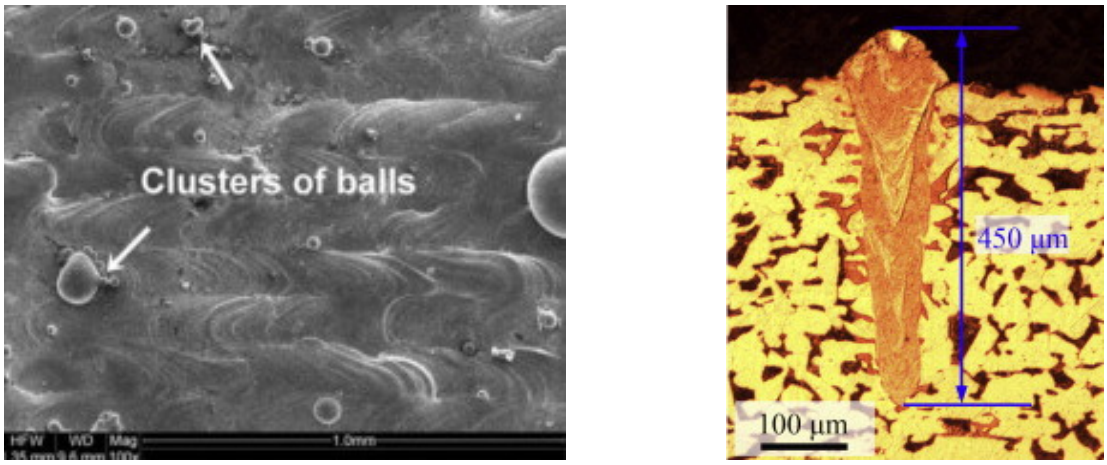

(a) (b)

Figure 14: Common SLM Defects. (a) SEM of balling, adapted from [38] (b) Cross Sectional Image of Keyhole-mode Melting, adapted from [184].

SLM technology allows for complex geometries and internal structures of parts to be created and therefore provides an exciting possibility for producing porous biomedical implants [185]. It also allows components to be manufactured from a wide range of metal powders, including Ti and Ti alloys. Leuders et al. highlighted that implants produced using SLM can be customised to match the requirements of the patient and as such SLM is an optimal technology for creating parts with this purpose [32]. Despite the preliminary focus of research into SLM production of Ti components being maximising the part density due to the negative impact of porosity on mechanical properties [38], porous Ti scaffolds have also been produced using a variety of techniques.

2.3.4.1 Altering Process Parameters

Stamp et al. produced porous Cp-Ti scaffolds with pore sizes ranging from 400 to 800 μm by employing a beam overlap procedure where the hatch distance was increased so there was no overlap between each parallel laser scan track [24]. A hatch angle of 90° was used and the result was that rectangular interconnected pores were formed. The obvious drawback of this method is that the porosity is anisotropic which is undesirable for implants. Additionally, the regular porous structure produced does not resemble the random (stochastic) porous structure of bone, as highlighted in Figure 15, and there are no curved surfaces present. Using a very similar technique Zhang et al. were able to produce interconnected rectangular pores with sizes ranging from 250 to 450μm [186]. The effect of the hatch distance on porosity was investigated and they found that it needed to be greater than 500μm in order to create suitably interconnected pores. The structures manufactured displayed mechanical properties within the region of those exhibited by cortical bone. However, this method suffers from the same drawbacks as those discussed for the work of Stamp et al. [24].

2.3.4.2 Unit Cell Geometry

Unit cell geometry has been explored as a way of producing porous structures using SLM. Geometries such as cubes [185], octahedrons [22, 187] and rhombic dodecahedrons [11] have been used as hollow unit cell geometries that are repeated to populate scaffolds. Mullen et al. were able to produce structures from Cp-Ti where porosity and mechanical properties could be tailored by altering the sizes of the octahedral unit cells [22]. The range of pore sizes created initially by altering unit cell size was 600 to 1400 μm, most of which are larger than the optimum pore sizes discussed in

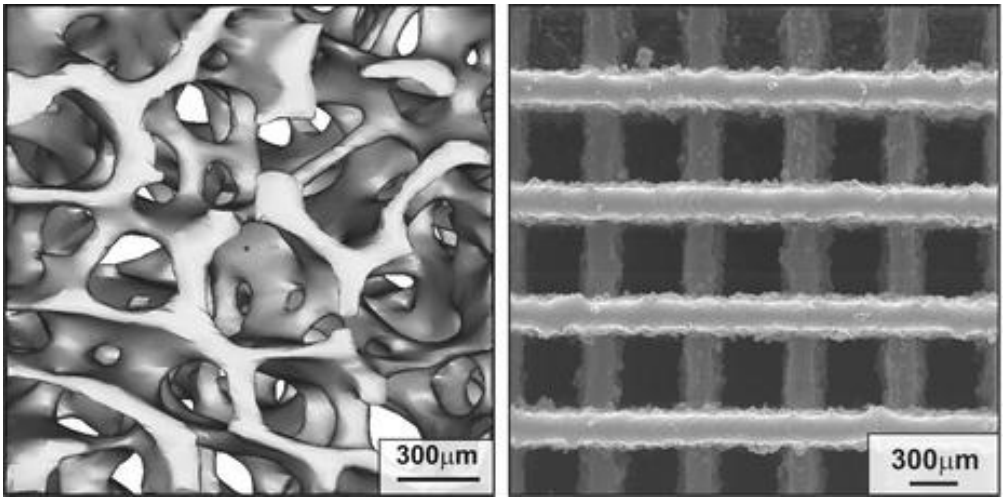

Figure 15: CT scan of human trabecular bone (left) and porous Cp-Ti scaffold produced using 'beam overlap' technique (right). Adapted from [24].

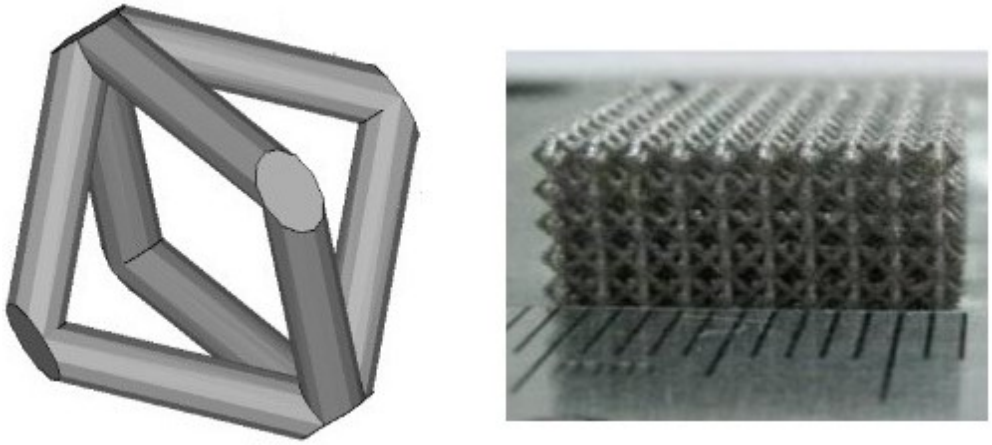

Figure 16: SLM Octahedral unit cell (left) and scaffolds produced using octahedral unit cells (right). Adapted from [187].

Section 1.1.1 for osseointegration. However they were then able to produce a hip augment with a major pore diameter of 500 μm and a porosity of 65 % by adapting the results obtained from their study, which lie within the optimal values outlined in Section 1.1.1. This work clearly shows that the unit cell approach can be specifically tailored to match the desired properties for orthopaedic implants in terms of porosity, however implants manufacturing using this method still suffer from a number of drawbacks. Firstly, the computational design processes used can be very complex and costly, as there are many factors that need to be considered when designing a unit cell structure such as strut diameter, unit cell size, strut angle and powder adhesion [187]. Another issue with

this method is that the structures are still much more uniform and regular than the stochastic porous structure of human bone, and do not provide the preferable concave curved surfaces that promote bone in-growth.

2.3.4.3 Minimal Surfaces

Minimal surfaces are a mathematical concept that arose from exploring what a surface bounded by a given contour looks like when it has the smallest possible surface area [188]. Minimal surfaces are characterised by having a mean curvature of zero at any given point on the surface, or the average curvature spanning from any given point is equal in magnitude and opposite in terms of being concave or convex, which visually can be described as a 'saddle' shape. It has been proven that every simple closed boundary curve is spanned by at least one minimal surface. Triply periodic minimal surfaces (TPMS) can be defined as minimal surfaces that have translational symmetries in three dimensions [188]. There are a wealth of known TPMS, some examples of which are shown in figure 17. A single unit cell of such a surface can be multiplied infinitesimally resulting in a smooth continuous surface that forms a partition which creates two intertwined labyrinths, each being continuously connected with no isolated cavities within the entire geometry [189]. This presents an exciting opportunity for the production of porous implants where good interconnectivity between pores is vital for osseointegration. Before the development of AM technologies, manufacturing such complex geometries would have been virtually impossible, however in more recent years SLM has been used to produce scaffolds based upon TPMS [189, 190].

TPMS have proven to be extremely versatile building blocks for producing porous scaffolds where porosity can be controlled not only by the contour geometry chosen to generate the TPMS, but also by varying the thickness of the surface whilst keeping the overall unit dimensions constant [190]. By combining this method with SLM, Bobbert et al. were able to produce a wide variety of Ti64 scaffolds with porosities ranging from $43-77$ % and mean pore sizes ranging from $361-896$ μm [190]. Figure 18 shows the CAD images of the TPMS employed and the cylindrical Ti scaffolds produced using SLM. This study shows that combining TPMS with SLM can provide an impressive level of control over porosity. Also, the resulting scaffolds are fully interconnected and provide an array of curved surfaces which are beneficial for osseointegration. As a result, scaffolds created in this way are some of the closest in their structural properties to the requirements outlined in

Section 1.1.1 out of all the methods discussed in this review. The only potential issue with this method is the level of complexity involved in creating the initial surfaces and modifying parameters such as surface thickness. Also, in vivo testing would be useful in order to determine which of the more common TPMS promote the highest amount of bone in-growth.

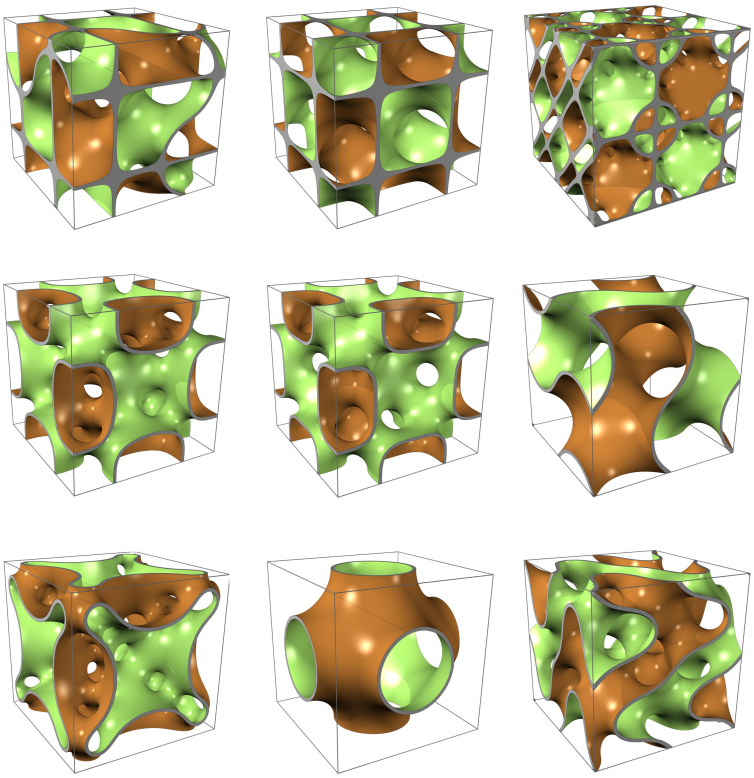

Figure 17: Examples of known TPMS. Taken from [189].

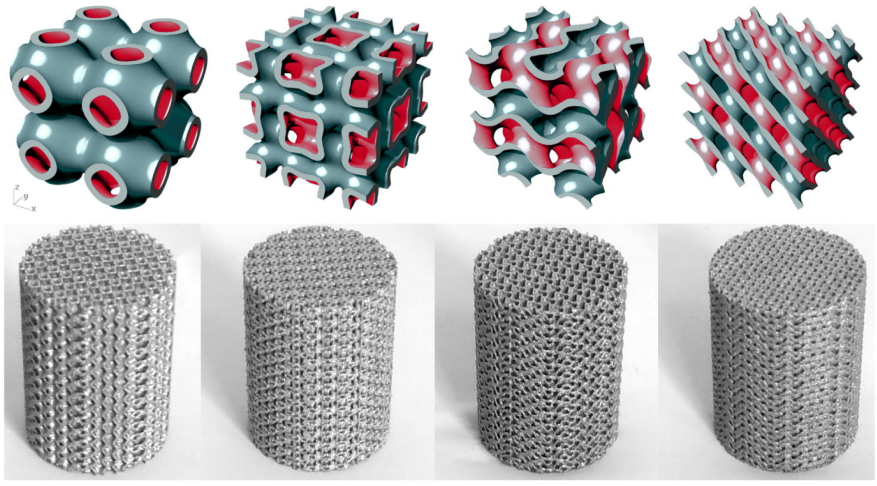

Figure 18: CAD images of TPMS structures and cylindrical Ti64 scaffolds produced by populating TPMS. Taken from [190].

2.3.4.4 CT Scan Replication

Porous scaffolds have been produced with stochastic structure resembling human trabecular bone by using data obtained from CT scans [191]. The scanned images were used to directly create a replica of the bone section imaged, and alternatively an image of bone structure was used as a unit cell that was stacked to produce a scaffold (Figure 19a. This is an accurate way of producing scaffolds with a structure similar to human bone, however it requires access to a CT images of bone which are not readily available. Also, the image had to be carefully altered to account for limitations of the SLM process, such as minimum wall thickness that can be produced, and the complex path that the laser has to follow leads to an increased build time. Therefore, although this is a seemingly promising way to produce porous scaffolds, the procedure is complicated and requires access to very specific resources and so there is still a need for alternative methods to be developed that can simplify the process.

2.3.4.5 Bubble Generation

Porous Ti structures were produced by Wang et al. by blending Ti powder with Ti hydride (TiH_2) [192]. By using a high laser power ($1000W$) and a low scan speed ($20\ mm/s$) the laser deposited a large amount of energy which caused the thermodynamic decomposition of the TiH_2, releasing the hydrogen gas which floated to the surface during solidification leaving open interconnected pores in its path. The result was that a structure was created which had a porosity close to 70 % with pore sizes ranging from 200 to 500 μm. The porous structure produced also more closely resembles the stochastic nature of pores within trabecular bone (Figure 19b. The results of this work are very promising; however, the drawback of this method is that the laser parameters have to be very specifically controlled in order to ensure decomposition of the TiH_2 and the right level of viscosity of the melt pool. Small changes in the laser scanning speed in either direction resulted in insufficient porosity being attained. Also, the laser power used is difficult to replicate as it significantly exceeds the maximum laser power of most commonly available SLM machines.

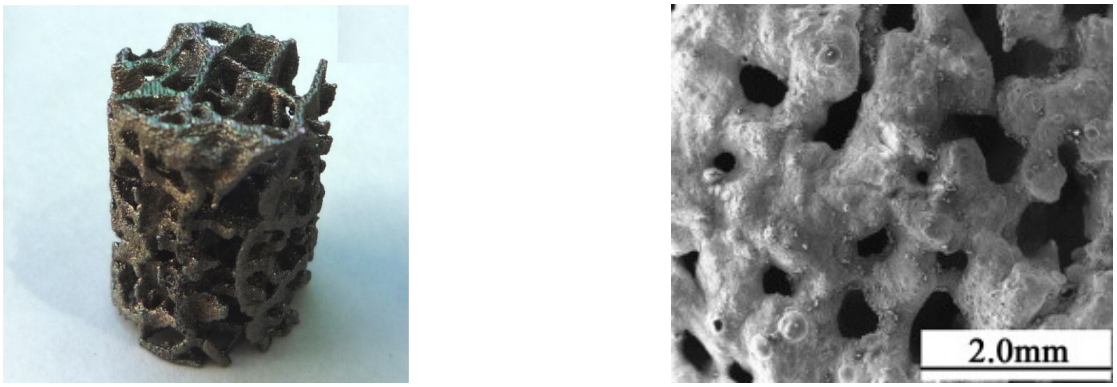

(a) (b)

Figure 19: Porous titanium scaffolds manufactured using SLM in conjunction with 'CT scan replication' (a) adapted from [192] and 'bubble generation' (b) adapted from [191].

2.3.4.6 Space-Holder Technique

More recently, Zhao et al. introduced the idea of creating porosity by combining SLM with the space-holder technique using NaCl [193]. As investigated in Section 2.3.3, space-holder sintering be used to produce porous Ti structures with very promising properties for implants, and NaCl has been highlighted as an easily removable and effective space-holder material. Until this recent work it had not been combined to SLM. Zhao et al. mixed Ti64 with NaCl at various volume fractions prior to feeding the mixture into an SLM machine to build 3D structures and then the NaCl was removed by dissolution in water leaving a porous Ti64 scaffold. Increasing the volume fraction of NaCl lead to an increase of inter-connected pores and a decrease in the relative density of the final parts. The resulting porous structures were highly stochastic and well interconnnected, as shown in Figure 20, and so this method seems to present a promising way of producing porous implants by SLM without complex computational design and laser parameter processing. However the maximum level of porosity achieved was only 49 % by using a 60 % blend of salt in the feedstock, and the salt particles had a mean size of only 150 μm which means that the pore sizes were probably below the optimal region for implants, although no analyses of pore sizes is provided so it is difficult to conclude. As layer thickness for SLM builds is often small ($\sim$ 50 μm) in order to ensure sufficient melting of the powder, the size of powder and space-holder particles is fairly restricted which means that it could be difficult to achieve large pore sizes through this method. It was discovered that less NaCl was removed during dissolution than was present in each of the initial volume fractions,

suggesting that evaporation of NaCl occurred during the irradiation process. This is highly likely as the boiling point of NaCl is $1465°C$ and the melting point of Ti64 is $1604 - 1660°C$, therefore for melting of the Ti to occur the temperature had to be raised above the NaCl boiling point. It is possible that the evaporation of the NaCl during the SLM process caused collapsing of what would have been pores which would explain why the relative density of the final parts produced was lower than the initial volume fractions. This work emphasises a need for further understanding to be developed regarding the behaviour of NaCl under laser irradiation. It is also possible that another similar space-holder material could be used that has a boiling point above the melting point of Ti64 which could reduce the issue of evaporation. NaCl has many advantages as a space-holder including solubility in water, low cost and reduced etching of metal during dissolution [194]. The low toxicity of NaCl is also an advantageous property especially in the case of a biomedical implant as it can be difficult to ensure that all the material is dissolved out [162, 195]. It is therefore important to consider these properties when exploring alternative space-holder materials that are more suited to the high temperatures that are reached in the SLM process.

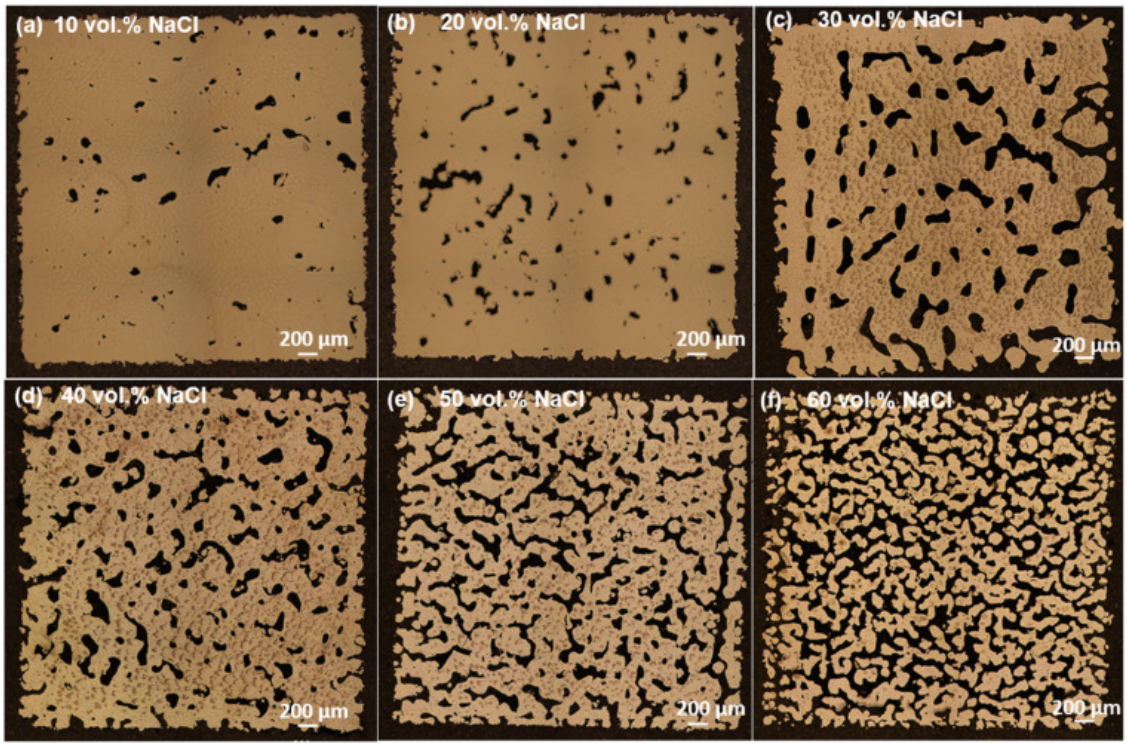

Figure 20: Optical micrograph sections showing porous structure of scaffolds produced using the SLM space-holder technique with NaCl. Taken from [193].

2.3.5 Other AM Techniques for Producing Porous Ti

2.3.5.1 Sacrificial Scaffolds

The space-holder method was combined with 3D-printing technology by Ryan et al. who created a sacrificial wax template using a 3D-printer and then poured a Ti slurry around the template before heating to melt away the wax template. The remaining Ti structure was then sintered to produce a stable Ti scaffold [196]. The resulting scaffolds achieved porosities of 66.8 % $\pm$ 3.6 % with a Young's modulus of $20.5 \pm 2.0\ GPa$ and pore sizes ranging from 200 to 400 μm. The wax templates created in this study were restricted by the maximum dispensing angle of 7° for the 3D-printer (Figure 21) which resulted in the final mechanical properties and porosity of the scaffold being significantly anisotropic. This is undesirable for implants, as outlined in Section 1.1.1.

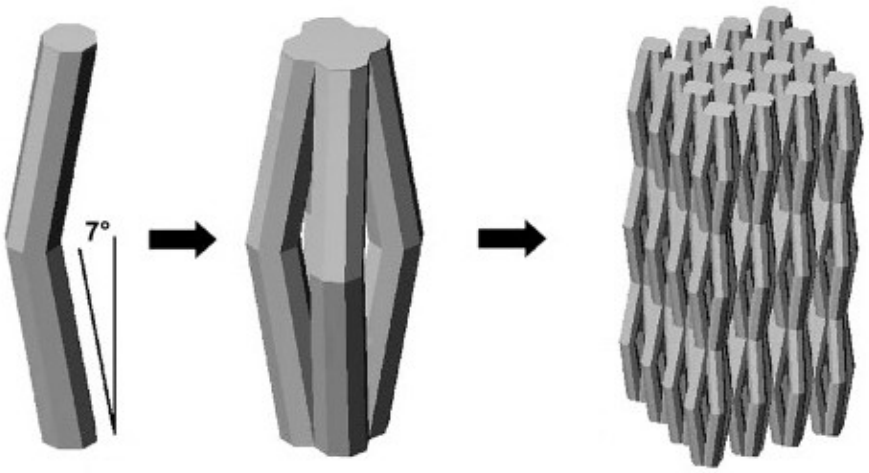

Figure 21: CAD design used to 3D print sacrificial wax structure space-holder. Taken from [196].

A similar technique was employed by Lopez-Heredia et al. to produce highly porous CpTi scaffolds [197]. To begin with, a porous cylinder was designed using CAD by cutting a series of cylindrical channels that are perpendicular in three dimensions from an initial solid cylinder, as shown in Figure 22a. The diameter of these channels provides the control over the pore sizes, and in this study two implants were designed with 800 μm and 1200 μm. Sacrificial wax templates were then 3D printed from the CAD designs, before a refractory material was cast around the templates to create moulds. The wax was burned out and then the moulds were filled with melted Ti and then quenched, before breaking apart the mould and cleaning off any remaining refractory material.

The resulting mean pore sizes of the Ti scaffolds were 805 μm and 1142 μm, with both achieving porosities close to 60 %. The results show that the resulting pore geometries matched closely the initial CAD designs, meaning that it is possible to have a high level of control using this method and that it is reproducible. However, it is explained that the reason for the larger than necessary pore sizes that were created is that reducing the channel sizes below 600 μm is not possible due to difficulties with adequately filling the mould with the liquid Ti. The other key issue with this method is its complexity. The casting process involves several steps between printing the initial sacrificial wax template and finally removing the refractory mould. Also, whilst the initial 3D printed wax template provides a high level of customisation to the structure and geometry, both the wax template and the mould are destroyed during each cycle to produce a single Ti scaffold which make it an inefficient process. Therefore, whilst this adaptation is an improvement from the work by Ryan et al. [196] in terms of the resulting structure, it still suffers from these drawbacks that mean it is unsuitable.

(a) (b)

Figure 22: (a) CAD drawing used to 3D print sacrificial wax template and (b) resulting Ti scaffold structure. Adapted from [197]

2.3.5.2 Material Extrusion

Material extrusion is an AM process typically used for thermoplastics, where the material is heated and loaded into an extruder then fed through a nozzle to form tracks by the movement of the extruder that combine to create a full layer of material, which solidifies through cooling or other

means. The platform then drops, or the extruder is raised, and the process is repeated to form 3D builds. The key parameters within the process are the layer height and extrusion nozzle diameter, along with the merging between adjacent tracks and successive layers of material [28]. The original material is typically in filament form (as with FDM), however there are examples of this process being applied using powder based slurry type materials.

Li et al. developed a process referred to as '3D fibre deposition', which is described as a process where powder based slurry is deposited as fibres (tracks of extruded slurry), where fibre diameter, spacing and orientation can be defined for each layer [21, 198]. This method has been used to build Ti64 scaffolds with controllable pore sizes, porosity and interconnecting pore sizes. A viscous Ti slurry was created by dispersing Ti64 powder (66 $vol\%$) in a 0.5 % aqueous Methylcellulose solution (34 $vol\%$) which was extruded through a syringe nozzle of diameter 400 μm. The viscosity of the slurry was optimised by altering the concentration of powder in the slurry in order to be able to deposit uniform fibres but also to still achieve sufficient adhesion between successive layers. Scaffolds with various levels of porosity were produced by altering the fibre spacing and orientation patterns. After structures had been built by fibre deposition, they were dried out and then sintered. Figure 23 shows the resulting structures that were produced.

By altering fibre spacing various structures were produced with mean pore sizes ranging from 160 to 680 μm and porosities of 39 to 68 %, which corresponded with the fibre spacing employed for each build, showing clearly that the fibre parameters can be used to porosity and pore size. Pores were well interconnected in every scaffold, with the highest level permeability measured for the most porous scaffold with largest pore sizes. The scaffolds were tested in vivo by implantation within goats and measuring bone formation into them over 12 weeks. No signs of toxicity or deviating inflammation related to the implants were observed, concluding that the process and material are biocompatible. The greatest amount of bone in-growth over the 12 week period was observed within scaffolds with the highest measured levels of permeability and mean pore sizes of both 400 and 680 μm.

Whilst this method provides a high level of control over porosity, pore size and even scaffold geometry (which is restricted by most other conventional porous Ti manufacturing routes), it does suffer from a number of drawbacks. Firstly, as can be seen in Figure 23, the structures are highly regular and anisotropic, and as such are not an accurate replication of the stochastic nature of

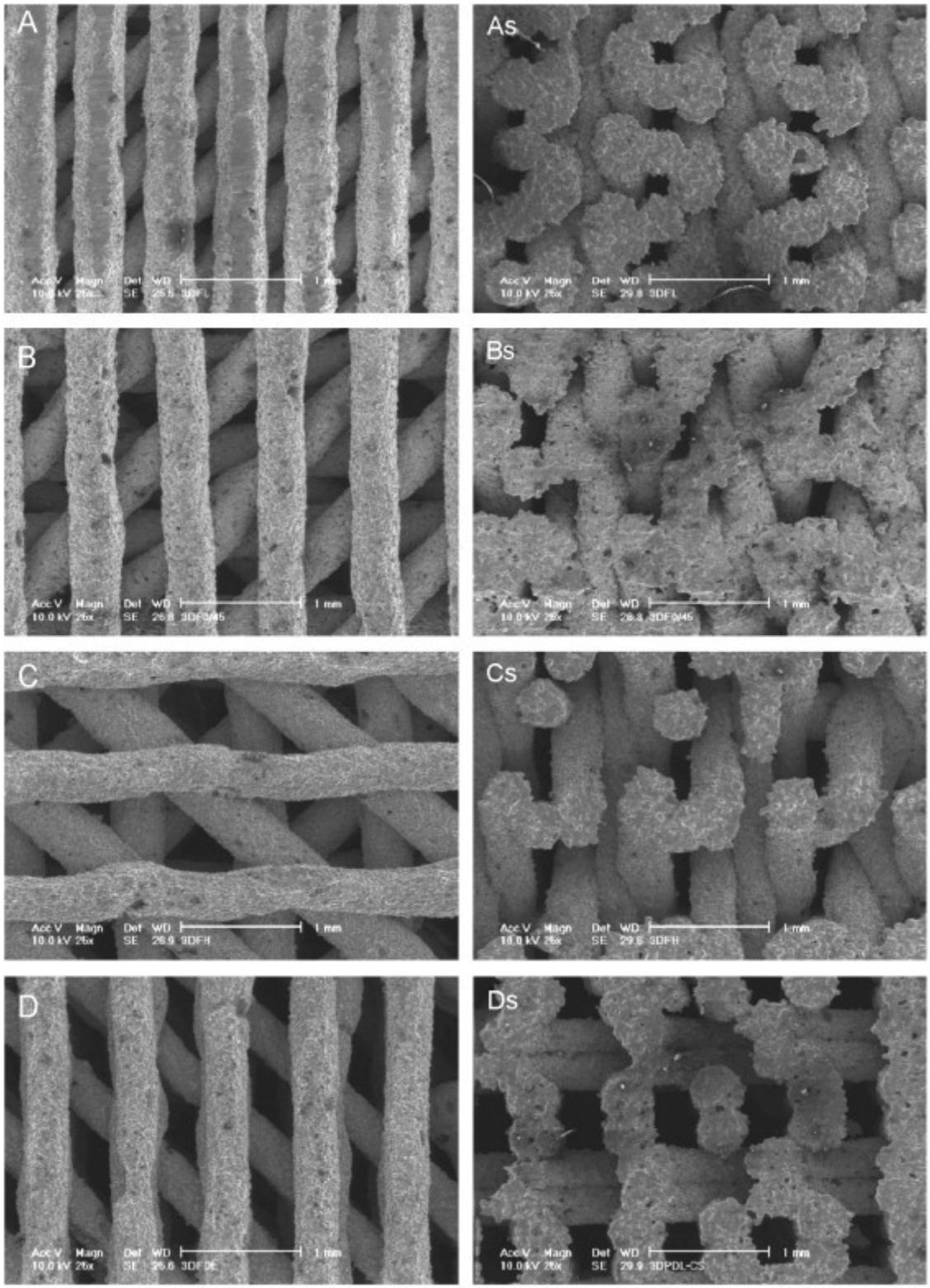

Figure 23: Electron microscope images of 3D fibre deposited porous Ti structures with various fibre configurations. 's' denotes side view. Taken from [21].

trabecular bone. Also, all of the pore surfaces are convex due to the fact that the deposited fibres are cylindrical in shape. As explained in Section 1.1.1, convex surfaces do not promote osseointegration as well as concave surfaces, which may explain how although some bone in-growth was measured within all the scaffolds in this study, the amounts were all relatively low. Also, the authors state that the fibre spacing can only be specified for each layer rather than being variable within an individual layer, which means that porosity could only be controlled in one direction and it would not possible to create concentric geometries with different levels of porosity using this method. Despite these drawbacks this study presents novel and very promising techniques which present scope for further development, in particular the creation a titanium powder suspended slurry which can be directly 3D printed using material extrusion to achieve greater geometric flexibility.

2.3.6 Methods of Producing Gradient Porosity

2.3.6.1 PM Space-holder Technique

Trueba et al. successfully produced CpTi cylinders with radially graded porosity by developing and employing a custom sequential compaction device (Figure 24a) which enabled various mixtures of Ti powder and space-holder particles to be combined within a single compaction process [199]. Using the custom device compacted powder cylinders consisting of 3 concentric layers, each with a different % mixture of space-holder particles, were produced. NaCl and ammonium bicarbonate (NH_4HCO_3) with mean particle diameters of 206 μm and 265 μm respectively were used as space-holders in separate cylinders. Once the various mixtures of powders had been compacted, the space-holder particles were removed by immersion in water at controlled temperatures for set time periods, and then the cylinders were sintered.

Lower than expected porosities were observed within the most dense layer within each of the cylinders, which was due to the difficulty of removing the space-holder because of the low inter-connectivity of pores in this layer. Table 3 shows the final porosity and pore sizes achieved within each layer of the Ti cylinders for both space-holder materials where the layers were created from compacting powder mixtures with 20 %, 40 % and 60 % space-holder quantities. The final porosity values achieved are very promising for orthopaedic implants, and the reported Young's Modulus

(8.3 $\pm 1.9\ GPa$) for the NaCl space-holder cylinder is also close to that of human cortical bone. Arguably, however, the gradient of the layers should be the reverse of what was achieved in this work in order to match that of human bone (a dense outer layer with a porous core), but this work clearly shows that it would be possible to achieve this by simply altering which Ti/space-holder mixtures are applied to which region within the compaction device. It was also noted in this work that extreme differences in % space-holder between each layer cause non-homogeneous shrinkage to occur during sintering, which increases damage at the layer interfaces. Therefore, whilst only two grades of porosity are technically required to mimic cortical and trabecular bone, at least one intermediate layer is required with space-holder quantity/porosity that bridges the gap between the dense layer and highly porous layer in order to prevent this defect occurring in the sintering stage. Within this process the geometry of the produced cylinder is restricted by the custom compaction device that was created initially, which presents a huge drawback of this method when using it to produce implants. In order to alter the geometry of the porous Ti structures to suit individual applications, either significant post-processing would be required or a new custom set of die and punches would be needed each time which would be impractical.

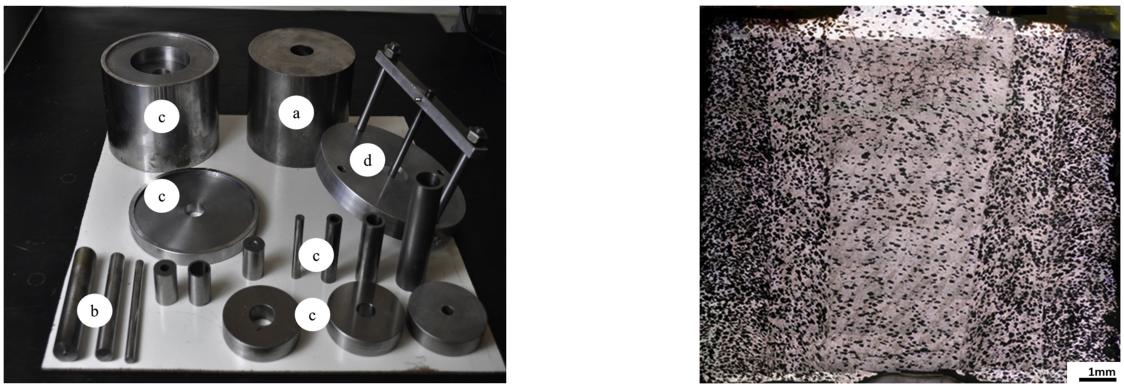

(a) (b)

Figure 24: (a) Custom powder compaction device and (b) cross section of Ti cylinder with 3 layers of varying porosity. Taken from [199]

		Porosity (%)		**Mean Pore Diameter (μm)**	
Space-holder Material		NaCl	NH_4HCO_3	NaCl	NH_4HCO_3
Section	Core	14.5 ± 1.5	16.8 ± 1.7	142 ± 69	94 ± 45
	Inner	38.3 ± 1.2	23.7 ± 0.7	120 ± 49	75 ± 31
	External	57.5 ± 2.1	54.1 ± 1.9	94 ± 29	62 ± 19

Table 3: Porosity and pore sizes of Ti cylinders with graded porosity. Adapted from [199].

2.3.6.2 SLM

Li et al. were able to control porosity of SLM produced SS 316L samples by simply altering the scan speeds within the build process, whilst keeping the other parameters constant [26]. Graded porosity of $4-35$ % was obtained by varying scan speed from $90-180 mm/s$. It is concluded that the porosity is a result of the changes in melt pool characteristics. Increasing scan speed caused a reduction in melt pool width and depth resulting in gaps forming between tracks and layers, whilst also reducing the temperature which results in incomplete melting of the powder. Ti64 dental implants with graded porosity have been produced through DMLS by employing a similar strategy [200]. In this work, rather than altering scan speed, laser power was decreased in order to cause incomplete melting of the powder. By altering the power within a single build they were able to produce implant scaffolds with a dense outer layer and a porous core, with a reduced Young's modulus of 35 GPa which is close to the values for Cortical bone discussed in Section 1.1.1. The samples produced presented porosity that visually appears similar to bone in its stochastic nature, however no measurements of pore geometries or values for overall porosity are reported.

These studies show that it is possible to produce different grades of porosity within a single implant by altering laser parameters within a build. Although, the results achieved by Li et al. produced levels of porosity well below the desired region for this application [26] which suggests that this method alone is incapable of meeting the porosity requirements. This does however present the opportunity to develop this idea further in future work, and possibly combine it with other methods of producing porosity to enable further control over porosity.

Gradient porosity was created by Fousova et al. using the SLM unit cell approach [11]. Rhombic dodecahedron unit cells were used to create cylinders with either a porous core or porous surface layer. 62.1 % porosity and a Young's modulus of 30.5 GPa were achieved by the structure with a 2 mm porous surface. These properties are encouragingly similar to those of cortical bone, however the porosity is actually the inverse of structure of bone i.e. a highly porous outer layer and a dense core as opposed to the dense outer layer of cortical bone and the highly porous core of trabecular bone. Also, the dense part of the scaffold produced was actually completely solid, rather than having a low level of porosity like cortical bone. No analysis of the size of the pores is provided. Li et al. also produced functionally graded biodegradable porous scaffolds from pure iron using diamond

unit cells [201]. Gradient porosity was achieved by altering the strut diameter throughout the scaffolds within the design stage which created variations in density. Promising values of porosity and pore sizes were achieved, however the mechanical strength of the scaffolds only matched that of trabecular bone and were quite significantly below the values reported for cortical bone. Therefore these implants would most likely be unsuitable for load-bearing applications, however were Ti64 used instead of iron then this method could be used to produce graded porosity implants with near optimal properties.

2.3.6.3 Material Extrusion

Using the 3D fibre deposition technique as outlined in Section 2.3.5, Li et al. were also able to create scaffolds with graded porosity [21]. As previously explained, it is possible to change fibre diameter, spacing and orientation for each deposited layer. Gradient porosity was achieved in this study by varying fibre spacing between $200 - 800\ \mu m$ between layers, which resulted in a corresponding range of mean pore size between $160 - 660\ \mu m$ within the scaffold. The graded porous structure is shown in Figure 25. The issues with this technique have already been explained, however this study shows, along with the SLM methods overviewed in Section 2.3.6, how the versatility of AM technology can be exploited to provide a solution to the problem of graded porosity.

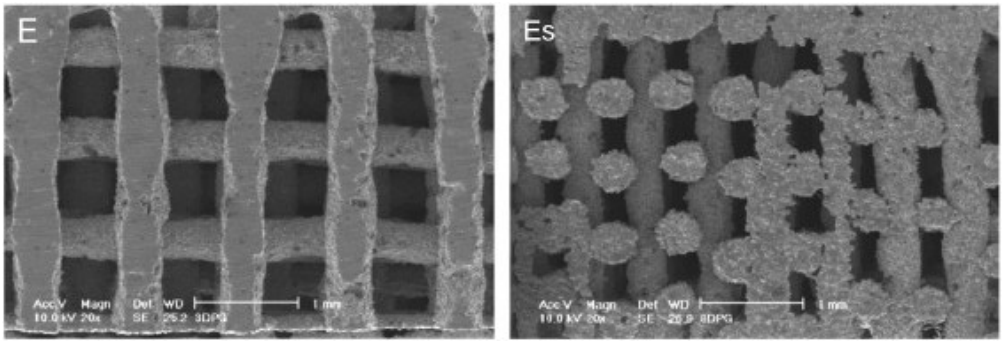

Figure 25: Electron microscope images of 3D fibre deposited Ti structures with graded porosity, created by altering fibre spacing. 's' denotes side view. Taken from [21].

2.3.7 Summary of Porous Ti Manufacturing Methods

Table 4 provides a summary of the manufacturing methods explored within this section for producing porous Ti structures, and assesses the suitability of each method against the requirements

of artificial orthopaedic implant material. Overall, a number of manufacturing techniques meet all-but-one of the criteria (PM space-holder, various SLM techniques and 3D fibre deposition), which with further development could provide optimal material for artificial implants.

			Implant Requirements						
Process	**Method**	**Ref.**	*Porosity 60 – 80 %*	*Pore Sizes 300 – 600 μm*	*Interconnected*	*Concave Surfaces*	*Tailorable Geometry*	*Graded Porosity*	Additional Notes
PM	Loose Sintering	[158–161, 166, 199, 202]	✗	✗	✗	✗	✗	✗	Most logistically simple method of producing porosity
	Space-Holder	[166, 167, 169]	✓	✓	✓	✓	✗	✓	Porosity is often limited and only just exceeds 60%. Method used to create graded porosity requires building of complex custom compaction die.
	Powder Tapping	[170]	✓	✓	✓	✓	✗	✗	Improved porosity and interconnectivity compared with basic space-holder
	Hollow Powder	[171–174]	✗	✗	✓	✗	✗	✗	Produces excessive levels of porosity and overly large pore sizes
SLM	Basic Methods	[24, 26, 186, 200]	✓	✓	✓	✗	✓	✓	Methods that achieve graded porosity fail to meet porosity and pore size requirements - and vice versa.
	Unit Cell	[11, 22, 185, 187]	✓	✓	✓	✗	✓	✓	Generation of scaffold CAD designs is a computationally complex process

			Implant Requirements						
Process	**Method**	**Ref.**	*Porosity 60 – 80 %*	*Pore Sizes 300 – 600 μm*	*Interconnected*	*Concave Surfaces*	*Tailorable Geometry*	*Graded Porosity*	Additional Notes
SLM	Minimal Surfaces	[189, 190]	✓	✓	✓	✓	✓	✗	Not yet been adapted for graded porosity. Also generation of scaffold CAD designs is a computationally complex process.
	CT Scan Replication	[191]	✓	✓	✓	✓	✓	✗	Complex design process and requires access to CT scans of trabecular bone.
	Space-Holder	[193]	✗	✗	✓	✓	✓	✗	Porosity could be increased by increasing space-holder ratio. Pore sizes are controlled by space-holder size, which is limited due to thickness of layers that are deposited using SLM.
Other AM	Sacrificial Templates	[196, 197]	✓	✓	✓	✓	✗	✗	Has not previously been used to create graded porosity but could easily be adapted to do so. Creates more steps in the build process and requires new template to be produced for each application.
	3D Fibre Deposition	[21, 198]	✓	✓	✓	✗	✓	✓	Porosity is significantly anisotropic.

Table 4: Summary of various methods for manufacturing porous Ti scaffolds assessed against requirements for artificial orthopaedic implant material.

2.4 Structural Analysis of Porous Structures

As explained in Section 1.1.1 the porosity, pore sizes and interconnectivity of pores within orthopaedic implants are key properties in order to ensure adequate fusion between the bone and implant whilst allowing fluid transportation and vessel in-growth. Therefore it is vital when manufacturing porous implants to be able to accurately measure these parameters in order to asses the material against the implant requirements.

2.4.1 Pore Size

2D cross-sectional analysis has been used as a method of measuring pore sizes [160, 179, 203]. It typically involves cutting several slices through the porous material, taking an image of the sliced surfaces and using image analysis software to measure the sizes of the exposed pores. This method provides fairly limited information as the imaged slices may not be a fair representation of the pore size distribution throughout the material. Also, it is unlikely that many pores within the sliced surfaces will have been cut through the centre and therefore measurements of the pore diameter for some pores are smaller than the true diameter. However it does provide a relatively straightforward way to obtain pore size information and only requires access to equipment and software that are commonly available such as optical microscopes and open-source imaging software like Fiji [204], therefore can be used as a preliminary source of information but ideally should be followed up with more detailed 3D analysis [205].

Computer tomography (CT) has been employed in some studies in order to perform 3D analysis of pore size distribution [165, 169, 196, 206]. This technology takes 2D x-ray images of a sample as it is rotated around 360°, which are then combined using computational software to build up a full 3D representation [207], an example of which can be seen in Figure 26. In order to differentiate between materials it relies upon the presence of various levels of absorption, which is certainly true for porous materials, and is therefore able to reproduce highly accurate computational representations of pore distribution which can then be analysed using appropriate software. CT technology is able to provide much more accurate and detailed information regarding distribution and morphology of pores within a material than 2D cross-sectional analysis, and as such should ideally be used to analyse pore sizes where possible. However, access to such equipment is often limited or expensive

and therefore this is not always possible.

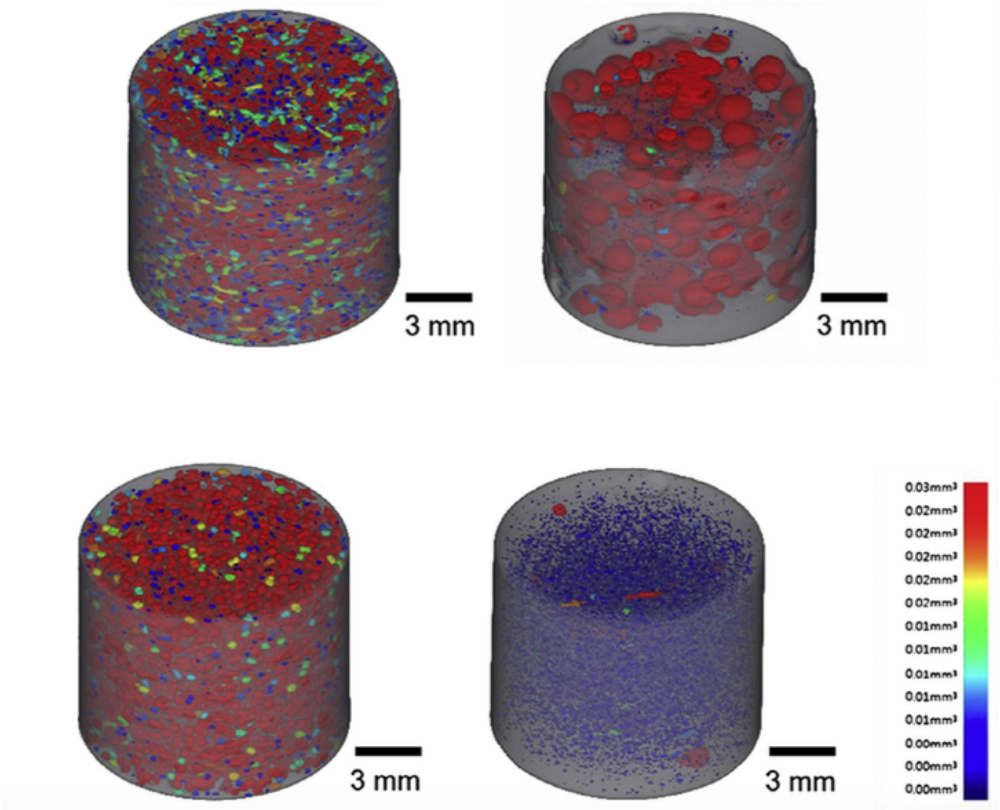

Figure 26: Examples of 3D computer generated representations of pores within a scaffold from CT scan data. Taken from [165].

2.4.2 Porosity

Taking dry mass and volume measurements and comparing to the bulk density of the material is the most straightforward method of calculating relative density and therefore porosity, which has been employed in many previous studies. Archimedes' method is another commonly used method of calculating the relative density of a material. This method finds the volume of the object from the volume of water displaced by immersing the object, and uses this to calculate the relative density. This is done by simply weighing the object in air and in water and applying Equation 1 to calculate relative density.

$$\rho_r = \left(\frac{M_a}{M_a - M_w} \right) \rho_w \tag{1}$$

Where ρ_r is the relative density, M_a is the mass of the object in air, M_w is the mass of the

object in water and ρ_w is the density of water ($1000kg/m^3$).

This method is advantageous as it provides a relatively straightforward means of measuring density/porosity. However, this method is typically only suitable for entirely closed-cell porous structures as it relies on the air trapped within the pores creating buoyancy and reducing the mass of the sample when weighed in water. Therefore any pores that break the surface of the material will allow water infiltration and cause erroneous results [207]. In order to apply this method to open-cell structures with interconnected pores, the surface of the material must be first coated in vacuum grease to prevent water infiltration within the pores [171, 195].

In some cases porosity has been measured using both Archimedes' and 2D slice imaging and found the results to be reasonably consistent between the two methods [160, 199, 208], however there are a few results that are quite significantly different between the methods which highlights the level of uncertainty that both present.

2.4.3 Interconnectivity

Some studies have used Archimedes' method to calculate the level of isolated and interconnected porosity [160, 161, 199, 202]. The method is applied to calculate the level of isolated porosity within the material where the liquid cannot infiltrate. Combining this information with the total porosity provides a value for interconnected porosity which is an insightful value particularly for implant material as a high value suggests that fluid transportation and vessel growth is possible throughout almost all of the implant. However this method provides no information regarding the size of the connections between pores, which as explained in Section 1.1.1 has an influence on the level of osseointegration that occurs.

2D cross-sectional imaging and analysis can be used to provide measurements of connecting windows, however the drawbacks of this method have been previously outlined in Section 2.4.1. CT scanning and 3D reconstruction can be used to analyse interconnectivity either by measuring the size of connecting windows or the level of interconnectivity as a percentage, depending on the capabilities of the software used to analyse the 3D reconstruction.

2.5 Mechanical Properties of Porous Ti

2.5.1 Young's Modulus of Porous Ti

Whilst a significant emphasis is generally placed on porosity and structure in previous studies aimed at manufacturing porous Ti implants, many studies in the literature have also assessed the mechanical stiffness of the material by measuring the Young's modulus. As previously explained in Section 1.1.1, implant materials with Young's modulus similar to that of the surrounding bone can reduce the stress shielding effect, and in turn increase the life-span of the implant [34]. It is well known that porosity within a material reduces the Young's modulus, which presents the opportunity to create porous Ti64 implants with a modulus close to that of human bone by controlling the porosity. Whilst there exist models for calculating the Young's modulus of porous materials, most famously the Gibson-Ashby model [209, 210] shown in Equation 2, the relationship between porosity and modulus remains vaguely defined and is significantly influenced by factors within the manufacturing process and the geometry of the porous structure. However, Figure 27 has been compiled to act as a reference guide that collects together the Young's modulus and porosity of porous Ti64 produced using various manufacturing methods as discussed throughout Section 2.3.

$$E_{\mathrm{r}} = C(1-\phi)^n \tag{2}$$

Or alternatively written:

$$E_{\mathrm{r}} = C(\rho_r)^n \tag{3}$$

Where E_{r} is the relative Young's modulus (the ratio of the modulus of porous material to dense material), ϕ is the porosity (%) of the material, ρ_r is the relative density, C is a constant typically assumed to be equal to 1 and n is a constant with a value of around 2 which can be determined experimentally. In the work of Cabezas-Villa et al., using data gathered from porous Ti64 scaffolds produced by PM and comparing against the Gibson-Ashby model, they found that using $n = 5$ provided a much more accurate prediction of modulus against porosity [158]. The Gibson-Ashby model predictions have been plotted in Figure 27b using both values of n to compare against the data collected from the literature for porous Ti64.

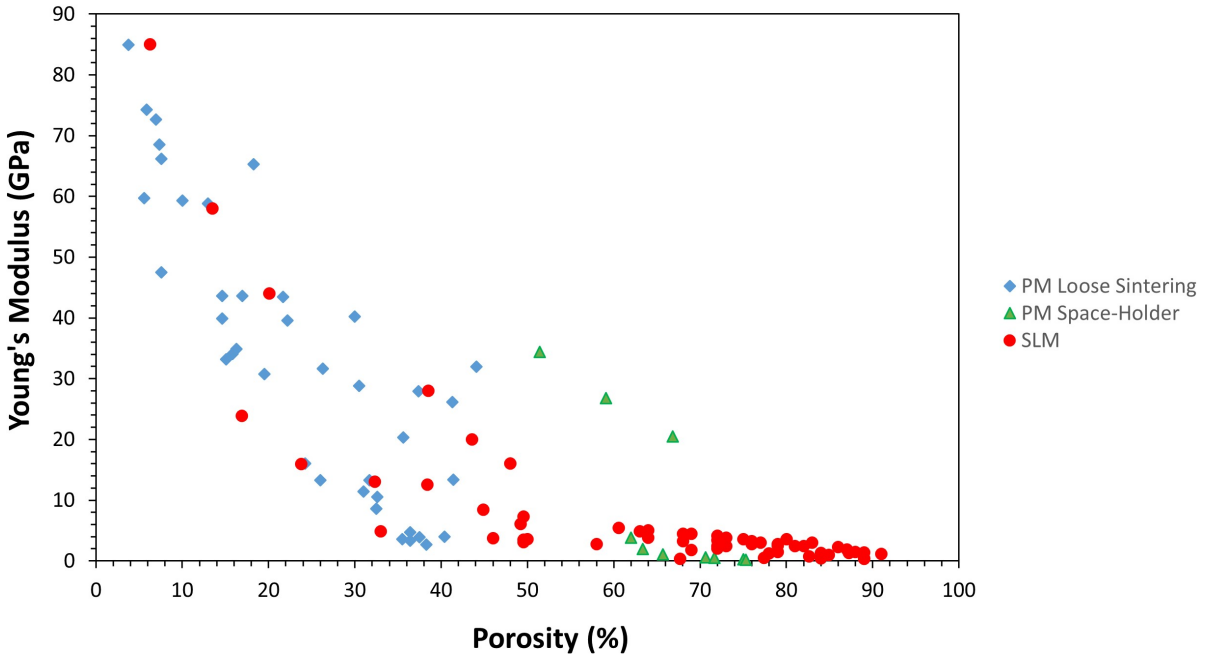

(a)

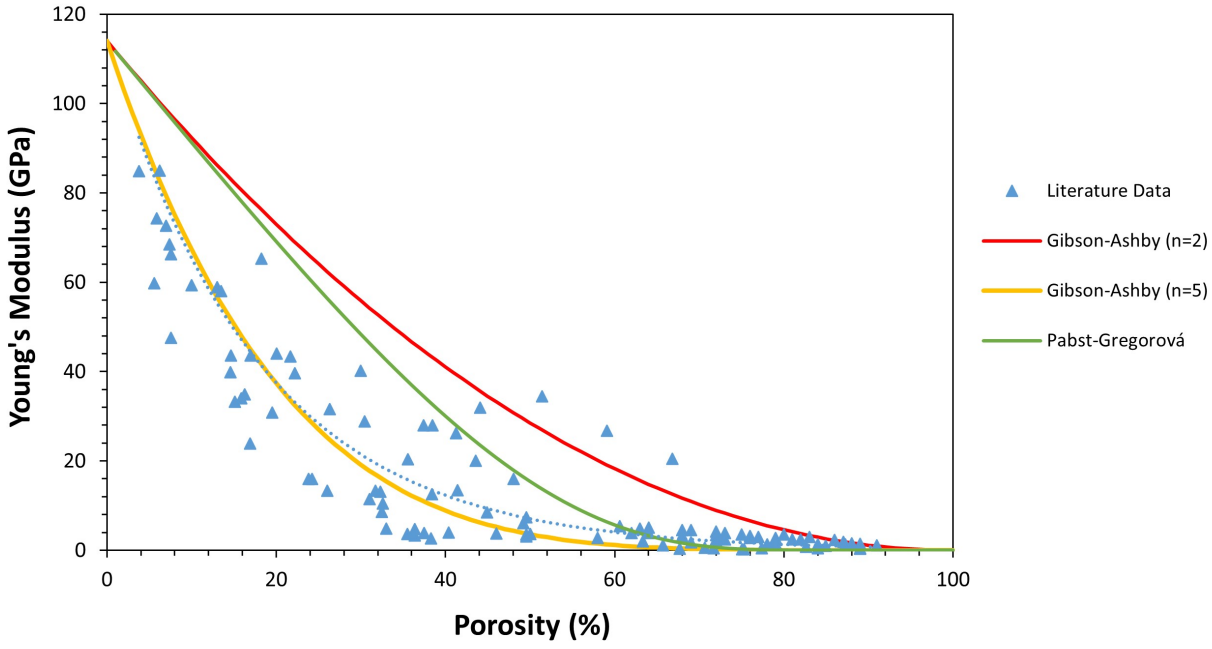

(b)

Figure 27: Graphs showing summary of Young's modulus against porosity of porous Ti64 scaffolds manufactured using various methods (a) and all methods combined compared with the Gibson-Ashby model (b). Data collected from [158, 160, 161, 167, 186, 193, 196, 202, 211–213].

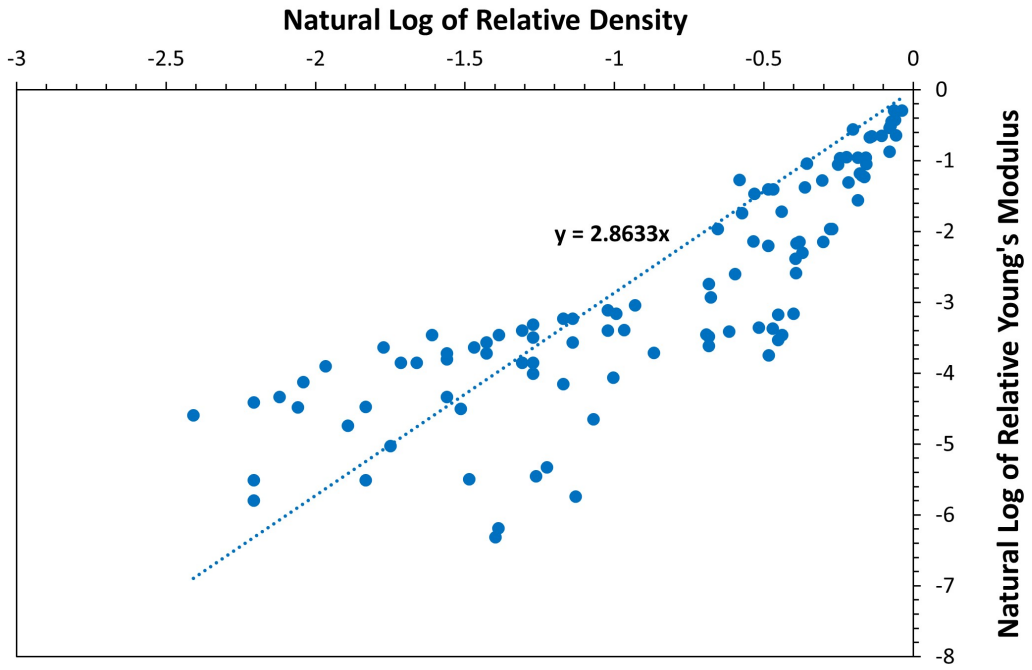

(a)

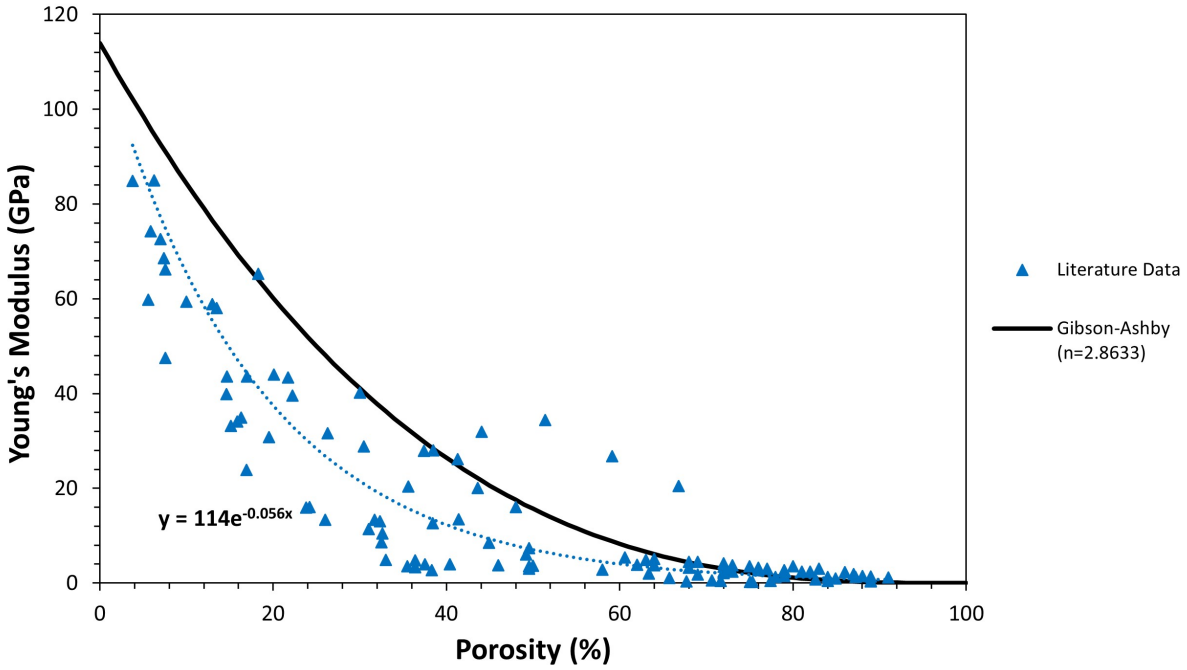

(b)

Figure 28: Graph showing the natural log of Young's modulus against natural log of relative density for porous Ti64 manufactured using various techniques (a) and literature data for Young's modulus against porosity compared with Gibson-Ashby model using n value obtained from plot (a).

Alternative models that approximate Young's modulus of porous materials have been developed in more recent years, including the Pabst-Gregorová exponential relations model [214] which is shown in Equation 4. This model has also been plotted in Figure 27b.

$$E_{\mathrm{r}} = exp\left(\frac{-2\phi}{1-\phi}\right) \tag{4}$$

The modulus of porous scaffolds with similar porosities can also be impacted by a number of manufacturing parameters such as the geometry of the unit cell used in SLM [211], the sintering temperature and particle size used in powder metallurgy [158] and the geometry of a sacrificial template used for space-holder casting [196]. This explains the level of scatter that is observed within the data in Figure 27. Despite this the data all tends to follow an exponential trend. The space-holder data points that lie significantly above the curve are from the work of Ryan et al. who used a 3D printed wax template as a sacrificial space-holder [196]. These values can be explained by the fact that the structures presented significantly anisotropic mechanical properties, and the Young's modulus presented here was measured axially, whereas their work found that the modulus measured in the transverse direction was approximately 69.3 % lower.

For porosities between $60-100$ % the relationship between modulus and porosity is reasonably linear and within this region can be approximated using Equation 5.

$$E = -0.0921\phi + 9.271 \tag{5}$$

As is clear from Figure 27b, neither the original Gibson-Ashby model nor the Pabst-Gregorová model provide a particularly accurate prediction for Young's modulus values of porous Ti64 scaffolds. The adapted Gibson-Ashby model using $n = 5$ based on the work done by Cabezas-Villa et al. provides a more accurate prediction, however between $40-90$ % porosity it predicts modulus values significantly below those recorded in literature. In order to obtain a value for the constant n which is specific to the data set presented in Figure 27b obtained from the literature, Equation 3 can be manipulated to produce Equation 6 which presents the equation of a straight line.

$$ln(E_r) = ln(C) + nln(\rho_r) \tag{6}$$

By applying Equation 6 to the literature data for Young's modulus at various porosity values, and assuming that the constant $C = 1$ as previously stated forcing the line through the origin, a value of the constant n can be extracted from the gradient of the line which for this data provides a value of 2.8633 as presented in Figure 28a. This n value can then be substituted back into Equation 3 to provide a plot of Gibson-Ashby model theoretical values for Young's modulus of porous Ti64, as presented in Figure 28b. Whilst this plot provides more accurate predicted values of Young's modulus at higher porosities (> 60 %), it still fails to accurately predict these values when compared against the exponential trendline plotted for the data. It is clear that modelling the relationship between Young's modulus and porosity presents significant challenges. This is in part a result of the fact that the various models are often developed for specific types of porous/cellular structures and therefore their accuracy is impacted by several parameters including pore connectivity/isolation, strut geometry, curvature of surfaces and regularity of porous structure [215]. In addition to this, the manufacturing processes themselves influence the mechanical properties of the material regardless of the level of porosity due to the impact of the heat exposure on the atomic crystalline structure. Thus it is virtually impossible to use modelling to accurately predict and design the porosity of scaffolds in order to achieve a specific modulus value, unless a large data set is acquired for each manufacturing process and porous structure. However, the collected literature data in Figure 27 as well as the Gibson-Ashby model with the calculated n constant value presented in Figure 28b provide a useful baseline estimation for porous Ti64 scaffolds which can be used to optimise the balance between porosity and modulus for this application.

All literature data modulus values beyond 60 % porosity are below $\sim 5\ GPa$, which is below the range of human cortical bone. This presents a challenge in that to achieve the desired level of porosity ($60-80$ %), an implant manufactured from Ti64 will almost certainly have a modulus below that of cortical bone. However, the modulus values are still greater than that of trabecular bone ($< 0.5\ GPa$). In this case two options can be considered, one being to attempt to produce Ti64 implant material with gradient porosity where the porosity of the outer material is reduced in order to ensure mechanical properties equal to that of cortical bone. The other option is to produce a single grade of porous material with porosity within the optimal pore size range for osseointegration, which presents sufficient mechanical properties for weight bearing applications. The challenge presented here is that there is not currently sufficient data available to suggest what mechanical

properties would be sufficient, which presents scope for further in-vivo testing to be conducted using implant material with mechanical properties of Ti64 with porosity of $<$ 60 % as presented in Figure 2.5.1. The dangers of reducing the porosity of the outer implant material are that this would likely have a negative impact on osseointegration and therefore the stability of the fixation between implant and surrounding bone, resulting in greater chance of implant failure. Therefore, it can be suggested that the primary concern with producing porous Ti64 implant material should be to achieve suitable levels of porosity and optimal pore structure/interconnectivity, and then to use methods of post-processing to improve mechanical properties to provide sufficient mechanical strength for load bearing applications.

2.5.2 Yield Strength

Yield strength (σ) is also a key property when assessing implant material as it is important that the implant is able to elastically deform up to at least the same level of stress as the surrounding bone. The yield strength of Ti64 is known to be $\geq 828\ MPa$, and a range of values for cortical and trabecular bone have been reported. Yield strength of bone varies with patient age and location within the body, however the general range has been recorded as $100 - 140\ MPa$ for cortical bone [35, 216, 217], and $75 - 100\ MPa$ for trabecular bone [35]. Like Young's modulus, yield strength has been shown to vary with porosity [210]. Figure 29 shows a summary of yield strength values against porosity for various porous Ti64 scaffolds from previously discussed literature.

Gibson and Ashby applied the same model as the Young's modulus to predict yield strength of porous materials, as shown in Equation 7.

$$\sigma_{\mathrm{r}} = C(\rho_r)^n \tag{7}$$

Where σ_0 and ρ_0 are the yield strength and density of the dense material, C is a constant again typically assumed to be equal to 1, and n is a constant that can be determined. Cabezas-Villa et al. observed that their data for yield strength against porosity matched closely to the Gibson-Ashby model when a value of $n = 5$ was applied. This model was plotted against data gathered from literature in Figure 29b using the value $n = 1.5$ as defined by Gibson and Ashby [210] and $n = 5$ as suggested by Cabezas-Villa [158].

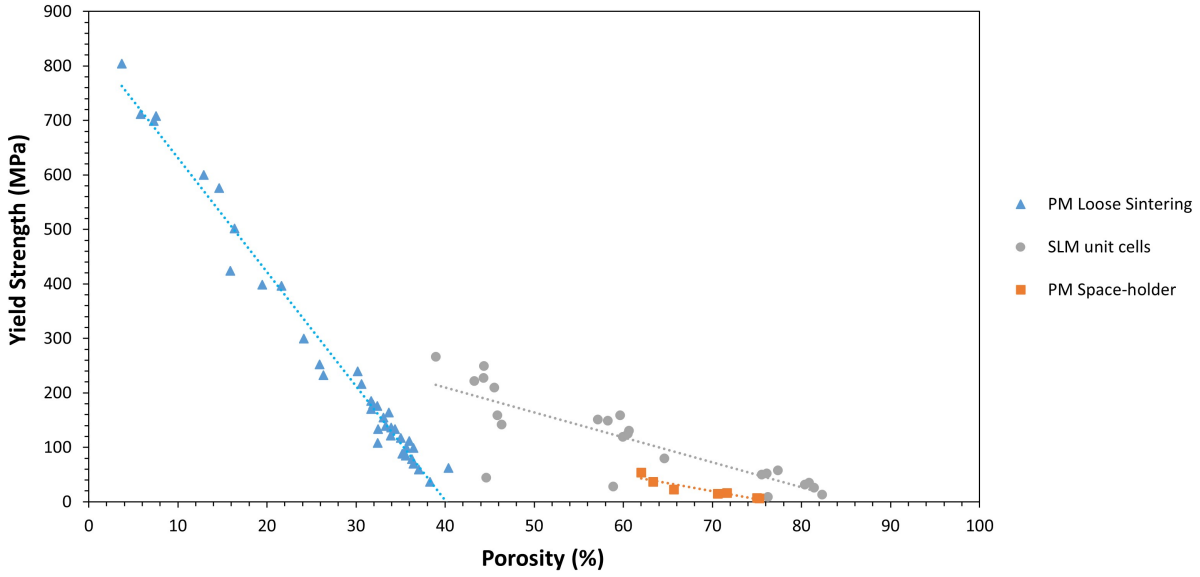

(a)

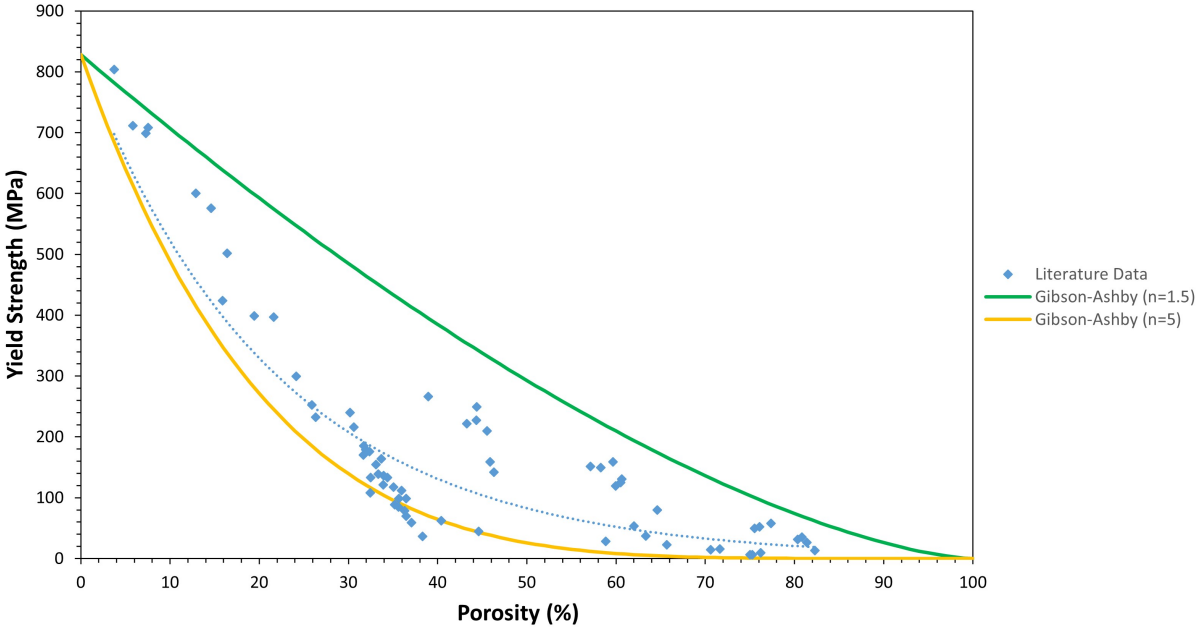

(b)

Figure 29: Graphs showing summary of Yield Strength against porosity of porous Ti64 scaffolds manufactured using various methods (a) and all methods combined compared with Gibson-Ashby models (b). Data collected from [158, 161, 167, 205].

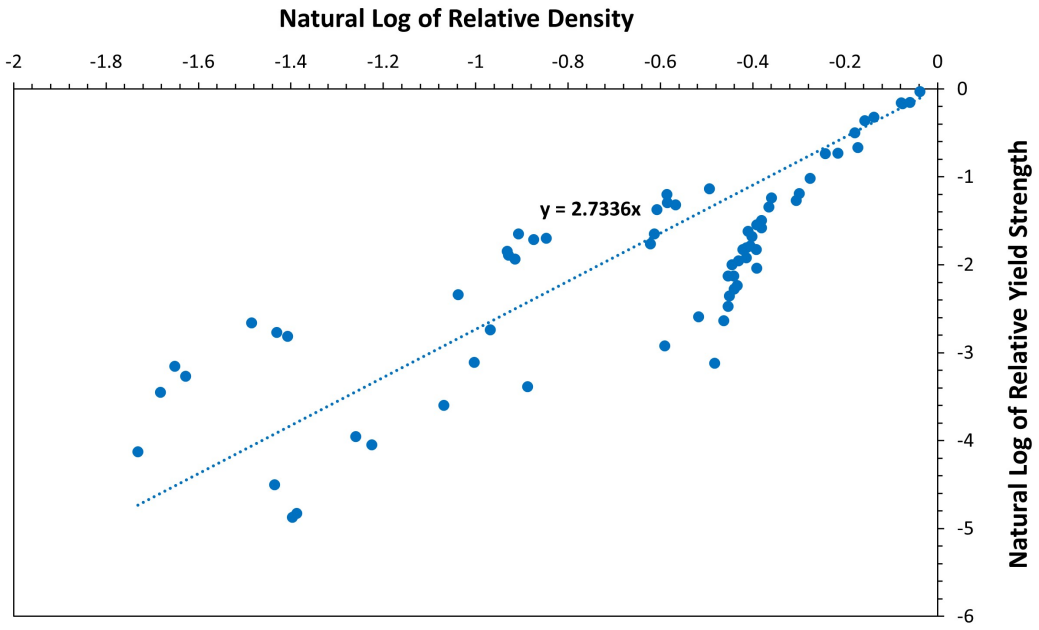

(a)

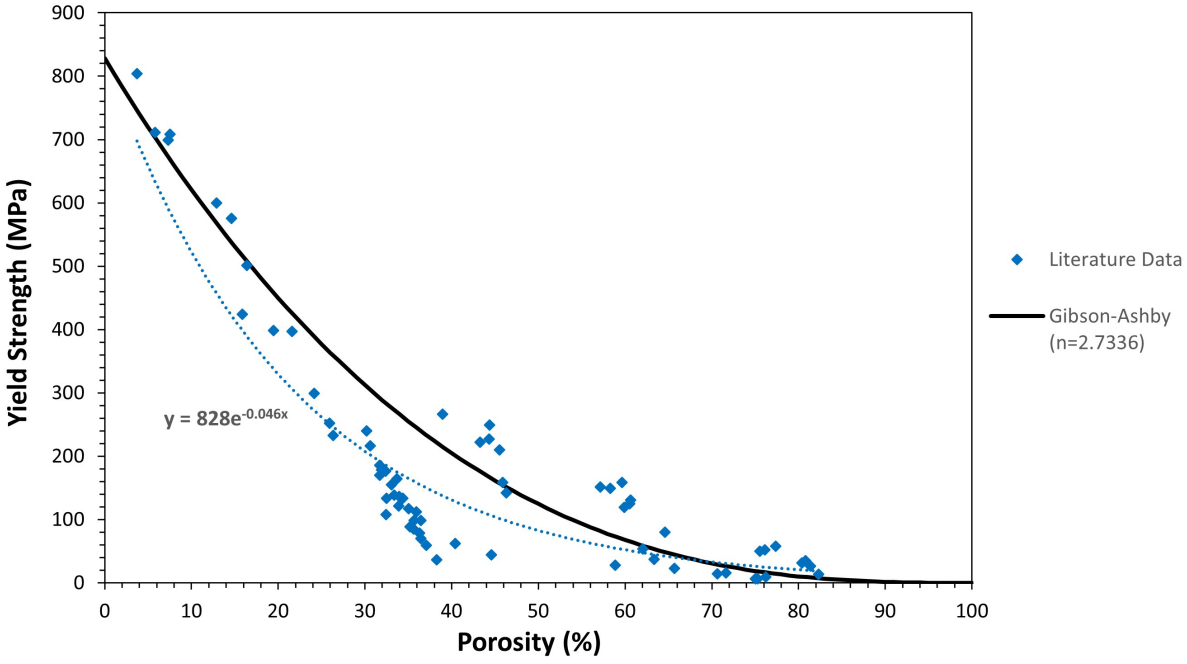

(b)

Figure 30: Graph showing the natural log of yield strength against natural log of relative density for porous Ti64 manufactured using various techniques (a) and literature data for yield strength against porosity compared with Gibson-Ashby model using n value obtained from plot (a).

Neither of the n values presented in Figure 29b provide an accurate estimation of the yield strength values when compared against the literature data, and therefore the same method was applied as for Young's modulus (Equation 6) so that a value for n specific to the data set gathered from the literature could be obtained from the gradient of the straight line as presented in Figure 7. This was then used to plot the Gibson-Ashby model again (Figure 30b), which provides a much more accurate estimation of yield strength at various porosity levels when compared against the literature data. The model fit for yield strength is more accurate than for Young's modulus (Figure 28b), which is likely due to the greater amount of scatter in the initial data for Young's modulus values at various porosity levels compared with the yield strength data, which then has an impact on the n value obtained from the natural log straight line gradient. However, as is clear from Figure 29a, the yield strength of porous Ti64 structures is significantly dependent on the manufacturing method used to produce them. As explained in Section 2.5.1 the mechanical properties of porous structures are impacted by a number of parameters aside from porosity. The literature data suggests that Ti64 with porosity of around 60 % and yield strength values similar to human cortical can be produced by SLM ($125 - 130\ MPa$) [205], whereas PM space-holder produced Ti64 with the same porosity resulted in yield strength values below that of even trabecular bone ($22.6 - 53.4\ MPa$) [167]. It should be highlighted that Figure 29 uses data collected from a limited number of sources and potentially provides biased trends particularly for SLM and space-holder methods as the data for each of these has been collected from a single study. However, as with the Young's modulus plots, Figures 29b & 30b provide a useful estimation of yield strength values for Ti64 with a given level of porosity, which can be used along with the Young's modulus plots to provide an idea of mechanical properties of porous Ti64 if the porosity can be measured.

2.6 Gel Casting

Gel casting was first developed in 1990 at Oak Ridge National Laboratories as a way of overcoming some of the challenges faced by injection moulding and slip casting [218]. The process involves creating a slurry by dispersing ceramic or metal powder within a solution usually comprising of water, a gelling agent (which when activated causes the slurry to form a high viscosity gel known as the green body), and a dispersant (which causes the powder particles to separate in order to ensure even distribution of the powder throughout the slurry) [218, 219]. The gelling agent is activated to

initiate the gel formation either chemically (the addition a chemical catalyst/initiator) or thermally [220]. The slurry is transferred to a mould where it gels to produce an in situ green body which can then be removed and sintered to burn away the gelling agent and other substances and melt the powder to form the solid part. Figure 31 presents the outline of the process.

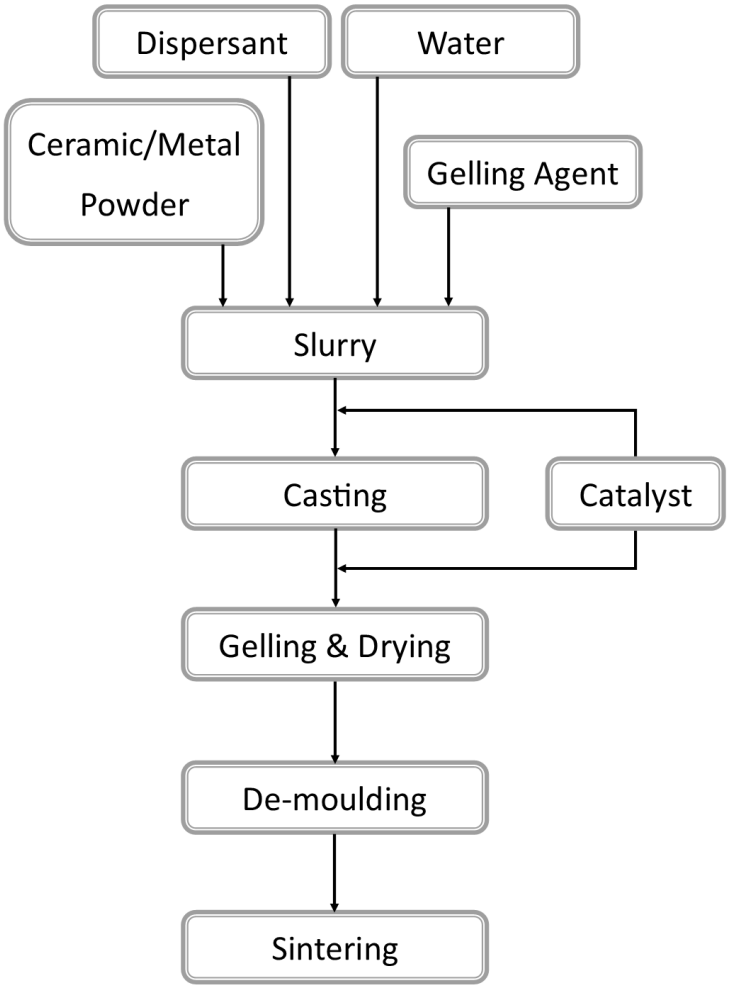

Figure 31: Schematic outlining the gel casting process

2.6.1 Gelling Agents

Previously industry has been reluctant to adopt the use of gel casting as gels were primarily composed of acrylamide which is a neurotoxin [218]. In response to this low toxicity gelling agents have since been developed [218, 221, 222]. Cellulose ethers and their hydroxyalkyl derivatives have been highlighted as water-soluble, non-toxic polymers that present a thermoreversible gelation charac-

teristic [218]. Thermoreversible gel casting involves using a reversible polymer gel that behaves as a low-viscosity slurry at a certain temperature and as a gel at either a raised temperature or a reduced temperature. Powder is combined with the slurry in liquid form, which is then poured into a mould cooled/heated resulting in the suspension of the particles within the gel. A number of nontoxic polymers have been used to create thermoreversible gels including gelatine, agarose, agar, carrageenans, methylcellulose, hydroxyethyl methylcellulose and hydroxypropyl methylcellulose [218, 223]. Agarose has been considered a promising gelling agent as it quickly forms a strong gel upon cooling [224]. A challenge that this can present is that the slurry suspension needs to be heated prior to casting in order to behave as a fluid, which can lead to an increase in viscosity due to evaporation of the water and results in difficulties when attempting to fill the mould. Therefore, it is preferable to use a gelling agent that behaves as a fluid at room temperature and forms a gel when heated.

2.6.2 Gel Casting Porous Ceramics

Initially gel casting was designed to produce dense ceramic parts, but has since been developed to introduce porosity [223, 225]. Porous ceramics have been given great attention due to their range of industrial applications including filters, membranes, catalyst support and thermal insulation, as a result of their specific properties including low bulk density, high surface area and low thermal conductivity [226]. Porous ceramic parts have been manufactured by gel casting using techniques such as increasing gelling agent content [227, 228], decreasing the content of ceramic powder particles within the slurry (solid loading) [229], introducing air into the slurry via the foaming technique [230, 231] and combing ceramic powder with a sacrificial space-holder that is removed either before or during the sintering process [225, 232].

2.6.3 Stability of Powder Based Slurries for Gel Casting

The role of dispersants within gel casting slurries is essential for maintaining low slurry viscosity at high solid loadings of powder, as well as preventing/reducing sedimentation of the powder particles [225, 233, 234]. When developing porous silicon nitride structures through gel casting combined with the sacrificial space-holder technique, Alem et al. investigated the effect of the concentration additions of different dispersants within the slurries upon the sedimentation behaviour [225]. The

results from this study show that some dispersants were more effective than others at preventing sedimentation of the powder within the slurries, and it is suggested that the reason for this is linked with the pH of the slurry and how this interacts with the charge of the particles and therefore the ability of the dispersant to cause repulsion between individual particles. Figure 33 shows the sedimentation heights of various slurry compositions from this work. The results suggest that all the slurry suspensions were highly stable, particularly those which presented only a small amount of sedimentation after 24 hours. It is worth noting that the particle size of the powder used in this study was $< 10\mu m$, which will have contributed to the impressive stability of the suspensions.

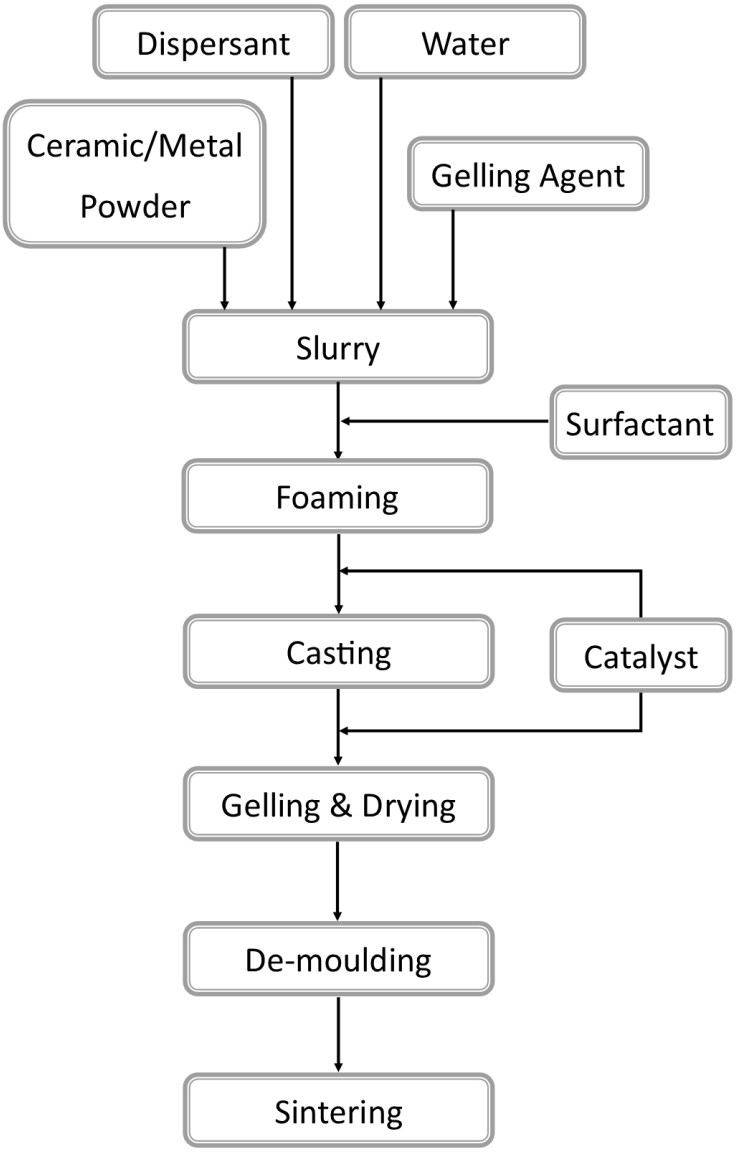

Figure 32: Schematic outlining the foam gel casting process

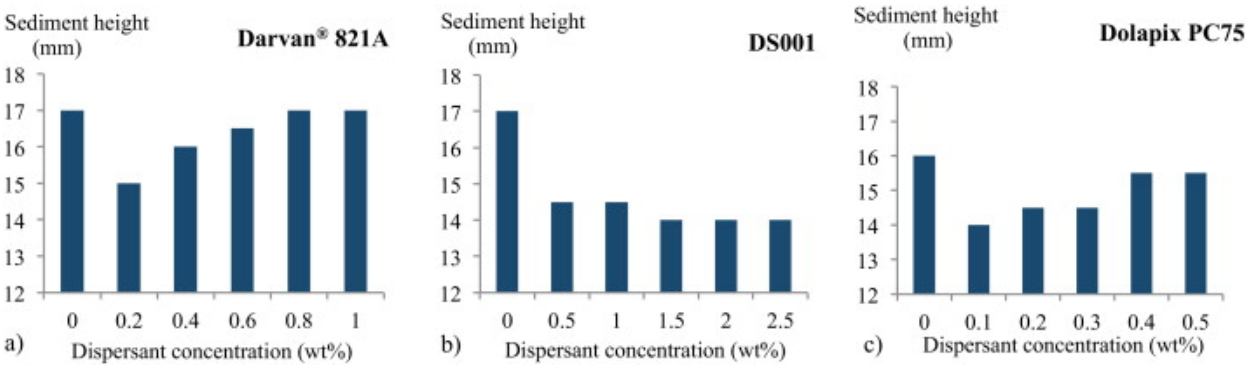

Figure 33: Bar charts showing sedimentation heights of silicone nitride powder slurry suspensions containing varying concentrations of different dispersants after 1 day.

Another study where dispersant addition was varied when producing porous HA scaffolds by gel casting showed that simply increasing dispersant concentration within the slurry did not decrease viscosity and sedimentation, but rather the work highlighted the importance of finding the optimal dispersant concentration addition [234]. This work agrees with the results from Alem et el. (2014) as presented in Figure 33 where it is clear that increasing the concentration of each dispersant initially resulted in a reduction in sedimentation height, but further increases in concentration had either no impact or actually resulted in an increase in sedimentation.

2.6.4 Foam Gel Casting

Gel casting can be combined with foaming to create porous green bodies by introducing air into a slurry using a number of techniques including mechanical whisking, injection of gases, blowing agents, evaporation or chemical reactions that produce gas [235]. In order to produce a stable enough slurry for foaming, the gelling agent used to produce the solution must minimise sedimentation of the suspended powder. The composition of the slurry and the loading of the powder has to be carefully considered in order to produce a gel with sufficiently low viscosity to allow aeration, whist also maintaining a self-supporting structure. Surfactants (or foaming agents) are often used to stabilise the air bubbles within the slurry by reducing the surface tension between gas and liquid [219, 235]. Surfactants are made up of two parts, one that is hydrophobic and the other is hydrophilic. The hydrophobic part is repelled by the liquid whereas the hydrophilic part remains attached to the liquid, which results in the surfactant being absorbed onto the gas-liquid interfaces within the foamed slurry, preventing it from collapsing [235]. The foamed slurry can then

be gelled to produce a green body and then sintered to form a porous structure. This technique has been successfully employed to create porous ceramic scaffolds by gel casting for a number of years [220]. Of the methods used to create porous ceramics using gel casting, the foaming technique has emerged as a preferable method because the porosity can be controlled in a number of ways, as outlined in Sections 2.6.4 - 2.6.4.

2.6.4.1 Effect of Surfactant Concentration and Foaming Time on Final Porosity

Kim et al. produced porous silica ceramics using foam gel casting, with a particular focus on the effect of altering the concentration of the foaming agent (surfactant), sodium lauryl sulphate (SLS) [230]. To begin with, the foaming time was increased and the resulting foam volume expansion was measured. Using this information, it was determined that the acceptable foam expansion ratio for this experiment should equal to two times the initial volume. As SLS concentration was increased, the time taken to reach this expansion ratio decreased and the size of the bubbles formed within the foamed slurry also decreased. This trend was observed up to a certain concentration where both these values plateaued. It was also observed that the final pore sizes in the sintered samples were significantly larger than the bubble sizes within the foamed slurry. As a result, structures of $65 - 70$ % porosity, and controllable pore sizes between $50 - 70$ μm were produced by increasing SLS concentration. In addition to investigating surfactant concentration, Kim et al. also examined the effect of foaming time on the volumetric expansion of the silica powder slurry and found that increasing foaming time initially resulted in a correlating increase in slurry volume, but beyond a certain point the slurry volume remained constant even upon further whisking, as shown in Figure 34 [230]. A very similar trend was observed by Jana et al. when producing porous silicone carbide, as shown in Figure 35 [236].

Similarly, Deng et al. investigated the effect of altering foaming agent concentration, triethanolamine lauryl sulphate, when producing porous mullite ceramics [237]. Increasing the foaming agent concentration from 0.025 to 1 % caused an increase in average pore size from 57 to 313 μm. Smaller windows that connected the pores were observed above a surfactant concentration of 0.2 %, and increasing the concentration from 0.2 to 1 % caused an increase in window size from 25 to 91 μm. Beyond 1 %, additional increase in foaming agent concentration had no effect on porosity and pore sizes. This observation appears to contradict the findings of Kim et al. who observed a

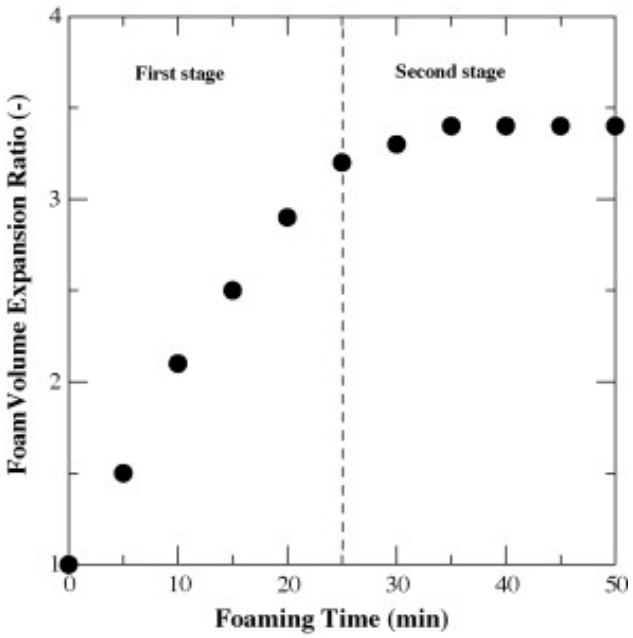

Figure 34: Graph showing foamed silica powder slurry volume expansion ratio against foaming time. Taken from [230].

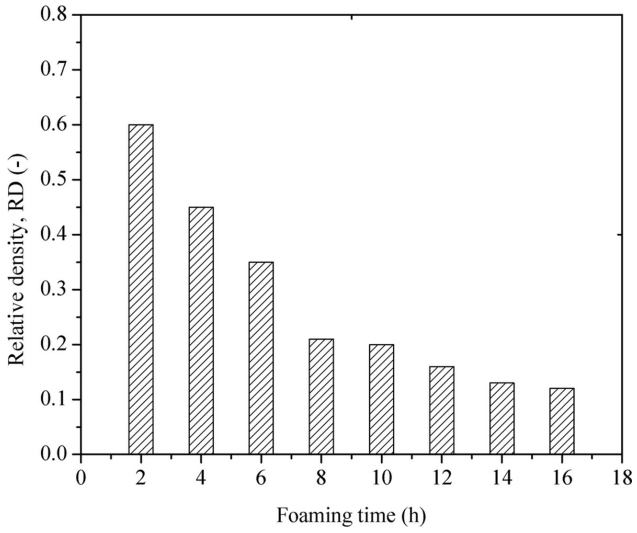

Figure 35: Graph showing relative density against foaming time of sintered porous silicone carbide produced by foam gel casting. Taken from [236].

decrease in pore size when foaming agent concentration was increased. Kim et al. attribute the presence of small bubbles at a higher foaming agent concentration to high slurry viscosity preventing coalescence of the bubbles into larger ones, however they provide no viscosity measurements so it is difficult to assess the reliability of this explanation. It is known that greater viscosity results in a smaller foamed volume [226], so it may be that the viscosity of the suspension in this case was

high, caused by a higher gelling agent concentration of 3.5 % polyethyleneimine and 1.2 % epoxy resin compared to the 0.5 % Isobam gelling agent applied by Deng et al.. The concentration applied by Deng et al. was selected by experimentally altering the concentration and measuring viscosity of the slurry. On increasing concentration from $0.3 - 1$ % the lowest viscosity was measured at 0.5 % and so this value was taken forward. On the other hand, Kim et al. provide no insight into the selection of the gelling agent concentration used. Therefore, it seems likely that a difference in viscosity caused by gelling agent concentration is the reason for the contrast in conclusions drawn from these studies.

2.6.4.2 Effect of Solid Loading on final porosity

The effect of solid loading on the viscosity of the slurry and density of the final sintered part produced by foam gel casting has been examined by several authors [226, 231, 236, 237]. Solid loading is defined by the weight percent ($wt\%$) of the ceramic powder compared to the weight of the liquid component within the slurry. Increasing solid loading has been observed to cause a decrease in porosity of the final sintered part (Figure 36) [226, 231, 236]. It has also been clearly shown that increasing it results in an increase in viscosity of the slurry as shown in Figure 37 [226, 237], and so it has been suggested this increase in viscosity decreases the foaming capacity of the slurry and therefore restricts the porosity and pore sizes of the sintered part [231]. This was demonstrated by Sharifi et al. who investigated the effect of both solid loading and foaming time simultaneously upon the foaming capacity of alumina powder slurries, and demonstrated that greater solid loading results in a more restricted foaming capacity (Figure 38) [238]. These findings show that solid loading could be used as a parameter to tailor the porosity of a component when foam gel casting, however it should be altered cautiously it is possible that decreasing the solid loading within the slurry could lead to excessive shrinkage during the drying/sintering processes. It is important that the viscosity of the slurry remains within the required limits for gel casting when altering solid loading [237]. Also, it is understood that greater solid loading improves the foamed stability of the slurry, which helps to ensure the foam structure remains stable for long enough for casting of the slurry [239, 240]. Using solid loading to control porosity is a method that has been developed for metal powders for gel casting *without* foaming of the slurry, which is discussed further in Section 2.6.6.

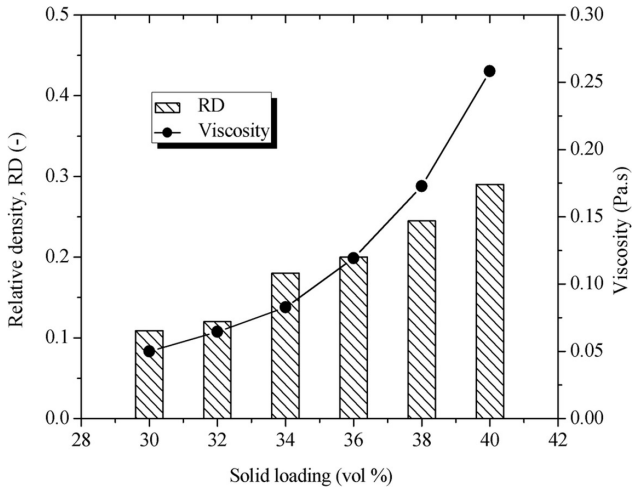

Figure 36: Graph showing foamed slurry viscosity and relative density of final sintered foams against solid loading for sintered porous silicone carbide produced by foam gel casting. Taken from [236].

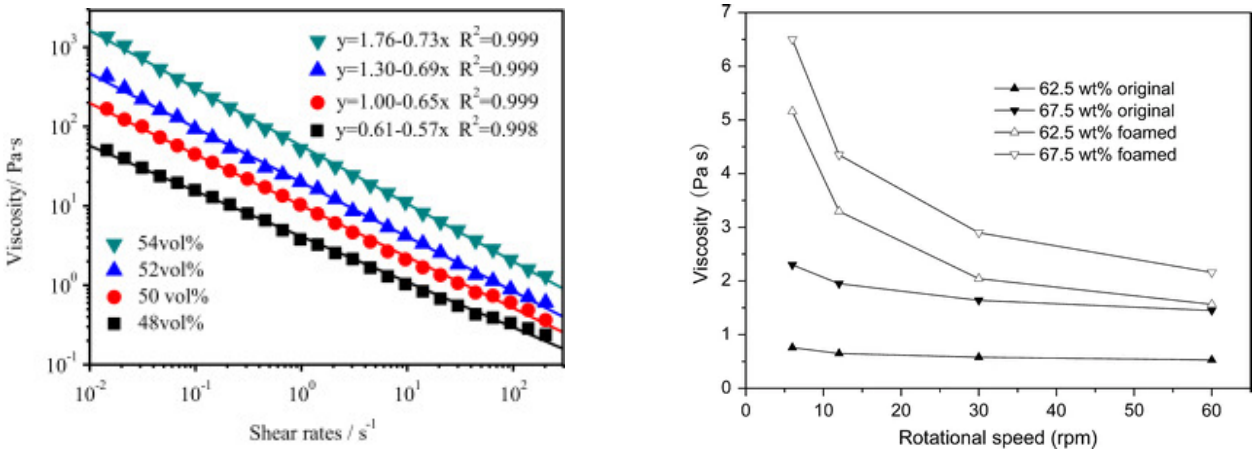

(a) (b)

Figure 37: Viscosity against shear rate of foamed mullite powder slurries with various solid loading percentages (a), taken from [237]. Viscosity against rotational speed of foamed and non-foamed mullite slurries with various solid loading percentages (b), taken from [226].

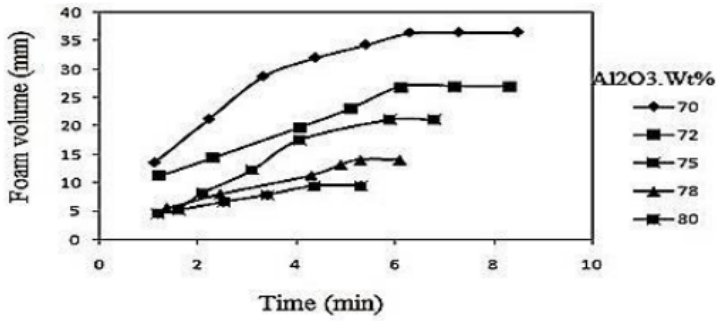

Figure 38: Graph showing foamed slurry volume against foaming time for alumina powder slurries with different solid loadings. Taken from [238].

2.6.4.3 Starch Consolidation Technique for Creating Porosity

Starch consolidation is an adapted space-holder technique which involves using starch particles as space-holders within a slurry mixture. Starch is insoluble in water below $50°C$ so can be easily mixed into a water based slurry, but when the temperature is raised the particles experience swelling as they absorb water and they can then be burned out leaving behind open pores. Barea et al. developed this method to produce porous mullite ceramics [241]. A slurry suspension was created by mixing mullite powder in water with dispersants and a potato starch powder. Increasing starch content from $15 - 55$ $wt\%$ resulted in porosity of $47 - 76$ % and a decrease in pore size from $42 - 30$ μm. It is suggested that this decrease in size was due to less water being available to each particle for absorption and so less expansion occurred at higher concentrations. Interestingly, however, the original average size of the starch particles prior to mixing was 55 μm, suggesting that the starch particles shrunk during sintering. No explanation of this is offered by the authors, but if this is the case then starch actually offers no additional benefit as a space-holder to alternative materials. Mao et al. developed a novel method of combining the foaming technique with starch consolidation to produce porous silica ceramics [231]. Raising the surfactant concentration caused an increase in foam volume up to a certain point when it plateaued and then began to slowly decrease. This information was used to obtain the optimal surfactant concentration. It was observed that foamed slurry had a higher viscosity than the original. By increasing the silica solid loading from $62.9 - 71$ $wt\%$, porosities of $82 - 70$ % were created. Pores of 3 different sizes were observed in the sintered ceramics; 50 μm, 10 μm and small voids. The larger pores were attributed to the trapped air bubbles in the foamed slurry and the medium sized pores were caused by the starch particles. The medium pores proved beneficial as they formed windows in the walls between air bubble pores, creating an interconnected pore network. Similarly to Barea et al., the pore sizes formed by starch particles were slightly smaller than the initial particle sizes, again suggesting shrinkage during sintering. Gong et al. applied this same method to produce porous mullite ceramics [226]. Porosities of $73 - 86$ % were achieved with pore sizes ranging from $150 - 200$ μm. Likewise to Mao et al., smaller windows in the pore walls were observed, forming connections between pores, the formation of which are attributed to the removal of organic matter during sintering. In this case no information on the geometry of the smaller windows is provided.

2.6.4.4 Summary of Foam Gel Casting Processes

Foam gel casting offers the ability to not only produce porous components but also to tailor the porosity by controlling a number of parameters. This, however, means that the composition of the slurry must be carefully considered and significant preliminary testing is required to determine optimal values for parameters such as solid loading, foaming agent concentration and foaming time. The use of this technique to produce porous ceramic scaffolds specifically for biomedical implants, and also how it has been adapted to produce porous metal scaffolds, is discussed in Section 2.6.6.

2.6.5 Metal Gel Casting

The primary application of gel casting has been producing ceramic components, with limited research focusing on adapting this process for metals [242]. It has been suggested that this is due to the wealth of alternative production methods available for metals, and because of the difficulties associated with suspending metal powder with high densities in a slurry [219]. Li et al. investigated methylcellulose (MC), hydroxyethyl methyl cellulose (HEMC) and hydroxypropyl methyl cellulose (HPMC) as potential gelling agents for gel casting using metal powders [218]. The metal powders used were course (30 μm) and fine (3 μm) iron powders, and the effect of powder size was analysed. A defoamer, antioxidant and dispersant were also added to the water-based solutions. HEMC was quickly disregarded because of concerns that its higher gelation temperature could cause excessive oxidation and because of its low gel strength. The effect of solid loading of the iron powders and the concentration of gelling agent were also investigated. It was discovered that the viscosity of the solution increased as concentration of gelling agent is increased, particularly beyond 0.52 wt%. Increasing solid loading of the metal powder led to a weaker green body strength, and beyond 57 wt% the green bodies were not strong enough to be removed from the mould. For HPMC it was shown that increasing concentration improved the green body strength, which would allow for higher solid loading of the powder leading to a higher final part density. However, this has to be balanced out with the effect on viscosity of increasing HPMC concentration. The viscosity of a slurry must be within certain parameters in order to effectively fill a mould. Therefore, an optimal concentration of 0.39 wt% was concluded for both MC and HPMC. The MC solution displayed superior viscosity to HPMC, but HPMC produced a higher green body strength. Both gelling agents are concluded

to be suitable for the gel casting of metal powders, and the choice between them should made based on the specific application. The viscosity of the solution was far greater when the course powder was added than the fine powder, and interestingly, when a mixture of course and fine was used, the viscosity was similar to the fine powder solution. As a result, the authors recommend using either a fine powder or a mix of course and fine when preparing slurries with metal powders.

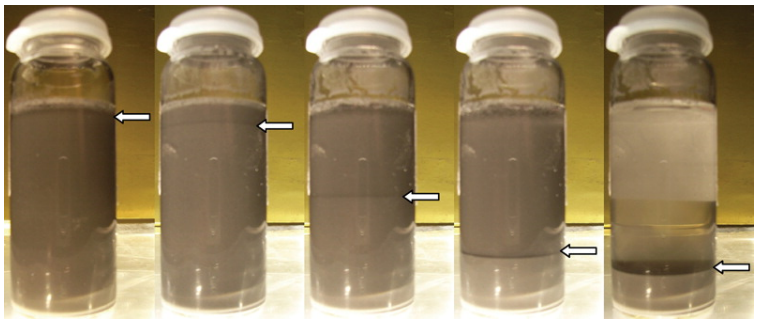

Figure 39: Images showing observed sedimentation of a SS 316L powder slurry over time. Taken from [220].

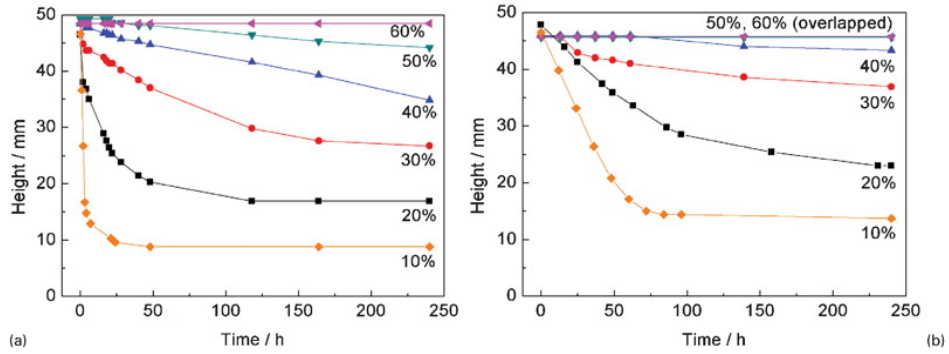

Figure 40: Graphs showing measured sedimentation height of SS 316L slurries produced with various solid loading percentages, using a MC solution concentration of 2 % (a) and 4 % (b). Taken from [220].

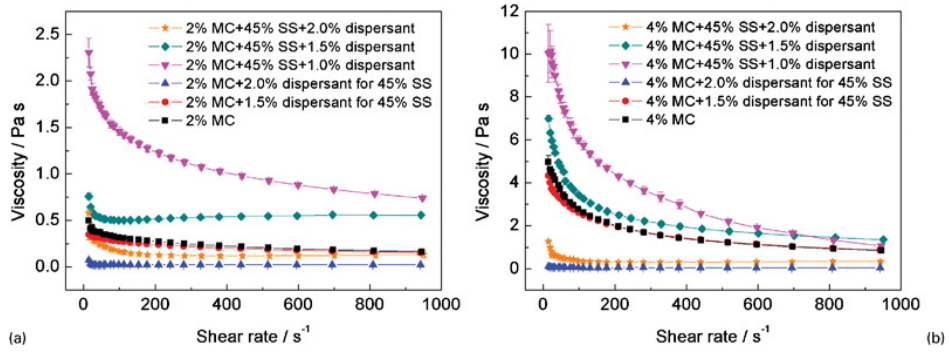

Figure 41: Graphs showing viscosity against shear rate for different SS 316L powder slurries containing various dispersant additions and solid loadings, mixed using both 2 % and 4 % MC solution concentrations. Taken from [220].

MC has been applied in more recent work as a gelling agent for producing SS 316L powder slurries for gel casting [220, 243]. In the development of this process for SS 316L the stability of the metal powder based slurry was investigated by observing the sedimentation height (Figure 39), and the sedimentation height was measured over time for various slurry compositions as shown in Figure 39. The results show that it is possible to produce stable suspensions of a high density powder such as SS 316L, which is very promising for further development of this process for other metal powders. By increasing the solid loading within the slurry up to as high as 60 %, highly stable slurries were achieved which showed no observable sedimentation over 250 hours, even when a MC solution concentration of only 2 % was used within the slurry. The impact of various slurry composition parameters on both the stability and viscosity of the slurries was investigated, and Figure 41 presents graphs that show the viscosity of the slurry mixed with both 2 % and 4 % MC solution concentrations, and with different solid loadings of powder as well as varying $wt\%$ additions of the dispersant. The development of this work is discussed further in Section 2.6.6.

2.6.6 Manufacturing Porous Implants using Gel Casting

Much of the research on using gel casting to produce porous scaffolds for biomedical implants has focused on hydroxyapatite (HA) and related calcium phosphates as implant materials because of their high biocompatibility and similarities to bone in composition [244–246]. However, a few studies have also aimed to produce porous Ti scaffolds using different gel casting techniques.

2.6.6.1 Space-Holder Metal Gel Casting

Erk et al. were able to produce porous Ti components using thermoreversible gel casting with pore sizes ranging from $30 - 70\ \mu m$ and porosity of $4 - 44$ % [242]. Poly(methyl methacrylate)–poly(n-butyl acrylate)–poly(methyl methacrylate) (PMMA–PnBA–PMMA) was the copolymer dissolved into 1-pentanol at a concentration of 7 % to produce the gel. Two different space-holder materials were used to produce pores; chromatographic grade polypropylene beads and poly(methyl methacrylate) beads. The geometry of the pores produced closely matched the geometry of the space-holder applied. Based on previous work the assumption was made that particle sizes of the metal powder would have to be kept at $<5\ \mu m$ in order to ensure suspension of the powder within the gel solution. With particle sizes this small, the level of oxidation that would occur on

the surface of each Ti particle would introduce a large level of oxygen into the gel which would deteriorate the mechanical properties of the final sintered structure. Therefore, TiH_2 powder was used to avoid oxidation. Once the powder and gel were mixed at an elevated temperature, the solution was poured into a mould and cooled. It was then removed from the mould, sintered at a low temperature ($<400°C$) to remove the copolymer and space-holder, then sintered at a high temperature ($1000°C$) to cause the decomposition of the hydride and sinter the Ti particles, and then left to cool. Whilst this study shows that gel casting combined with the space-holder technique can produce porous components, the porosity and pore sizes produced are significantly below the optimal values for biomedical scaffolds. However, this work does clearly show that gel casting can be adapted to produce Ti components by using a non-water-based gel solution.

2.6.6.2 Gel Casting Porous Ti by Reducing Solid Loading

Porous Ti scaffolds have been produced by altering the solid loading of Ti powder [13, 247, 248]. Yang et al. achieved porosity range of $38.34\ \% - 58.32\ \%$ and pore sizes of $5 - 102\ \mu m$. Mechanical properties of the scaffolds were also tested and the Young's modulus ranged from $7 - 25\ GPa$, which are within the regions discussed in Section 1.1.1 for human bone [13]. The slurry used in this study consisted of a monomer (acrylamide), a cross-linker (N, N'-methylene-bisacrylamide), a catalyst (N, N, N', N'-tetramethylethylenediamine) and an initiator (ammonium presulphate) all dissolved in deionised water. Ti alloy (Ti-Co and Ti-Mo) powders were added at controlled solid loadings along with a dispersant (Oleic acid). The average particle sizes of the Ti-Co and Ti-Mo powders were identified as 46.6, 39.5 and 10 μm respectively. Porosity was controlled by altering the monomer content and solid loading of Ti alloys so that the monomer acted as a space holder which was burnt out to leave behind pores. Using a very similar technique and slurry composition, Yang et al. also produced porous scaffolds from Ti-Mo and Ti-Nb alloys with porosity $39.15 - 49.66\ \%$ with pore sizes $5 - 120\ \mu m$ and Young's modulus $5 - 18\ GPa$ [247]. Li et al. applied this same method to produce porous scaffolds using Cp-Ti powder (46.6 μm average size) [218]. By optimising the sintering process, porosity of 46.5 % and Young's modulus of 8.5 GPa were achieved, however no analysis of the pore sizes is reported. Whilst the porosities and Young's moduli achieved in these studies appear promising, the pore sizes produced using this method are mostly below the optimal sizes discussed in Section 1.1.1. Oxidation on the surface of the Ti particles prior to dispersing in

the slurry was not a concern when using the method outlined by Yang et al. [13]. This was because the composition of slurry solution allows for larger particle sizes to be used which significantly reduces the surface area and the amount of oxygen imported by the particles. In addition to this, the Oleic acid used not only acted as a dispersant, but also prevented oxidation of the metal powder within the water-based slurry.

2.6.6.3 Metal Foam Gel Casting

Pore size is one of the most important factors to consider when designing porous components for specific applications [230]. Alternative manufacturing methods used to produce porous Ti scaffolds using gel casting have struggled to increase pore size to the values desired for bone in-growth within orthopaedic implants. It has been outlined previously that foam gel casting is able to produce ceramic parts with high porosity and large pore sizes (up to several hundred micrometres) [223]. Using foam gel casting, porous HA scaffolds have been produced with pore sizes and connecting window sizes of 150 μm and $10 - 80$ μm [246]. Also, Potoczek et al. were able to produce HA scaffolds with pore sizes of $250-900$ μm and window sizes of $25-250$ μm [244]. In this study agarose was employed as the gelling agent, and gelation was initiated by cooling the foamed slurry from the foaming temperature of $60°C$ to $15°C$ and then drying at room temperature before sintering. The high level of porosity was achieved by dissolving the initial agarose solution at a temperature of $121°C$ under overpressure of 1.4 bar [224]. This allowed for complete dissolution of the agarose whilst maintaining a lower viscosity than solutions prepared by simply heating, allowing a larger foaming capacity of the slurry. These studies show that the foam gel casting technique can produce ceramic scaffolds with large pore sizes suitable for biomedical implants. HA has a similar density to that of Ti64 which suggests it should be possible to develop methods that are able to produce porous Ti64 scaffolds with high levels of porosity.

Gel casting is an easily adaptable process for use with new materials [221], and the combination of gel casting and foaming has been adapted to produce porous metal in more recent years [220, 243]. Lin and Kennedy successfully developed a method for producing porous SS 316 L using this technique [243]. The composition of the slurry used to produce the structures was extensively optimised in previous work [220]. Methylcellulose (MC) was used as both a suspending agent and gelling agent, and a polyacrylate dispersant (Darvan 7-N, Vanderbilt Minerals, Norwalk CT) was

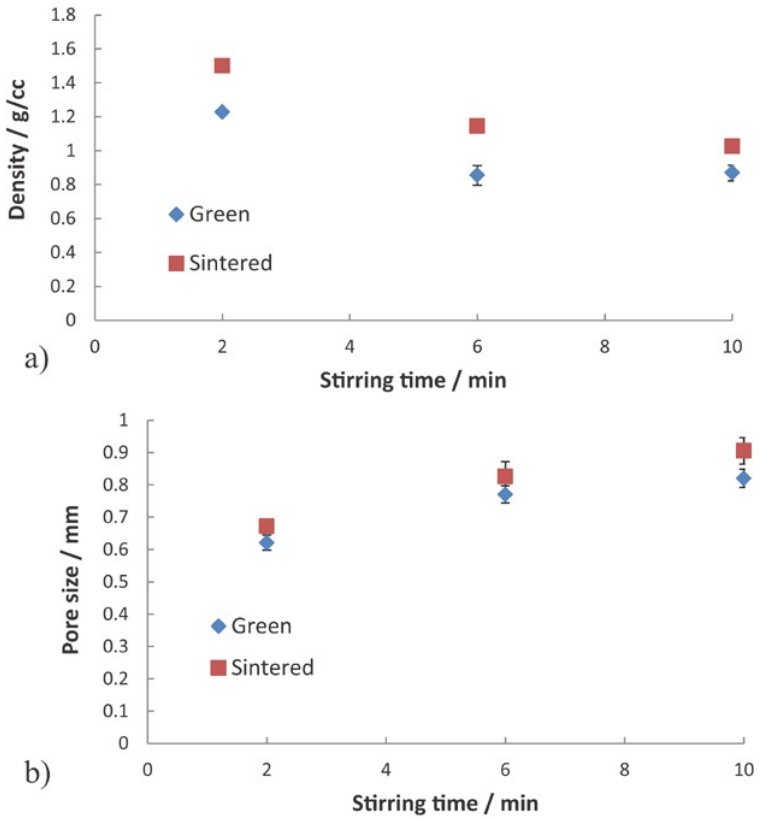

Figure 42: Density and pore size against slurry whisking time for sintered porous SS 316L produced by foam gel casting. Taken from [243]

added to prevent agglomeration of the powder particles. SS 316 L powder, with average particle size of 9 μm, was dispersed in the slurry. The porous structures were created by mechanical whisking of the slurry to introduce air, along with the addition of a surfactant (Triton X-100, Dow Chemicals) to activate bubble formation. It was discovered that the pore sizes of the sintered structures were larger when the aeration time was increased (690 and 900 μm for 2 and 10 minutes whisking respectively), however the same relationship discussed in Section 2.6.4 was observed where a greater increase in porosity and pore size was observed with initial increase in whisking time, but then beyond a certain point (around 4-6 minutes) these values plateaued with further whisking (Figure 42). The density of the structures increased by $15 - 25$ % during the sintering process. The pores were connected by smaller windows that formed in the walls separating the pores, and the window sizes were also observed to increase with aeration time (210 and 482 μm for 2 and 10 minutes whisking respectively). By increasing aeration time from $2-10$ minutes, the porosity of the sintered structures increased from 82 to 88 % and Young's modulus decreased from 7.8 to 3.6 GPa.

No information regarding the stability of the foamed slurry is provided as it was transferred into moulds and placed in an oven to gel immediately after whisking, however it is suggested that the presence of interconnecting windows between adjacent pores is a result of the instability of the foamed slurry as the bubbles within the slurry begin to coalesce through thinning and rupture of the cell faces [243, 249]. The sedimentation of the powder particles within the slurry prior to foaming was investigated in the previous work where the gel casting procedure was developed for SS 316L [220], as discussed in Section 2.6.3.

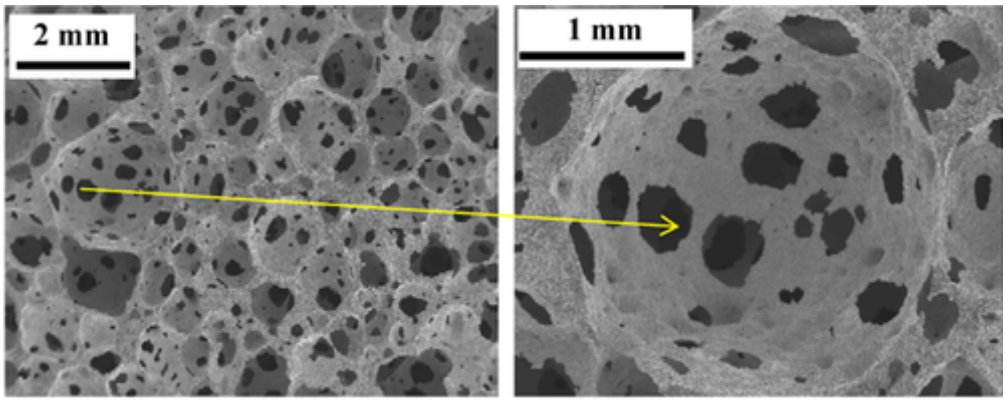

Figure 43: SEM micrographs showing pore geometry for steel samples producing using foam gel casting. Taken from [243].

The combination of larger pores and smaller windows observed in this work could prove to be a beneficial characteristic for a biomedical implant. As discussed in Section 1.1.1, human bone contains a variety of pore sizes, and so replicating this in a scaffold could further promote bone in-growth. This work shows clearly that gel casting combined with slurry foaming can produce highly porous scaffolds from metal powders, with desirable pore geometries for this application. It should be possible therefore to replicate this process for other metals such as Ti, and achieve the ideal levels of porosity discussed in Section 1.1.1 for the promotion of bone in-growth. Lin and Kennedy observed a dense surface layer around the outside of the green bodies when removed from the various moulds they were cast in [243]. It is likely that this is due to the slight expansion of the foamed slurry during casting, compressing it around the outside layer of the mould and causing a dense skin surrounding the porous inner structure. In this case, the outer skin had to be removed before analysing the samples. The use of a mould to produce the desired geometry restricts this process, particularly for the application of orthopaedic implants implants where geometry needs to

be tailored to specific applications, meaning that a new mould must be produced each time.

2.6.7 Combining Foam Gel Casting and Material Extrusion

As described in Section 2.3.5, the material extrusion AM process has been applied to powder based slurries in the form of '3D fibre deposition' to produce porous Ti structures. A similar process was developed by Muth et al. to 3D print highly porous ceramic structures [250]. The slurry (referred to as 'ink') used in this study was mixed using fine alumina powder ($\sim$ 300 nm particle size), de-ionised water and sodium hydroxide as a gelling agent along with other components to make the powder hydrophobic and strengthen the printed structures. The slurry was mechanically whisked to introduce air bubbles resulting and then the foamed slurry was extruded using syringe pump and a custom-built 3D printer. The structures were dried and then residual chemicals removed by burnout before sintering. Unit-cell structures were printed using the foamed slurry (Figure 44) with geometric porosity of 62 %, and the extruded struts themselves contained porosity of $\sim$ 80 %, resulting in an overall porosity of $\sim$ 94 % for the final structures. The porosity within the struts was entirely closed-cell, allowing it to be measured using Archimedes' method as described in Section 2.4.2. The authors of this work conclude that it should be straightforward to adapt this process for other ceramics and metals to produce either open or closed cellular materials.

In both of these instances the main porosity of the structures was produced by the lattice deposition arrangement of the tracks ('fibres' or 'struts'), and as highlighted in Section 2.3.5 the porous structures are not necessarily optimal for orthopaedic implants, particularly compared with those achieved through foam gel casting. Therefore there is significant potential scope to adapt the process developed by Lin and Kennedy [220, 243] in order to produce highly porous Ti, and combine this process with material extrusion in order to make the geometry of the structures more customisable by removing the need for a mould. This method could provide a novel way forward for manufacturing porous Ti implants with specifically tailored porosity as well as geometry.

Most commercially available 3D printers are filament based, however, more recently models have been developed that allow the option to switch the tool head to perform other functions including paste extrusion [251]. Amza et al. developed an extrusion toolhead that can act as a direct replacement for a conventional thermoplastic extruder in a desktop FDM machine [252]. The custom toolhead includes a range of nozzle sizes between 0.15 and 1.54 mm, and was able

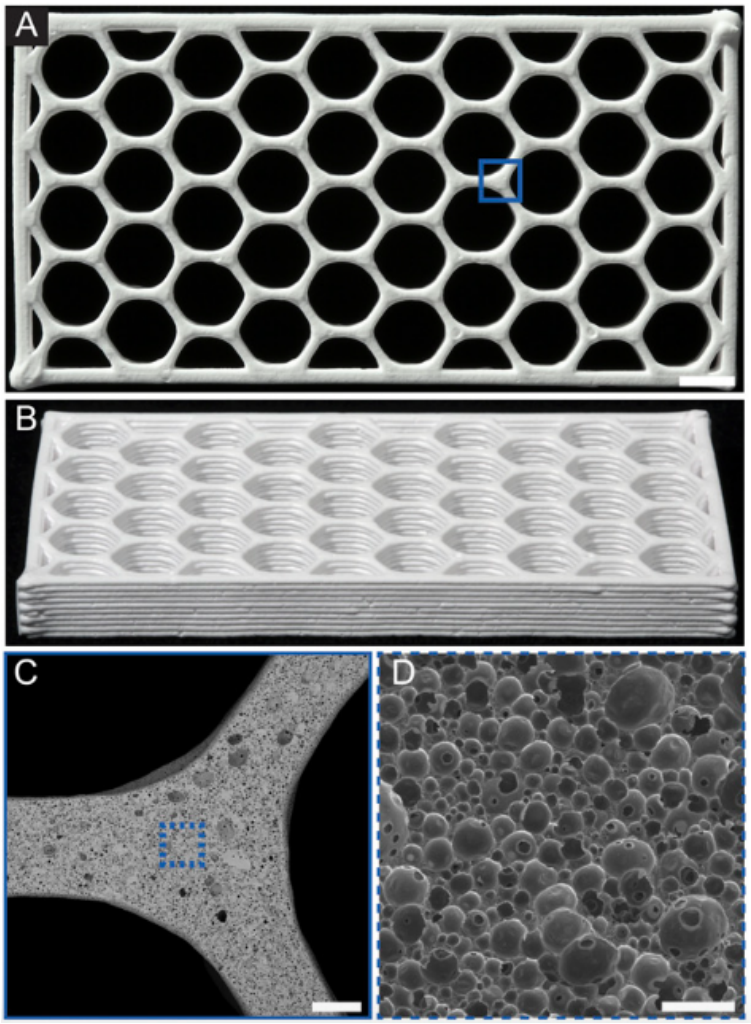

Figure 44: 3D printed porous ceramic hexagonal unit-cell structures printed using foamed alumina slurry. Taken from [250].

to produce simple 3D structures from a range of paste materials including silicone, dental gel and a cement mixture 45. The study highlights the wide range of potential applications for this technology, particularly within the medical and food sectors, as well as the lack of commercially available systems that offer this functionality. The limitations of this system include the lack of capacity for generating support structures, which means that only geometries with limited overhang can be produced. The authors highlight this limitation, and state that future research will aim to develop a hybrid system where thermoplastic support structures can be deposited in conjunction with the paste extrusion toolhead.

The ZMorph 2.0 3D printer is a commercial grade printer that provides this functionality using a motorised syringe pump (Figure 46). This function is primarily recommended for printing foods

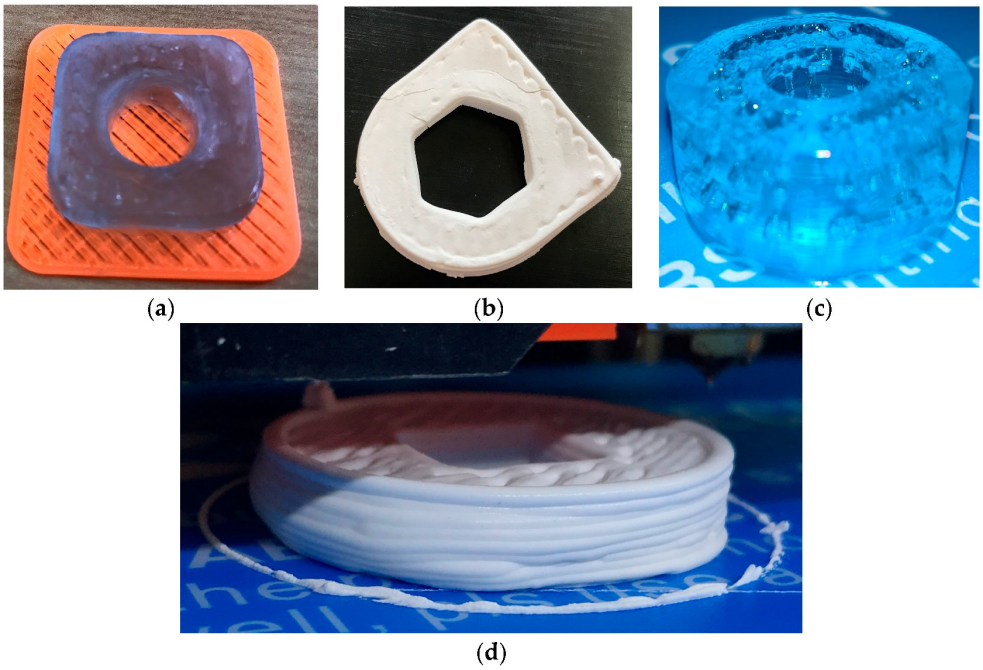

Figure 45: Simple 3D structures deposited using various paste-like materials through a bespoke extrusion toolhead developed to replace conventional FDM toolhead. Taken from [252].

such as cream cheese, chocolate spread and pâté [253]. There are also examples of this function being used to print other premixed solutions, with a viscosity within the recommended range of $20,000 - 70,000\ mPas$ [254]. ZMorph 2.0 also offers the ability to print on a heated bed, which should enable the user to print slurry containing thermally activated gelling agents that will gel once deposited, allowing for more complex shaped green bodies to be produced without the need for a mould. The viscosities of the foamed slurry mixtures produced by Lin and Kennedy are below the recommended range for thick paste extrusion, however, it is clear from the literature covering porous ceramic gel casting that there are a number of ways to increase viscosity of a slurry. If foamed Ti64 slurrys could be created that have a viscosity suitable for printing with a paste extruder, whilst also producing sintered scaffolds that achieve the desired porosities for implants, this would provide a completely novel process capable of addressing the challenges outlined in Section 2.9. The effect of extrusion through the nozzle on the porous structure would have to be carefully monitored to ensure that the resulting structures maintain the same porosity characteristics as when they are simply poured into a mould.

(a) (b)

Figure 46: ZMorph thick paste extruder toolhead (a) and toolhead being used to extrude decorative chocolate (b). Taken from [253].

2.7 Mathematical Modelling of Drying Behaviour of Thin-Layer Solids

There has been a growing interest in modelling the drying behaviour of solids over the past century, particularly within the area of thin-layer drying of fruits and vegetables for preservation purposes as well as across a range of applications across the agricultural, manufacturing, paper, polymer, chemical and pharmaceutical industries [255]. The primary focus of such models has been the moisture content of the material over time during the drying process, the oldest and most basic of which was developed by Lewis [256] which is presented in Equation 8. Several factors affect the drying rate of thin-layer materials including air velocity, drying temperature, size and shape of material, and the relative humidity. The most influential of these have been identified to be drying temperature and material thickness [257–260]. Drying behaviour models can be used to predict moisture content over time, as well as energy consumption and heat and mass transfer throughout the drying process [261]. The various models that have been developed and adapted over the past century have been used in the calculation for design of drying systems, in order to optimise the drying process both in terms of drying time as well as energy consumption [255].

2.7.1 Thin-Layer Drying Models and Classification

Thin-layer drying models can be categorised into three classifications; theoretical, semi-theoretical (or semi-empirical) and empirical. Empirical and semi-empirical models rely heavily on experimental data, but as such provide more accurate predictions of drying behaviour than theoretical models by making fewer assumptions [255]. As a result, these categories of models have been the most commonly applied to thin-layer drying of fruits and vegetables. These models are based on assuming isothermal conditions, as well as a number of other assumptions including the material being up to a few particles thick, evaporation only occurring at the surface of the material and temperature distribution throughout the material being uniform [262]. In general, semi-empirical models can be split into two sub-sections; models built upon Newton's law of cooling, and models build upon Fick's second law of diffusion [260, 262]. The Lewis model (often referred to as the Newton model) is derived from Newton's law of cooling, and is described as the most simple semi-empirical model because it contains only one model constant, as presented in Equation 8.

$$MR = exp(-kt) \tag{8}$$

Where k is the drying constant (s^{-1}), MR is the moisture ratio (the ratio of the mass of water removed from the sample to the initial mass of water within it) at a given time t (s). The Page model (often referred to as the Modified Lewis model), was developed from the Lewis model which introduced a dimensionless empirical constant (n) in order to reduce the errors associated with this model, as presented in Equation 9.

$$MR = exp(-kt^n) \tag{9}$$

These two semi-empirical models that are derived from Newton's law of cooling have been widely applied to thin-layer drying of a range of fruits and vegetables including melon, green bean, kiwifruit, mango, onion, pumpkin, quince, starfruit, red chili and strawberry [263–274], with the Page model being found generally to be the most suitable for describing the drying behaviour. In addition to the Lewis and Page models, there exist three versions of the Modified Page Model (I, II and III) [262] as well as a range of over twenty other adapted versions of these models with

varying levels of complexity which have been developed to describe the behaviour of specific thin-layer materials [255, 260]. Empirical models are those which are derived wholly from experimental data, without being built upon specific fundamental drying principles. These include models such as the Weibull Model, Wang and Singh Model, the Thompson Model and the Kaleemullah Model [275–278]. These models, whilst having been applied to the drying behaviour of thin-layer fruits and vegetables, are less commonly used due to the limitations outlined in Section 2.7.2.

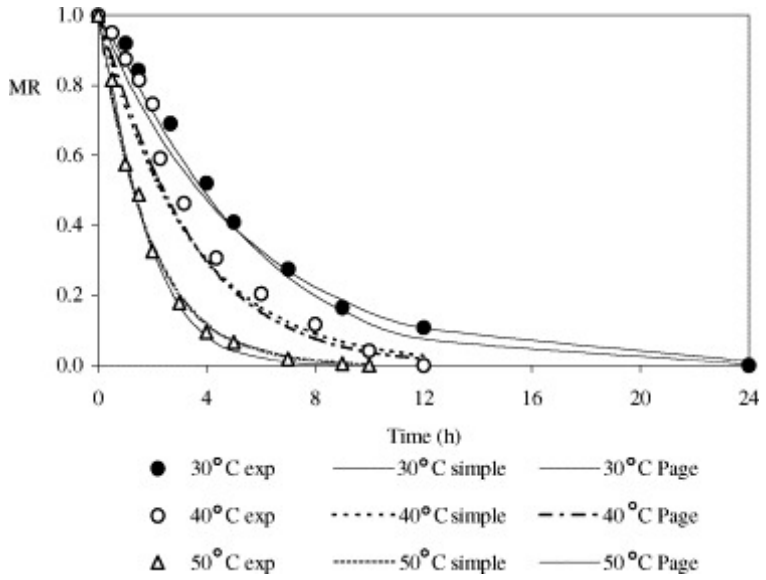

Figure 47: Newton (referred to as 'simple') and Page drying behaviour models applied to experimental data gathered from the drying of thin-layers of peas. Taken from [279].

Figure 47 shows both the Newton and Page models applied to experimental data gathered from drying thin layers of peas which is taken from Senadeera et al. [279]. This work concluded that both models could be applied to adequately predict the drying behaviour of various thin-layer vegetables, however the Page model provided a more accurate prediction. Da Silva et al. analysed the statistical fit of five different drying models (including semi-empirical and empirical) applied to the drying data obtained from drying whole bananas [280]. This study concluded again that of the existing models analysed the Page model provided the best statistical fit, as well as developing a new adapted model which produced similar accuracy to the Page model. Similarly, Kumar et al. applied the Lewis, Page, Fick's and Modified Page III models to experimental data gathered from the drying of onion layers and concluded that the Modified Page III model provided the best statistical fit [281]. The predicted drying behaviour plotted against the experimental data from

this study is presented in Figure 48. As is clear from Figures 47 & 48, once the most suitable model has been identified these semi-empirical models are able to provide accurate predictions of drying behaviour.

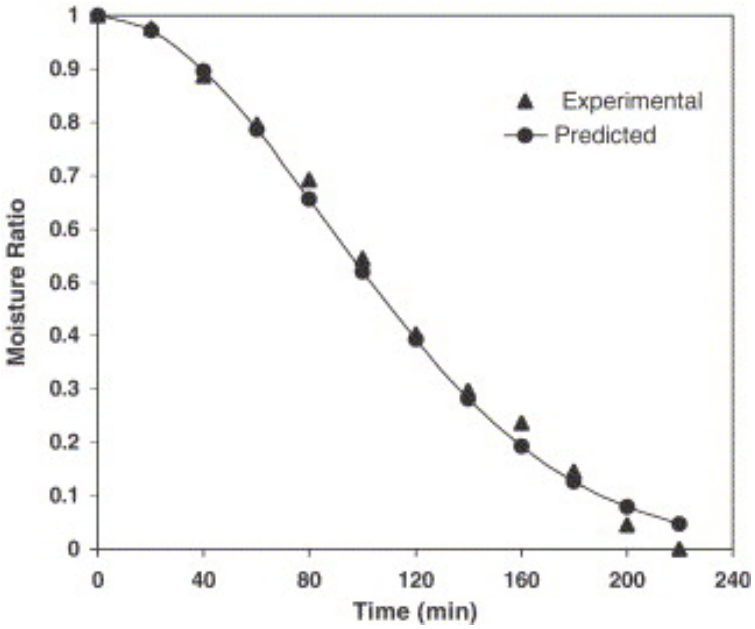

Figure 48: Modified Page III drying behaviour models applied to experimental data gathered from the drying of thin-layers of onions. Taken from [281].

2.7.2 Selection of Thin-Layer Drying Behaviour Models

Across the extensive range of studies in this area covering a wide variety of different fruits, vegetables and crops, there is no identifiable single model that provides the best universal prediction of drying behaviour, rather each study identifies the model which is the most appropriate for the specific application [255]. In general, the semi-empirical models derived from Newton's law of cooling and Fick's second law of diffusion provide the best fit against experimentally gathered data for the thin-layer drying of fruits and vegetables. However, as previously specified, this covers a range of over twenty models with varying degrees of complexity. Therefore a suitable model must be selected for each application based upon the experimental data available, however the less complex models including Lewis, Page and the various Modified Page models have all been successfully applied to a wide range of experimental data to produce accurate predictions of drying behaviour, and as such these can be all be recommended. Some empirical models have been demonstrated to be suitable,

however these models are generally limited in their ability to describe drying behaviour due to the fact that they are built entirely from experimental data and not derived from fundamental principles [255].

2.7.3 Thin-Layer Drying Models and AM Processes

The thin-layer drying behaviour models discussed in this section have potential to be applied to the development of AM processes, specifically processes such as material extrusion whereby material is deposited in layers upon a heated platform and dried. The drying rate and moisture content of each deposited layer of material, as well as the impact of the initial platform temperature on the drying of each layer, are all important factors to consider when designing such processes. The thin-layer models are built upon certain assumptions as highlighted in Section 2.7.1, most importantly that the layer is sufficiently thin so that the temperature throughout the material can be considered to be uniform [260, 262], as as such it is suggested that the material being dried should not exceed three particles in thickness [255]. In addition, these models assume the drying process to be isothermal, or at least that period of time the material takes to reach the drying temperature is negligible compared to the overall drying time [262]. For most material extrusion processes this is unlikely to be the case, with layer heights typically starting at 0.1 mm, and therefore the time taken for a layer of extruded material to reach the drying temperature is unlikely to be negligible compared to the overall drying time. However, the work conducted by Da Silva et al. showed that various semi-empirical drying models provided an accurate prediction of the drying behaviour of whole bananas (with an average diameter of around 30 mm), which clearly demonstrates that these models are not simply limited to true thin-layer applications. Therefore, it can be suggested that there is scope for these models to be applied to the development of material extrusion AM processes which rely on the drying of layers of deposited material.

2.8 Knowledge Gaps and Future Research

2.8.1 Developments in AM for Medical Applications

As explored in Section 2.2 there has been a wide range of research around how AM can contribute to solving the variety of complex issues faced within the medical sector. As discussed, many of these are

still in development, although there are a number of areas where AM has been established including the use of SLS and SLA for manufacturing hearing aids with patient-customised geometries and the production of porous coated acetabular cups using EBM. Aside from this there has been significant progress in the dental market, particularly with the FDA approval of SLA resin produced by Dentca for the manufacture of 3D-printed dentures, along with successful in-vivo studies of SLS fabricated titanium dental implants. AM fabricated surgical models and guides have been used to assist with various surgical procedures, and their benefit has been demonstrated, however the use of such models is still not widely implemented. The limited adoption of AM technology despite the wealth of ongoing developmental research can be explained by the fact that most of the technology is still relatively young, and there are necessary long and thorough procedures that have to be followed before new developments can be approved and implemented in the medical sector. Therefore, there is plenty of opportunity for the continued development of the application of AM in many areas within this sector, including the need for in-vivo testing in order to meet the necessary requirements in order to achieve official approval. In addition to this there is a clear need for the development of additional biomaterials suitable for AM.

2.8.2 Methods of Manufacturing Porous Ti for Orthopaedic Implant Material

As outlined in Section 2.3, various methods of producing porous Ti have been explored with some methods producing material more suitable for orthopaedic implants than others (as summarised in Table 4). Porous Ti can be produced using basic PM techniques including loose sintering, space-holder technique and hollow particle sintering. Levels of porosity achieved through loose sintering are generally limited to levels well below what is required for orthopaedic implant material (pore sizes $< 100\ \mu m$), however the other PM techniques have succeeded in producing the desired levels of interconnected porosity and pore sizes. The space-holder PM technique in particular offers a relatively straightforward method for producing porous Ti, however the best results have been observed when the Ti powder and space-holder particles have been compacted together rather than simply mixed [170]. As outlined, this method is restricted in terms of the geometric flexibility due to the need for a mould and die system for the compaction of the powders.

2.8.3 AM and Porous Ti

AM clearly presents the potential to meet the requirement for geometric flexibility when manufacturing patient-specific orthopaedic implant material. SLM is an especially promising technique even compared with other AM processes due to the fact that the residual powder in the build chamber acts as support meaning that support structures are not required, and therefore virtually any geometry can be achieved. As discussed in Section 2.3.4, various methods have been employed to produce Ti scaffolds with specifically controlled levels of porosity using SLM, with the most impressive structures being achieved through the application of TMPS and the replication of CT scanned trabecular bone structure. Whilst the results using these methods are very promising, the processes required to achieve them are extremely time and cost-intensive and therefore not easily replicable. The SLM space-holder technique developed more recently by Zhao et al. offers a more straightforward route to producing porous Ti scaffolds using SLM [193], however further process optimisation is required to develop this method in order to achieve the desired levels of porosity and pore sizes, as well as experimenting with alternative space-holder materials that can be exposed to the high melting temperatures of Ti64 without evaporating and resulting in the collapsing of pores. Currently SLM technology is restricted by high cost of the equipment (£250,000 +) as well as lengthy build times and requirement for high-skilled operators, however this technology offers very promising capabilities for solving complex issues within the medical sector and beyond. The cost of SLM technology highlights the demand for the development of alternative low-cost and user-friendly AM technologies for the production of complex metal parts. Recently metal-polymer composite FDM filament has become commercially available for SS 316L [282], however the choice of metal FDM filaments available is still very limited. SLA technology could offer substantial scope for the production of metal components if stable metal powder resin suspensions were to be developed, however to date there have been no significant developments in this area. Overall there is clear demand for AM technologies to be developed in order to offer the ability to produce complex metal parts more readily, and there is no doubt that this will be area of significant investment in the near future.

2.8.4 Foam Gel Casting and Porous Ti

Foam gel casting has proved a highly successful technique for producing porous ceramic scaffolds for biomedical applications, however there is clearly still significant scope for developing this technique to produce porous metals which has only been achieved recently for SS 316L [220, 243]. This presents the opportunity to adapt this method to Ti alloys that are a popular choice of implant material. However, as highlighted in Section 2.6.6, this method is restricted by the need for a mould to produce desired geometry, whereas implant geometries need to be specifically tailored to their individual applications. 3D fibre deposition is a technique that has been developed which is able to directly print porous structures through extruding a powder based slurry for both alumina and Ti powders (Sections 2.3.5, 2.3.6 & 2.6.7). Porosity has been typically achieved by increasing the spacing between deposited 'fibres' (or tracks), or by depositing the tracks to form a unit-cell type structure. Fibres containing nano-scale porosity have been produced by mechanically whisking the slurry [251], however this has not been scaled up to extrude slurry tracks that themselves contain micro-scale pores. This presents the opportunity to combine this concept with foam gel casting to create a novel method for producing porous Ti scaffolds with tailored porosity suitable for orthopaedic implant material. If foamed Ti powder slurry could be deposited using a 3D printer with a syringe toolhead, with the gelling agent within the slurry being activated upon deposition, the need for a mould could be removed and individually tailored scaffolds could be easily produced directly from CAD data.

2.8.5 Manufacturing Implants with Gradient Porosity

There has been limited research into creating implant scaffolds with gradient porosity, despite it being well known that bone is made up of two grades of material that each present significantly different porosity and properties, as outlined in Table 1. Two of the studies discussed in this review were able to produce implants with a combination of fully dense material and porous material [11, 200]. Also, other studies have been able to produce structures containing different grades of porosity using a variety of methods including the space-holder technique combined with a multi-die compaction system [199], SLM and DMLS either through altering laser parameters within the build process [26, 200] or the unit cell geometry method [201], and 3D fibre deposition by con-

trolling fibre spacing for each deposited layer [21]. Each of these methods suffer from different drawbacks and complications, which are outlined in detail in Section 2.3.6. In addition to this, it is not clear whether gradient porosity is actually optimal for orthopaedic implants, and therefore it is recommended that a hybrid implant material which presents the high porosity of trabecular bone combined with the mechanical properties of cortical bone is more suitable. Impressive osseointegration has been observed within highly porous Ti scaffolds in a number of studies, and it could therefore be suggested that creating a more dense outer structure would actually inhibit bone in-growth. Therefore, further in-vivo testing and clarification is required in order to provide clear guidance on whether gradient porosity is beneficial. However, there is extensive evidence presented in the literature that implant material with interconnected highly porous structure promotes osseointegration, and that it is vital that the material presents mechanical properties comparable to those of human cortical bone.

2.9 Research Brief

Chapter 1 outlined the properties of human bone and the research covering the desired properties for artificial bone implant materials in terms of material selection, material porosity and mechanical properties. This chapter (Chapter 2) has provided an in-depth summary of the manufacturing processes that have been employed in previous research that has aimed at producing porous Ti for orthopaedic implant material, as well as highlighting the strengths and limitations of each process. As highlighted in Section 2.8 and summarised in Table 4, the structures produced using most of these methods fail to meet all the criteria of orthopaedic implants, particularly in terms of required porosity, as outlined in Section 1.1. The AM processes discussed clearly offer the ability to produce bespoke geometries, which is important for this application, however where these processes have been applied in this area they have either been unable to produce adequate levels of porosity, or required complex computational processes in order to generate the geometry.

Foam gel casting has been highlighted as a process which presents the most promising capability to easily produce material with the required porosity, with the main drawback of this method being that it requires the use of a mould, and therefore is limited in its ability to produce bespoke geometries. Therefore, to overcome this, the primary aim of this work was developing the foam gel casting process for Ti64 powder, and then combining this with AM using material extrusion,

as discussed in Section 2.6.7, in order to be able to easily produce porous Ti64 structures with bespoke geometries. As discussed in Section 2.8.5 the primary objective when developing artificial orthopaedic implant material should be to achieve levels of porosity that match that of human trabecular bone, as this is vital in order to achieve successful fusion between the implant and surrounding bone, as well as allowing for vessel in-growth and fluid transportation. As such, the following refined project aims were identified for this work:

- To combine the understanding acquired from existing literature on gel casting, along with systematic experimental development, in order to establish and optimise the foam gel casting procedure for Ti64 powder slurry that is able to produce material with optimal porosity for the application of orthopaedic implant material that mimics the structure of human trabecular bone.
- To understand and enhance the composition and properties of this newly developed powder-based slurry in order to optimise it for the application of 3D material extrusion.
- To develop the 3D material extrusion process through the systematic extrusion and in-depth analysis of tracks and layers, in order to produce bespoke 3D structures from this slurry using a desktop 3D printer with a paste extrusion toolhead attachment.
- To build an in-depth and robust understanding of this manufacturing process through both experimental development and mathematical modelling, in order to optimise the process parameters to produce the highest possible quality extruded 3D structures, as well as highlight the limitations of the process and routes for further development.

In order to provide quantifiable criteria to assess the porous Ti64 produced in this work, using the information gathered from literature and presented in Section 1.1 regarding the porosity of human trabecular bone and the optimal porosity for artificial implant material, the following target values and characteristics were identified for the porosity of the material developed in this work:

- Porosity of $60 - 80$ %
- Pore sizes ranging from $300 - 600$ μm
- The pores must be interconnected with connecting 'windows' at least 40 μm in diameter
- Pores should be concave in curvature.

3 Chapter 3: Experimental Procedures

3.1 Materials for Developing Metal Powder Slurries

As highlighted in Section 2.6.4, foam gel casting offers the ability to control porosity of the material produced by altering a number of parameters within the process. The composition of the slurry and mixing process must be fine tuned in order to produce the desired final material properties. This process has recently been developed for SS 316L, and the final sintered samples presented porosities similar to those outlined in Section 2.9 as optimal for artificial bone implants [220, 243]. Therefore the first aim in this project was to adapt this system in order to produce highly porous Ti64, and optimise the slurry composition to achieve desirable levels porosity. This section outlines all the materials used to produce metal powder slurries within this project.

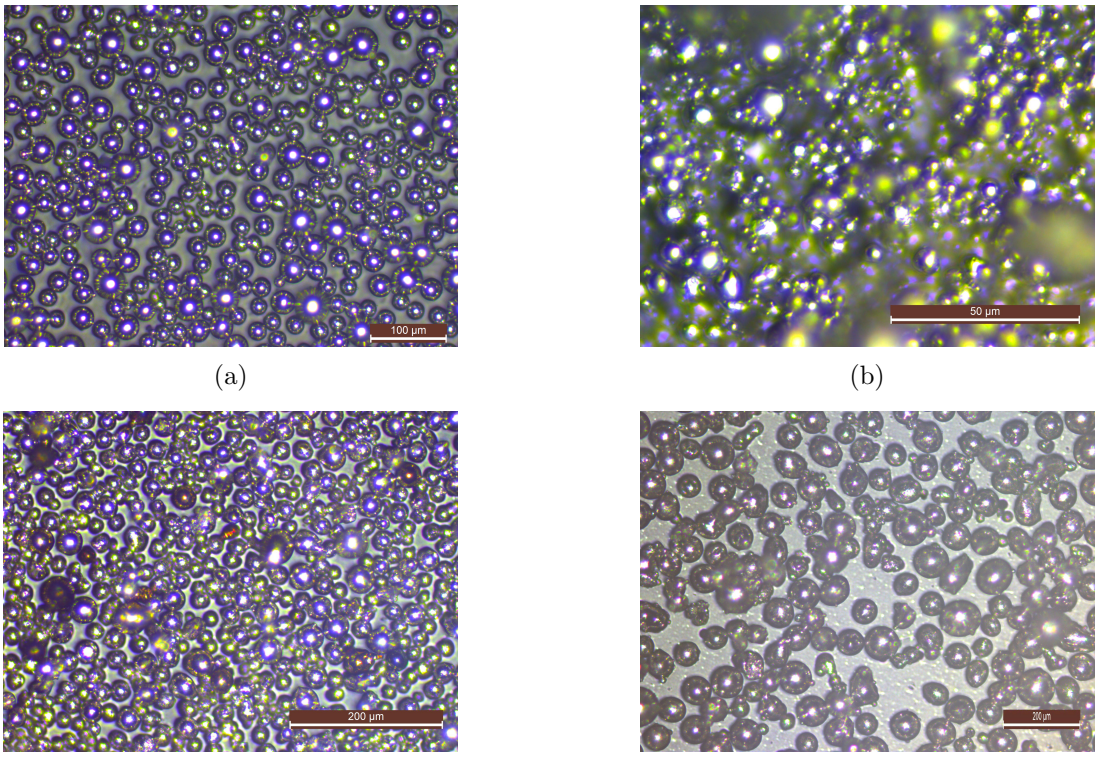

(a) (b)

(c) (d)

Figure 49: Optical micrographs showing AM grade Ti64 powder (a), fine non-AM grade SS 316L powder (b), AM grade SS 316L powder (c) and course AM grade SS 316L powder (d), used to create metal powder slurries for foam gel casting. Taken using Leica DM2700 M Upright Materials microscope (Leica Microsystems, UK).

3.1.1 Ti64 Powder

The main powder used throughout this project to create the slurries was AM grade Ti64 powder (particle size $15 - 45\ \mu m$ stated by the supplier), supplied by Carpenter Additive (Chesire, UK). This powder is produced using plasma atomisation which results in superior sphericity of the particles. The particle sphericity increases the ability of the powder to flow and pack compared with angular powder, and these characteristics are what make it suitable for AM applications. This powder was selected for producing Ti64 powder-based slurries for gel casting and extrusion because these characteristics should theoretically mean that less liquid is required, resulting in a reduction of shrinkage during drying and sintering. The actual particle size distribution of the powder was obtained using a Mastersizer 2000 (Malvern Panalytical Ltd. UK). The median particle size was measured to be 32.4 μm, with a 10^{th} and 90^{th} percentile of 23.2 μm and 44.9 μm respectively. The full particle size distribution is displayed in Figure 50.

3.1.2 Stainless Steel Powder

Slurries were also produced using stainless steel (SS) 316L powder in this work for comparison, particularly regarding viscosity and stability of the slurries. The primary SS powder used in this work was AM grade SS 316L F powder supplied by Carpenter Additive (Cheshire, UK), with a particle size range of $15 - 53\ \mu m$ stated by the supplier. As with the AM Ti64 powder, the actual particle size distribution was measured using the Mastersizer 2000, giving a median size of 28.7 μm, with a 10^{th} and 90^{th} percentile of 17.9 μm and 45.5 μm respectively. The full particle size distribution is displayed in Figure 50, which shows the distribution of the AM Ti64 and AM SS 316L powders to be very similar. In addition to this SS powder, two alternative SS powders were used for comparison purposes. The first of these was a fine, non-AM grade SS 316L powder, supplied by Sandvik Osprey LTD (Neath, UK), with a median particle size of 7.2 μm and a 10^{th} and 90^{th} percentile of 3.5 μm and 15.1 μm respectively. Interestingly, whilst the fine SS 316 powder is not described as spherical or AM grade, Figure 49b shows that this powder is also reasonably spherical, although not as spherical as the AM grade powder. The second SS powder used for comparison was a more course AM grade powder supplied by LPW (Carpenter Additive, UK), which when measured presented a median particle size of 76.4 μm and a 10^{th} and 90^{th} percentile of

47.7 μm and 111 μm respectively. The particle size distribution plots for all the SS 316L powders used, as well as the Ti64 powder, are presented in Figure 50, and the key values are summarised in Table 5.

Size Distribution (μm)	Metal Powder			
	Ti64 (AM)	Fine SS 316L (non AM)	SS 316L (AM)	Course SS 316L (AM)
Median	32.4	7.2	28.7	76.4
10^{th} percentile	23.2	3.5	17.9	47.7
90^{th} percentile	44.9	15.1	45.5	111

Table 5: Table providing size distribution summaries for the metal powders used for creating slurries.

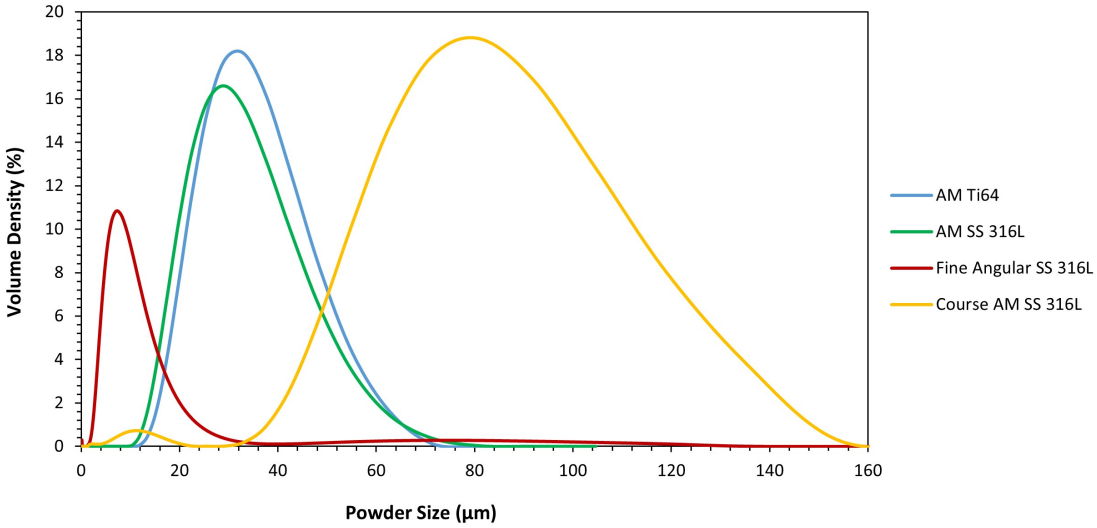

Figure 50: Graph showing distribution of powder particle sizes for AM grade Ti64 powder, fine SS 316L powder (non-AM), AM grade SS 316L powder and course AM SS 316L powder. Measured using Mastersizer 2000 (Malvern Panalytical Ltd., Uk).

3.1.3 Slurry Chemical Components

The slurry composition was initially based on the work completed by Kennedy and Lin [220], with methylcellulose (MC) (Sigma, UK, Product Number M0262) used as the gelling agent. MC solution experiences thermoreversible gelling at a temperature dependent on the percentage concentration of the solution. For the product used in this work, a 2 $wt\%$ solution has a gelation temperature of approximately 48 $^{\circ}C$ and a viscosity of approximately 400 cP at 20$^{\circ}C$ (Appendix A). The gelation

temperature decreases linearly, and viscosity increases linearly with increasing concentration, as outlined in the data sheet. The Ti64 powder was dispersed in the MC solution using the dispersant Darvan 7-N (Vanderbilt Minerals, Norwalk CT), a solution compromising of sodium polymethacrylate and water (Appendix B). Darvan dispersants work by increasing the strength of the anionic charge on the powder particles, causing them to repel one another and disperse throughout the slurry. Triton X-100 (Sciencelab.com Inc., Texas) was used as the surfactant (Appendx C), which is a nonionic surfactant used in a wide variety of household and industrial products.

3.2 Production Process for Porous Metals

The first important phase of experimental work for this project was developing Ti64 slurry for foam gel casting, by adapting the previous method for SS 316L as discussed in Section 2.6.6, and showing that it is possible to extrude the foamed slurry through a syringe nozzle without causing the bubbles within the slurry to collapse, and as such retaining the resulting porous structure in the dried samples.

3.2.1 Slurry Composition Calculations

The first parameter to calculate was the packing density of the powder, both tapped and non-tapped. This was achieved by placing a quantity of powder within a measuring cylinder and measuring the mass and volume of the powder. The powder was then mechanically tapped 500 times within the cylinder using a Quantachrome Autotap tap density analyser (Anton Paar Ltd., UK), before measuring the volume again. Using the mass and volume values, the bulk density and tapped bulk density of the powder were calculated using Equation 10.

$$\rho_b = \frac{m_p}{V_t} \tag{10}$$

Where ρ_b is the bulk density, m_p is the mass of the powder and V_t is either the total tapped or non-tapped volume of the powder in the measuring cylinder, depending on which density is being calculated. Next, the packing fraction range of powder was calculated for both the tapped and non-tapped bulk density values by applying Equation 11.

$$PF = \frac{\rho_b}{\rho_p} \tag{11}$$

Where ρ_p is the density of Ti64 ($\rho_p = 4.5\ g/cc$ [133]). The purpose of calculating the PF range for the powder is to provide a guide for the initial ratio of powder and gelling agent solution that should be mixed in the slurry. The PF provides the proportion of a volume of powder that actually contains powder particles, and the method follows that ideally the initial volume of gelling agent solution used in the slurry should be enough to fill the voids between the powder particles. Therefore, the volume of gelling agent solution was calculated using Equation 12, and the initial mass of powder within the slurry was also calculated similarly using Equation 13.

$$V_{MC} = (1 - PF) \times V_{slurry} \tag{12}$$

$$m_p = PF \times V_{slurry} \times \rho_p \tag{13}$$

Where V_{MC} is the volume of the methylcellulose gelling agent solution and V_{slurry} is the total slurry volume.

3.2.2 Preparation of Methylcellulose Solutions

MC was purchased in powder form and the solutions were prepared using deionised water following the method outlined in the product information sheet provided by the supplier (Appendix A). One third of the volume of deionised water was heated to at least $80°C$ and combined with the desired mass of methylcellulose powder and mixed manually. The remaining two thirds of water was stored in the fridge and added to the dispersion cold. The solution was then stored in a fridge for 24 hours whilst periodically agitating until all the powder has dissolved. Solutions were prepared in this way with concentrations of $1 - 4\ wt\%$ to be used for preparing Ti64 powder slurries.

3.2.3 Slurry Mixing, Whisking and Gelling/Drying

The slurries were mixed and whisked using a KitchenAid tilt-head stand mixer, along with various attachments as shown in Figure 51. The calculated quantities of powder and gelling agent solution were combined in the mixing bowl, and the dispersant was added at an initial volume of 1.5 $wt\%$ of

the powder mass as recommended in the method [243]. These components were gently mixed using a paddle mixer until a consistent slurry was formed before the surfactant was added at 1 $vol\%$ of the slurry volume. The slurry was then mechanically whisked in the bowl at 220 rpm for $2-10$ minutes using the balloon whisk attachment to incorporate air bubbles before being transferred into moulds and placed in a pre-heated oven (SciQuip Oven-55S, SciQuip Ltd. UK) set to $60°C$ for 24 hours to gel and dry. $60°C$ was selected as it is above the gelation temperature of the MC solution, but not so high as to cause rapid evaporation of the water resulting in cracking of the samples. Once dried, the samples were then removed from the moulds and analysed as the green bodies in order to obtain information regarding the porous structure without having to sinter each sample. Two types of moulds were used in this process, rectangular flexible silicone moulds ($12 \times 25 \times 48$ mm), and rigid tapered ice-cube tray moulds with a silicone base (25×25 mm to 33×33 mm over 24 mm height). These are shown in Figure 51.

3.2.4 Altering Porosity within the Foam Gel Casting Process

As explained in Sections 2.6.4 and 2.6.6, the porosity and pore sizes of structures produced using foam gel casting can be controlled by altering a number of parameters within the process. Therefore, in order to achieve the desired values outlined in Section 2.9, a number of parameters within the slurry composition and whisking procedure were altered including the solid loading (powder volume fraction), MC solution wt% concentration and whisking time. A summary of the composition parameter values that were varied is provided in Table 6, and these values are discussed in more detail in Section 4.1.

	Slurry Composition Parameters				
	Varied			**Constant**	
	Volume Fraction	MC Solution Concentration (wt%)	Whisking Time (mins)	Dispersant Addition (wt% of powder mass)	Surfactant Addition (vol% of non-foamed slurry volume)
Values	$0.5-0.6$	$1-4$	$2-10$	1.5	1

Table 6: Table providing a summary of the slurry composition values which were varied, and those which were kept constant, when optimising the Ti64 powder slurry composition to achieve specific porosity in dried samples.

(a)

(b)

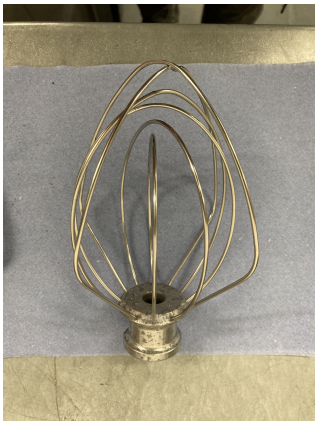

(c)

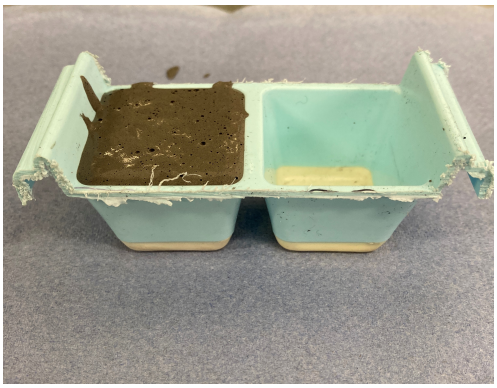

(d)

(e)

Figure 51: Photograph showing KitchenAid tilt-head stand mixer (a), paddle mixer attachment (b) and balloon whisk attachment (c) used to mix and whisk powder slurries, as well as ice-cube moulds (d) and flexible silicone moulds (e) filled with foamed slurry to be transferred to the oven.

3.3 Controlled Slurry Extrusion Experimental Setup and Procedure

In order to explore the feasibility of 3D printing the powder-based slurries by observing their behaviour when extruded through a nozzle, controlled extrusion experiments were set up using the paste extrusion syringe supplied for the ZMorph 2.0 3D printer. The compressions were applied using an Instron 6800 Single Column Series 68SC-5 universal testing system (Instron, US) to drive the plunger, as shown in Figure 53b.

3.3.1 Loading ZMorph Syringe

The foamed slurry was transferred into the ZMorph paste syringe immediately after whisking, either by pouring or scooping using a spatula (depending on the viscosity of the slurry). A maximum of 100 ml of slurry can be loaded in to the syringe, so it was filled up to this limit depending on the volume required for each experiment. The plunger was lubricated using a silicone lubricant and placed within the end of the syringe, but not compressed. The syringe was then turned upside down and gently tapped whilst slowly compressing the plunger, in order to expel trapped air out through the nozzle. Once all the air was removed and slurry began to be extruded from the nozzle, it was then placed within the compression rig. Figure 52 shows the main steps of syringe loading process.

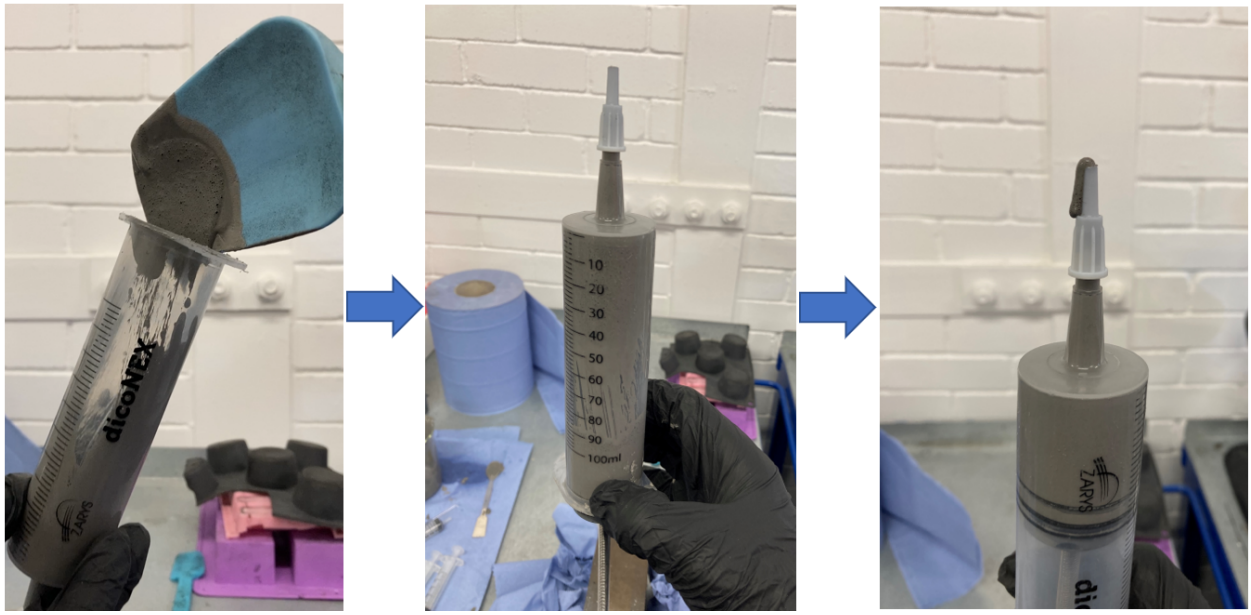

Figure 52: Images showing the process of loading the ZMorph thick paste syringe with foamed slurry, and removing trapped air pockets by compressing the plunger with the nozzle facing upwards.

3.3.2 Custom Syringe Compression Rig

In order to be able to extrude slurry from the syringe in a controlled manner, a custom compression rig was designed and manufactured in-house (Figure 53). The rig was designed to house the ZMorph syringe and allow it to be used in conjunction with the Instron compression plates to

apply controlled compressions to the plunger.

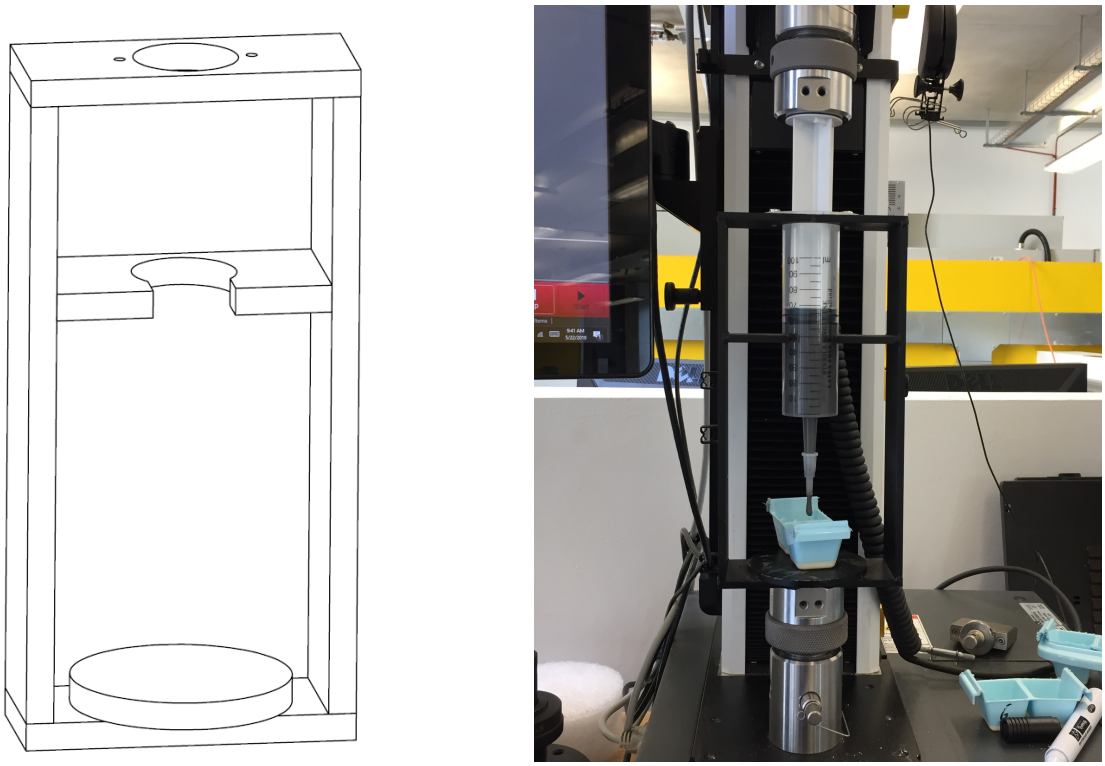

(a) (b)

Figure 53: Controlled syringe compression rig CAD design (a) and positioned within the Instron universal testing system (b).

3.3.3 Controlled Syringe Plunger Compression Parameters

The custom syringe compression rig was used to investigate the impact of two main parameters; extrusion speed and hold time. Hold time refers to the duration for which the slurry is stored within the syringe prior to extrusion. Experiments were designed in order to analyse the affect of these parameters on the stability of the foamed slurries. Test files were set up using the corresponding Instron software (Bluehill Universal), in which the compression speed and distance were specified. For all of these experiments the tests were programmed to extrude 10 ml of slurry by displacing the plunger using the compression plate. The typical extrusion speed when using the ZMorph paste extruder is around $0.05 - 0.1$ ml/s, depending on the specific values of various input parameters. Therefore, extrusion speeds between $0.05 - 0.4$ ml/s were tested in order to see if going beyond the typical extrusion speeds would have any impact on the stability of the foamed slurries. For the hold

time experiments, the extrusion speed was set to 0.1 ml/s, and the extrusions were simply repeated at certain time intervals. For each test the slurry was extruded directly into a mould which was immediately transferred into an oven to gel and dry, using the same parameters as defined in Section 3.2.3. Force/displacement data was also gathered within the software for each extrusion. The final 10 ml of slurry in the syringe was never extruded as part of these experiments, as the assumption was made that the plunger force and pressure experienced by the slurry would be significantly higher as the plunger approached the nozzle end of the syringe due to the shape of the syringe. Figure 54 shows the velocity profiles of material being extruded from a syringe, which highlights that there is a noticeable increase in velocity (and hence shear forces acting upon the material) as the plunger gets close to the bottom of the syringe chamber. The model used to create Figure 54 was produced using Ansys Fluent (Ansys, USA), and is a very basic model in which the syringe was modelled with the same dimensions as the ZMorph thick paste extruder, but the fluid properties were based on the MC solution properties alone and as such were not representative of the actual extruded slurry. It was created simply to demonstrate the behaviour of a fluid being extruded from a syringe of these dimensions and geometry, and to inform the decision not to extrude the final 10 ml of slurry for each of these experiments. In order to compare the effect of storing the foamed slurry inside the syringe against the decomposition of the slurry when simply left to settle, several samples were also placed directly into moulds after mixing which were then left to settle for set time periods before transferring into the oven to gel and dry.

3.4 Analysis of Slurries and Dried Samples

3.4.1 Viscometer Model and Spindle/Speed Selection used for Measuring Slurry Viscosity

The viscosity of the metal powder slurries produced in this work was significantly influential in determining the stability and printability of the material. As such, viscosity was measured for all of the main slurry compositions investigated. Slurry viscosity was measured using a Brookfield DV1MLV Viscometer (Brookfield Engineering Laboratories Inc., USA). The viscometer was supplied with a set of four spindles (LV1-4, as shown in Figure 55a) and a narrow guardleg, and is capable of measuring viscosity within the range of $15 - 2,000,000$ cP. The rotational speed of the

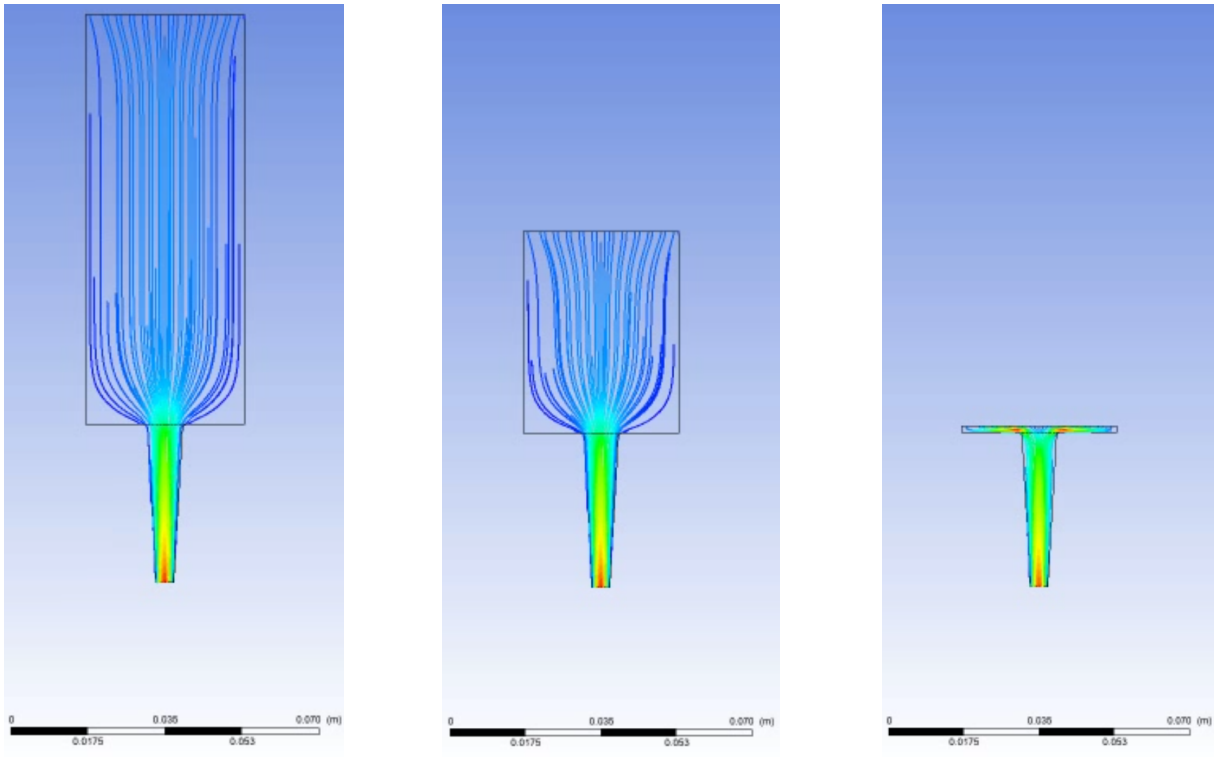

(a) Velocity profiles during initial extrusion of fully loaded syringe.

(b) Velocity profiles during extrusion when the plunger is in middle of the syringe.

(c) Velocity profiles during the final 10% of the syringe volume extrusion.

Figure 54: Basic CFD model created using Ansys Fluent showing velocity profiles of a fluid being extruded from the ZMorph thick paste extender toolhead syringe.

spindle can be set between $0.3 - 60$ RPM at defined intervals. Each spindle and speed combination is able to measure viscosity within a specific range, and so when measuring multiple fluids with various viscosities usually either the spindle *or* the selected speed have to be altered. Measuring the viscosity of a slurry that contains suspended powder particles presents certain challenges, in particular that the powder particles will tend to migrate away from the rotating spindle, causing changes to the measured viscosity value over time. Brookfield do provide specialist spindles for measuring slurries where suspended solids may migrate away from the spindle, which offer minimal disruption of the sample during spindle immersion, however these were not available for this work. This issue is amplified with increasing spindle rotation speeds, and previous studies in literature have demonstrated how high shear rates can cause collapse of the foamed slurries which means the viscosity data gathered is not comparable, and as such it is recommended to obtain viscosity data for foamed slurries at low spindle rotational speeds [283]. Therefore, for measuring the viscosity of

the slurries in this work a rotational speed of 1.5 RPM was selected. Also, whilst viscosity was measured over 60 seconds, the initial viscosity (after 1 second) for each slurry was used to define its value. Because the rotation speed was kept constant for measuring slurries with various viscosities, specific spindles were selected so that the spindle/speed combination viscosity range was suitable for each slurry.

(a) (b)

Figure 55: (a) Brookfield DV1MLV viscometer spindle selection, LV 1-4 from left to right and (b) chamber tube supplied with the enhanced UL adapter.

3.4.2 Viscometer Setup and Viscosity Correction

The spindles provided with the DV1MLV viscometer (LV 1-4, shown in Figure 55a) are designed to be used with a container/beaker with an internal diameter of 8.25 cm (a 600ml low form Griffin beaker is suggested), and also in conjunction with the provided guardleg (Figure 56a). The operating instructions state that alternative containers can be used at the user's convenience, but this will impact the viscosity measurements obtained. However, it does clarify that results obtained using an alternative container will provide repeatable results, but just not necessarily 'true' results, meaning that the measurements may not provide strictly accurate viscosity values however can still provide a consistent comparison between fluids. Each spindle also has an immersion groove on the

(a) (b)

Figure 56: Photographs showing Brookfield Viscometer set-up with LV 2 spindle in conjunction with a beaker of the recommended diameter (a) and the chamber tube alternative container used to reduce required volume of slurry for viscosity measurements (b).

shaft, as can be seen in Figure 55a, which represents the level to which the spindle should be immersed within the sample. The combination of using a container with a diameter of 8.25 cm whilst also immersing the spindle up to the immersion groove means that typically a minimum volume of $250-300$ ml of the sample is required in order to sufficiently fill the beaker. This presented an issue in this work because producing this volume of slurry would require around $300-600$ g of metal powder (depending on which specific powder and volume fraction is being used). Only a limited supply of each powder was available due to their high cost, and therefore using this quantity of each powder every time viscosity measurements were required would have been an inefficient use of the available powder. In order to overcome this challenge an alternative container was used for viscosity measurements (Figure 55b). The chamber tube supplied with the *enhanced UL adapter* was filled with slurry to the required depth, and then the appropriate spindle was inserted (Figure 56b). This container has an internal diameter of only 27 mm and so only ~ 30 ml of each slurry

was required to fill it up to the immersion groove of the LV spindles. For *true* results this container is only designed to be used in conjunction with the UL adapter to measure low viscosity materials, however, in order to minimise powder consumption it was used for all viscosity measurements in this work using the LV 1-4 spindles. Once all the slurry viscosity measurements had been obtained, the slurry with the lowest viscosity was measured again but using the correct experimental setup as recommended in the operating instructions (Figure 56a). The viscosity measurements for the other slurries were then corrected against this least viscous slurry, so that data gathered using the adapted experimental setup (Figure 56b) could be used to draw meaningful conclusions without the need to mix large volumes of each slurry and waste high quantities of expensive metal powder.

3.4.3 Structural Analysis of Green Samples

As outlined in Section 2.9, the porosity and pore sizes of the material produced in this work were key properties, therefore it was important during the experimental phases to be able to measure pore sizes and porosity of the samples produced by each batch of slurry. For this reason the dried samples were analysed as green bodies, rather than going through the complex and time-consuming sintering process for each batch of samples. This provided more immediate feedback which meant the process could be developed in a much more time efficient manner. Also, once the samples have been sintered it would be considerably more difficult to break them open to analyse the porous structures. Therefore, during the slurry composition and mixing process development, the porous structures of the green samples were analysed using the following techniques.

3.4.3.1 Optical Micography and 2D Image Analysis for Pore Size Measurement

To obtain measurements of pore and connecting window diameters, green samples from each batch were scored and fractured in several places (see Figure 57) and then images of the exposed surfaces were taken using an optical microscope (Leica S6D stereozoom, Leica Microsystems, UK). The images were transferred to the open-source image processing program Fiji [204], where the pores and windows were outlined as shown in Figure 58. The *measure* tool within Fiji was used to analyse the dimensions of the outlined pores/windows. This tool provides a value for each circle/oval called the *Feret's Diameter*, which describes the longest distance between any two points along the boundary of the selection (or maximum diameter). This was identified as being an appropriate

form of measurement due to the natural sphericity of the pores (as seen in Figure 58), which is a result of them being formed by bubbles within the slurry generated through whisking. For each set of samples produced from a particular batch of slurry, the mean pore size along with standard deviation was calculated from these measurements. At least 50 pores or windows were measured in order to provide the mean diameters for samples produced from each slurry composition batch.

3.4.3.2 Porosity Measurement

As well as the pore and window sizes, the porosity was measured for samples from each slurry composition batch. To measure porosity, the mass of each green sample was weighed upon removal from the mould and the volume of the mould was measured. If the sample did not completely fill the mould, a line was drawn inside the mould to mark the top level of the sample, and after removal the amount of liquid required to fill the mould to that level was measured by filling the mould up to the marked level with water and recording the mass, which was then converted to volume. The density (ρ_s) for each sample was calculated using Equation 14, and the porosity calculated using Equation 15.

$$\rho_s = \frac{m_s}{V_s} \tag{14}$$

$$\phi = 100 - \left(\frac{\rho_s}{\rho_p} \times 100\right) \tag{15}$$

Where m_s is the sample mass and V_s is the volume of the mould cavity.

3.4.4 Gelling Agent Burnout Test

In order to test the stability of the green samples a burnout test was conducted to check whether they would maintain their structure during the sintering process or simply collapse when the MC is removed. A burnout test was conducted on a number of samples produced from different slurry batches using an Elite TSH15 single zone horizontal tube furnace (Elite Thermal Systems Ltd., UK) in a nitrogen atmosphere. The furnace was heated to $650°C$ at a rate of $10°C/min$ and held for 2 hours before cooling again. It has been shown previously using thermogravimetric analysis that the burn off temperature of MC is in the region of $450 - 500°C$ [284], and so the temperature

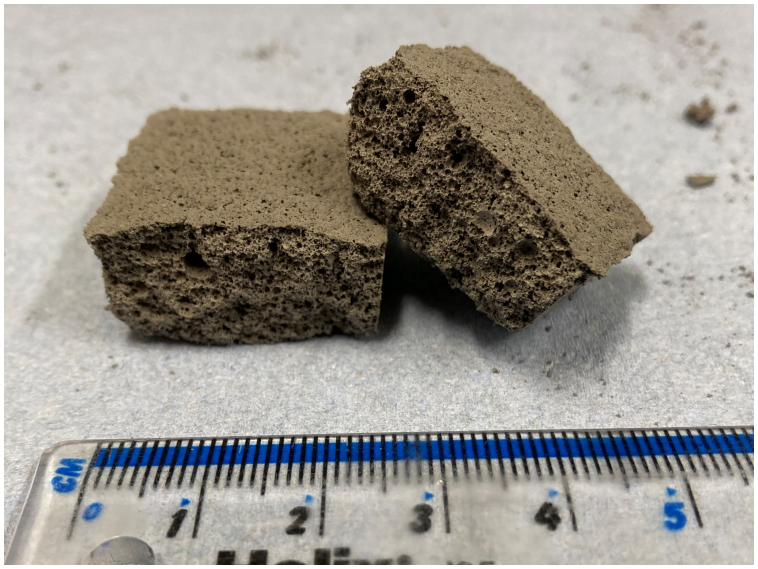

Figure 57: Green porous Ti64 sample fractured to expose internal porous structure for analysis using optical micography

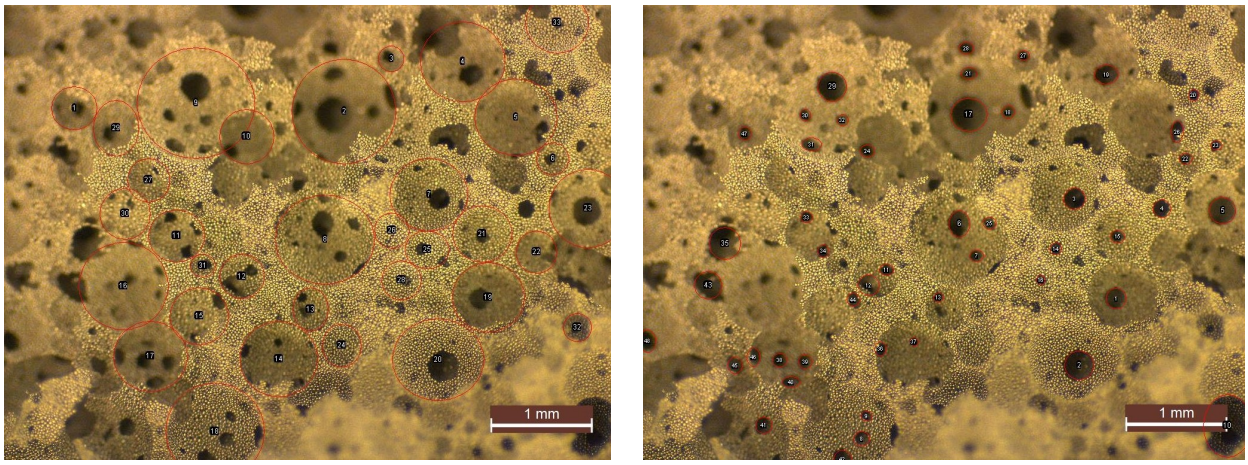

(a) (b)

Figure 58: Optical Micrographs showing open surfaces of porous Ti64 green sample with highlighted pores (a) and windows (b), as measured in Fiji.

for the burnout test was selected to be safely above this region to ensure complete burn off. Once the test samples were removed from the tube furnace, they were then fractured and imaged using the same process as described in Section 3.4.3 in order to examine their structure with the MC removed.

3.4.5 Compression Testing of Green Samples

Basic mechanical tests were set up to analyse the green strength of samples produced from a number of specific slurry compositions. These samples were subjected to compression testing using the Instron 6800 Single Column Series 68SC-5 universal testing system (Instron, US), along with compression plates (Figure 59). The samples were compressed to failure at a rate of 0.5 mm/s, and the force/displacement data for each compression was collected and plotted.

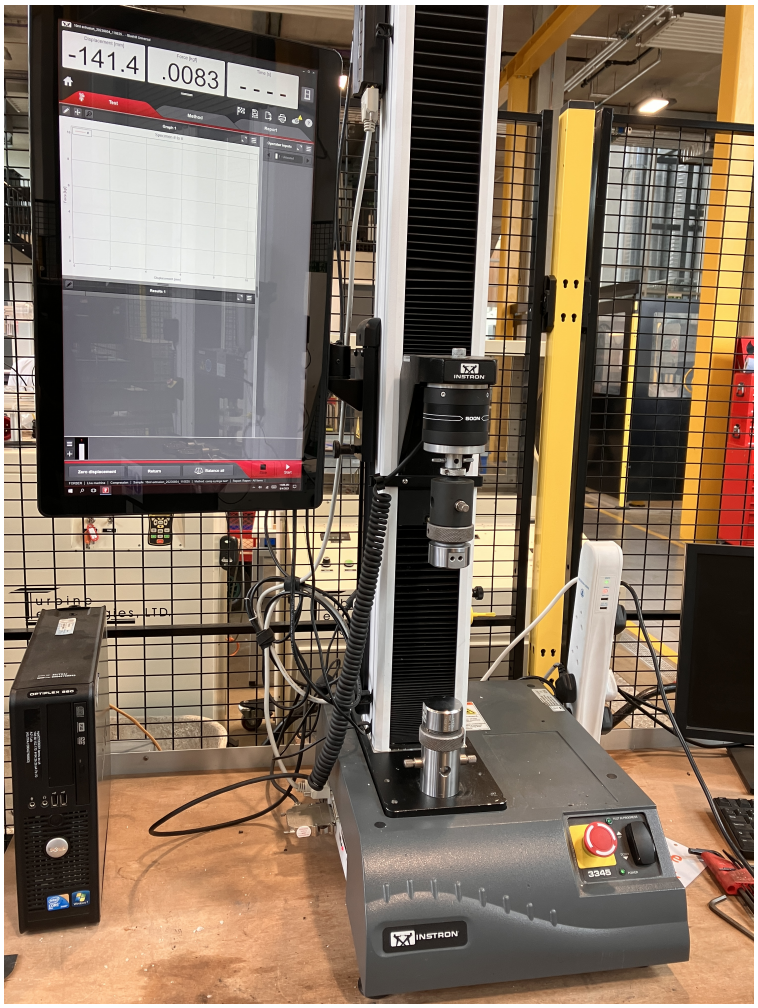

Figure 59: Instron 6800 Single Column Series 68SC-5 universal testing system (Instron, US) used for green sample compression testing.

3.5 3D Material Extrusion Process

As highlighted in Section 2.6.7 the ZMorph 2.0 3D printer provides a thick paste extrusion toolhead (Figure 46) [253], which is typically recommended for extruding soft foods for decoration such as cream cheese or melted chocolate, but can be used with any liquid which has a viscosity within the recommended range [254]. Material extrusion, like all processes available with the ZMorph, is controlled through the Voxelizer software [285]. In order to be able to build 3D structures out of foamed Ti64 slurry using material extrusion, it was necessary to develop an understanding of key aspects of the deposition process including optimising the extrusion parameters, understanding track geometry and stability, and the interaction between adjacent tracks and successive layers of deposited slurry. This was achieved by breaking the process down into single-track deposition, single-layer deposition, and finally multi-layer builds.

3.5.1 ZMorph Thick Paste Extruder Toolhead and Build Platform Setup

Foamed slurry was loaded into the ZMorph paste syringe following the same process as described in Section 3.3.1. Once the plunger had been compressed and excess air removed from the syringe, it was then inserted into the mounting base as shown in Figure 60. The height of the syringe nozzle above the build platform (nozzle offset) was adjusted using the manual z-calibration thumbscrew. The nozzle offset was adjusted throughout the process development such that the distance between the nozzle and platform was always greater than or equal to the measured track height. The platform was pre-heated to a temperature of $100°C$, which is controlled within Voxelizer, so that the foamed slurry would rapidly gel when deposited and then subsequently dry. In order to make sure it is easy to remove the deposited material from the platform once dried, it is recommended to add an additional thin sacrificial layer between the platform and deposited material. In this work aluminium foil was used because of its good thermal conductivity ($253\ W/mK$), which ensured that the heat generated by the platform was transferred to the deposited slurry. The foil was secured to the platform by applying Dimafix (ID3 Digital Media SL, Spain), a thermally activated adhesion spray developed for providing adhesion for FDM processes between the extruded material and glass platform. This meant that whilst the platform was heated the foil would have good adhesion to the platform, and when cooled it could be easily removed.

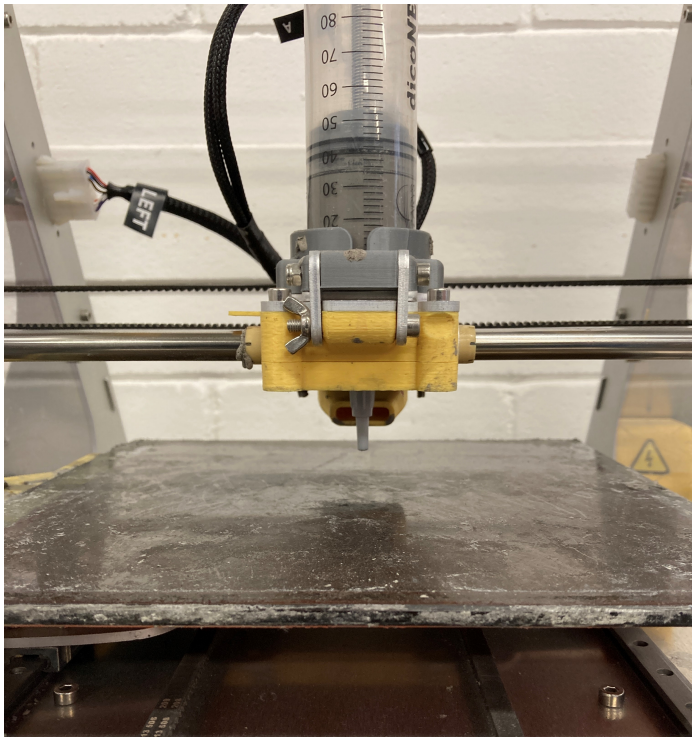

Figure 60: ZMorph thick paste syringe loaded with foamed slurry and mounted above the build platform.

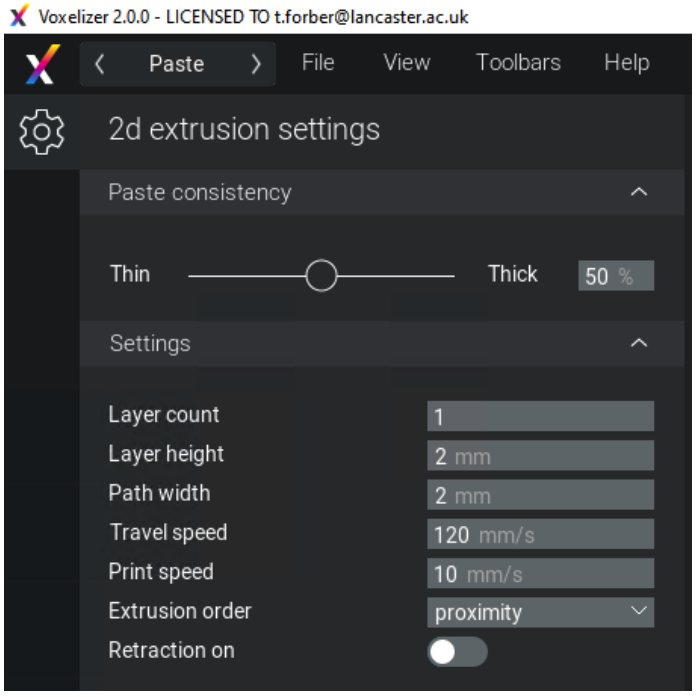

Figure 61: ZMorph thick paste workflow parameters.

3.5.2 File Generation for ZMorph Thick Paste Extrusion

The geometries to be printed using the ZMorph thick paste extruder were modelled in Solidworks (Dassault Systems, USA). The 2D sketches were exported as Drawing Exchange Format (.DXF) files which are a universal format for storing CAD files. These 2D .DXF files can then be imported by Voxelizer and used to create a .gcode file which contains the information required by the 3D printer in order to complete the build. The software does not provide the capability to automatically create hatches to in-fill the shell of a sketch when working in the *thick paste extrusion* workflow, and therefore these must be manually created when drawing the 2D sketch in order to be able to print a complete surface rather than individual tracks (Figure 62).

The imported 2D sketch represents a single layer which can then be deposited several times successively as determined by the *layer count* parameter. Once all the other parameters have been defined the build can then be directly submitted if the software is connected to the printer, or saved to an SD card as a .gcode file and transferred to the ZMorph.

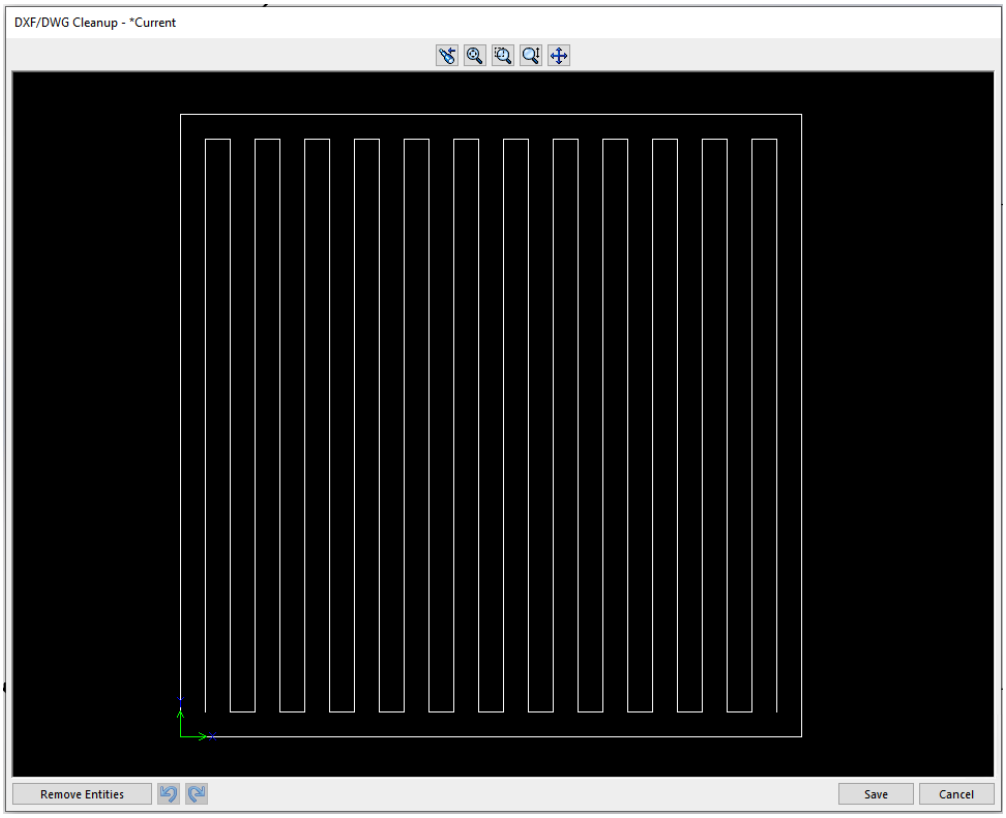

Figure 62: .DXF file square with manual hatching used to print a single layer with the ZMorph thick paste extruder.

3.5.3 Extrusion Parameters for Ti64 Slurry Deposition

The *thick paste extrusion* workflow within Voxelizer contains are a variety of parameters that can be controlled including *thickness*, *layer height*, *layer count*, *path width* and *print speed*, as well as the option to control the *retraction* of the material (Figure 61).

3.5.3.1 Track Dimension Parameters for ZMorph Thick Paste Extrusion

The *path width* and *layer height* parameters define the cross-sectional geometry of the deposited tracks. The nozzle attached to the ZMorph thick paste extruder toolhead has a 2 mm diameter, and so the *path width* was initially set to be equal to this value. It would be virtually impossible to successfully deposit a track with a width less than the nozzle diameter, and to create a track wider than the nozzle would be extruding excess material and rely upon it spreading evenly into the correct width. The track height was set to 1 mm based on the assumption that the cross-sectional geometry of tracks would be roughly semi-circular where the width is equal to the nozzle diameter and height equal to the radius, as presented in the schematic in Figure 63.

3.5.3.2 Thickness Parameter for ZMorph Thick Paste Extrusion

The *thickness* (or *consistency*) value can be varied from 0 % (thin) to 100 % (thick). No guidance is provided that matches *thickness* % with specific material viscosities, it is simply recommended to experiment with this parameter to find the optimal value for the material being extruded. The guidance provided by ZMorph [253] explains that this parameter values alters the extrusion volume by adjusting the extrusion speed, and simply recommends selecting a greater *thickness* value for 'thicker' materials.

3.5.3.3 Print Speed Parameter for ZMorph Thick Paste Extrusion

The *print speed* value is defined in mm/s and refers to the linear speed with which the toolhead travels whilst extruding material. It is recommended to set an initial value of $1mm/s$ and then increase to suit the material being extruded. Initial testing showed that this speed was too slow for the Ti64 slurry and so for the process parameter optimisation experiments values between $2 - 10mm/s$ were selected.

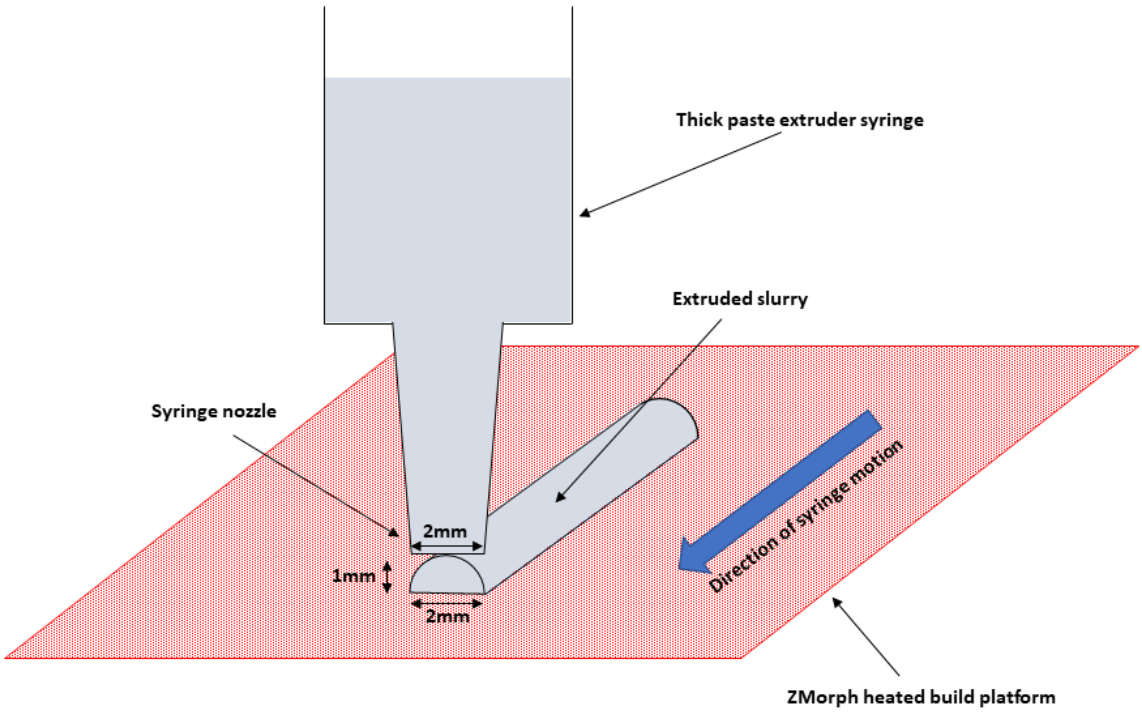

Figure 63: Schematic showing anticipated slurry cross-sectional profile dimensions when extruded from the thick paste extruder syringe nozzle onto the heated platform.

3.5.4 Calibrating Material Flow Rate for ZMorph Thick Paste Extrusion

It was initially assumed that the flow rate (Q) of the extruded material (measured in cc/s or ml/s) could be approximately calculated simply using Equation 16

$$Q = \frac{h \times w \times v}{1000} \tag{16}$$

Where h and w are the track height and width respectively measured in mm, and v is the print speed measured in mm/s. These values when multiplied together give a flow rate measured in mm^3/s which is then divided by 1000 to convert to cc/s.

However, it is stated within the ZMorph Thick Paste Extrusion guidance that *print speed* has an impact on the mass of material that is extruded and increasing the speed reduces the mass [253]. It was also discovered in previous initial testing that the *thickness* parameter affects the flow rate of the material being extruded. This suggests that the *path width* and *layer height* parameters actually

provide little control over the dimensions of the deposited track, and that it is recommended to optimise the other parameters to produce the desired track dimensions.

Therefore, in order to link the information obtained from the controlled extrusion experiments described in Section 3.3 to the *print speed* values defined in Voxelizer, and to discover the relationships between the printing parameters and flow rate, the flow rate was measured for various parameter combinations. It was measured by manually timing how long it takes for the syringe plunger to move 10 ml, repeated 3 times for each set of parameter combinations and calculating an average value. This could then be used to calculate a flow rate value in cc/s.

3.5.5 Optimising Track Dimensions and Flow Rate

As previously outlined, several of the extrusion parameters that can be altered within Voxelizer (particularly *thickness* and *print speed*) affect the flow rate of the material through the syringe nozzle, making it difficult to print tracks with geometries that match the values defined within Voxelizer. A series of single-track deposition tests were conducted in order to analyse the track geometries as certain extrusion parameters were altered. Tracks of length 100 mm were extruded in a zig-zag pattern with foamed Ti64 slurry on the build platform pre-heated to $100°C$, leaving enough space between each pass so that they did not converge. The width and height parameters were kept constant at the values described in Section 3.5.3, and the thickness and speed parameters were varied between $35 - 55$ % and $2 - 10$ mm/s respectively based on observations from previous initial tests. After being extruded onto the heated platform, images of the tracks along with a ruler for scale were taken with a camera, as shown by the example in Figure 64. The images were transferred to Fiji and the scale was set using the ruler markings. The width of each individual track was measured at 10 mm intervals to provide a mean track width for each set of extrusion parameters. The continuity of the tracks was also assessed using these images by observing whether there were any breaks in the deposition caused by insufficient material being extruded to form a continuous track.

Once the track widths had been measured for each combination set of parameters, certain parameters were selected for completing track height measurements. The reason that the track width was analysed first is that the process of taking images and measuring the widths using Fiji is straightforward and not time consuming, and by visually inspecting the tracks and analysing the

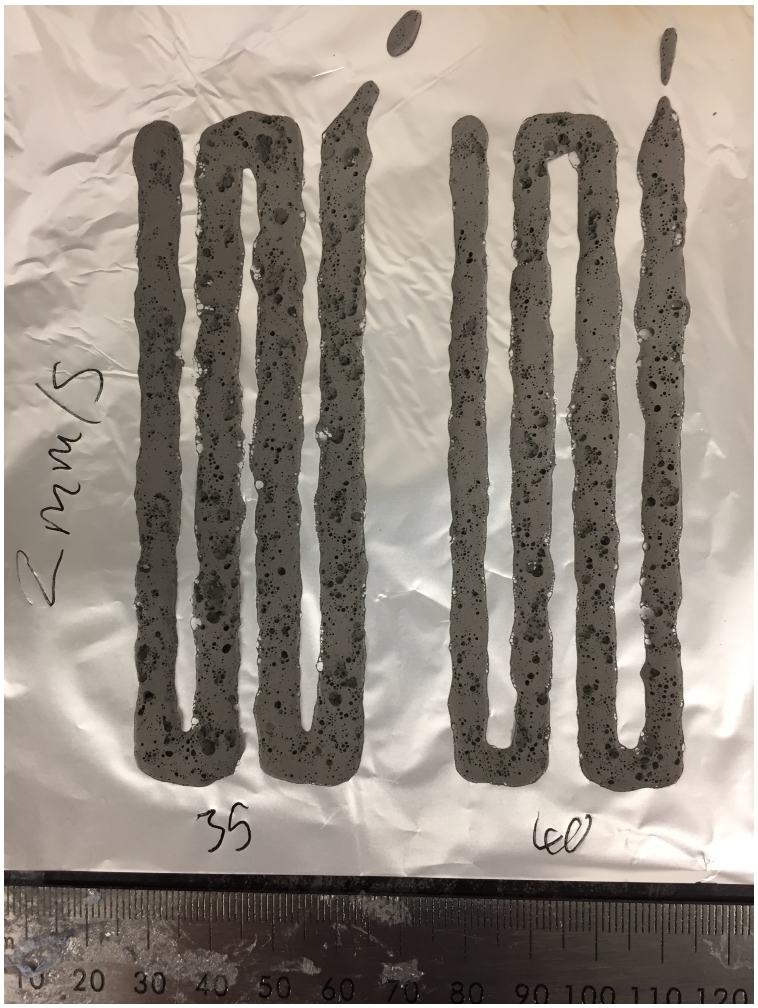

Figure 64: Example of an image taken of Ti64 extruded tracks used to measure width and optimise *thickness* and *print speed* parameters.

measured width values, many of the parameter combinations could be discarded hence reducing the number of tracks for which the height needed to be measured. In order to measure track height, the tracks were first left on the heated platform for two hours in order to ensure they were fully dried (Section 7.1.4). Then the aluminium foil was then carefully removed with the tracks remaining intact on top by sliding a thin blade underneath it and transferring it to a flat tray for transportation. The tracks were then transferred to the LEXT OLS5000 laser confocal microscope (Olympus Scientific Solutions Americas Inc., USA) for measurement. The OLS5000 is a 3D measuring laser microscope that is able to measure height by acquiring multiple confocal images by automatically shifting the focus pattern. It then combines these images into a 3D profile which can then be analysed and used to take measurements. The 3D scanning process is time

consuming and so rather than scanning the entire region of each set of deposited tracks, a number of representative sections were selected for each to be scanned and measurements to be acquired from. Figure 65 shows an example of a 3D view of section of tracks that has been scanned using the OLS5000 used to generate a 2D height profile in order to obtain track height measurements. Track height was measured from the surface of the foil up to the highest point on each track. Where the foil was not flat due to deformation during removal from the platform, the measurement baseline was drawn from the level of the foil on one side of the track across to the level on the other side, and then the height was measured from this baseline to the peak. At least 2 sections of each set of tracks were selected for 3D scanning and height measurement, meaning that between $5 - 10$ measurements were obtained for each set of tracks. These values were then used to measure an average. Track widths were also measured in the same way for the sections that were scanned, in order to compare and validate against the values obtained from 2D measurement using images and Fiji.

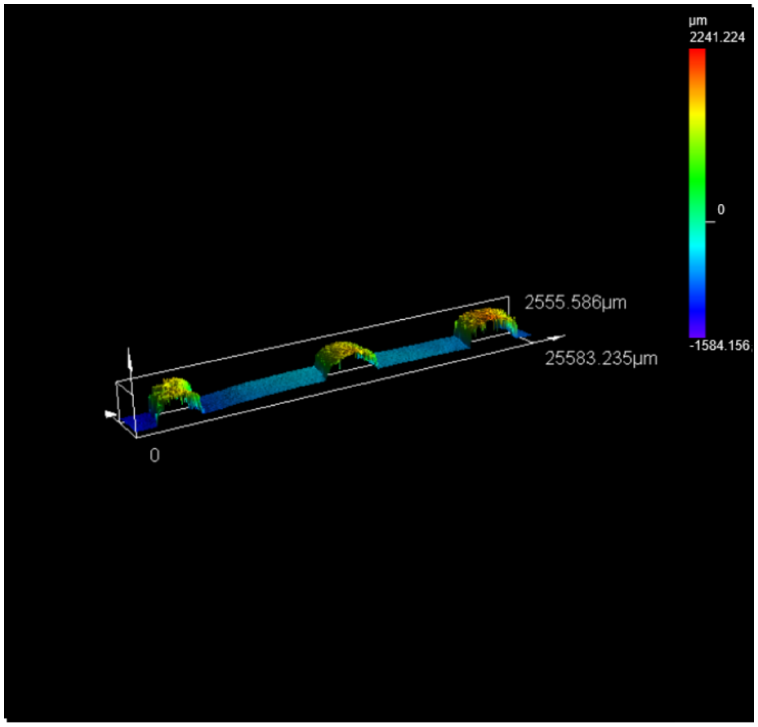

Figure 65: Screenshot showing example of 3D image of several single extruded tracks of slurry used to obtain track height measurements, taken using the LEXT OLS5000 laser confocal microscope.

3.5.6 Overlap of Extruded Slurry Tracks

Having developed an understanding of the individual track dimensions for given sets of extrusion parameters, the next step was to investigate the optimal overlap between adjacent tracks in order to create a single continuous layer. As explained in Section 3.5.2, the .dxf file created from a 2D CAD sketch maps the path that the toolhead will follow when depositing the slurry on the platform. Using the information gathered from measuring track widths, the spacing between adjacent hatch lines can be altered to produce varying amounts of overlap between adjacent tracks. Single layer depositions made up of 4 adjacent tracks with a specified overlap in the region of $0 - 50\%$ were set up using the previously determined optimal extrusion parameters. Tracks with 0% overlap were set up so that the spacing between each track was equal to the average track width, and an increase in overlap refers to a proportional decrease in the spacing between each track. The .gcode files were generated as described in Section 3.5.2, and the tracks were deposited on the pre-heated platform then left to dry. The tracks were inspected visually and also analysed using the LEXT OLS5000 laser confocal microscope in order to capture the cross-sectional profiles of the overlapping tracks. Figure 66 shows an example of a 3D image showing a section of 4 overlapped tracks scanned using the OLS5000.

3.5.7 Multi-Layer Slurry Extrusions

The final stage of the 3D extrusion development process was to be able to deposit multiple successive layers of foamed slurry. The key areas of interest were whether each layer would be stable enough to support the next layer deposited on top, and also whether each deposited layer would merge to form one continuous 3D porous structure or whether separations between each layer would be observed. Build files for simple square shaped layers consisting of zig-zag hatched tracks were generated, and the layer count within Voxelizer was set to 3. Some builds were completed where each layer was deposited immediately after the previous layer, and others were manually paused between layers in order to examine the effect of fully drying each layer prior to depositing the next.

A 2-layer deposition was set up where each layer consisted of a series of hatched tracks as shown in Figure 67. A .dxf file was created that consisted of a long hatched rectangle, with the hatches spaced as to provide 15% overlap between tracks (Figure 67). Within Voxelizer the *layer count* was

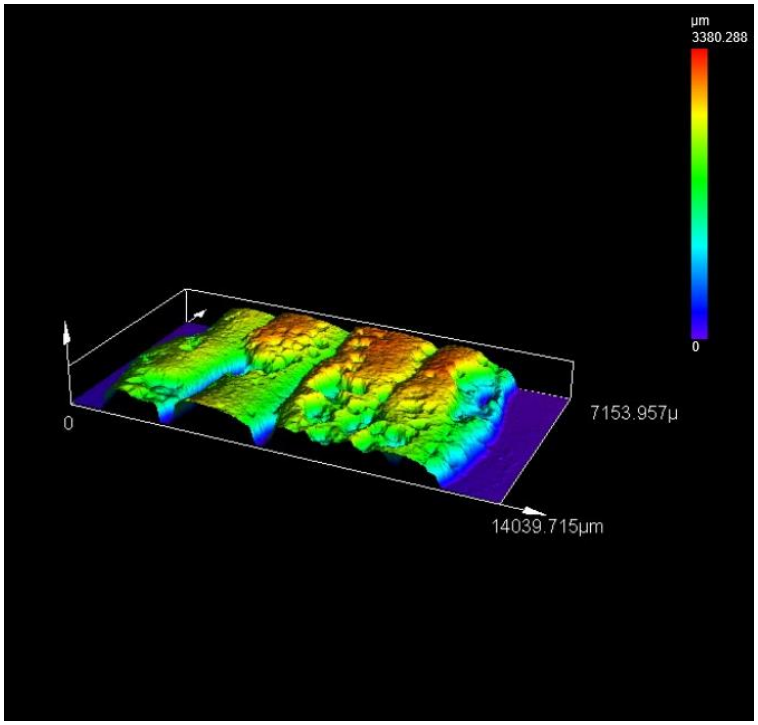

Figure 66: 3D image showing example section of a single deposited layer of Ti64 slurry consisting of 4 overlapped tracks. Acquired using LEXT OLS5000 laser confocal microscope

set as 2 and *Extrusion Order* was set to 'proximity', which meant that when the 1st layer had been deposited, rather than the nozzle returning to where it started to begin depositing the 2nd layer, it deposited the next layer in the reverse order starting in the position where it ended the previous layer. The total length of the hatched lines was designed such that at a *print speed* of 5 mm/s the time taken to deposit the full layer would be $300s$. As such, by the time the second layer extrusion reached the point at which the first layer was started, the time between the deposition of the layers would be $600s$, hence producing a 2-layer build where the drying time for the first layer prior to deposition of the second layer varied between $0 - 600s$ along the length of the build. The build could then be analysed at various sections in order to examine the effect of altering the drying time. Cross-sectional images were taken at various locations within the 2-layer structure using the Leica S6D in order to examine the merging between tracks and layers.

3.5.8 Full 3D Builds by Extruding Multiple Tracks and Layers

Having optimised extrusion parameters, adjacent track overlap and multi-layer deposition parameters for various slurry compositions (including Ti64 powder and SS 316L powder slurries), the final

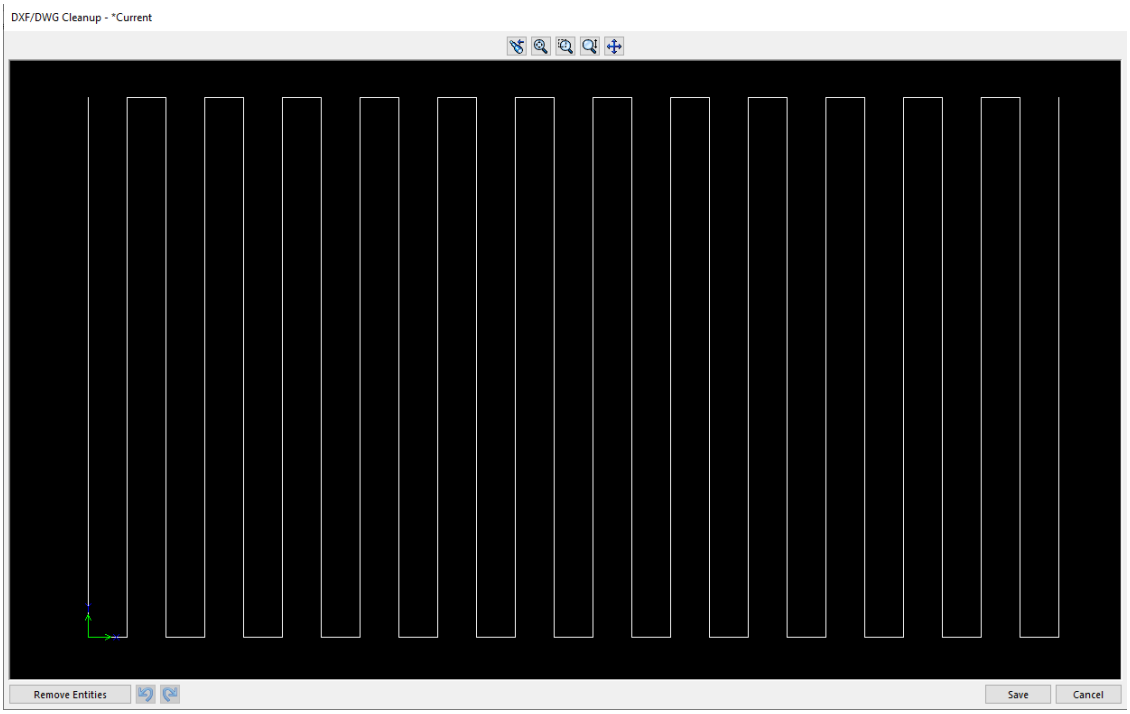

Figure 67: Screen-shot showing hatching pattern used for 2-layer deposition timing experiment.

stage of experimental work was to produce various 3D builds using the ZMorph thick paste extruder which could then be assessed geometrically and also in terms of track and layer merging/adhesion. .dxf files of simple geometries and hatching patterns were created for these builds, predominantly squares and circles with hatching as shown in Figure 68, and the layer count was set to be 4 in order to sufficiently demonstrate the capabilities of the process whilst also keeping the temperatures safely above the gelation temperature of the MC solution. After deposition, these 4-layer builds were left on the heated platform overnight to be allowed to completely dry before being removed for analysis. Images were taken with a ruler to provide a scale, which were then transferred to Fiji to be used to measure the dimensions of the builds in the XY-plane. Selected sections of each build were also scanned using the LEXT OLS5000 in order to analyse the overall height profiles. Finally, each build was fractured in a number of places and analysed using the Leica S6D optical microscope in order to inspect the boundaries between adjacent tracks and successive layers.

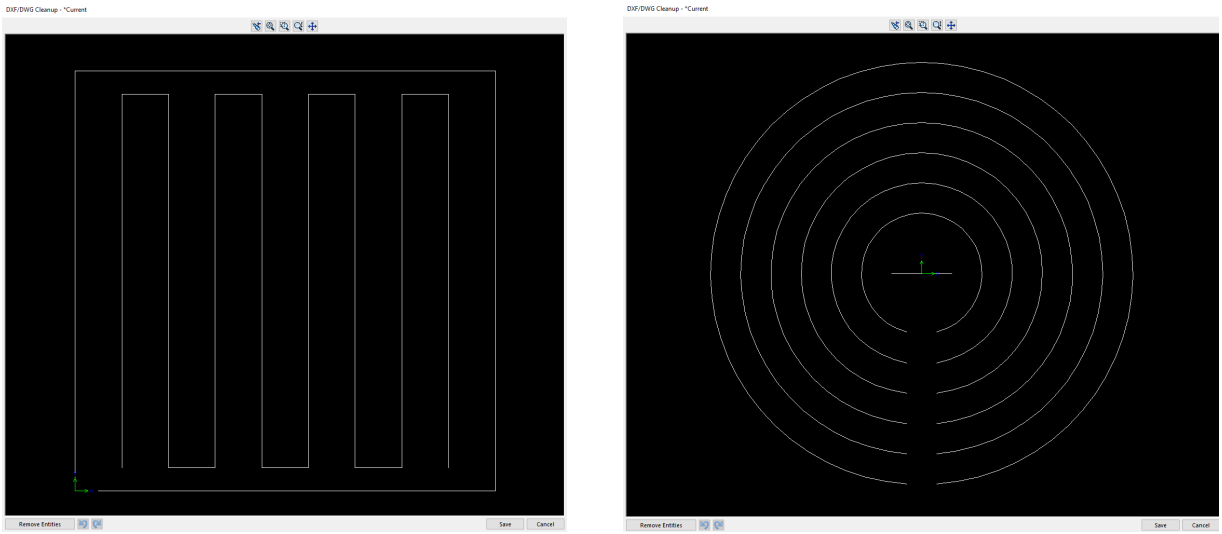

(a) (b)

Figure 68: Screen-captures of .dxf files showing geometries and hatching patterns used to generate .gcode files for 3D builds using the ZMorph thick paste extruder.

3.6 Thermal Behaviour and Modelling of Foamed Titanium Powder Slurry

As explained in Section 3.1.3 the foamed slurry is created by dispersing metal powder within a MC solution, which is a thermally activated gelling agent. Therefore, understanding the thermal behaviour of the slurry when deposited on a pre-heated platform, or several layers of slurry deposited successively, was fundamentally important in order to be able to successfully develop the 3D extrusion process. Also, the drying rate of each layer of deposited slurry was of significance for determining the deposition timing for the following layer, as mentioned in Section 3.5.7. A series of experiments were conducted in order to gain an understanding of the gelling and drying behaviour of the slurry, and the data that was gathered was used to develop a number of empirical models that could then be used to determine important information regarding the thermal behaviour.

3.6.1 Temperature Profiles and Drying Rates

Temperature data for various tracks and layers of foamed slurry deposited on the pre-heated ZMorph platform was acquired using a Flir C2 thermal imaging camera in conjunction with FLIR Tools + thermal analysis and reporting software (FLIR Systems, USA). The camera can be used to take single images which display the temperature of the material. Alternatively, when connected to the FLIR Tools + software, a continuous recording can be taken which can then be post-processed

within the software. Using this method several regions of interest within the camera frame can be highlighted and continuous temperature data can be plotted against time, which can then be exported as a graph or as raw data in a .csv file.

3.6.2 Thermal Camera Emissivity Calibration

In order to measure temperature accurately using the thermal camera, the emissivity of the material being imaged has to be defined within Flir Tools +. The emissivity of the slurry was not previously known and so a calibration experiment was set up in order to obtain the emissivity value. The experimental setup and schematic are shown in Figure 69. A mass of slurry was deposited on the pre-heated platform and the temperature profile of the slurry was measured by inserting a thermocouple just below the surface, and the data was captured at 1s intervals using a Pico Technology TC-08 thermocouple data logger in conjunction with PicoLog 6 data logging software (Pico Technology, UK). The thermal camera was also positioned to capture a thermal recording of the slurry from directly above. From this thermal recording the temperature of the surface of the deposited slurry was measured within Flir Tools + and the data exported. The emissivity value was varied within the software, and the resulting temperature profiles were compared against the profile acquired using the thermocouple data in order to find a value which provided the most accurate match between them. The temperature of the platform and atmospheric temperature were also measured using thermocouples throughout the experiment.

3.6.3 Slurry Temperature Profiles

Having found the emissivity value for the foamed slurry, the thermal imaging camera could then be used as an accurate way of easily acquiring thermal data from slurry deposited on the pre-heated ZMorph build platform, without the need for careful positioning of thermocouples. Surface temperature data was gathered using the thermal camera in the same way as described in Section 3.6.2. In order to build an understanding of the thermal behaviour of the slurry as multiple layers are deposited (or as the thickness of deposited slurry increases), temperature data was gathered for slurry that was deposited at various thicknesses. Foamed titanium powder slurry was prepared using the methods described in Section 3.2.3, but rather than being transferred into a mould or loaded into the ZMorph thick paste extruder syringe, it was loaded into a Kitchener Jerky Gun (Figure

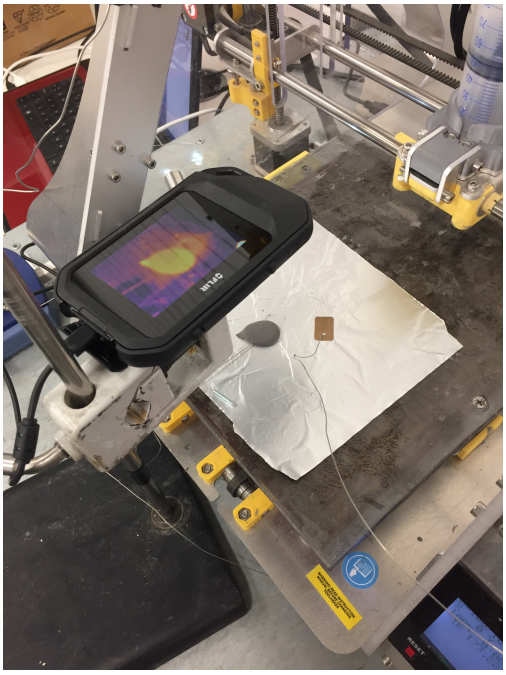

(a)

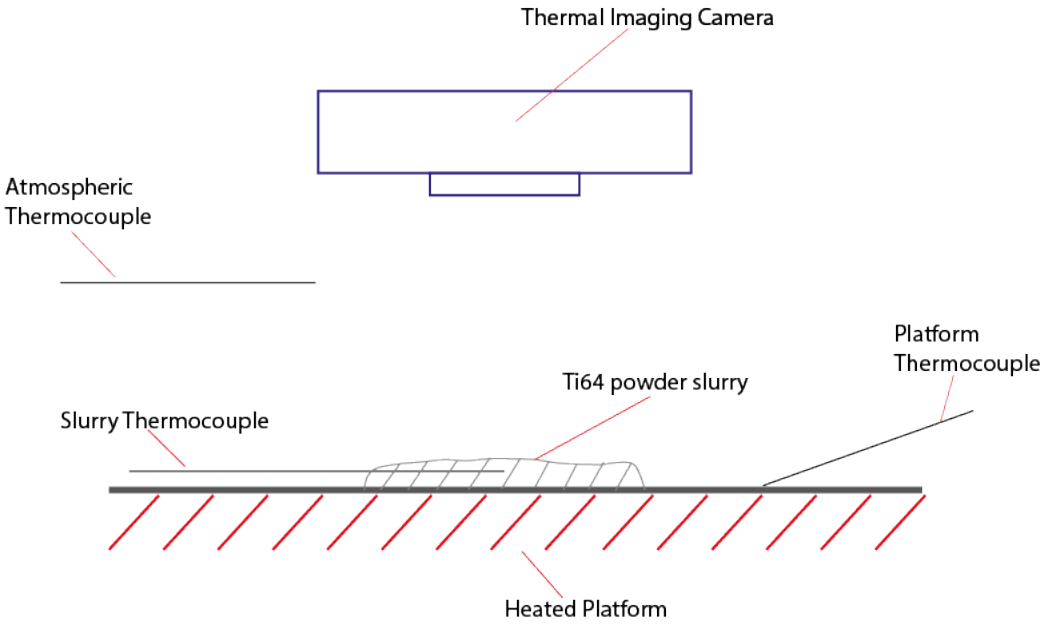

(b)

Figure 69: Experimental set-up used for thermal camera emissivity calibration (a) and schematic explaining the components of the experimental set-up (b).

71a). Using the trigger to compress the plunger, slurry could be extruded at a controlled rate through the nozzle (Figure 71b) which has a rectangular aperture of dimensions 4 mm by 29 mm. By extruding slurry in this way whilst slowly moving the nozzle over the pre-heated ZMorph build platform, a square or rectangular single layer of slurry was deposited. The thickness of the layer of slurry was then controlled using a simple foam levelling tool designed and manufactured in-house (Figure 71c) that contains channels with the same width as the Kitchener gun nozzle but varying height gaps of 2, 4 and 6 mm. This tool was carefully passed over the deposited slurry using the channel that corresponded with the desired layer thickness, thus removing any slurry above the desired layer height. Slurry had to be extruded from the gun in such a way as to deliberately deposit more material than was required, in order to ensure that the levelling tool was able to remove the excess material and produce the desired layer thickness. Temperature profile data was collected using this method for slurry layers of thickness 2, 4 and 6 mm. The impact of platform temperature was also investigated by depositing these layers on the platform pre-heated to temperatures of 80, 90 and 100$°C$.

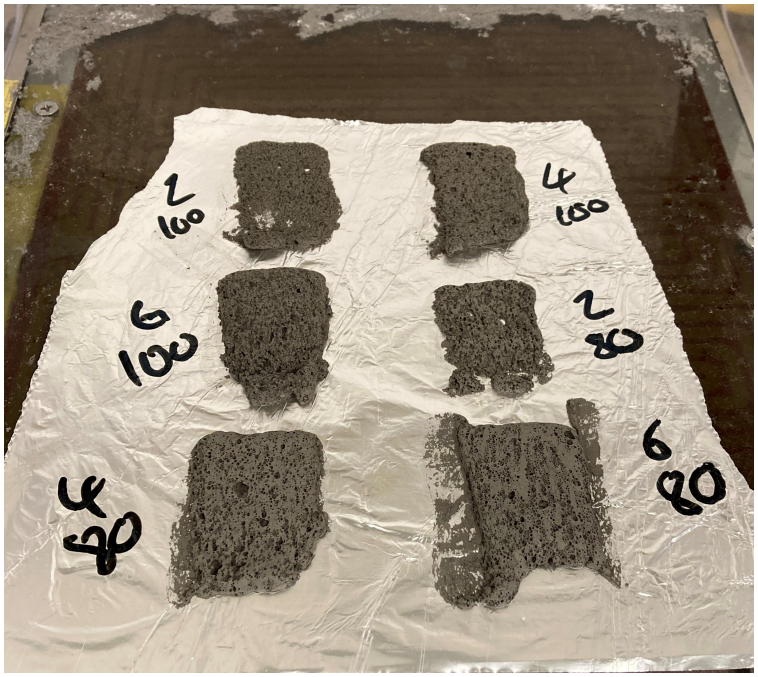

Figure 70: Image showing various full layers of slurry used to gather thermal data, deposited using Kitchener gun and foam levelling tool.

(a)

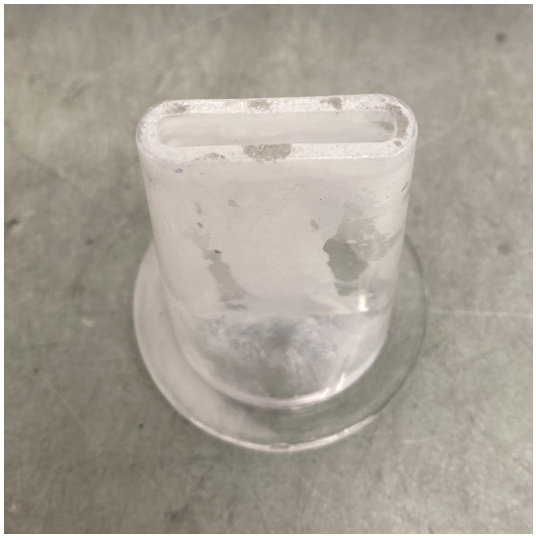

(b)

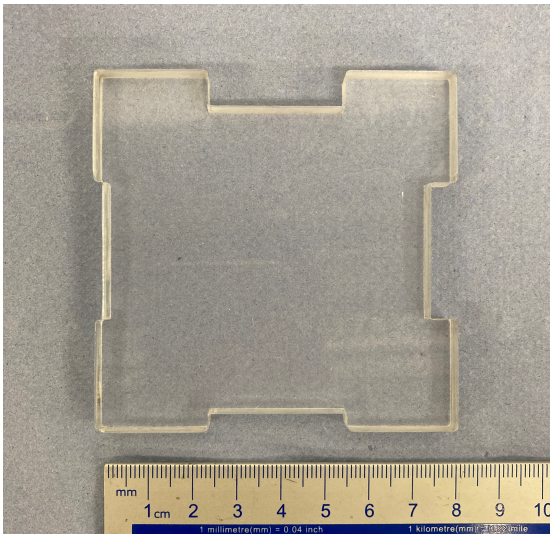

(c)

Figure 71: Images showing equipment used to deposited full layers of foamed slurry with controlled layer thickness on the ZMorph platform including (a) Kitchener Jerky Gun, (b) gun nozzle and (c) foam levelling tool.

3.6.4 Measuring Drying Rate of Deposited Slurry

In order to understand the level of moisture remaining within the slurry at various key points on the temperature profiles, a set of experiments was conducted where the mass loss of the slurry was measured at specific intervals during the drying process. It is clear that removing a sample from the heated platform several times would disrupt the drying process and alter the temperature profile, therefore an alternative experimental method was developed in order to be able to gather the mass loss data. For each layer thickness and platform temperature combination, between 10 and 20 samples were extruded onto individual pieces of aluminium foil using the method described in Section 3.6.3. After being extruded and levelled, each sample was immediately weighed and then transferred onto the heated platform for a pre-determined duration, before then being removed and weighed again. From the measured change in mass, the mass loss percentage was then calculated for each sample. The duration of time each sample was dried for was determined using the temperature profiles previously acquired to create a spread of data points throughout each profile for each layer thickness and platform temperature combination. The mass loss data points were then plotted against the existing temperature profiles. Thermal recordings were taken using the thermal camera for all the samples that were dried, as well as a control sample for each layer thickness and platform temperature combination that was completely dried on the platform. Using these recordings, the final temperature of each sample was measured immediately prior to being removed from the platform, so that the temperature of each individual sample could be compared against the full temperature profiles for the same sample thicknesses and platform temperatures (as presented in Section 7.1.4).

4 Chapter 4: Results & Discussion Part I - Foam Gel Casting Process Development and Stability Testing of Foamed Ti64 Powder Slurries

This chapter presents and discusses the results relating to the development of the foam gel casting process using Ti64 powder, including the development of the slurry composition and mixing procedure in order to optimise the process to produce structures with optimal porosity for the application of orthopaedic implant material. It also covers the stability and extrusion testing of the foamed slurry, both under atmospheric conditions and when held within the syringe within the thick paste extrusion toolhead of the ZMorph 2.0 printer, and the analysis of the impact of extrusion speed and time held within the syringe on the structural properties of the extruded and dried slurry samples.

4.1 Developing the Foam Gel Casting Process for Ti64 Powder

As highlighted in Section 2.6.5 there has been limited work around the development of the gel casting and foam gel casting manufacturing processes using metal powder slurries as the main focus in this area has been around ceramic materials. Recent studies have developed this process for SS 316L and iron powder slurries [218, 220, 243], however applying this process to Ti64 remains almost entirely unexplored. Section 2.6.6 highlights how the porous structures within samples produced using the foam gel casting technique appear strongly suited to the application of orthopaedic implant material, and as such there is clear motivation for developing this technique using bio-compatible materials, and Ti64 in particular, which has been highlighted as a popular choice of material for artificial orthopaedic implants. Section 3.2 outlines the experimental procedure followed when optimising slurry composition for the foam gel casting process with Ti64 powder. The results from this procedure are presented in this section and the justifications for the selection of the final optimised slurry composition and mixing procedure are provided.

4.1.1 Powder Packing Density Calculations

Following the process outlined in Section 3.2.1 the volume and tapped volume of a mass of the Ti64 AM grade powder were measured, and these values were used to calculate the bulk and tapped

densities of the powder, 2.65 and 2.78 g/cc respectively. These density values were then divided by the density of Ti64 ($\rho_p = 4.5\ g/cc$ [133]) to provide a packing fraction (PF) range of $0.59 - 0.62$. As previously explained, this PF range provides an initial guide for the ratio of powder to gelling agent solution (referred to as volume fraction) to be used for mixing the powder-based slurry, by applying Equations 12 & 13, in order to calculate the volume of gelling agent solution and mass of powder required.

The calculated PF range for this powder was a surprisingly tight range for powder packing, suggesting that the powder naturally packs quite efficiently without the need for mechanical tapping, and hence tapping the powder within the container only produced a slight increase in packing density. In contrast, Kennedy and Lin reported that the packing density range of non-AM grade SS 316L powder used to produce slurries ranged from 0.45 without tapping to 0.6 when mechanically tapped [220]. The superior ability of the AM grade Ti64 powder to naturally pack itself in a dense manner is a result of the sphericity of the powder particles, which, as described in Section 3.1.1, is due to the way the powder is manufactured deliberately to increase the flow of the powder for AM applications, and also increase packing density in order to decrease shrinkage during melting/sintering (typically melting using an electron or laser beam). Random packing of perfect spheres typically results in a packing density of around 0.637 [286], which is only slightly higher than the PF range calculated for the Ti64 powder used in this work.

4.1.2 Initial Ti64 Slurry Batch Composition and Analysis

A volume fraction (VF) of 0.6 was selected to mix the initial batch of Ti64 slurry. The mass of powder was calculated to be 135 g and the MC solution volume of 20 ml required in order to mix a 50 ml batch of slurry (non-foamed volume). Initially a 2 $wt\%$ concentration of MC solution was used and, as described in Section 3.2.3, the Darvan 7-N dispersant was added at 1.5 $wt\%$ of the powder mass (2 ml) and the Triton X-100 surfactant added at 1 $vol\%$ of the non-foamed slurry volume (0.5 ml) prior to whisking for 4 minutes. After whisking, the slurry was transferred into rectangular silicone moulds and then transferred to the oven to gel and dry, as described in Section 3.2.3 and presented in Figure 51. Once fully dried, the samples were removed from the moulds and pore size and porosity measurements were acquired using the techniques outlined in Sections 3.4.3 & 3.4.3. Figure 72b shows the porous structure of the dried sample taken using an optical

microscope. The mean pore diameter was measured to be 289 μm, with an interquartile range of $200-338$ μm and the porosity was calculated from the mass and volume measurements to be 63 %.

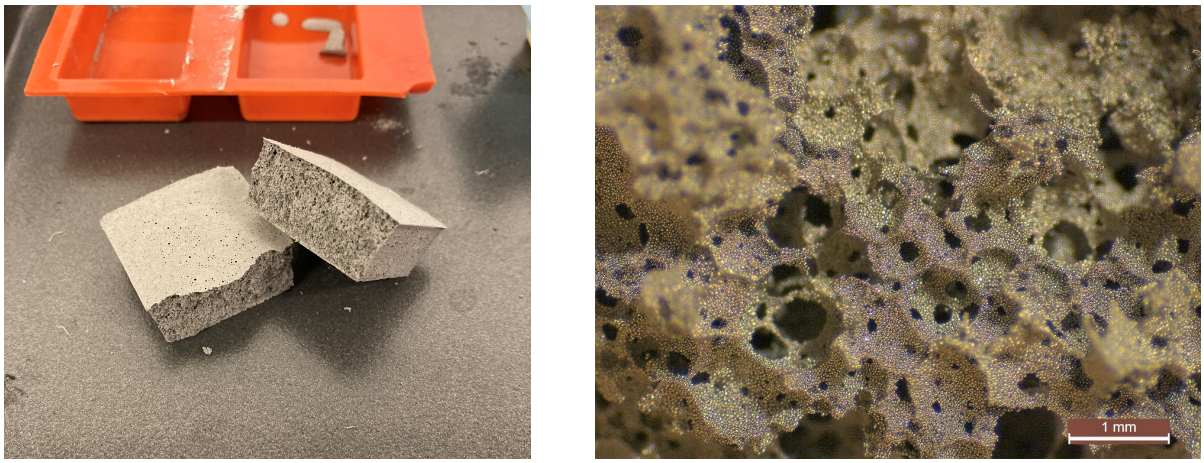

(a) (b)

Figure 72: Image (a) and optical micrograph (b) showing porous structure of Ti64 produced using foam gel casting with a slurry VF of 0.6.

The porosity of the samples (63 %) produced from this initial batch of Ti64 slurry sits just within the lower end of the optimal porosity range for orthopaedic implant material as outlined in Section 2.9, however the mean pore diameter of 289 μm is below the optimal range. Also, it was highlighted by Lin and Kennedy that the SS 316L powder samples experienced a shrinkage of $15-25$ % as a result of sintering [243], and so if this theoretical reduction is applied to the pore size distribution measured for these Ti64 samples then the pore sizes would be significantly below the desired range. Whilst the viscosity of the slurries was not measured as this stage, this initial batch was observed to be highly viscous, and there is clear evidence within the literature that this reduces the capacity for the slurry to be foamed [226], which may explain the limited pore sizes observed within this batch of samples. The green strength of the samples was more than sufficient for the samples to be removed from their silicone moulds after drying in the oven, but the samples could be easily broken by hand in order to expose the internal porous structure for analysis. It is likely that the high packing density of the powder contributes to the high green strength of the samples, particularly if the VF used to calculate the slurry composition is close to the PF range of the powder, as in the case of this batch.

4.1.3 Controlling Porosity by Varying Slurry Composition Parameters

In order to understand the impact that certain key slurry composition parameters has on the porosity of the resulting dried samples, and to be able to produce structures with porosity and pore sizes with the specified target values, a range of slurry batches were mixed and whisked where these parameters were varied and the resulting dried samples were analysed using the techniques outlined in Section 3.4.3. It was highlighted in Section 2.6.4 that the major advantage of the foam gel casting process is that it offers the ability to control porosity optimising various parameters within the slurry composition and mixing process [223]. The parameters which were investigated in order to optimise the porosity of the dried samples produced from the foamed Ti64 powder slurries in this work included the volume fraction, MC solution concentration and slurry whisking time as summarised in Table 6 (Section 3.2.4).

As previously explained the PF range provides a guide for the initial VF value to use to calculate the mass and volume of powder and gelling agent solution. The VF can be varied to suit the application and required properties of the slurry/resulting material, although increasing the VF from the value used to produce the initial slurry batch (or using a higher ratio of powder to gelling agent solution) would have most likely resulted in a slurry which is too viscous to mix or whisk as it would not contain enough liquid to the powder to fill the void spaces between particles and produce a fluid slurry. Therefore, the initial VF value of 0.6 was selected as the upper limit and a number of slurry batches were mixed using VF values in the range of $0.5 - 0.6$. The whisking time was kept constant at 4 minutes, and the dispersant and surfactant addition was calculated using the same $wt\%$ and $vol\%$ of the powder mass and slurry volume respectively as described for the initial batch in Section 4.1.2. The measured porosity and pore/window sizes of the resulting samples are presented in Figure 73.

It is clear from Figure 73 that reducing the VF used to calculate the slurry composition from its initial value of 0.6 resulted in a dramatic increase in pore size and porosity. These results agree with the observations drawn from the literature (Section 2.6.4), and is typically attributed to the fact that increasing the VF (or solid loading) of the slurry results in an increase in viscosity which, as previously stated, reduces the capacity for the slurry to be foamed [231, 238]. A VF of 0.5 produced samples with a mean pore diameter of almost 1 mm and a porosity of 84 %. Even after applying

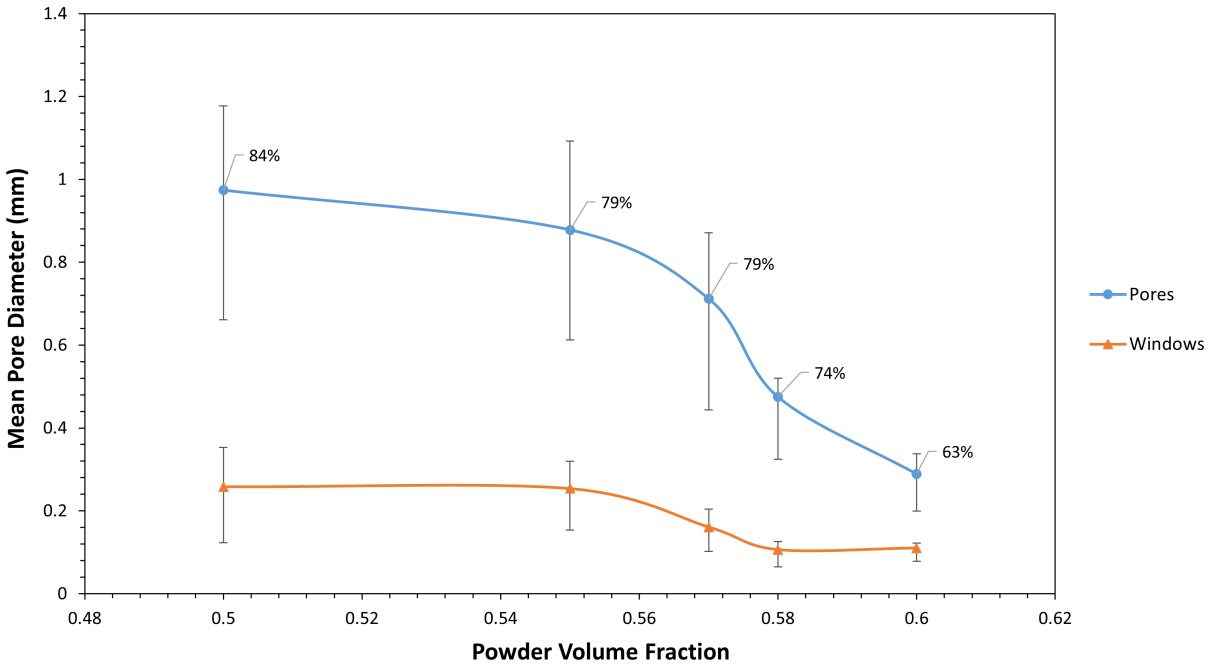

Figure 73: Graph showing porosity and mean pore size (with interquartile range) of dried Ti64 samples against volume fraction used to calculate slurry composition.

a theoretical shrinkage to account for sintering (as discussed in Section 2.6.6) would produce pores above the highlighted optimal range. Also, the green strength of the samples was compromised which meant that when removing the samples from the silicone moulds some fragments broke off, and the samples had to be handled very delicately in order to avoid them disintegrating. This also was observed, but to a lesser extent, for samples produced using a VF of 0.55. 0.57 was selected as the VF value to proceed with because the samples still presented sufficient green strength to be easily removed from the moulds and handled, whilst also presenting a mean pore diameter of 712 μm with an interquartile range of $444 - 871$ μm, which, when shrinkage due to sintering has been accounted for, results in a pore size slightly higher than the desired values of $300 - 600$ μm. Increasing the VF to 0.58 resulted in a significant reduction in pore size, and therefore 0.57 was selected for further optimisation by varying alternative parameters.

In order to further control the porosity of the resulting samples the MC solution concentration was altered. Various batches of MC solution were prepared following the methods outlined in Section 3.2.2 to produce concentrations of $1 - 4$ %. These were then used to prepare Ti64 powder slurry batches with a VF of 0.57 where all the other composition parameters were kept constant.

The measured porosity and pore/window sizes of the resulting samples are presented in Figure 74. The porosity of the samples produced from a slurry mixed with a 1 $wt\%$ concentration MC solution could not be calculated because the samples collapsed when being removed from the silicone moulds and therefore the mass could not be measured. Pore size measurements were still acquired using the fragments of the samples that remained after removal.

Figure 74 shows that increasing the wt% concentration of the MC solution from $2-4$ $wt\%$ had no noticeable impact on the pore size of the samples, although a slight reduction in porosity was observed (4 %). Reducing the concentration to 1 $wt\%$ caused an increase in pore size from 712 μm to 1284 μm, but also resulted in a significant reduction in the green strength of the samples, to the extent that the porosity could not be calculated because the samples collapsed upon being removed from the moulds. Whilst the viscosity of the slurries were not measured at this stage, it was observed that the viscosity increased with MC solution concentration, which agrees with what was observed in previous studies when developing the gel casting process for different metal powders [218, 220]. However, Kennedy and Lin highlighted that increasing the concentration of MC solution used to prepare SS 316L powder slurries up to 4 % resulted in greater slurry stability. It is desirable to keep the viscosity of the slurries low in order to allow for sufficient foaming and ensure that they are able to flow, however if required the concentration can be increased to improve the stability of the slurry. Therefore, the MC concentration was kept at the original 2 $wt\%$ in order to allow for sufficient foaming, and the stability of the slurry was assessed separately (Section 4.2).

The final parameter that was investigated was the whisking time of the slurry. Using the highlighted VF of 0.57 and a 2 $wt\%$ concentration MC solution, batches of the same composition were mixed and then whisked for $1-6$ minutes in 1 minute intervals. The measured porosity and pore/window sizes of the resulting samples are presented in Figure 75. Figure 76 shows a comparison between the porous structure of samples whisked for 1 minute and 4 minutes. As discussed in Section 2.6.6, when developing the foam gel casting process for SS 316L powder slurries, Lin and Kennedy observed that increasing the whisking time of the slurry caused an increase in pore size and porosity of the resulting samples [243]. The results displayed in Figure 75 confirm that whisking time has a significant impact on pore size and porosity of the samples, however this plot does not present a linear relationship between these variables. Increasing whisking time from 1 to 4 minutes resulted in an increase in mean pore diameter from 269 to 710 μm and porosity

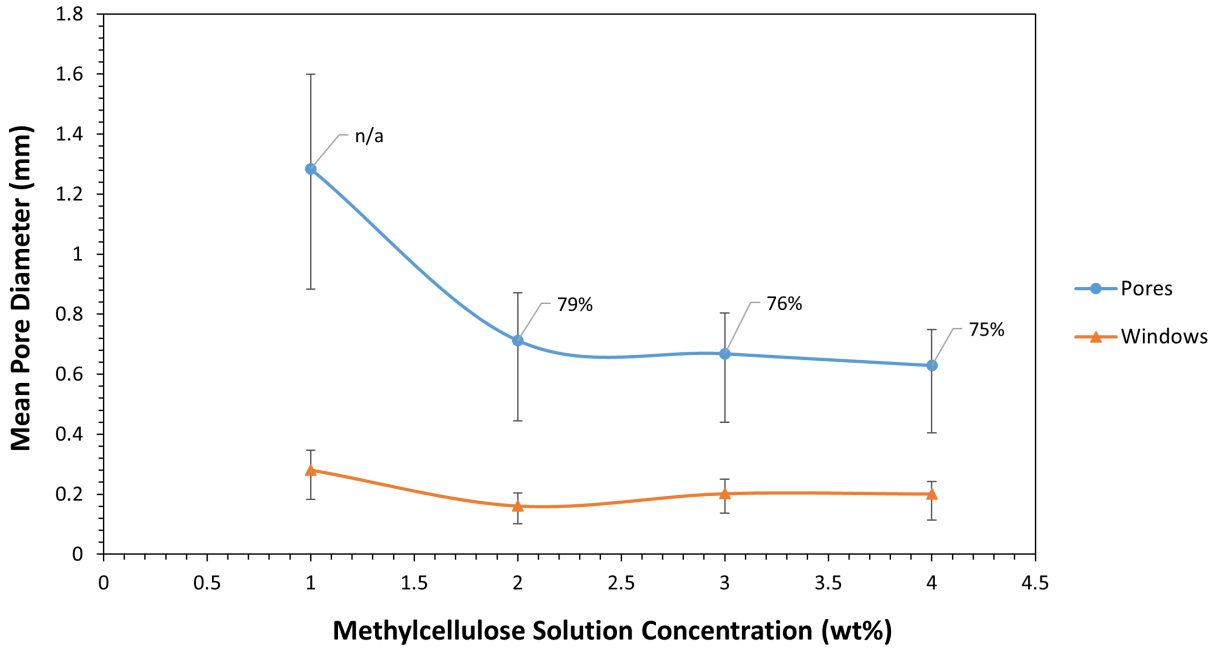

Figure 74: Graph showing porosity and mean pore size (with interquartile range) of dried samples against wt% MC solution used in the slurry composition.

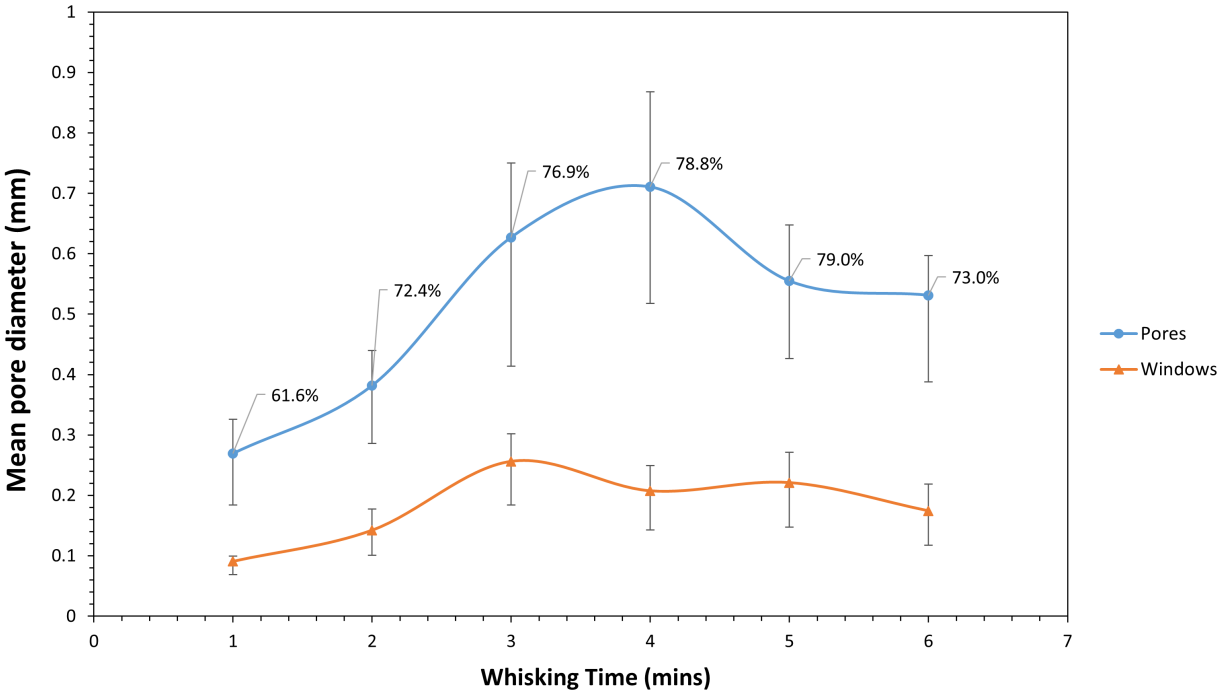

Figure 75: Graph showing porosity and mean pore size (with interquartile range) of dried samples against whisking time of the Ti64 slurries.

from 61.6 % to 78.8 %. A further increase to 6 minutes resulted in a reduction of mean pore diameter and porosity to 531 μm and 73 % respectively. The observed 'linear' relationship in Lin and Kennedy's work between whisking time and pore size/porosity most likely does not represent the whole picture due to the limited data points used to determine the relationship. It is more accurate to suggest that whisking time increases porosity/pore size up to a point (4 minutes in this case), beyond which further whisking causes the air bubbles within the slurry to collapse resulting in a reduction of these properties. It is likely that if whisking was then increased further a periodic fluctuation of pore size and porosity within a defined range would be observed.

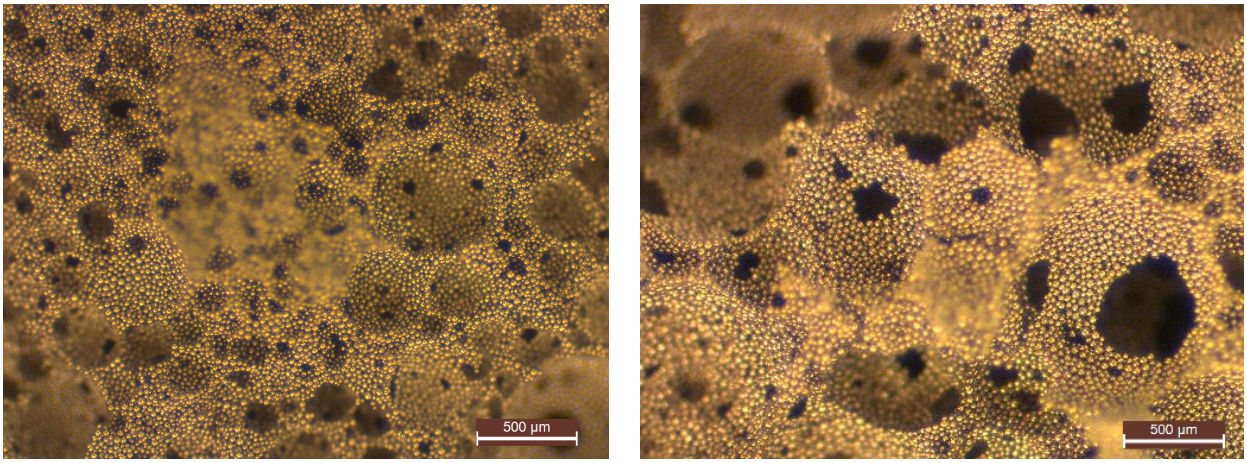

(a) (b)

Figure 76: Optical micrographs showing porous structure of Ti64 samples produced from slurry whisked for 1 minute (a) and 4 minutes (b).

Of all the slurry composition process parameters, it is evident that whisking time had the most significant impact on the porosity of the samples. Therefore it can be recommended that when developing this system for different powders, the other parameters can be optimised to achieve the desired slurry viscosity and stability of the green samples, and then subsequently the porosity can be controlled by experimenting with whisking time. For the purpose of this work, a whisking time of 3 minutes was selected as optimal as it produced dried samples with a pore size distribution and porosity value that meet the requirements set out in Section 2.9, as discussed further in Section 4.1.4.

4.1.4 Optimised Slurry Composition and Dried Sample Properties

From the results outlined this section, an optimal set of slurry composition parameters was highlighted that produced Ti64 with porosity and pore size distributions that meet the criteria set out in Section 2.9, once shrinkage during the sintering process has been accounted for. Figure 77 outlines the optimised composition and mixing process for the Ti64 powder slurry. A summary of the final measured pore size distribution and porosity of the samples produced using the optimised Ti64 slurry composition is provided in Table 7, as well as providing theoretical values for the pore sizes that account for a 20 % shrinkage due to sintering. When this theoretical shrinkage is applied, the pore size distribution closely matches the optimal range specified in Section 2.9 of $300 - 600\ \mu m$, with over 50 % of the pores being within this size range. As mentioned in Section 1.1.1, previous studies have shown that bone growth occurs within scaffolds with pore sizes ranging from $100 - 1200\ \mu m$ [20, 197], which means that bone in-growth should in theory be possible throughout the entire porous structure of the samples produced using this method.

	Pore Diameter (μm)					
	Mean	Lower Quartile	Upper Quartile	Minimum	Maximum	**Porosity (%)**
Measured	627	414	750	302	1570	76.9
With 20 % Shrinkage	501	331	600	242	1256	/

Table 7: Table summarising the measured pore size distribution and porosity of the dried samples produced using the optimised Ti64 slurry composition and mixing procedure.

The results presented in this section demonstrate clearly how foam gel casting can be used to provide significant control over porosity of resulting material, as highlighted in numerous studies as discussed in Section 2.6.4. The initial powder VF and whisking time of the slurry in particular are parameters that can provide a significant level of control over the final porosity of the resulting dried samples. Previous studies that focus on optimising porosity using the foam gel casting process have also demonstrated that surfactant concentration can provide further control over the resulting porosity of dried samples [230, 236, 237], however this parameter was not investigated in this work because sufficient control was achieved by altering the parameters described in this section.

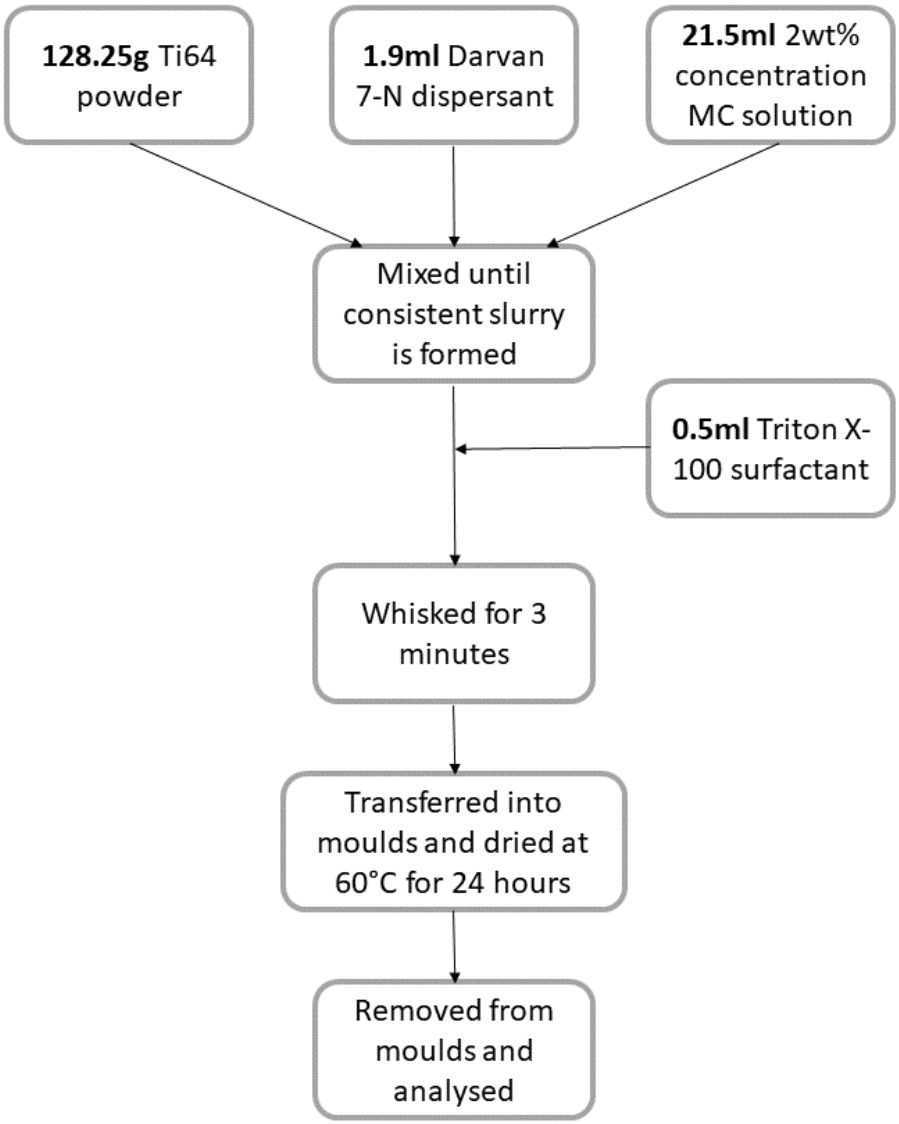

Figure 77: Schematic showing the optimised Ti64 slurry composition and mixing process for producing material with porosity and pore size distribution that meet the outlined requirements.

The high level of control over porosity that can be achieved by optimising parameters within this process suggests that this is a very suitable process for the development of porous scaffolds for orthopaedic implant material which require specific levels of porosity and pore sizes as already discussed. Also, due to the nature of the way in which the pores are generated by introducing air bubbles into the slurry and the natural tendency of these bubbles to coalesce, the resulting porous structures are well interconnected with large connecting windows with a mean diameter of 256 μm, which are above the minimum required size for interconnecting windows for optimal bone in-growth [23]. If in further work the shrinkage due to sintering is found to be different to the 20 % applied to estimate the final pore sizes, the process can be easily tweaked to produce the desired final pore size distribution.

The samples produced using the optimised slurry composition and process present high green strength, enabling them to be easily removed from the moulds and handled, as well as maintaining their structure when fractured in order to examine the interior porosity. This strength can be attributed to the properties of the powder used to develop the slurry. As mentioned in Section 4.1.1, AM grade powders are produced to be as spherical as possible because they are required to flow readily and be easily spread into thin layers so they can then me selectively melted using typically electron or laser beams (EBM and SLM processes). In addition to being able to flow, the powders need to be able to pack in a dense manner in order to reduce shrinkage when the powder is melted/sintered, and it is well understood that spheres can be packed efficiently. As a result, these powders present suitable properties for developing powder-based slurries that produce highly stable structures when foamed, gelled and dried. Also, it is likely that these properties contribute to the high stability of the foamed slurries themselves, as discussed further in Section 4.2.

4.1.5 Testing Mechanical Stability of Dried Foamed Ti64 Slurry Samples

As outlined in Section 3.4.4, a stability test was conducted in order to examine whether the dried samples would maintain their structure when the MC binder was removed during sintering. Upon examination after this binder burnout test, the samples retained their structural integrity and could be safely handled without disintegrating. When fractured to expose the internal porous structure and examined under a microscope, it was discovered that the porous internal structure of the samples had remained stable during the burnout of the MC. Figure 78 shows the internal structure

of a Ti64 powder sample produced using the optimised slurry composition and mixing process as outlined in Figure 77, after the 650°C MC burnout test. Whilst the focus of this work is developing the slurry composition and 3D extrusion process and as such the samples produced in this work were all analysed as green samples to enable their structures to be analysed quickly and easily, it was highly important to perform this burnout test at this stage in order to ensure that the samples can be sintered without simply collapsing.

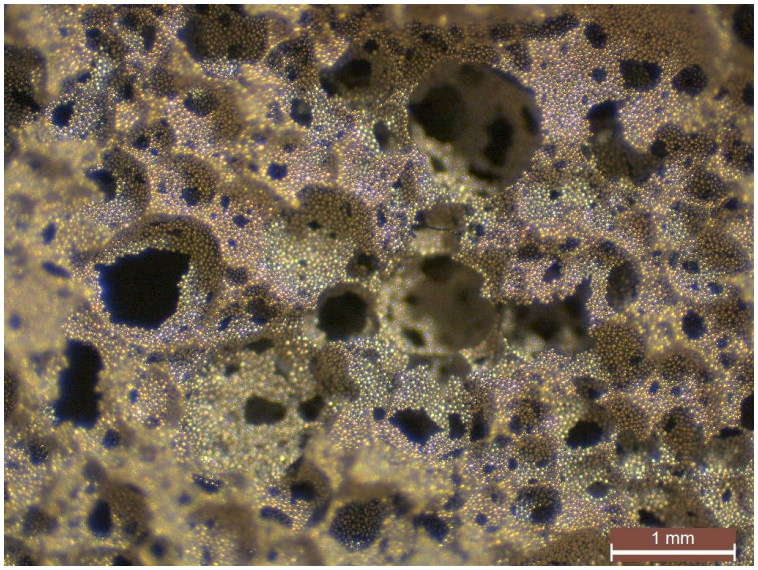

Figure 78: Optical micrograph showing internal porous structure of optimised Ti64 sample after MC burnout test.

4.1.6 Estimating Mechanical Properties of Sintered Ti64 Slurry Samples

The highly porous samples produced in this work were not sintered, as discussed further in Section 8.2, and as such it was not possible to analyse the mechanical properties and draw a comparison against the properties of human bone as well as the data gathered from literature as presented in Section 2.5. However, using data available in the the literature for porous SS 316L samples produced using the same method that presented very similar structures and porosities to the porous Ti64 produced in this work, the mechanical properties were estimated.

Lin and Kennedy [243] reported that for a SS 316L sample produced using foam gel casting with a porosity of 82 % and a mean pore size of 672 μm, the yield strength was measured to be 32.5 MPa, which is 19 % of the yield strength of wrought SS 316L. The structure of this material

closely resembles the optimised Ti64 samples produced in this work, which presented porosity and measured pore size (not sintered) of 77 % and 627 μm respectively. Therefore, this same ratio between porosity and yield strength was applied to the properties of Ti64 to provide an estimate for the mechanical properties of the material developed here once it has been sintered. Applying this reduction gives an estimate of 158 MPa, which is slightly greater than the reported range for cortical bone ($100 - 140$ MPa). Comparing this against the literature data for yield strength for a range of porous Ti64 scaffolds (as summarised in Figure 29 in Section 2.5.2), is is clear that this value is higher than those reported in literature for this level of porosity. This may be explained by the high packing fraction of powder used to create the slurries which means that the walls of the scaffold contain densely packed powder which, when sintered, results in an increased mechanical strength compared with other highly porous scaffolds. Applying the same process to the Young's modulus reported by Lin and Kennedy [243] of 7.8 GPa for the SS 316L sample results in an estimated modulus of 4.7 GPa for the Ti64 material. Whilst this value is slightly below the range reported for cortical bone ($10 - 30$ GPa), it is significantly greater than that of trabecular bone ($<$ 0.5 GPa) and also greater than the values reported in literature for Ti64 with this level of porosity (as summarised in Figure 27 in Section 2.5.1). Again, this suggests that this process is capable of producing highly porous structures that maintain impressive mechanical properties when compared to other processes used to achieve the same level of porosity, which makes it ideal for this application where the implant material is required to provide structural support in load-bearing applications whilst also providing a highly porous scaffold.

Overall, whilst these calculated figures are only estimates of the mechanical properties of the novel material developed in this work, the values are very promising as they suggest that despite the high level of porosity within the material it may still provide mechanical strength similar to that of human cortical bone, whilst presenting a porous structure that mimics trabecular bone.

4.2 Extrusion and Stability Testing of Foamed Ti64 Powder Slurry

Having optimised the composition and mixing procedure for the Ti64 slurry to produce dried samples which presented the desired properties in terms of its porous structure, it was next vital to determine whether extruding this foamed Ti64 slurry using the syringe from the ZMorph paste extruder toolhead would have a detrimental effect on this porous structure. It was also important

to develop an understanding of the stability of the foamed slurry when stored within the syringe, as this is an influential factor in determining the feasibility of 3D-printing by material extrusion as a manufacturing method. As described in Section 3.3, a series of experiments were conducted in order to analyse the stability of the foamed Ti64 slurry when stored within the ZMorph thick paste syringe, and also in ambient conditions (in an open container). Also, these experiments examined whether extruding the foamed slurry through a 2 mm diameter nozzle at various speeds has any effect upon the bubbles and as such the final porous structure of the dried samples.

4.2.1 Observable Decomposition of Foamed Ti64 Powder Slurry Over Time

In order to obtain an initial understanding of the stability of the foamed Ti64 slurry, 50 ml of slurry was placed in a beaker and left to decompose naturally over time in ambient conditions. Images were taken of the slurry at regular intervals to observe how it behaved over the timescale. These images are displayed in Figure 79. Separation of the slurry was observed from 90 minutes onwards, as shown in Figure 4.2.1, where a layer of sediment can be seen forming at the bottom of the beaker and bubbles can be seen rising above this layer. By 150 minutes, the foam had completely collapsed leaving behind a mass of compact powder that was removed after drying, as shown in Figure 79. Whilst this doesn't provide a detailed view of the behaviour of the bubbles within the slurry during this time, it does serve as a basic demonstration that the slurry presents impressive natural stability. The results from the controlled extrusion experiments presented in Section 4.2.3 provide a more detailed insight into the stability of the foamed slurry over time when stored both within the syringe and in an open container for up to around 20 minutes.

4.2.2 Effect of Syringe Extrusion Speed on Resulting Porous Structures

As stated in Section 3.5.3 the ZMorph thick paste extruder syringe nozzle has a 2 mm diameter. With this being greater than the maximum pore size measured within samples produced using this optimised slurry composition of 1.57 mm, it should in theory be possible to extrude the slurry through the nozzle without collapsing the bubbles. However, it was necessary to evaluate this in a controlled environment as described in Section 3.3 in order to determine whether the pressure applied by the plunger or the shear forces experienced within the slurry as it is extruded through the nozzle would result in collapsing or coalescing of the bubbles within the slurry. As

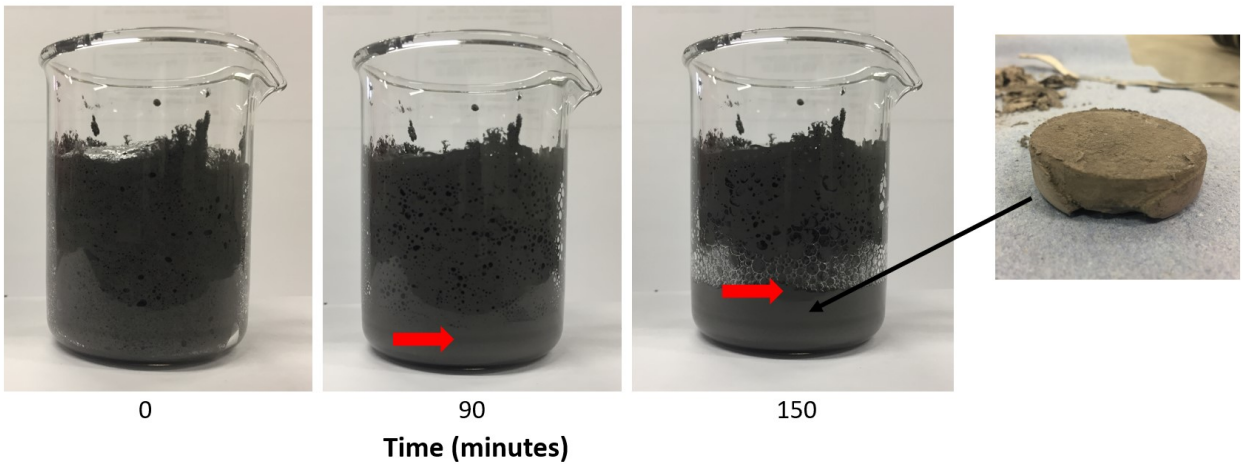

Figure 79: Images showing the decomposition of the Ti64 foamed slurry over time when stored in a beaker with sediment layer highlighted, and dried sediment from final sample.

mentioned in Section 3.3.3, the typical recommended extrusion speed for the ZMorph paste extruder is $0.05-0.1\ ml/s$. Therefore a number of samples of foamed Ti64 slurry were extruded at controlled speeds between $0.05-0.4\ ml/s$ using the custom built syringe driver rig in conjunction with the Instron 6800 Single Column testing system, before being dried and analysed. Figure 80 shows the measured pore and window sizes of the samples extruded at various speeds in comparison to the 'control' samples which were simply dried immediately after whisking the slurry. The porosity of each sample was also calculated from the mass and volume measurements, and for all the samples this value was within the range of $68-78$ %, but there was no observable relationship between porosity and extrusion speed.

Figure 80 clearly shows that increasing the extrusion speed from $0.05\ ml/s$ up to $0.4\ ml/s$ had no measurable effect on the mean pore or window size of the resulting porous structures. The mean pore diameter of the control samples was measured to be $594\ \mu m$, and the measured mean pore diameters of all the samples extruded at the various speeds were within ± 10 % of this value with no observable relationship between extrusion speed and pore size. It is worth highlighting here that the mean pore diameter of the control samples from these experiments is encouragingly similar to the quoted mean pore size of the optimised slurry of $627\ \mu m$ (Table 7). The slight difference between the values can be explained by a number of factors related to the sensitivity of the the slurry mixing procedure and the methods used to measure pore size and porosity as discussed in Section 2.4.1. These factors also explain the observed scatter that is evident in Figure 80. As

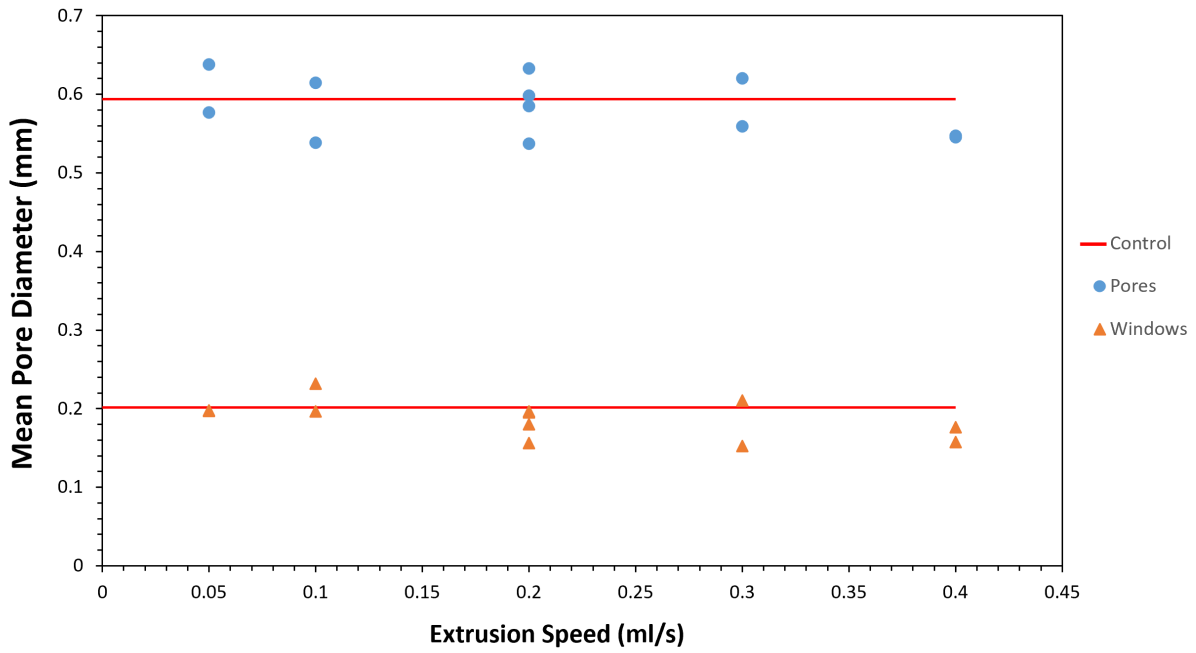

Figure 80: Graph showing pore and window sizes of dried Ti64 samples against extrusion speed of the slurry when extruded from the syringe through the 2mm nozzle.

previously stated, scatter is also observed within the calculated porosity values for the samples extruded at various speeds, however despite this scatter it was evident that no relationship exists between extrusion speed and porosity/pore size within the range covered by these experiments. These results suggest that the compressive and shear forces experienced by the foamed slurry are not sufficient to cause any alterations to the bubbles formed during the whisking process, even when the extrusion speed is increased beyond the typical range of speeds recommended when using the ZMorph paste extruder toolhead. It is likely that increasing extrusion speed further would at some point produce a noticeable difference in porosity of the resulting samples because this would require a greater pressure to be applied by the plunger resulting in a greater surface tension in the bubbles within the slurry, which would cause them to coalesce and possibly collapse, as highlighted in Equation 17 in Section 4.2.3. However, the speeds evaluated in this work already exceed the speed at which it the slurry is likely to be extruded when deposited using the ZMorph paste extruder.

4.2.3 Effect of Syringe Hold Time on Resulting Porous Structures

Figure 82 presents the measured pore and window sizes against the duration the slurry was stored within the syringe prior to extrusion, along with the pore sizes of control samples which were stored in an open container in ambient conditions for set durations before being transferred into the oven to gel and dry, with the first sample being transferred into the oven immediately after the slurry was whisked. Again, the calculated porosities of the samples extruded from the syringe were all within a range of $64 - 74$ % but there was no observable relationship between hold time and porosity. Figure 81 compares optical micrographs of samples both held for 20 minutes, with one being held in the syringe for that time and the other in ambient conditions.

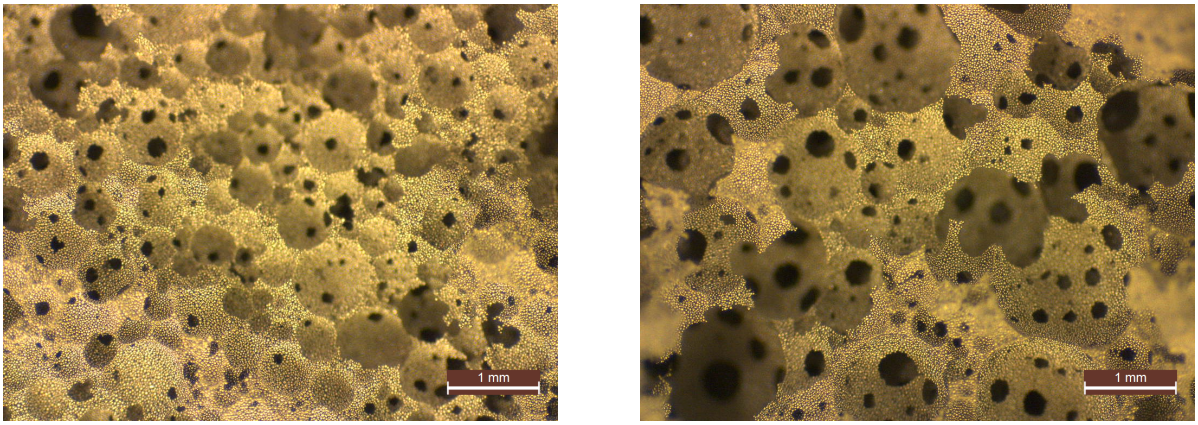

(a) (b)

Figure 81: Optical micrographs of samples from syringe hold time experiment stored for 20 minutes in the syringe (a) and in an open container (b).

Whilst more control data points would have helped determining the true relationship between hold time and pore size distribution when the slurry is stored in an open container, the results clearly show an increase in both mean pore diameter but also in the range of pore sizes present in the sample over time. This suggests that coalescence of bubbles within the slurry occurs under atmospheric conditions, meaning bubbles merge together over time forming larger bubbles which result in larger pores within the dried samples. Initially this occurs without any change in overall volume of the slurry, until sedimentation begins to occur as discussed in Section 4.2.1. Figure 81 confirms this as it clearly shows an observable increase in pore sizes between control samples dried after 0 and 20 minutes, with the measured mean pore diameter at these points being 529 μm and 938 μm respectively. The coalescence of bubbles is driven by the natural inclination of bubbles to

reduce the surface tension within the air/liquid interface. When two bubbles coalesce, the resulting larger bubble has a lower surface area to volume ratio than the two original bubbles, and therefore has a reduced surface tension. The widely used Young-Laplace equation (Equation 17) defines how surface tension relates to the internal and external pressures of a spherical bubble.

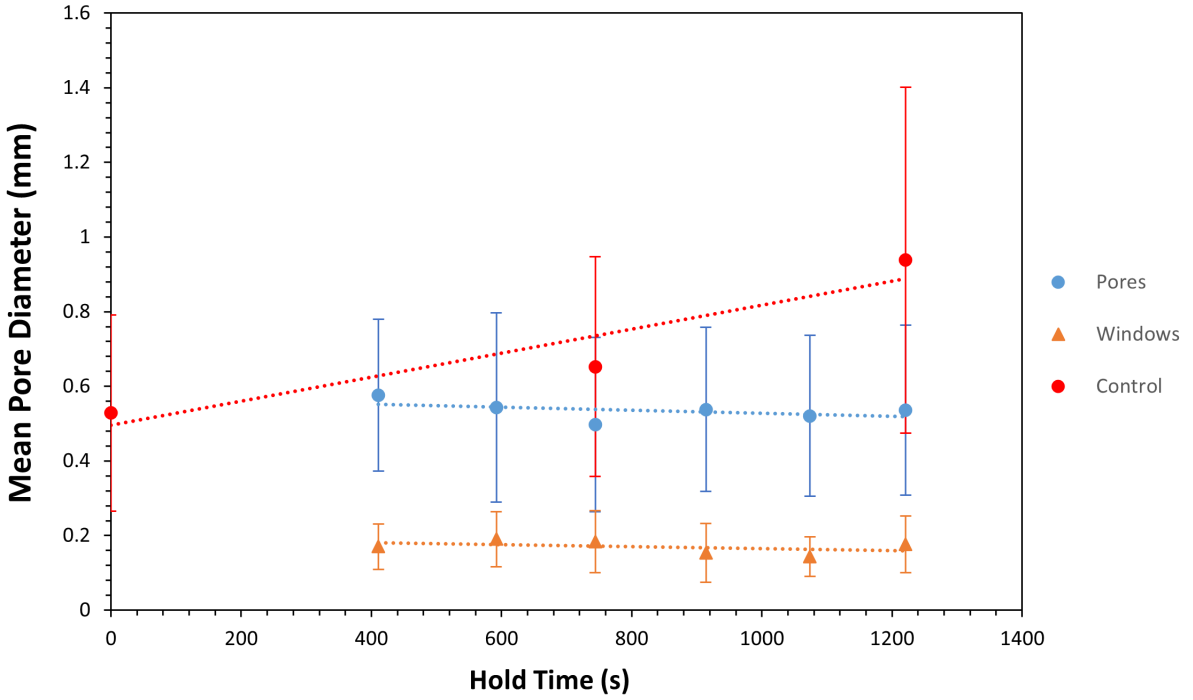

Figure 82: Graph showing pore and window sizes (with interquartile ranges) of dried Ti64 samples against time stored in the ZMorph syringe and in an open container.

$$P_{vap} - P_{liq} = \frac{2\gamma}{R} \tag{17}$$

Where P_{vap} and P_{liq} are the pressure inside (vapour phase) and outside (liquid phase) of the bubble, γ is the surface tension and R is the radius. Under atmospheric conditions the difference between the pressure inside and outside the bubbles within the foamed slurry causes coalescence resulting in instability of the foam, hence why an increase in bubble size over time is observed. The rate of coalescence of bubbles within pure liquids is rapid, to the point where it often appears instantaneous when observed, meaning that pure liquids cannot be foamed [287]. The mixing of a liquid or slurry with a surfactant is well known to increase the capacity for foaming as well as the stability of the bubbles within the foamed mixture by reducing the rate of coalescence to an order

of minutes rather than seconds, as is observed within the foamed slurry presented in this work. Interestingly, no meaningful difference in porosity was observed within the control samples over the 20 minutes despite the clear increase in pore size. This suggests that whilst bubbles clearly coalesced over that time to form larger pores, the slurry still remained stable in terms of the bubbles being retained within the slurry rather than rising to the surface and bursting which would result in an observed reduction in porosity due to air being released from the slurry.

As can also be seen in Figure 82, for the samples obtained from the foamed slurry held within the syringe, no difference in mean pore diameter or pore size distribution was observed over the 20 minute time-frame other than typical scatter within the data. Relating this observation to the Young-Laplace equation (Equation 17), it can be explained by the fact that the syringe plunger increases the outside pressure (P_{liq}) hence reducing the pressure difference and surface tension experienced by the bubbles within the slurry. As outlined in Section 3.3.1, after the syringe has been loaded with slurry the plunger is compressed whilst the syringe is held upside down in order to expel excess air. This plunger force increases the pressure on the slurry within the syringe, and whilst this pressure is not enough to cause slurry to be extruded from the nozzle, it does appear to have a beneficial impact on the stability of the slurry by preventing the coalescence of bubbles. The foamed Ti64 slurry is likely to be stable even beyond the 20 minute time-frame, however even at an extrusion speed of 0.1 ml/s, a full 100 ml syringe load of slurry could be extruded in under this time. These findings are fundamentally important for demonstrating the feasibility of this manufacturing method, as it demonstrates that the foamed slurry is stable for long enough when held within the syringe to be able to extrude all of the material without any decomposition of the slurry occurring. This means that, providing a track and layer based method of deposition can be developed, that a 3D structure could be extruded using up to 100 ml of foamed slurry. It also shows that there is no urgent need to increase the extrusion speed beyond what is typically recommended in order to ensure that all the slurry can be extruded, which would have been the case if the slurry showed signs of instability at a certain time.

4.3 Summary of Foamed Ti64 Slurry Development and Extrusion Testing

The work in this chapter presents the systematic development and optimisation of the foam gel casting process for Ti64, using AM grade powder suspended in a MC solution to create a metal

powder-based slurry which was then mechanically foamed before gelling and drying. The foamed slurry composition and mixing procedure development process discussed in Section 4.1 demonstrates that by carefully controlling various parameters within the process the slurry can be optimised to produce porous samples with specifically tailored properties, as has been demonstrated broadly for ceramic powder slurries within previous studies [226, 230, 231, 236–238, 241], and also for a SS 316L powder slurry [220]. The optimised slurry composition developed in this work produced dried samples containing porous structures that match the requirements outlined in Section 2.9 as being optimal for orthopaedic implant material. The porous structures not only present the required porosity and pore size range values, but also are highly interconnected and even contain exclusively concave surfaces due to the pores being generated by air bubbles, which has been shown to promote bone in-growth within the material compared with flat or convex surfaces [18]. Figure 77 presents the final optimised slurry composition and mixing procedure. The final parameters were selected in order to produce the optimal porosity once a shrinkage factor of 20 % has been applied to account for shrinkage during sintering, and this shrinkage figure was obtained from existing literature. If the actual shrinkage of the samples during sintering is discovered to be a factor different to this in future work, then the information gathered in this section can easily be applied to tweak the slurry in order to maintain the optimal porosity.

The controlled slurry extrusion experiments discussed in Section 4.2 show that the optimised slurry can be extruded through the 2 mm nozzle of the ZMorph thick paste extruder toolhead at a range of speeds both equal to and greater than the typical extrusion speed of this process without having any detrimental impact on the porous structure of the extruded samples. This work also highlighted that this slurry is highly stable over 20 minutes (and possibly even longer), particularly when stored within a syringe with the plunger inserted because the plunger pressure helps to reduce surface tension and therefore bubbles have a lower tendency to coalesce. Overall, the stability of the slurry when stored within the syringe and extruded at various speeds is very promising in terms of being able to progress to extruding full 3D structures with this kind of foamed slurry. This work demonstrates that the AM grade powder used to develop the slurry, whilst being manufactured to have optimal properties for AM processes, is also highly suited to this application because of its ability to pack at high densities due to the sphericity of the powder, contributing the the stability of the slurry.

The mechanical properties of the porous samples produced using this process after sintering have been estimated by comparing against the reported properties of SS 316L samples produced using the same process which presented very similar porosity, and the estimates suggest that this process is able to produce highly porous scaffold material which maintains mechanical properties comparable to those of human cortical bone. These mechanical properties are superior to those reported in literature for Ti64 with similar levels of porosity manufactured using different processes, which suggests that this process is ideal for the production of porous Ti64 orthopaedic implant material due to being capable of producing optimal porous structures which maintain sufficient mechanical stability for load-bearing applications.

Having optimised the foam gel casting procedure for Ti64 to produce the desired level of porosity for orthopaedic implants, and demonstrated the high stability of the foamed slurry both over time as well as when extruded through a syringe nozzle, the next important phase of this work was to assess and enhance the properties of the slurry for 3D material extrusion. As such, Chapter 5 focuses on optimising the slurry composition in order to increase its suitability for 3D material extrusion, particularly in terms of balancing viscosity with slurry stability and green strength of the dried samples.

5 Chapter 5: Results & Discussion Part II - Optimisation of Slurry Composition for 3D Printing by Material Extrusion

A key aspect to the development of the 3D extrusion process in this work was the *printability* of the foamed slurry, which refers to the ability to extrude stable, continuous individual tracks that merge effectively and so can then be deposited in a specific pattern to form full continuous layers that can be built up into 3D structures which are stable and contain a uniform porous structure. The focus of the work presented in Sections 4.1 & 4.2 was optimising the composition of the Ti64 slurry in order to produce optimal levels of porosity, and also demonstrating the stability of the foamed slurry when extruded through a nozzle. However, in order to be able to deposit multiple tracks and layers that produce continuous 3D foams that are free from defects, the individual extruded slurry tracks themselves must be stable and continuous. Therefore the aim of this section of experimental work was optimising the composition of foamed powder-based slurry in order to be able to achieve this.

Observations from the slurry composition development work regarding the flow of the foamed slurry when transferring into moulds highlighted concerns about the feasibility of building 3D structures by depositing single tracks to form full layers. Observations of the initial single tracks deposited using the previously optimised Ti64 foamed slurry highlighted that the tracks were irregular in their geometry (track width and height), and even contained numerous points of discontinuity where no slurry was deposited resulting in breaks in the tracks. These issues in the single tracks were simply exacerbated when tracks were multiplied to form full single layers and then several successive layers, leading to significant defects and observable separation between tracks and layers within the resulting 3D structures, as presented in more detail in Sections 6.2.1 & 6.3.1.

5.1 Ti64 Slurry Viscosity Measurements

By simply observing the flow of the optimised Ti64 powder slurry after mixing/whisking it was clear that the slurry had a high viscosity. This high apparent viscosity caused issues with loading the syringe as it was not possible to pour the foamed slurry out of the container it was mixed in, but rather the slurry had to be manually scooped and transferred into the syringe. This process

made it difficult to ensure that there was no additional entrapped air within the syringe, and despite following the procedure outlined in Section 3.3.1 it was still likely that pockets of trapped air remained within the slurry when loaded within the syringe. As mentioned in Section 2.6.7, there is a recommended viscosity range when extruding material with the ZMorph thick paste extrusion toolhead and syringe of $20,000-70,000\ mPas$. Therefore, it was important to quantify the viscosity of the optimised Ti64 slurry in order to assess whether the apparent high viscosity was the cause of the issues with track irregularities/defects during extrusion. The viscosity was measured using the adapted setup as presented in Section 3.4.2 in order to reduce the powder consumption, which provides *repeatable* measurements but not necessarily 100 % *true* measurements. These viscosity values, along with all the viscosity measurements obtained for the various slurry compositions, are summarised and corrected against a baseline 'low-viscosity' slurry in Table 10, which was measured using both the correct and adapted setups in order to provide a baseline against which the rest of the results obtained using the adapted setup could be compared.

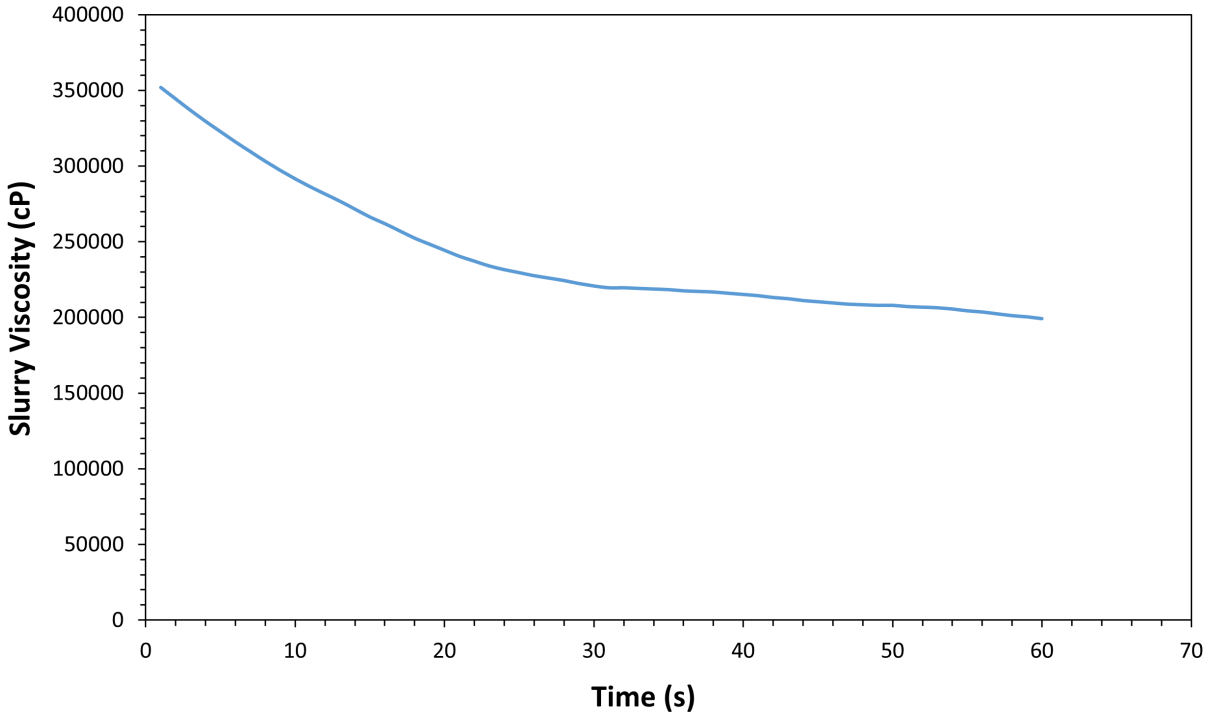

Figure 83: Graph showing viscosity of optimised Ti64 foamed slurry against time, measured using the adapted setup for the Brookfield viscometer at a rotational speed of 1.5 RPM and using the LV-4 spindle.

Figure 83 presents the measured viscosity of the optimised Ti64 foamed slurry over 60 seconds. As explained in Section 3.4.1, when measuring the viscosity of a slurry containing suspended particles, the particles tend to migrate away from the rotating spindle over time. This is observed in the results shown in Figure 83 as the viscosity steadily decreases over the 60 second interval. For this reason, the main value of interest was the 'initial' viscosity (i.e. the very first measured viscosity value), which in this case was $352,000\ cP$. This viscosity measurement confirms the initial concerns raised about the high viscosity of the slurry. The corrected viscosity value for the initial optimised Ti64 slurry was $246,154\ cP$, as presented in Figure 10. Therefore it was clear that the viscosity of the initial optimised Ti64 foamed slurry was too high and significantly above the recommended range for extruding material with the ZMorph thick paste extrusion toolhead and syringe. The issues with the deposited tracks showed that the high viscosity of this slurry prevented it from flowing continuously from the syringe nozzle and forming tracks with regular geometry. It was therefore important to focus on altering the composition of the slurry in order to reduce viscosity and ultimately be able to deposit stable and continuous tracks, which could then be used as the building blocks to deposited multi-layer structures.

As such, the focus of the next phase of the research was investigating what within the composition of the optimised Ti64 powder slurry caused it to have such a high viscosity, and also therefore to explore what aspects of the composition of a metal powder slurries in general have an influence on the viscosity of the slurry. The literature covering the gel casting process, including foam gel casting, reviewed in Section 2.6 highlights that various slurry composition parameters can affect viscosity including powder size, solid loading (volume fraction) and gelling agent concentration. Therefore, the composition parameters that were investigated in this work included; powder size, dispersant addition quantity, choice of specific chemical dispersant and the powder volume fraction used to calculate quantities of each of the slurry components. The high stability of the foamed optimised Ti64 slurry, as well as the strength of the dried samples and their internal porous structures, were all highlighted as being optimal for this application in Chapter 4. Therefore, it was important when optimising the slurry viscosity for extrusion from the syringe to maintain these properties as much as possible.

5.1.1 Investigating the Effect of Powder Size on Slurry Viscosity

The AM grade Ti64 powder described originally in Section 3.1.1 was the only Ti64 powder available for this work, due to the high cost of the material. However, a selection of SS 316L powders were available, as outlined in Section 3.1.2, which provided a range of powder size distributions that could be used to investigate the effect of powder size on slurry viscosity. The previously described powders are referred to as 'fine non-AM grade', '$\sim 50\ \mu m$ AM grade' and '$\sim 100\ \mu m$ AM grade'. The particle size distributions for each powder are presented in Figure 50 and Table 5, and the particle shape for each can be observed in Figure 49. Foamed slurries were produced using each of these three powders, following the same method outlined for the Ti64 powder slurry in Section 3.2. Table 8 presents a summary of the basic compositions the slurries produced using each of these powders. At this stage the dispersant and surfactant were added using the same ratios as the Ti64 powder slurry, which were 1.5 $wt\%$ of the powder mass and 1.5 $vol\%$ of the MC solution respectively. Also, each of the SS powder slurries were whisked for 2 minutes. Figure 84 presents the measured viscosity of the foamed slurries produced using each of the 3 grades of SS 316L powder over 60 seconds. The initial measured value for each slurry was $29,840\ cP$, $125,200\ cP$ and $136,400\ cP$ for *powders a, b* and *c* respectively.

		Grade of SS 316L powder used		
		Powder a - fine non-AM grade	**Powder b** - $\sim 50\ \mu m$ AM grade	**Powder c** - $\sim 100\ \mu m$ AM grade
	Calculated Packing Fraction Range	$0.45 - 0.6$	$0.57 - 0.63$	$0.55 - 0.63$
Slurry Composition	Volume Fraction	0.45	0.57	0.55
	2 % MC Solution Volume (ml)	13.75	10.75	11.25
	Powder Mass (g)	90	114	110
	Darvan 7-N Dispersant Volume (ml)	1.35	1.7	1.65
	Triton X-100 Surfactant Volume (ml)	0.2	0.16	0.17

Table 8: Table summarising slurry compositions produced using different grade of SS 316L powder.

The results presented in Figure 84 show that the size of the powder particles used to create a

slurry has a significant impact on its viscosity. The initial viscosity of the slurry produced with SS 316L *powder a*, which has median particle diameter of 7.2 μm, was $29,840$ cP. The median diameter of *powder b* was measured to be 28.7 μm, which is only a relatively small increase from *powder a*, however this difference resulted in an significant increase in the initial viscosity which was measured to be $125,200$ cP. *Powder c* has a much greater median particle size of 76.4 μm, however only resulted in a small increase in initial measured viscosity of $136,400$ cP. This data suggests that increasing powder particle size causes an initially significant increase in viscosity, but further increase in particle size has a lesser impact on viscosity. It is difficult to draw concrete conclusions with only 3 different powder sizes to compare, although it is clear that powder size has an observable impact on slurry viscosity and particularly that reducing the particle size can be a highly effective way to decrease slurry viscosity. As discussed in Section 2.6.5, Li et al. [218] also observed when mixing iron powder slurries using powders with average diameter of 3 μm and 30 μm that the larger powder size resulted in higher viscosity of the slurry. The slurries produced by Kennedy and Lin [220] which used SS 316L powder with an average diameter of 9 μm, whilst not being foamed, showed excellent stability with both 2 and 4 $wt\%$ MC solution at high volume fractions of 50 and 60 %.

The evidence from the literature along with the observations from this work regarding powder size and slurry viscosity collectively suggests that it is optimal, when mixing metal powder slurries, to use powder with an average diameter $<$ 10 μm in order to achieve relatively low viscosities whilst maintaining high slurry stability. This appears to provide a straightforward solution to the issue of very high foamed Ti64 slurry viscosity, however the volatility of Ti64 presents complications. Titanium powder has a high risk of spontaneous combustion due to oxidation, and even powders around 50 μm in size have to be handled carefully. Fine powder of $<$ 10 μm particle size would have to be handed in an inert atmosphere, and would therefore be unsuitable for this process. Also, because of the extreme volatility of very fine Ti64 powder it is difficult to source. It is possible to purchase AM grade Ti64 powder at $<$ 25 μm, which may produce better results in terms of slurry viscosity, however even with this slightly reduced powder size it is likely that further slurry composition optimisation would be required in order to achieve a suitable viscosity for this application.

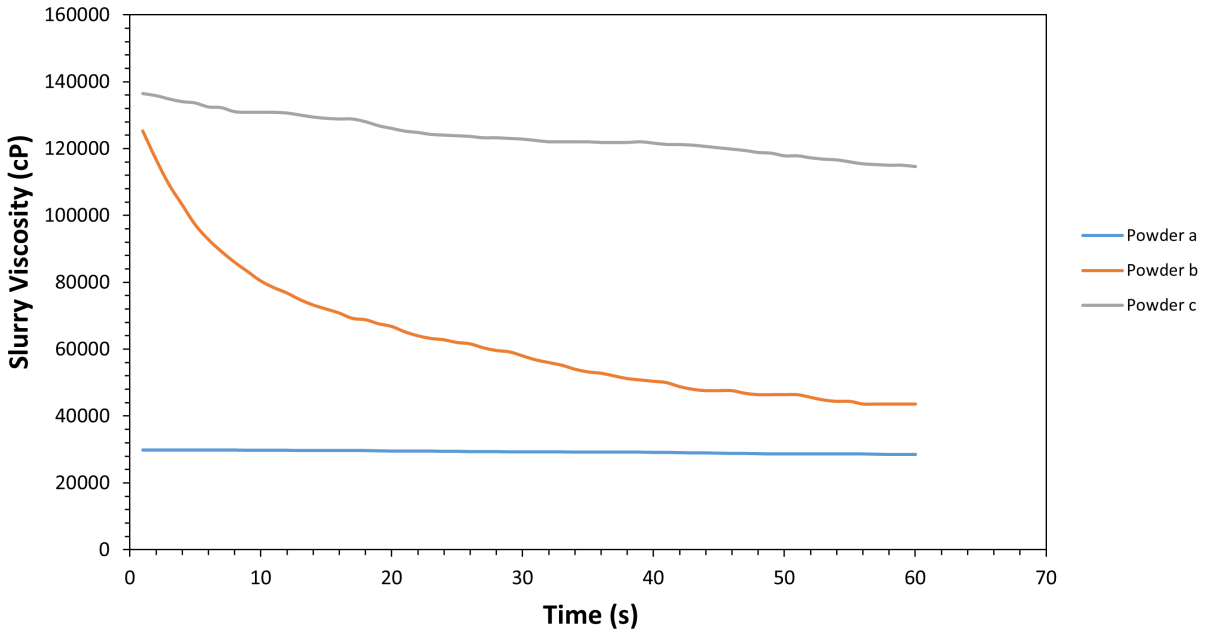

Figure 84: Graph showing viscosity against time for slurries produced using different SS 316L powders, measured using the adapted setup for the Brookfield viscometer at a rotational speed of 1.5 RPM.

5.1.2 Investigating the Effect of Dispersant Addition on Slurry Viscosity

The effect of dispersant addition on slurry viscosity was also investigated, for both AM grade Ti64 powder slurries and AM grade SS 316L powder slurries. Initially, the dispersant addition for the optimised Ti64 foamed slurry was increased from the existing addition of 1.5 $wt\%$ in 0.5 $wt\%$ intervals. The rest of the slurry composition parameters were kept constant as outlined in Figure 77. Viscosity was measured following the same methods as previously outlined, and Figure 85 shows the initial measured viscosity values for each $wt\%$ dispersant addition.

For comparison, the dispersant addition was also varied within the SS 316L *powder b* slurry, as this powder has very similar size and geometry to the Ti64 powder used. As the viscosity of this slurry was already significantly lower than the Ti64 slurry, rather than simply increasing the dispersant addition, it was both increased and decreased by intervals of 0.5 $wt\%$. As well as the volumetric quantity of dispersant being varied, the impact of using an alternative dispersant was also examined within the Ti64 foamed slurry. Dispex AA 4040 (BASF - Formulation Additives, Germany) was applied as a dispersant instead of Darvan 7-N. Dispex AA 4040 is a solution of

an ammonium salt of an acrylic polymer in water, and is typically used for the dispersion of pigments within paint solutions. Like Darvan 7-N it is defined as an anionic dispersant, and the two dispersants have a similar composition and behave in similar ways. Foamed Ti64 slurries were produced with a few different $wt\%$ additions of the alternative dispersant. Figure 86 compares the initial viscosity measurements for foamed Ti64 and SS 316L slurries with various Darvan 7-N dispersant additions, as well as the foamed Ti64 powder slurries with various additions of Dispex AA 4040 as an alternative dispersant.

There is limited literature that covers the impact of dispersant addition on slurry viscosity, or comparing different types of dispersant and how efficient they are at dispersing different powders. However, Kennedy and Lin examined the influence of dispersant addition on viscosity of SS 316L powder slurries at different powder volume fractions and gelling agent solution (in this case MC) concentrations [220]. The dispersant used in their work is the same as what was used in the development of the initial optimised Ti64 slurry composition in this work, Darvan 7-N. Figure 41 (Chapter 2) is taken from their work and shows that the increased addition of dispersant as a $wt\%$ of powder mass within the slurry resulted in a decrease in viscosity. For 2 % MC concentration slurries with high volume fractions of 0.55 and 0.6 (referred to as 55 % and 60 %), the initial increase in dispersant addition from 0 to 1 $wt\%$ resulted in significant reductions in viscosity, and then up to 2.25 $wt\%$ they observed further reductions but at a reduced rate. This suggests that for metal powder slurries with high powder volume fractions, as in this work, the addition of dispersant is essential for controlling viscosity, however there may be a limit on how much viscosity can be reduced solely by increasing dispersant addition. Therefore it was important to explore and understand the impact of dispersant addition on the Ti64 powder slurry developed in this work, and whether it could be used to control viscosity and produce a slurry more suitable for extruding through a nozzle to produce stable continuous tracks.

Figure 85 shows the graph of initial foamed slurry viscosity of Ti64 slurries mixed with various dispersant additions. The relationship observed is similar to that presented by Kennedy and Lin [220] in that increasing dispersant addition resulted in a decrease in viscosity, but the rate of decrease reduces at higher dispersant additions. The dispersant addition was increased from the initial amount of 1.5 $wt\%$ rather than from 0 $wt\%$ as the previously optimised slurry contained this dispersant addition but presented a very high viscosity, and therefore the aim was to see if viscosity

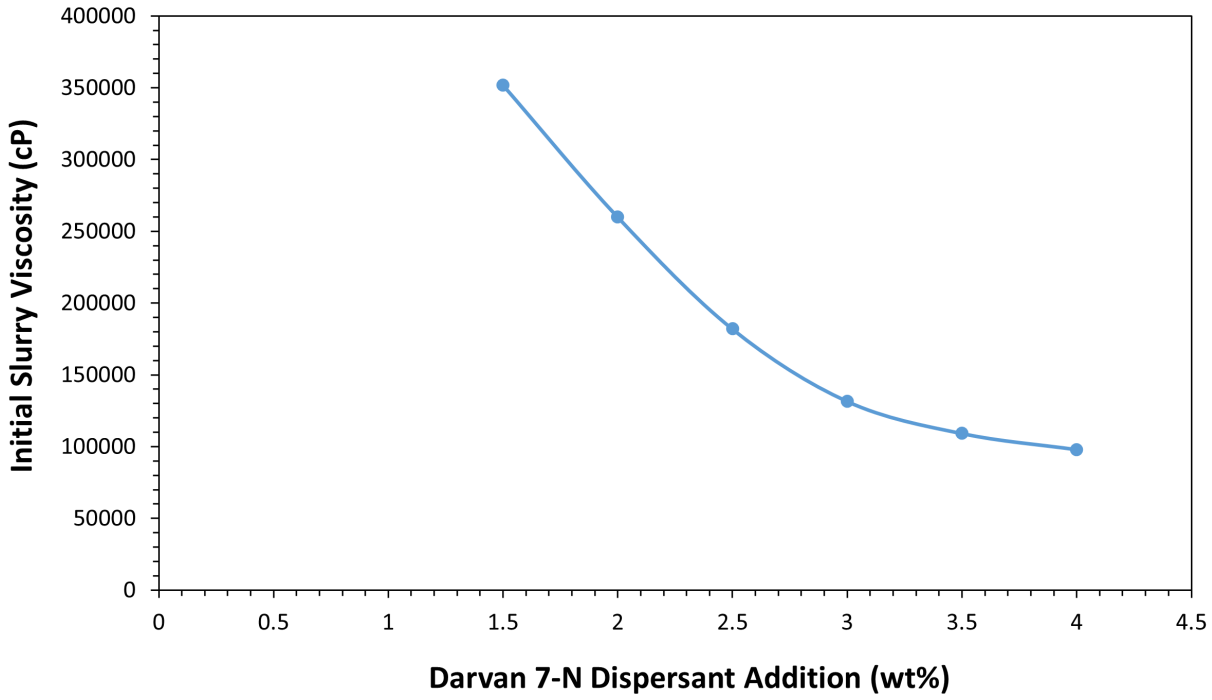

Figure 85: Graph showing 'initial' viscosity values of foamed Ti64 powder slurries mixed with various dispersant additions.

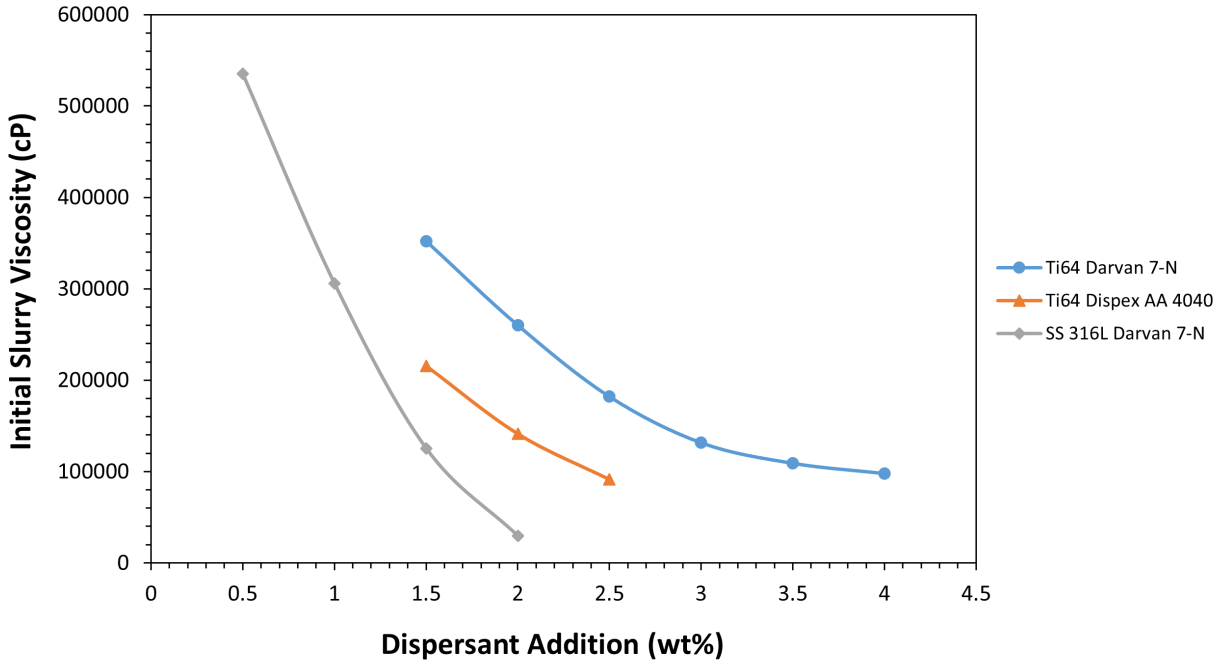

Figure 86: Graph showing initial viscosity values of foamed Ti64 and SS 316L powder slurries with various additions of Darvan 7-N or Dispex AA 4040 dispersants.

could be reduced by increasing dispersant addition. Whilst increasing the dispersant addition clearly reduced the measured viscosity of the foamed Ti64 powder slurry, there was observed to be a limit that the values approached which of around $100,000\ cP$. Also, as highlighted in Section 5.2.1, the higher dispersant additions of 3.5 and 4 $wt\%$ produced dried samples which were unstable and collapsed upon removal from the moulds, making them unsuitable for this application. The slurry produced with a 2.5 $wt\%$ dispersant addition was the greatest addition which still produced a suitably stable dried sample, but the initial viscosity of this slurry was $182,000\ cP$ which was still too high.

Figure 86 compares the impact of dispersant addition on the viscosity of both the AM-grade Ti64 powder slurry and the AM-grade SS 316L powder slurry (SS 316L *powder b*). Altering the dispersant addition within the SS 316L powder slurry had a more significant impact on the viscosity than it did for the Ti64 powder slurry. Increasing the addition to just 2 $wt\%$ reduced the viscosity of the foamed slurry down to $29,360\ cP$, although as highlighted in Section 5.2.1 this slurry produced samples that had inadequate stability when dried. The reason for the difference observed between the impact of dispersant addition on the Ti64 and SS 316L powder slurries is not clear, particularly because, as previously discussed, the size distribution, geometry and packing fraction of the powders are all very similar. The only major difference between them is the bulk density of the materials (4.5 g/cc for Ti64 and 8 g/cc for SS 316L). Initially it was assumed that the higher density of the SS 316L powder would make it more difficult to disperse within a slurry, however the results presented clearly show that the SS 316L powder produces lower viscosity slurries than the Ti64 when the slurries have the same composition. The difference in bulk density does however mean that for the same $wt\%$ addition of dispersant a greater volume of dispersant is added for the SS 316L slurries. This is due to the fact that the powder addition is based on volume which is converted into a mass as outlined in Section 3.2.1, and therefore a greater mass of SS 316L powder is added to a slurry than to a Ti64 powder slurry with the same VF. In order to draw a more accurate comparison between the impact of dispersant addition on Ti64 and SS 316L powder slurries the $wt\%$ additions were converted into $vol\%$ additions and Figure 86 was plotted again for $vol\%$ instead (Figure 87). Plotting the data in this way shows that the initial rate at which viscosity decreases with dispersant addition is similar for both SS 316L and Ti64 powder slurries, however beyond $12-13\ vol\%$ the viscosity of the SS 316L slurry continued to decrease whereas the Ti64 slurry

remained fairly constant at a higher value.

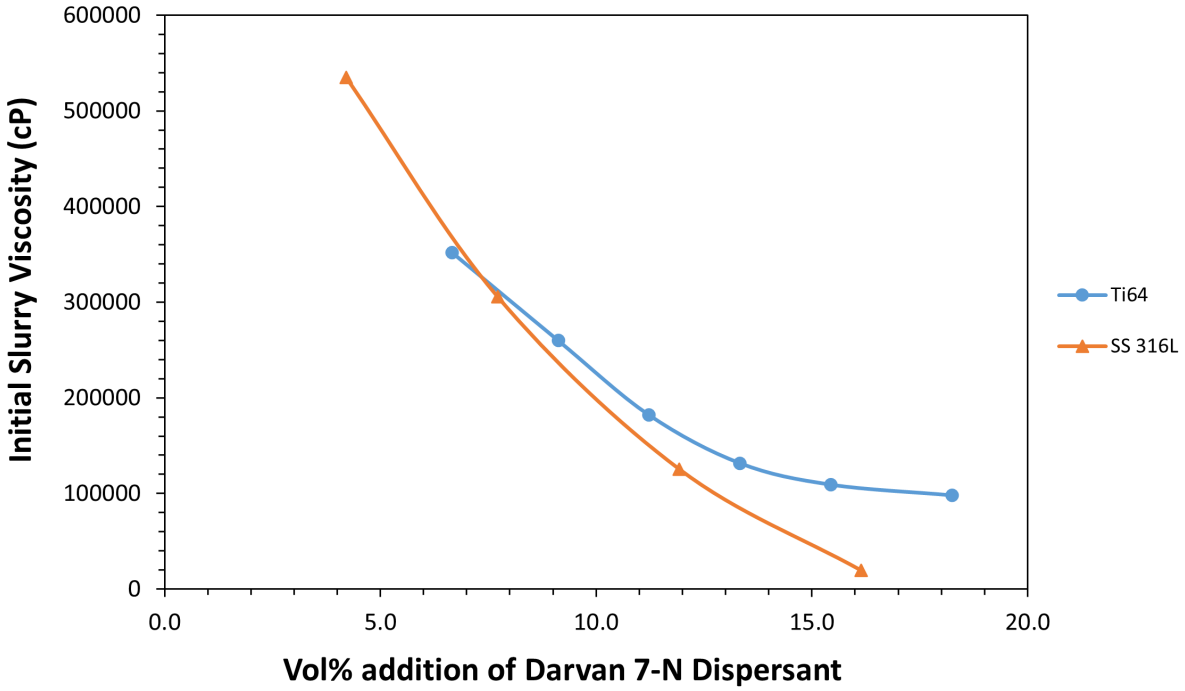

Figure 87: Graph comparing vol% addition of Darvan 7-N dispersant on the viscosity of foamed Ti64 and SS 316L powder slurries.

These experiments show that the Darvan 7-N dispersant appears to be more effective at dispersing SS 316L powder than Ti64 powder, and as a result slurries with lower viscosity can be achieved when using SS 316L powder than Ti64 powder slurries with the same composition. As outlined in Section 2.6.3, there is an understanding that certain dispersants are more effective than others at dispersing powders within slurry suspensions, which is likely to be linked with the pH of the slurry and how this interacts with the charge of the powder particles. Despite this however, there is very limited information available in existing literature comparing the effectiveness of different dispersants for producing metal powder slurries, and as such there is clear scope for work to be done in this area. Due to time and resource limitations within this research an extensive comparison of a variety of dispersants could not be conducted, however one alternative dispersant (Dispex AA 4040) was selected to produce foamed Ti64 slurries. The viscosity of the slurries produced with different $wt\%$ additions of this dispersant are also presented in Figure 86. Using this dispersant did result in a slight decrease in slurry viscosity for all $wt\%$ additions, however the viscosity of the slurries was still high, and as highlighted in Section 5.2.1 the stability of all the dried samples

produced from these slurries was insufficient.

Overall, altering the dispersant addition by itself was not able to produce foamed Ti64 slurries with suitable viscosities for extrusion. These experiments demonstrated that for both SS 316L and Ti64 powder slurries, it is possible to add up to around 12 $vol\%$ (corresponding to 1.5 $wt\%$ and 2.5 $wt\%$ for SS 316L and Ti64 respectively) Darvan 7-N dispersant and still produce suitably stable dried samples, but any increase beyond this has a detrimental impact. As a result, the lowest viscosity of Ti64 slurry achievable by increasing dispersant addition was $182,000$ cP and $125,200$ cP for SS 316L slurry. These viscosity values are still above the desired range for material extrusion using the ZMorph paste extruder toolhead, therefore alternative methods of reducing viscosity were explored.

5.1.3 Investigating the Effect of Powder Volume Fraction on Slurry Viscosity

As highlighted in Section 2.6.4, it is well documented that reducing the volume fraction (VF) used to calculate the ratios of powder to gelling agent solution when mixing a powder-based slurry (often referring to as 'solid loading' of the slurry), results in a decrease in the viscosity of the slurry. The VF values used when mixing the previous slurries had all been relatively high as a result of these values being selected using the calculated packing fractions for the individual powders which are greater than the values typically used for producing slurries using non AM-grade powders. This is likely to be a heavily influential factor in determining the viscosity of the slurries. A volume fraction of 0.57 was used for mixing slurries with both the AM grade Ti64 powder and the AM grade SS 316L powder with similar properties (*powder b*). Slurries were therefore mixed with both of these powders but using a VF of 0.5, with all the other quantities being calculated following the same method as outlined in Section 3.2.1. The only other value that was altered was the addition of Darvan 7-N dispersant which was increased to a 2.3 $wt\%$ addition for the Ti64 powder slurry only, so that the actual volume of dispersant added would be the same as the volume added to the reduced VF SS 316L slurry. The viscosities of these reduced VF foamed slurries were measured, and Table 9 presents the initial measured values, along with the initial viscosity values for the original foamed slurries with a VF of 0.57.

The data presented in Table 9 agrees with the information available in the literature that a higher ratio of powder to gelling agent solution results in a greater slurry viscosity. However, the

	Ti64 Powder		SS 316L Powder	
Volume Fraction	0.5	0.57	0.5	0.57
Initial Slurry Viscosity (cP)	176,000	352,000	44,960	125,000

Table 9: Measured initial viscosity values for Ti64 and SS 316L powder foamed slurries mixed using different VF values.

data also presents the same challenge highlighted in the dispersant addition experiments which is that the reduced VF Ti64 powder slurry still had a high measured initial viscosity value of $176,000\ cP$. Even with the combination of a reduced VF and increased dispersant addition it was not possible to create a foamed Ti64 powder slurry with a suitably low viscosity. However, the reduced VF SS 316L slurry had an initial measured viscosity of $44,960\ cP$ which is within the highlighted optimal range and, as described in Section 5.2.3, the stability of the resulting dried samples was sufficient in order to be easily removed from the mould and handled. This composition of SS 316L powder slurry was therefore highly significant as it was the only slurry which presented a viscosity within the desired $20,000 - 70,000\ cP$ range whilst also producing suitably stable dried samples. This slurry composition was selected, along with the Ti64 slurry with reduced VF and increased dispersant addition, for further stability and extrusion testing.

5.1.4 Foamed Slurry Viscosity Correction

As discussed in Section 3.4.2, an adapted viscometer setup was used when measuring slurry viscosity in order to reduce consumption of powder whilst still being able to draw direct comparisons between different slurries. In order to evaluate the 'true' viscosity measurements obtained for the various foamed slurry compositions using the adapted viscometer setup (shown in Figure 56), a viscosity measurement was taken for one of the slurries using the correct viscometer set-up (Figure 56a) to provide a baseline comparison between the two viscometer set-ups which could then be used to provide an estimate for what the true viscosity would be for each of the other slurries. The foamed slurry selected to provide the baseline measurement was the SS 316L slurry with a VF of 0.5 as this was the slurry with the lowest measured initial viscosity using a powder that closely matches the AM grade Ti64 powder in terms of morphology. The true initial viscosity for this slurry was

measured to be $31,360\ cP$ at a spindle speed of 1.5 RPM (as previously used), which gives a ratio of measured viscosity to true viscosity of 1.43 : 1. Interestingly, this same comparison was measured for a 2 $wt\%$ MC solution which gave measured and true viscosities of 396 cP and 276 cP, which also gives the ratio of 1.43 : 1. This ratio was then used to estimate values for true viscosity of each of the slurry compositions that were of particular interest, and the resulting values are presented in Table 10. The accuracy of these 'true' viscosity values cannot necessarily be fully relied upon, apart from the value for the specific that was actually measured correctly. However, having a true measured value for the selected SS powder slurry, as well as the adapted set-up measurement value, allows comparisons to be made between the various other slurries that were measured using the adapted set-up whilst significantly reducing the quantity of powder that would have been consumed if all the slurry viscosities were measured using the recommended viscometer set-up (Section 3.4.2).

Powder	**SS 316L**		**Ti64**			
Volume Fraction	0.5	0.57	0.5	0.57	0.57	0.57
Dispersant Addition	1.5 wt% Darvan 7-N	1.5 wt% Darvan 7-N	2.3 wt% Darvan 7-N	1.5 wt% Darvan 7-N	2.5 wt% Darvan 7-N	2.5 wt% Dispex AA 4040
Measured Viscosity (cP)	44,960	125,000	176,400	352,000	182,000	91,200
True Viscosity (cP)	31,360	-	-	-	-	-
Estimated True Viscosity (cP)	-	87,413	123,357	246,154	127,272	63,776

Table 10: Summary of measured viscosity values and estimated true viscosity values for key foamed slurry compositions.

5.2 Stability of Slurries with Reduced Viscosity and Resulting Dried Samples

It was highlighted in Section 4.2 that the initial optimised Ti64 foamed slurry presented high stability over a duration of at least 20 minutes, particularly when stored within the ZMorph thick

paste extruder syringe. Also, as mentioned in Section 4.1 the green strength of the extruded samples once dried is sufficient to allow them to be easily removed from the moulds and handled without crumbling or collapsing. The foamed slurry stability, as well as the green strength of dried samples, were analysed for the various slurry compositions where viscosity had been reduced, in order to understand the impact of the changes in composition on the stability of the slurry/dried samples. The results from the syringe hold time and extrusion speed experiments for the selected slurries with altered compositions are presented in this section, along with the observations regarding the stability of the dried samples. As highlighted in Section 4.2.3, no variation was observed in measured pore size or porosity of samples produced by extruding the initial optimised Ti64 slurry from the syringe after being held for up to 20 minutes. It was assumed that the viscosity of the Ti64 slurry, whilst causing issues with extrusion of stable tracks, may be the reason for the impressive stability of this slurry composition. Therefore, it was important to identify the impact of any composition alterations that resulted in a reduced slurry viscosity on the stability of the slurries.

5.2.1 Stability of Foamed Slurries with Increased Dispersant Addition

For the Ti64 slurries with increased $wt\%$ Darvan 7-N dispersant additions, the stability of the dried samples was initially analysed by simply examining them seeing if they could be removed from the moulds and handled without disintegrating. All the samples produced from slurries with up to 2.5 $wt\%$ were easily removed from the moulds and remained intact (Figure 88a). The 3 $wt\%$ dispersant sample experienced some crumbling and left behind a layer of disintegrated sample within the mould, and the 3.5 $wt\%$ and 4 $wt\%$ samples collapsed whilst drying and completely disintegrated into a powder when removed from the moulds (Figures 88c & 88d). It has been shown in previous studies that increasing dispersant concentration beyond the optimal point leads to a reduction in stability of the foamed slurry and an increased rate of sedimentation of the powder [225, 234]. Therefore, it seems logical that the green strength of the dried samples would also be detrimentally affected, as demonstrated in this work. Also, excessive addition of dispersant to the slurry will affect the concentration of the MC solution by increasing the liquid content, and it is well understood from literature that the green strength of dried samples is impacted by the gelling agent concentration [288]. It may also be the case that the dispersant chemically impacts the gelling process, which could explain the low green strength of the high dispersant addition samples. All

the Ti64 samples produced from slurries using Dispex AA 4040 dispersant instead of the original Darvan 7-N dispersant were quite weak in comparison, and proved difficult to remove from the mould without crumbling occurring. The samples produced from 1.5 $wt\%$ and 2 $wt\%$ retained some structure once removed from the mould, as shown in Figure 88b, however the 2.5 $wt\%$ sample could not be removed from the mould without disintegrating. Again, this may be explained by the way in which this specific dispersant interacts with the gelling behaviour of the MC.

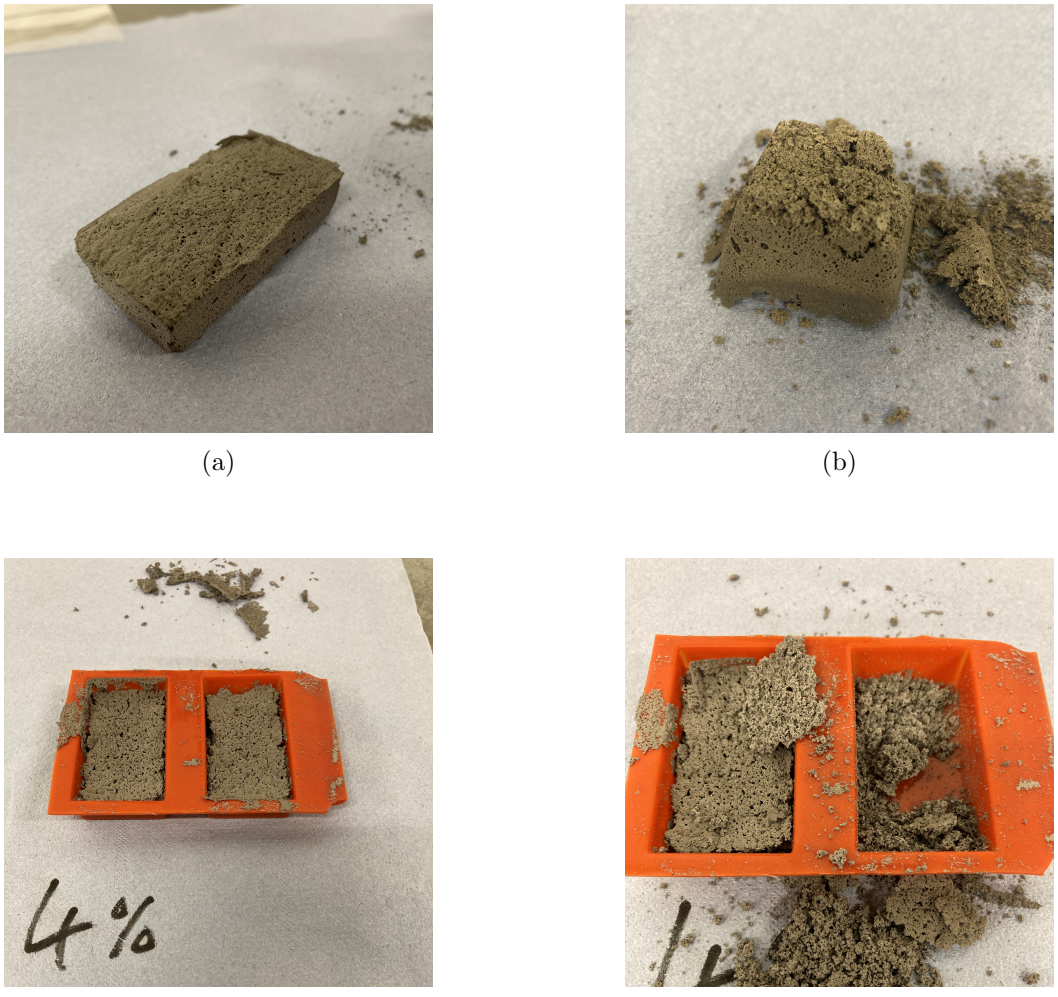

(a) (b)

(c) (d)

Figure 88: Images showing stable dried sample (a) produced from Ti64 powder slurry with 2.5 $wt\%$ Darvan 7-N dispersant addition, weak crumbling sample (b) produced from slurry with 2 $wt\%$ Dispex AA 4040 dispersant addition, and collapsed dried samples (c and d) produced from slurry with 4 $wt\%$ addition

The 2.5 $wt\%$ Darvan 7-N slurry was the lowest viscosity slurry using this dispersant that produced a suitably stable dried sample. The stability of this foamed slurry was investigated further by

completing syringe hold time and extrusion speed experiments as described in Section 3.3, so that it could be compared to the initial optimised Ti64 powder slurry. The results of these experiments are displayed in Figures 89 & 90. These plots show that it was still possible to extrude the slurry mixed with this composition from the ZMorph thick paste syringe at a range of speeds around the typical extrusion speeds without impacting the porous structure of the resulting samples when dried. However, the syringe hold time data (Figure 89) suggests that the stability of this foamed slurry was affected by the increase in dispersant addition. The mean measured pore diameter of the dried samples produced by extruding the foamed slurry after being held in the syringe for up to $800s$ was consistent with the pore sizes measured within the initial control sample. However, the samples produced after the slurry was held for longer than this time period showed an increase in mean pore diameter which suggests that the bubbles within the foamed slurry were beginning to coalesce and the slurry therefore beginning to decompose. These results suggest that this composition would still be suitable for the process of 3D-printing structures by extrusion as long as the build process could be completed with $800s$ of the slurry being whisked and loaded into the syringe. Beyond this, the decomposition of the slurry would be likely to have a detrimental impact on the quality of the 3D-printed structure.

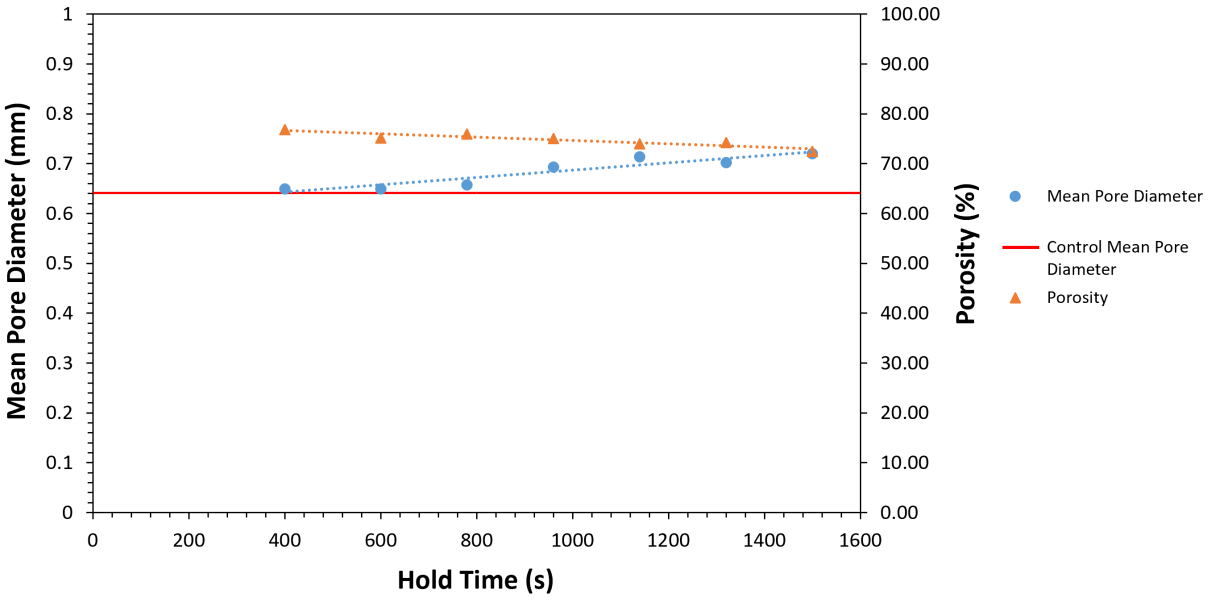

Figure 89: Graph showing porosity and mean pore diameter against time held in syringe, as well as mean pore diameter of a control sample, for Ti64 powder slurry mixed with 2.5 $wt\%$ Darvan 7-N dispersant.

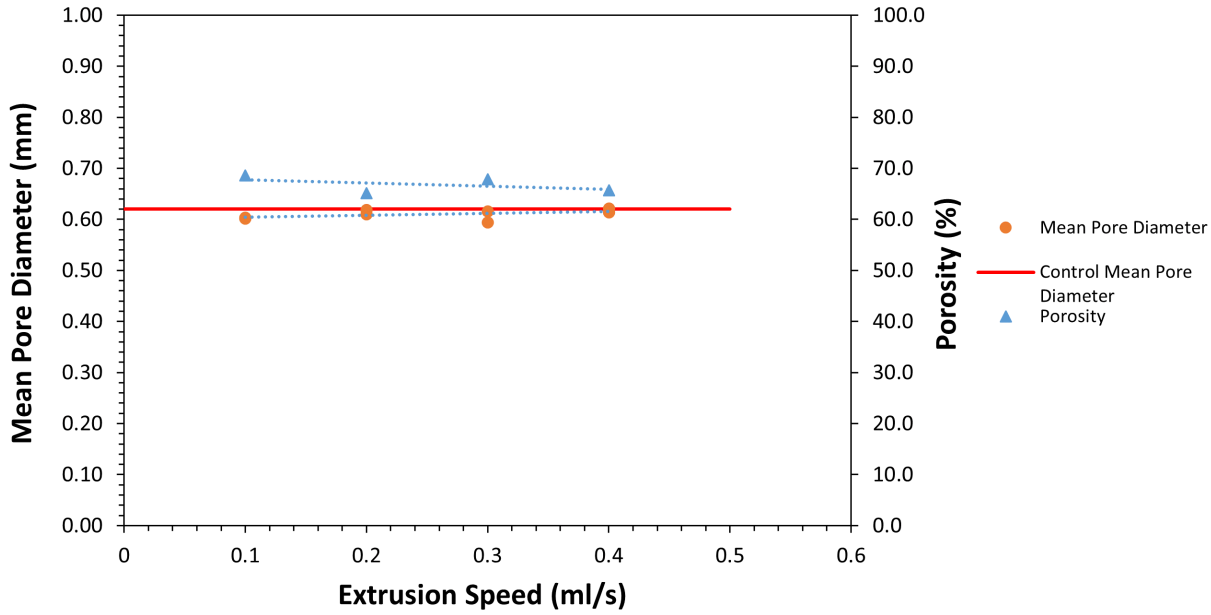

Figure 90: Graph showing porosity and mean pore diameter against syringe extrusion speed, as well as mean pore diameter of a control sample, for Ti64 powder slurry mixed with 2.5 $wt\%$ Darvan 7-N dispersant.

5.2.2 Stability of SS 316L Foamed Slurries

As the AM-grade SS 316L powder (SS powder b) was used produce slurries for viscosity comparison against the AM-grade Ti64 powder slurries, it was important to also be able to compare the stability of the slurries produced with these two powders. The SS 316L powder slurry with the same composition as the highly viscous and stable Ti64 power slurry presented a significantly lower viscosity ($125,200\ cP$ as opposed to $352,000\ cP$). For the samples produced from the different SS 316L powders (*a*, *b* and *c* as described in Table 8), the stability of each was initially examined by analysing the samples upon removal from the moulds after drying. Samples produced using *powders a* (Figure 92a) and *b* (Figure 92b) were easily removed from the moulds once dried and remained intact apart from some very light crumbling around the edges of the bottom surface, whereas the samples produced using *powder c* (Figure 92c) completely disintegrated upon removal from the mould, which again agrees with what has been observed in previous studies that larger powder sizes result in more stable slurry suspensions, which in turn has a detrimental impact on the green strength of the dried samples [218].

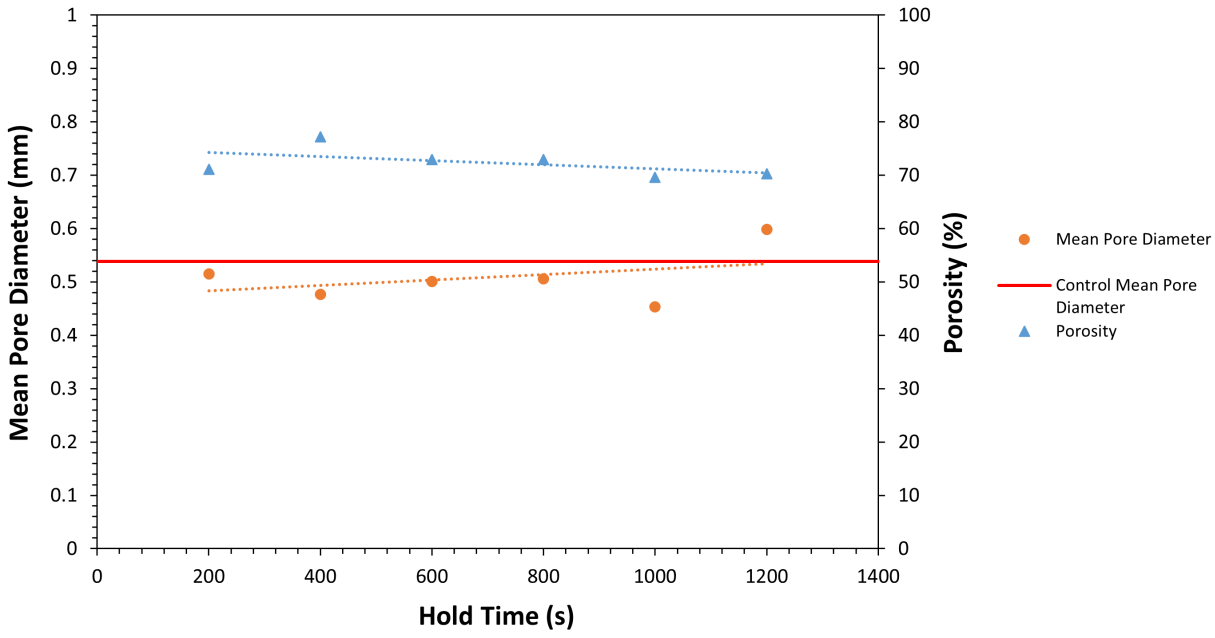

Figure 91: Graph showing porosity and mean pore diameter against time held in syringe, as well as mean pore diameter of a control sample, for SS 316L *powder b* slurry mixed with 1.5 $wt\%$ Darvan 7-N dispersant.

Increasing the Darvan 7-N dispersant addition to 2 $wt\%$ within the SS 316L powder b slurry resulted in an increase in the level of crumbling that was observed when the resulting dried sample was removed from the mould. The green strength of the original SS 316L *powder b* sample with 1.5 $wt\%$ Darvan 7-N dispersant addition was deemed to be sufficient, and so the stability of the foamed slurry itself was analysed by performing a syringe hold time experiment following the same method as described in Section 3.3. Figure 91 shows the average pore size and porosity of the dried samples against the time the foamed SS 316L slurry was held within the syringe before extruding. The results show that the slurry remained fairly stable within the syringe over the 20 minutes it was held. There is a reasonable amount of scatter in the data, however it doesn't show any continuous increase/decrease in the measured pore sizes or porosity of the dried samples suggesting that the structure of the foamed slurry remained consistent over the hold time. The final data point for pore size of the sample extruded after 20 minutes shows a higher value which suggests at this point the bubbles within the slurry may be beginning to coalesce, however prior to this point the pore sizes are reasonably consistent. It can therefore be concluded from this experiment that the foamed SS 316L slurry with the same composition as the initial optimised Ti64 slurry, whilst presenting significantly lower viscosity, is sufficiently stable when stored within the ZMorph syringe for up to at least 15 minutes, which at an extrusion speed of 0.1 mm/s would be more than long enough to extrude a full 100 ml syringe of slurry, if extruding continuously.

(a) (b) (c)

Figure 92: SS 316L powder samples produced from slurries using SS 316L *powders a* (a), *b* (b) and *c* (c) as described in Table 8.

5.2.3 Stability of Foamed Slurries with Reduced Powder Volume Fraction

For both Ti64 powder and SS 316L *powder b*, samples were produced from slurries that were mixed using a reduced powder volume fraction to calculate the ratio of powder to MC solution. The dried samples produced with both powders from slurries with $VF = 0.5$ were sufficiently stable and were cleanly removed from their moulds without any crumbling or disintegration, as can be seen in Figure 93. Syringe hold time experiments were also completed for both of these foamed slurries, and the results are presented in Figures 94 & 95. The Ti64 and SS 316L powder slurry initial compositions were calculated based on a VF that was as close as possible to the packing fraction range for each powder, as previous studies have demonstrated that a greater VF helps to produce slurries and dried samples that are highly stable, as well as reducing the shrinkage that would occur during sintering of the samples [239, 240]. The data presented in Figure 94 for the reduced VF Ti64 slurry presents no significant deviation in pore size or porosity over the 20 minute hold time, which demonstrates that the stability of the foamed slurry was not affected by reducing the powder VF. In contrast, the SS 316L data (Figure 95) shows a clear increase in mean pore diameter with hold time, particularly beyond $600s$, demonstrating that the bubbles within the slurry begin coalescing after around this duration. Before this point there is scatter within the data, but not necessarily enough to suggest that the slurry is decomposing. It can be recommended then that the slurry is suitable for 3D-printing by extrusion providing that the slurry is extruded within $600s$ of being whisked and loaded into the syringe, which presents complications as discussed in Chapter 7.

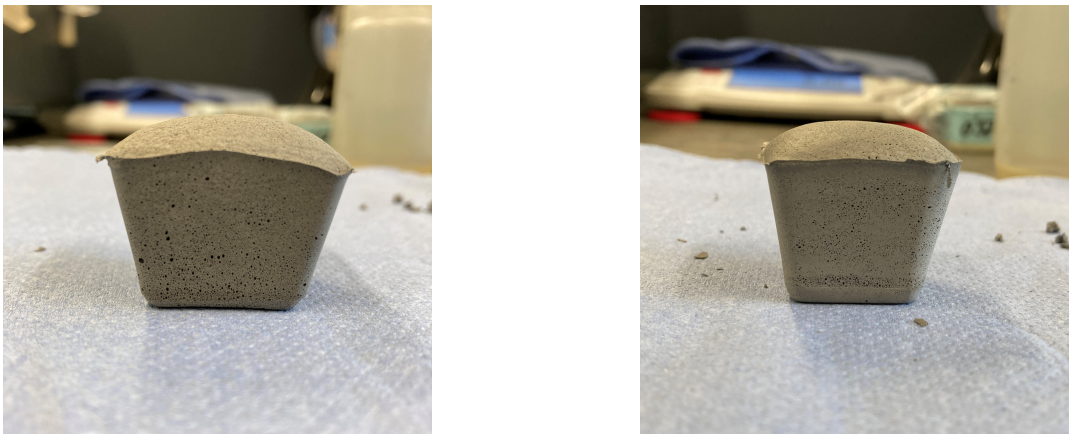

(a) (b)

Figure 93: Dried SS 316L (a) and Ti64 (b) powder samples produced from slurries using a reduced volume fraction of 0.5.

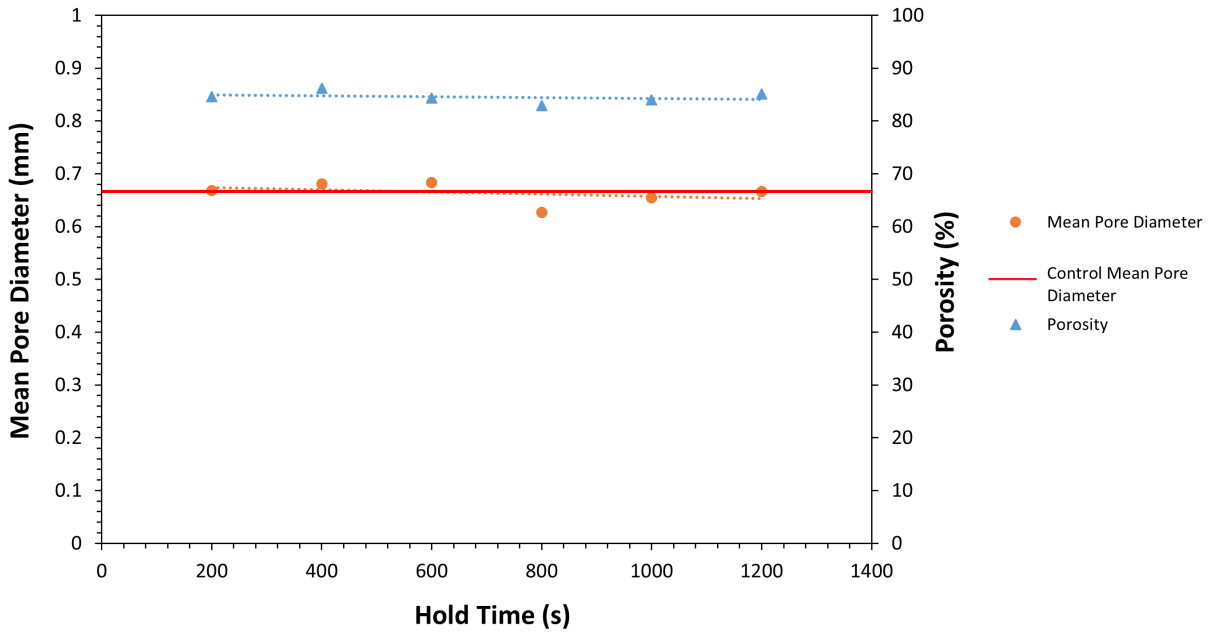

Figure 94: Graph showing porosity and mean pore diameter against time held in syringe, as well as mean pore diameter of a control sample, for Ti64 powder slurry mixed with powder VF of 0.5.

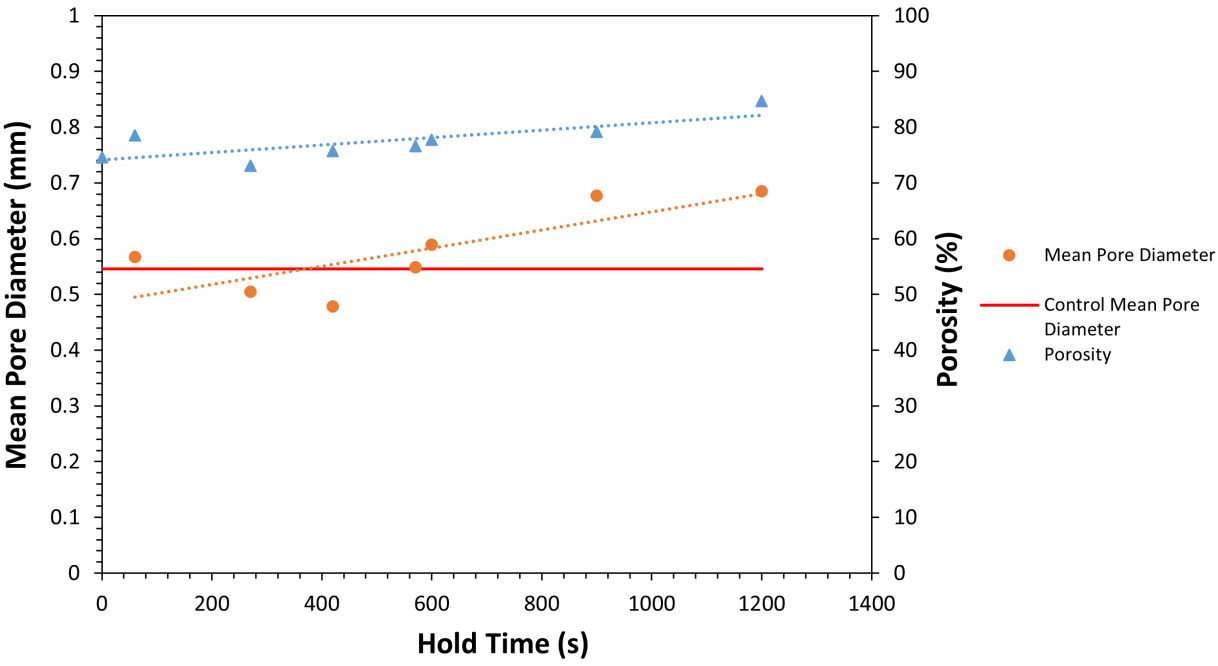

Figure 95: Graph showing porosity and mean pore diameter against time held in syringe, as well as mean pore diameter of a control sample, for SS 316L powder slurry mixed with powder VF of 0.5.

5.2.4 Relating Syringe Compression Force and Slurry Viscosity

The slurry compositions selected for syringe compression force testing were the Ti64 slurry with a VF of 0.57 and the SS 316L slurry with a reduced VF of 0.5, which are defined as 'Ti H' and 'SS L' slurries later in Table 11, as these offer the two extremes with regard to viscosity as presented in Section 9. It had been previously assumed that the viscosity of the powder based slurries was a highly influential factor regarding the ability to extrude stable continuous tracks that can then be built up into full deposited layers of slurry using the the ZMorph thick paste extruder toolhead syringe. Therefore, the extrusion behaviour of each of these key slurry compositions, particularly the compression force required to extrude the slurry through the nozzle, was investigated. Figure 96 presents the force/displacement data for extruded 10 ml samples of each foamed slurry composition, obtained using the methods outlined in Section 3.3. For each slurry composition, two plots are displayed which are labelled 'early' and 'late' extrusions. The 'early' extrusion corresponds to the first 10 ml extrusion where the syringe is fully loaded with slurry, and the 'late' refers to an extrusion when most of the slurry has been extruded and the plunger is positioned close to the bottom of the syringe. It should be noted that, as explained in Section 3.3.3 when discussing the velocity profiles of the fluid flow during different stages of extrusion (as presented in Figure 54), that the final 10 ml of slurry was not extruded because this would cause the foam to collapse and cause issues with the compression force data. Therefore, the 'late' extrusion for each slurry stopped at the point where 10 ml of slurry still remained in the syringe.

The syringe plunger force/displacement plots displayed in Figure 96 provide a number of insights that help to explain the relationships between slurry viscosity and extrusion behaviour. The initial steep gradient in all the curves represents the force required to overcome the plunger friction and compression of the fluid for extrusion to then begin. For the SS L slurry, both the early and late extrusions have very similar force plots, showing that there is little difference in the behaviour of the slurry regardless of the stage of extrusion in terms of how it flows from the syringe. It is interesting that the early extrusions for both Ti H and SS L slurries also have very similar force plots over the 10 ml extrusion, however the late extrusion for the Ti H slurry presents a much greater force value (roughly double that of the other plots) throughout the extrusion. The extrusion force of both SS L extrusions and the early Ti H extrusion are very similar values to the extrusion force

of the empty lubricated syringe. For these extrusions, this demonstrates that the force required to extrude the slurry through the nozzle is negligible compared with the force required to displace the plunger itself. Only the late Ti H slurry extrusion shows an increase in force applied beyond the plunger force.

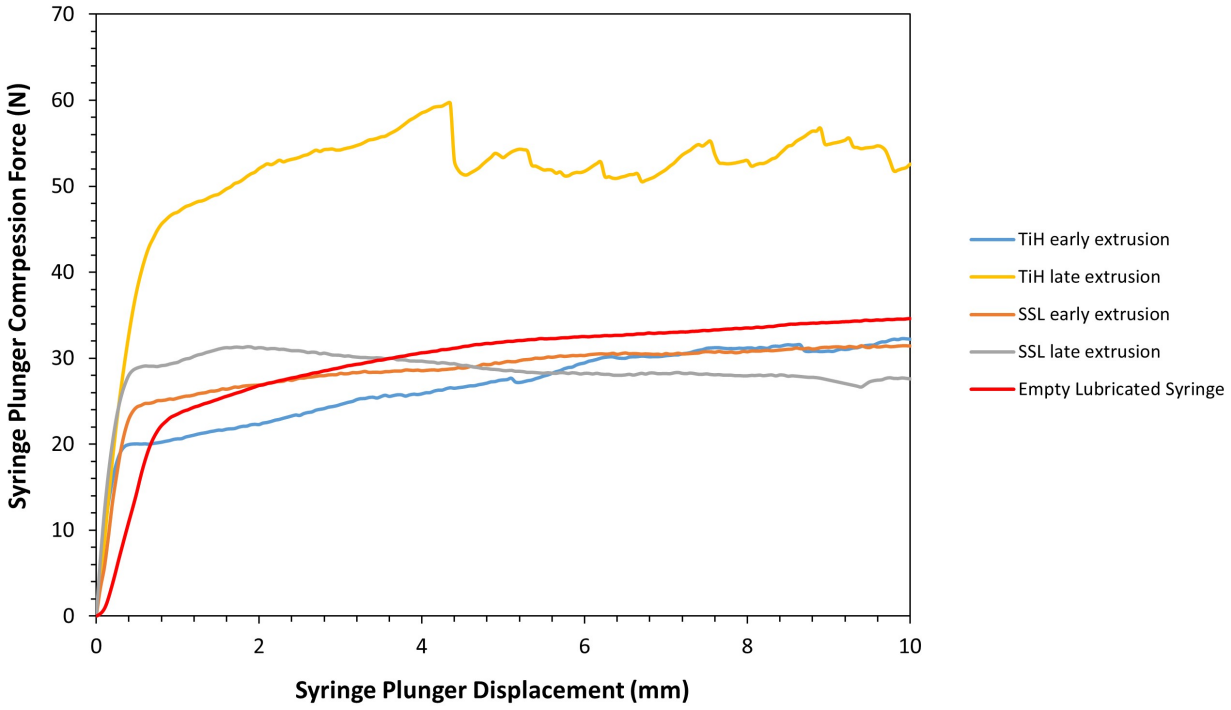

Figure 96: Graph showing plunger compression force against displacement for 10ml extrusions of foamed TiH and SSL slurries, and the empty lubricated syringe. The 'early' and 'late' extrusions refer to extruding when the syringe is full and nearly empty (but still $> 10\ ml$) respectively.

This suggests that during extrusion of a full syringe of Ti H slurry there is a steady build up of pressure, potentially due to compression of the foamed slurry. The scattered movement in plunger force during the late extrusion of the Ti H slurry shows that the extrusion of material from the syringe nozzle is inconsistent and pressure builds up and then is released in short bursts of extrusion, rather than forming a continuous flow of material from the nozzle. This scatter also suggests that, as mentioned in Section 5.1, there are small pockets of trapped air that are caused by the viscosity of the slurry and the syringe loading process. These pockets of air are likely to disrupt the extrusion of material, particularly when extruding the later extrusions because they will slowly move upwards within the syringe and then be forced through the nozzle later on. It is clear that there was no incremental build up in pressure within the syringe for the SS 316L slurry

extrusions, and no scattered force readings. This suggests that this slurry composition would be the most suitable for extruding regular and consistent tracks of material as there should be a steady flow of material from the nozzle from the initial compression of the plunger through to the final material being extruded (apart from the last 10 ml as previously discussed).

The observations from the plunger force displacement plots match logically with the measured viscosities of each slurry as presented in Figure 9. The extremely high measured viscosity of the initial optimised Ti H slurry composition causes the build up of pressure within the syringe throughout the four consecutive extrusions, because a greater plunger pressure is required to extrude the slurry. When this pressure is reached, the viscosity of the slurry prevents it from forming a steady flow and instead the slurry is extruded in inconsistent bursts. Also, the viscosity of this slurry makes it very difficult to load the syringe without incorporating unwanted pockets of air, and these air pockets disrupt the extrusion of material by compressing and also being forced through the nozzle causing drops in the plunger force and inconsistencies in the material flow, as observed later in Section 6.1.1. The SS L slurry presented a comparably low measured viscosity within the recommended range, and this slurry was able to produce a steady consistent flow of material from the syringe nozzle when the plunger was compressed even from the first extrusion. This is observed in the plunger force/displacement plots because the maximum force is consistent for each extrusion. These results confirm the prior assumptions that the viscosity of the foamed powder slurries has a significant impact on the ability to extrude them continuously through a syringe nozzle to produce consistent tracks of deposited material, which is discussed further in the development of the actual printing processes in Chapter 6.

5.2.5 Compressive Strength of Green Samples

The green strength of the dried samples produced from various slurry compositions and powders analysed in this work so far had been examined simply through observing how easily the samples could be removed from their moulds and manually handled. In order to gain a more accurate and quantifiable picture of the strength of the dried powder samples, mechanical compression testing was performed on samples produced from each of the key slurry compositions outlined in Table 11 using the method outlined in Section 3.4.5.

Figure 97 shows the dried SS L sample both during and after the compression testing, and

Figure 98 presents the force/displacement data for the compressions of each of the 4 samples. Only the initial 5 mm of the 20 mm overall displacement is presented, because the data beyond this simply shows a steady increase in force for all of the samples as the samples' structures have collapsed and the residual powder is simply being compressed between the plates which provides no relevant information regarding the strength of the green samples.

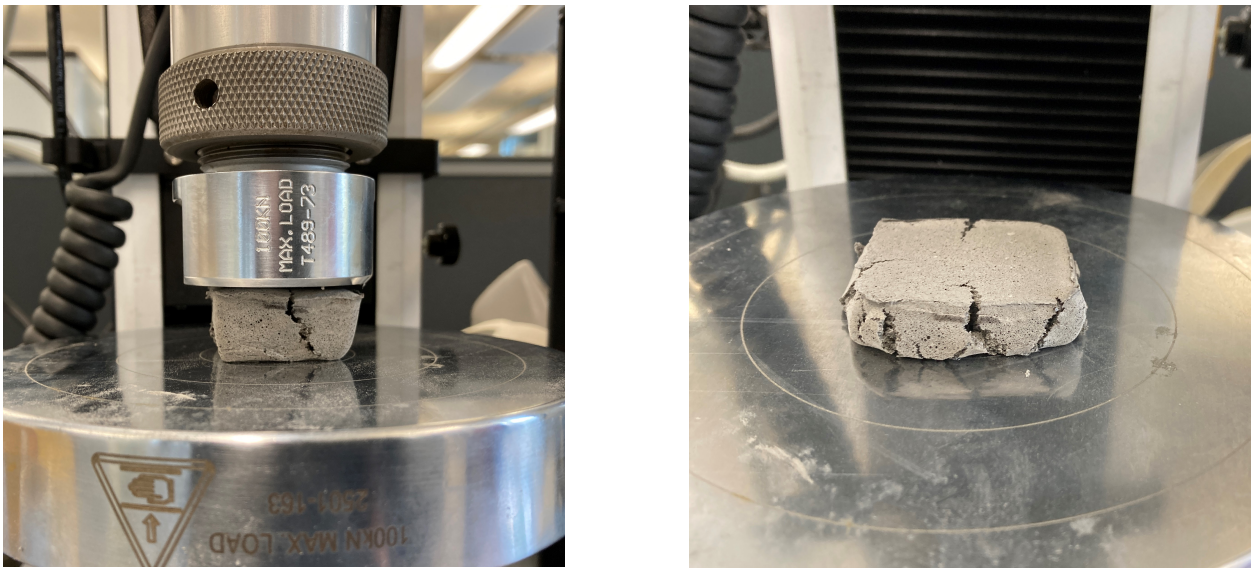

(a) (b)

Figure 97: Images showing compression testing of dried SS 316L sample produced from slurry with VF 0.5 (SS L).

It was previously assumed that reducing the powder volume fraction within the slurries would negatively impact the green strength of the dried samples, as well as the level of shrinkage that occurs during drying and sintering as highlighted in existing literature [289]. The compression force/displacement plots for the dried green samples produced from the four key slurry compositions presented in Figure 98 show that, whilst there is a slight reduction in the maximum compressive strength for both Ti64 and SS 316L samples with reduced powder volume fraction, the impact is not significant. Instead the data shows that it is the powder used that had a much more significant impact on the compressive strength of the green samples. The yield strength values for each sample were calculated using the load at yield as highlighted in Figure 98 and the known cross-sectional area of the samples. The SS 316L powder samples presented higher yield strength than the Ti64 powder samples of 0.034 and 0.03 MPa for SS H and L respectively, compared with 0.012 and 0.01 MPa for Ti H and L respectively. The reason for this difference is not clear, however it is

likely to be linked with the difficulties experienced with dispersing the Ti64 powder within the slurry, as discussed in Section 5.1.2. If the SS 316L powder was more evenly dispersed within the slurry, then the distribution of powder within the dried sample would be regular giving it a more rigid structure than the Ti64 samples which may have a slightly irregular distribution of powder.

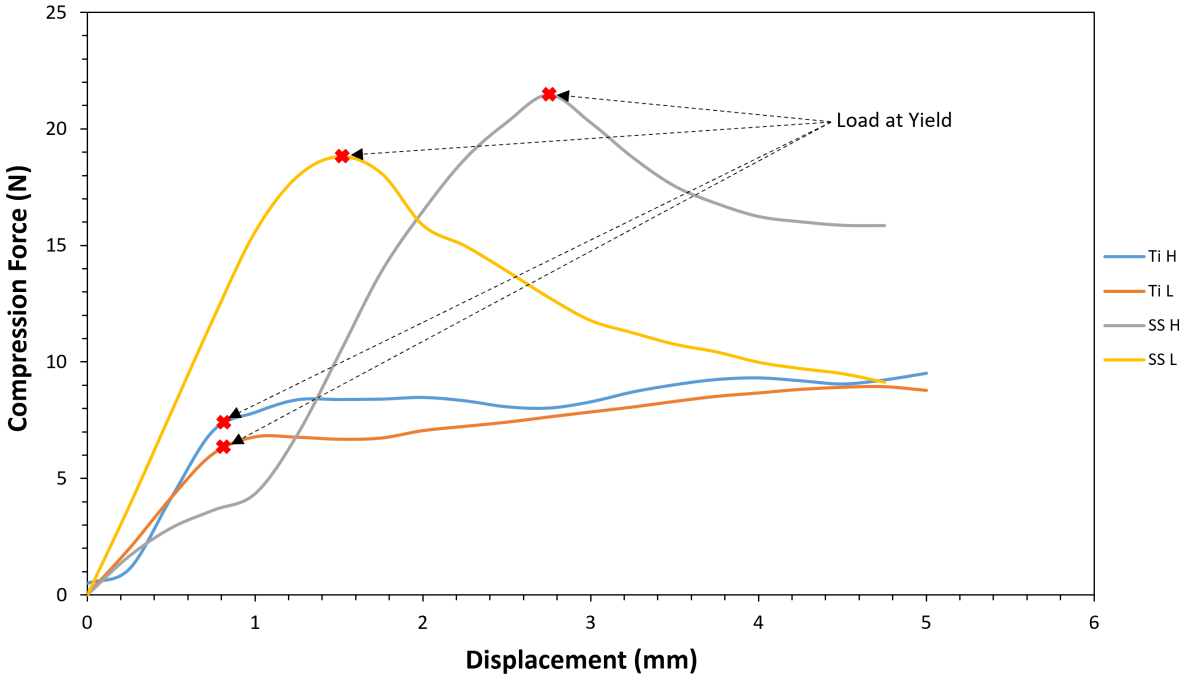

Figure 98: Graph showing compression force against displacement for compression tests of dried samples produced using Ti64 and SS 316L slurries with different compositions, with points highlighted where yield force data was extracted.

In general, these yield strength values are low when compared to many of the values reported within literature for compressive strength of green bodies produced from metal gel casting. When evaluating different gelling agents for gel casting with iron powder, Li et al. reported green strength values between $1.8 - 2.6\ MPa$ for samples produced using the same gelling agent as in this work (MC), when applying a VF in the same range as the slurries produced in this work $(0.5 - 0.6)$ [218]. The difference in strength can be explained by the fact that the green samples produced in this work are highly porous, whereas those developed by Li et al. were not foamed and as such had a relative density of over 95 %. Also, as discussed in Section 2.6.5, this study investigated powder size and the samples with the highest green strength were those that were produced using very fine iron powder (3 μm average particle size). However, the samples produced using iron powder

with similar size distribution to the AM grade Ti64 and SS 316L powders used in this work still presented green strength values much greater than those measured for the highly porous green samples in this work. Despite being lower than those reported in literature, the green strength of the samples produced from the key slurry compositions in this work was deemed sufficient due to the samples being stable enough to be removed from the moulds and handled without collapsing. If the green samples required shaping or machining prior to sintering, then a greater green strength would be required, however as the application of this material is to be able to create bespoke geometries through 3D material extrusion, this is not a requirement. Also, as discussed in Section 4.1.5, the dried Ti H slurry samples were stable enough to survive the burnout of the MC gelling agent without collapsing, demonstrating that the green stability of the samples is sufficient to allow the porous structures to be sintered. Therefore, when assessing the suitability of the various slurry compositions for the application of 3D material extrusion in Section 5.3, the 'green strength' criteria was assessed based on whether the samples were stable enough to be removed from a mould and handled without becoming damaged or disintegrating.

5.3 Summary of Slurry Composition, Viscosity and Stability

The work covered in this Chapter around optimising the composition of both Ti64 and SS 316L powder slurries highlights a significant challenge presented when trying to balance slurry viscosity, stability and the strength of the resulting dried green samples. In general, this development work has shown that producing highly stable foamed slurries using the AM-grade powders used here (of size range around $20 - 50\ \mu m$ for both Ti64 and SS 316L) requires the slurries to have a high viscosity. The initial optimised Ti64 slurry (composition outlined in Figure 77) presented high stability, particularly when stored within the syringe with the plunger inserted, but also had a very high measured viscosity. Various methods of reducing the viscosity of the foamed slurry to make it more suitable for 3D printing by extrusion were explored, however achieving suitable viscosity typically resulted in a compromise in either the slurry stability, dried sample green strength or both.

Figure 99 presents charts summarising the impact of two of the important composition parameters investigated in this Chapter on foamed slurry viscosity and stability, as well as the green strength of the dried samples. As presented in Section 5.1.1, the slurries mixed with different

powder size distributions were created using various SS 316L powders due to availability.

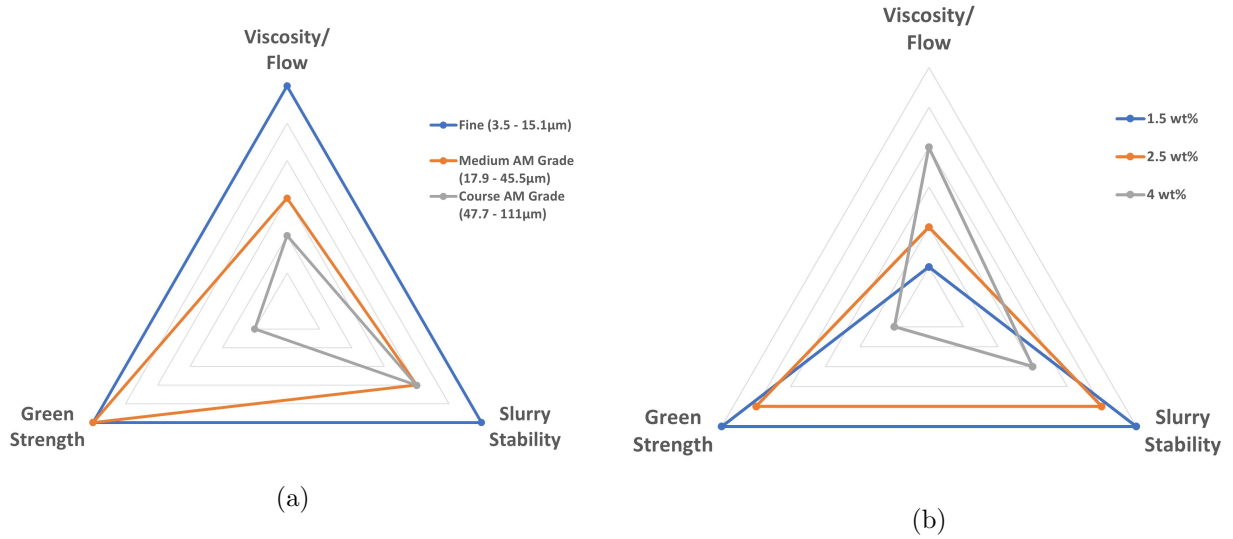

Figure 99: Dimensionless radar charts summarising the impact of powder size (for SS 316L slurries) suspended within the slurry (a) and dispersant addition (for Ti64 slurries) as a weighted percentage of powder mass on the viscosity and stability of the resulting foamed slurries, as well as the green strength of the dried samples. The centre of the chart for each criteria represents being unsuitable for 3D material extrusion, and the outer perimeter of the chart represents being the most suitable.

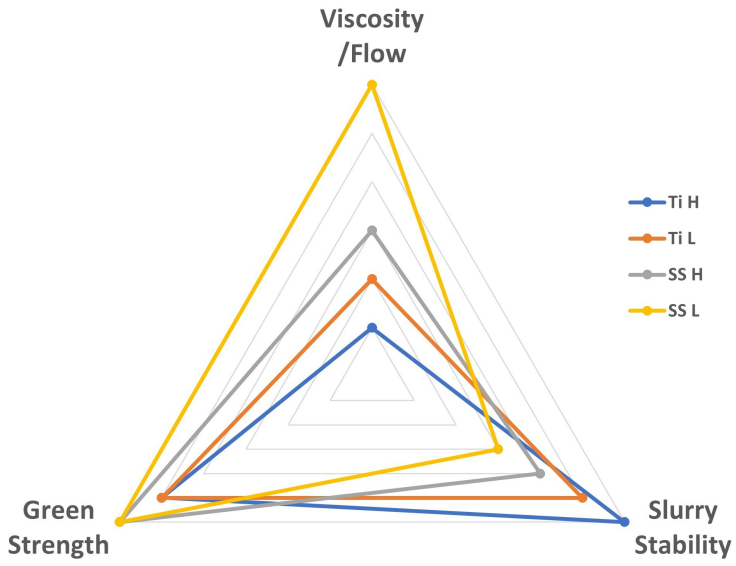

Figure 100: Dimensionless radar chart assessing the four key metal powder-based slurries developed against viscosity and stability, as well as the green strength of the dried samples. The centre of the chart for each criteria represents not suitable for 3D material extrusion, and the outer perimeter of the chart represents being the most suitable.

Figure 99a displays clearly, as already highlighted, that reducing powder size is the most effective way of producing slurries with optimal properties for 3D material extrusion which agrees with the observations from previous studies [218], however the issues this presents when working with Ti64 have been highlighted. Whilst the stability of the foamed slurry produced using fine SS 316L powder was not assessed due to limited availability, the evidence from literature is clear that smaller powder size results in greater slurry stability. The stable, low viscosity metal powder slurries presented in literature are all produced using powders with small size range [218, 220]. Therefore, there is certainly scope for further development and research into the size ranges of Ti64 powder available, and producing slurries using Ti64 powder with as small a size range as can be safely worked with. This could also include using sieving the AM-grade powder from this work in order to compare the viscosity and stability of slurries produced from the same powder but different size ranges. The impact of increasing dispersant addition within the Ti64 powder slurries is summarised in Figure 99b. As previously discussed within this chapter, this clearly shows that whilst increasing dispersant addition is a reasonably effective way to reduce slurry viscosity, it also has a direct detrimental impact on the stability of the foamed slurry itself and the strength of the dried samples. Many of the samples produced using slurries with increased dispersant addition were so weak that they crumbled upon removal from the moulds.

Figure 100 provides a simple summary of the four key slurry compositions highlighted in this chapter as being of interest for further development, and assesses each of them against slurry viscosity and stability, as well as the green strength of the dried samples. It also provides a summary of the impact that VF of powder used in the slurry composition has on these criteria. Comparing the VF for each of the two powders shows that reducing this value provides a method of decreasing viscosity whilst maintaining the green strength of the dried samples. Whilst it is apparent that it does have a slight detrimental impact on slurry stability, it is not to such an extent that it makes the slurry unsuitable for extrusion, as demonstrated in the stability tests. The dried samples produced using each of these key slurry compositions presented sufficient green strength in order to be handled after drying without decomposing, despite presenting lower compressive strength than what has been reported in literature for dense samples. Whilst the sintering stability test was only completed using samples produced from the Ti H slurry composition (Section 4.1.5), it was assumed that the samples produced using the other key slurry compositions would also be

suitable for sintering, especially considering the VF of powder within all these slurries was kept relatively high.

Figures 99 & 100 show overall that it is clearly possible to produce slurries that meet each of the individual important criteria in order to be suitable for this application. However, aside from the slurry produced using very fine SS 316L powder (which has been deemed unsuitable for Ti64), none of the slurries developed in this work were able to meet all three criteria. Producing Ti64 slurries with viscosity within the optimal range presents a significant challenge, with most attempts to reduce viscosity having a detrimental effect on the slurry stability, green strength of the dried samples or both. Therefore, whilst a range of options have been explored in this work, there still remains a huge potential scope for further research into the most effective methods for mixing stable foamed slurries using Ti64 powder, particularly focusing on powder size and dispersant selection and identifying dispersants that are capable of producing stable, low viscosity slurries.

	Slurry Reference			
	Ti H	**Ti L**	**SS H**	**SS L**
Powder	AM-grade Ti64		AM-grade SS 316L (*powder b)*	
Volume Fraction	0.57	0.5	0.57	0.5
Dispersant Addition (wt %)	1.5	2.3	1.5	1.5
Surfactant Addition (vol %)	1	1	1	1
Whisking Time (mins)	3	3	3	2

Table 11: Summary of final key slurry compositions selected for further development.

Having identified the key slurry compositions of interest, the next important phase of the work was to develop the 3D extrusion process through the analysis of single-track, single-layer and multi-layer extrusions. As outlined in Table 9 the foamed Ti L and SS H slurries presented similar viscosity values, and so the SS H slurry was not taken into extrusion process development as it would not have provided a beneficial comparison. The Ti H, Ti L and SS L slurries provide a sufficient range of viscosities ($246,154$, $123,357$ and $31,360$ cP respectively) in order to be able to examine the effect of viscosity on the printability of the slurry. Therefore, these three slurry compositions were selected for the developing the 3D extrusion process, as presented in Chapter 6.

6 Chapter 6: Results & Discussion Part III - Foamed Slurry 3D Extrusion Process Development

Section 3.5 outlines the method that was followed in developing the 3D extrusion process using foamed metal powder slurries in conjunction with the ZMorph 2.0 3D printer and thick paste extrusion toolhead. The development of the foamed slurry 3D extrusion process was broken down into the deposition of single tracks, single layers consisting of multiple adjacent tracks, and full 3D builds consisting of several successive deposited layers. This chapter presents the results and discussion from this development process.

6.1 Single Track Depositions of Foamed Metal Powder Slurries

6.1.1 Single Track Depositions using Initial Optimised Ti64 Powder Foamed Slurry

As highlighted in Section 3.5.3, there are a number of controllable parameters within the thick paste extrusion workflow in Voxelizer. Several of these parameters alter the flow rate and volume of material that is extruded, and so in order to identify parameter value combinations that produced the most suitable deposited tracks, certain values were kept constant whilst others were varied. For the initial Ti64 slurry (Ti H) deposition, the *path width* and *layer height* parameters were set at 2 mm and 1 mm respectively, as outlined in Section 3.5.3, and the the *print speed* and *thickness* parameters were varied between $2-10$ mm/s and $35-55$ % respectively. Figure 101 shows several sets of single track depositions using different combinations of extrusion parameter values (note - E5 T55 refers to a *print speed* of 5 mm/s and *thickness* of 55 %).

The tracks deposited with each parameter set combination were visually examined to determine whether the syringe was under-extruding or over-extruding material, as well as to observe the continuity of the tracks. The first set of tracks in Figure 101a shows an example of a set of tracks where the syringe has under-extruded due to the parameter selection resulting in a thin track with multiple points of discontinuity, whereas the first set of tracks in Figure 64 (In Section 3.5.5) shows an example of the syringe over-extruding material. Average track width values were then obtained for each set of tracks, as described in Section 3.5.5, which are presented in Table 12. Also, the standard deviation in track width for each set of tracks was calculated in order to provide a

comparison of the variation in track geometry.

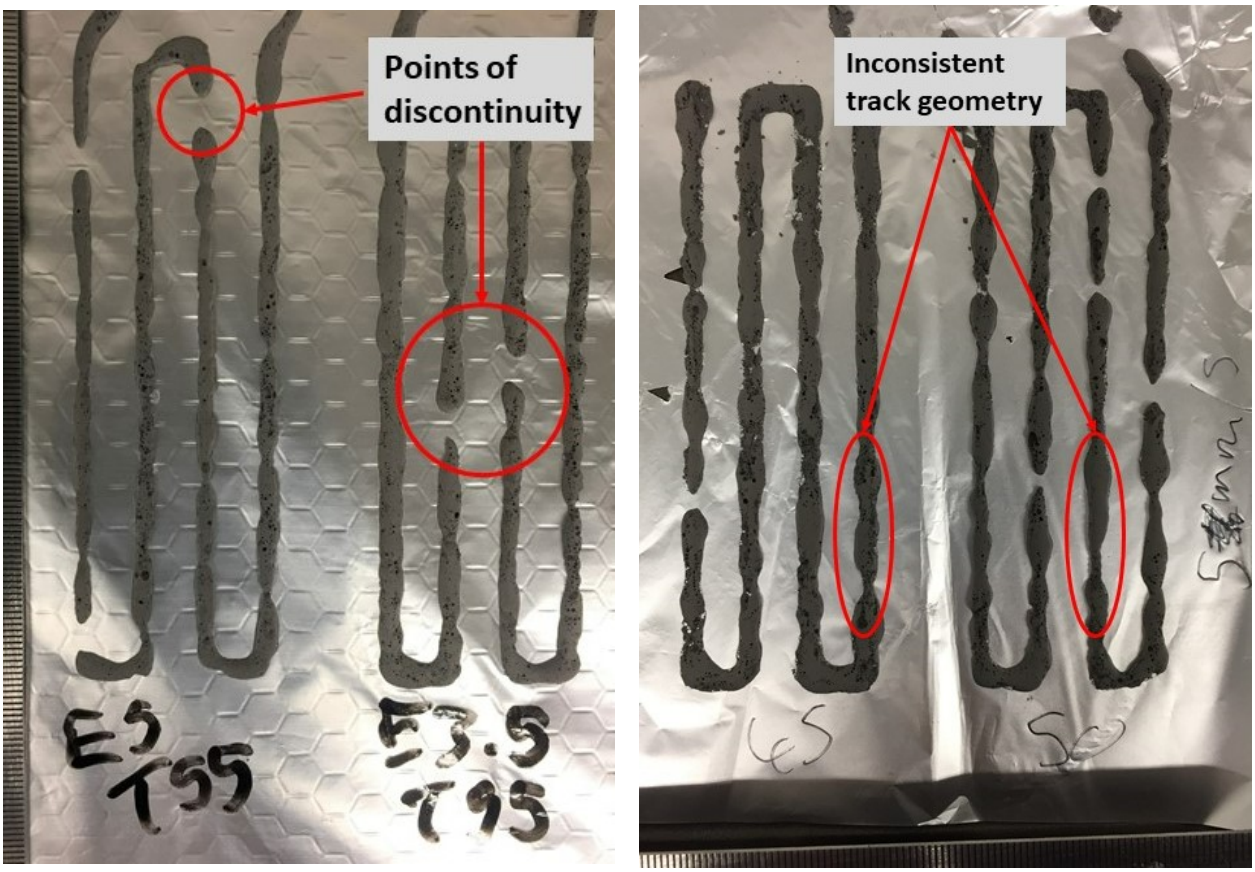

(a) (b)

Figure 101: Images showing single tracks of extruded foamed slurry using different combinations of extrusion speed and material thickness parameter values.

The aim of this work was to explore whether stable tracks could be deposited by altering the extrusion parameters to account for the high viscosity of the Ti H slurry. In general, increasing both the *print speed* and *thickness* parameter values within Voxelizer (as discussed in Section 3.5.3) resulted in a decreased average track width, demonstrating that the volume of slurry extruded decreased. It was expected that both of these parameter values would alter the extrusion volume, as this is stated in the guidance provided by ZMorph [253], as well as specifying that increasing the *print speed* reduces the volume of material extruded. This is a slightly unusual feature of the ZMorph Thick Paste Extruder system, as it would be more logical to assume that the track width would remain the same across all *print speeds* at a given *thickness* value as the software would alter the speed of the stepper motor that controls the plunger speed to account for the change in linear

speed of the nozzle. However, the guidance from ZMorph along with the measurements presented in Table 12 clearly demonstrate that this is not the case. This highlights the importance of testing a range of value combinations for these parameters in order to find the settings that produce the most consistent extruded tracks.

Print Speed	***Thickness* (%)**				
(mm/s)	**35**	**40**	**45**	**50**	**55**
2	5.65 ± 1.96	4.68 ± 0.89	3.68 ± 0.77	3.39 ± 0.76	3.34 ± 0.61
3.5	5.36 ± 0.79	4.17 ± 0.53	3.55 ± 1.02	3.28 ± 0.51	3.25 ± 0.51
5	4.46 ± 0.59	3.85 ± 0.57	3.5 ± 0.51	3.16 ± 0.92	2.58 ± 0.51
10	3.59 ± 0.78	3.43 ± 0.87	3.04 ± 0.55	2.66 ± 0.77	1.71 ± 0.56

Table 12: Table presenting calculated mean track width measurements and standard deviations (mm) for foamed Ti64 powder slurry extruded with different combinations of extrusion parameter values.

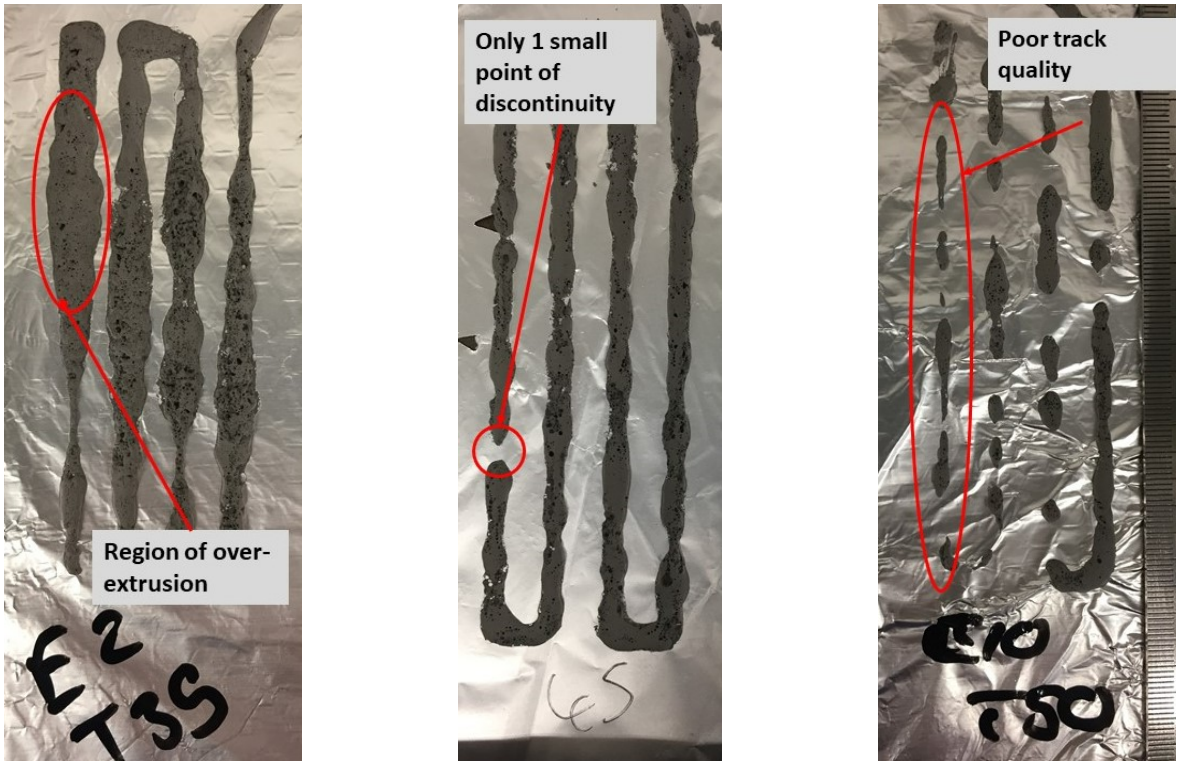

(a) (b) (c)

Figure 102: Images showing single tracks of extruded foamed slurry using different combinations of extrusion speed and material thickness parameters of E2 T35 (a), E5 T45 (b) and E10 T50 (c).

Figure 102 shows the tracks extruded using the extreme case combinations of *print speed* and *thickness* from Table 12. The tracks extruded using values of 2 mm/s and 35 % (Figure 102a) show clear signs of over-extrusion where the track width is significantly greater than the nozzle size, and also there is a huge variation in width throughout the tracks. As outlined in Table 12, the average measured width of these tracks was 5.65 mm, and also the calculated standard deviation in measured track width was 1.96 mm. Figure 102c presents the opposite extreme case where the parameter values of 10 mm/s and 50 % have resulted in under-extrusion of the slurry. In this case there are only very short continuous extrusions which are separated by a number of breaks within the tracks. Generally, the parameter value combinations in the middle of the experimental range produced the most consistent extruded tracks, with much lower variation in the measured track widths and fewer breaks. A number of parameter combinations produced the lowest deviation in track width of around 0.5 mm, however the parameter values selected for multi-track and multi-layer extrusion testing was 5 mm/s and 45 % because these values produced the lowest number of points of discontinuity over the course of the four extruded tracks, as presented and highlighted in Figure 102b. The average measured width value for each parameter set was not specifically used to select the parameter values to proceed with, however these values are required when setting up the .dxf files to programme the nozzle path when depositing multiple adjacent tracks to produce continuous layers. Only a few of the average measured track width values were close to the programmed *track width* parameter value of 2 mm, however these were tracks extruded using the higher *print speed* and *thickness* values including those presented in Figure 102c, and were all of very poor quality in terms of consistency and stability. Therefore, the consistency of the tracks was the main criteria, and providing the track widths were measured the spacing of the adjacent track paths in the .dxf files could simply be altered to account for this, as discussed further in Section 6.2.

6.1.2 Single Track Depositions using Ti L and SS L Slurry Compositions

From the key SS 316L slurry compositions highlighted in Table 11, only the slurry with the reduced VF (SS L) was selected for development of the 3D extrusion process. This was due to the fact that this slurry composition presented a measured viscosity significantly below the values of both the Ti64 slurries that was within the recommended range for the ZMorph thick paste extruder toolhead, whereas the SS H slurry measured viscosity was in a similar range to the Ti L slurry which was

used for 3D extrusion testing. For both the Ti L and SS L slurry initial single track extrusion testing, there was no need to repeat the range of combinations of extrusion parameters tested for the original Ti H slurry as a large number of these parameter combinations were clearly unsuitable for extruding this kind of material. Therefore, by selecting parameter combinations around the values concluded to be optimal for the Ti H slurry and conducting basic single track extrusion tests, it was determined that for both the foamed Ti L and SS L slurry compositions parameter values of 5 mm/s and 50 % for *print speed* and *thickness* respectively produced the best quality tracks. In order to obtain accurate average track width measurements for both slurries extruded with this parameter values, a set of 10 parallel 100 mm tracks were extruded for both, which are presented in Figures 103 & 104. Table 13 provides a summary of the mean track width and standard deviation in track width for the three slurry compositions used to conduct single track deposition tests.

Slurry Composition	**Mean Track Width (mm)**	**Standard Deviation (mm)**
Ti H	3.5	0.51
Ti L	4.14	0.38
SS L	4.23	0.29

Table 13: Table presenting mean track width and standard deviation of tracks deposited with different slurry compositions. All tracks were extruded with *print speed* 5 mm/s, and *thickness* of 45 % for Ti H and 50 % for Ti L and SS L.

Visually comparing these tracks with the Ti H tracks in Figure 102b clearly demonstrates the effect of reducing the viscosity of the foamed slurry on the quality of track that can be extruded. There is a significant improvement in the track consistency between the Ti H and Ti L tracks, which correlates to the respective corrected viscosities of the foamed slurries of $246,000$ cP and $123,357$ cP. Only a few minor defects can be observed in the tracks extruded using the Ti L slurry, as highlighted in Figure 103. There is a further improvement in track quality between the Ti L and the SS L extruded tracks, with the SS L corrected viscosity having been calculated to be just $31,360$ cP. Both the Ti L and SS L track sets presented show no breaks at all which shows that the slurries are able to flow consistently from the nozzle during extrusion. Also, the track width measurements show a reduced variation compared with the Ti H slurry tracks, with measured standard deviations of 0.38 and 0.29 mm respectively as presented in Table 13.

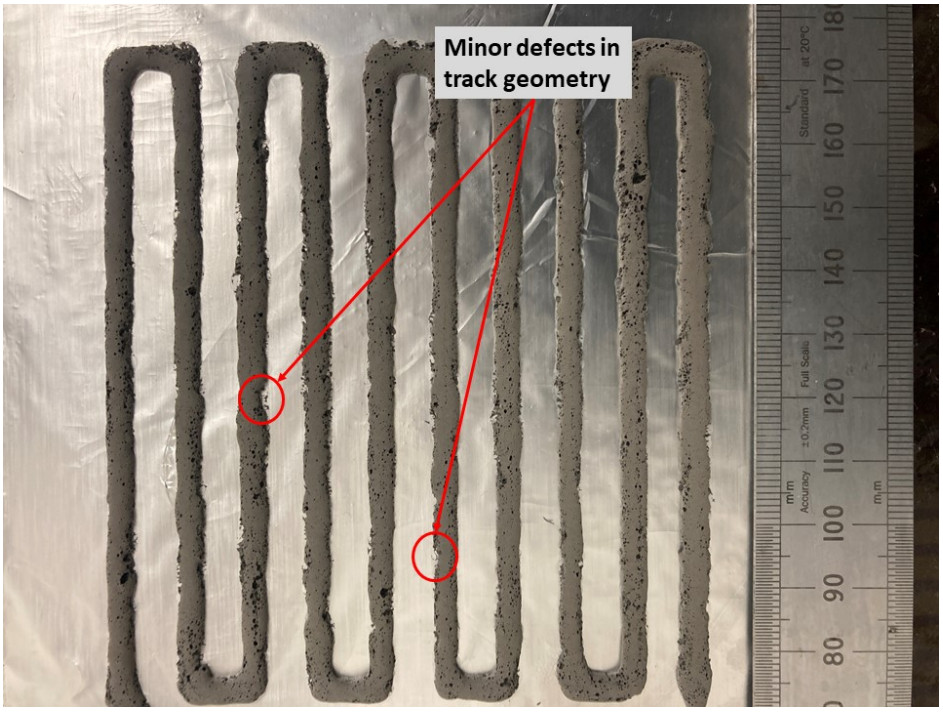

Figure 103: Image showing set of single tracks deposited with the Ti L slurry composition using optimal selected extrusion parameters.

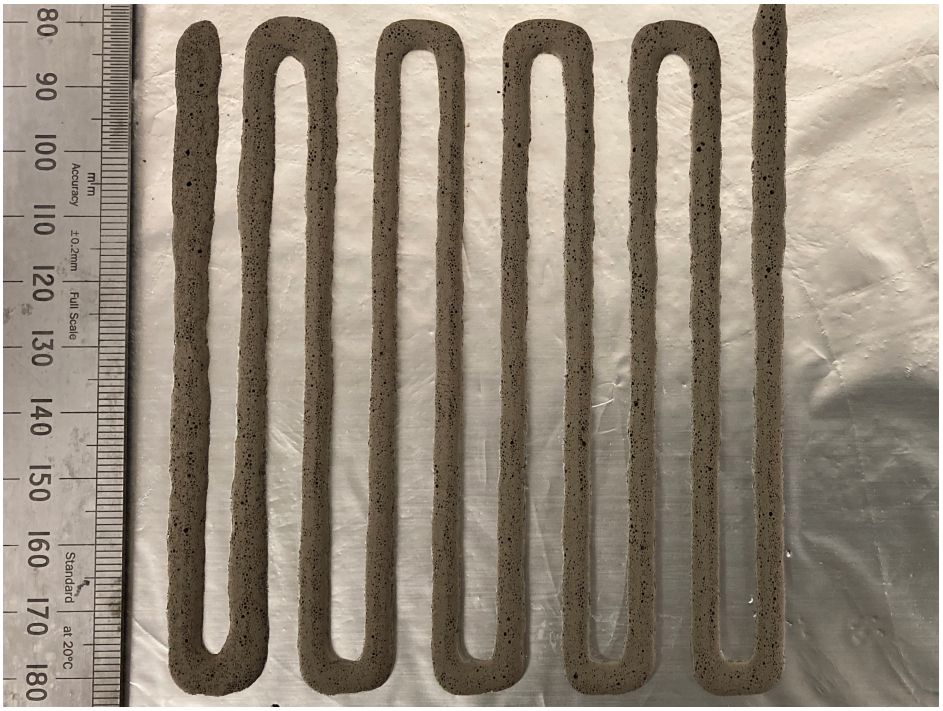

Figure 104: Image showing set of single tracks deposited with the SS L slurry composition using optimal selected extrusion parameters.

6.1.3 Measuring Deposited Track Height

In order to be able to deposit multiple layers of foamed slurry it was important to first measure the average height of extruded tracks. Once obtained this could be matched with the *layer height* parameter in Voxelizer to ensure that the z-height movement of the extruder toolhead between the deposition of each layer would be equal to the actual layer height, in order to avoid the distance between the nozzle and the previous track being either too close or too far. Track height values were obtained using a laser confocal microscope following the method outlined in Section 3.5.5. As previously mentioned, the scanning process to produce 3D profiles is time consuming therefore only certain sets of tracks were selected for obtaining height measurements. For each of the slurry compositions which were used for depositing sets of single tracks with different parameters, the tracks highlighted for having the most consistent geometries (as presented in Sections 6.1.1 & 6.1.2) were selected for height measurement, as these parameter combinations were those that would be used to develop the deposition process for each slurry. Track height values were obtained across multiple sections of each set of tracks, and the average obtained height values along with standard deviation values are presented in Table 14. This table also presents the width measurements obtained using the laser confocal microscope, in order to provide a comparison against the measurements previously obtained using 2D images. Also presented are the measured track dimensions of tracks deposited with Ti H slurry with different geometry parameter combinations in order to try and produce tracks where the measured height presented values close to the programmed *layer height* parameter value. Figure 105 shows examples of the height profiles obtained for both the deposited Ti H and SS L slurry tracks as obtained using the laser confocal microscope.

As can be seen in Figure 105, the tracks roughly fit a parabola shape, as was initially assumed when setting up the experimental procedure (Section 3.5.3), where the width of the track at the base is approximately equal to double the track height. The track cross sections for Ti H (Figure 105a) present significantly more scatter than those for the SS L tracks (Figure 105b), particularly across the top surface of the tracks. Some scatter is to be expected rather than a smooth surface as a result of the slurry being foamed, and as such there may be bubbles that break the top surface of the track during extrusion. However, the additional scatter observed in the Ti H tracks agrees with the observations from Sections 6.1.1 & 6.1.2 regarding the inconsistency and defects present

within these tracks compared with the SS L tracks.

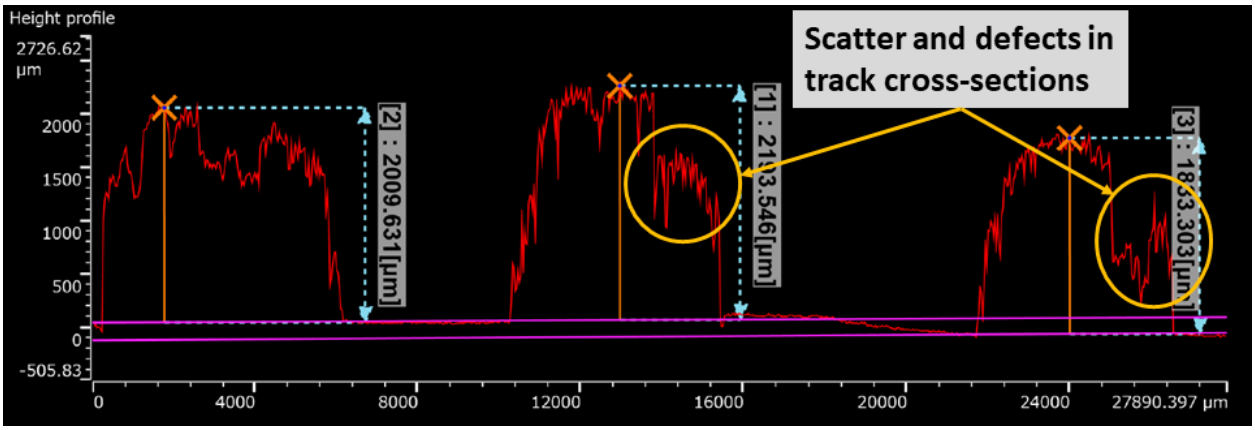

(a)

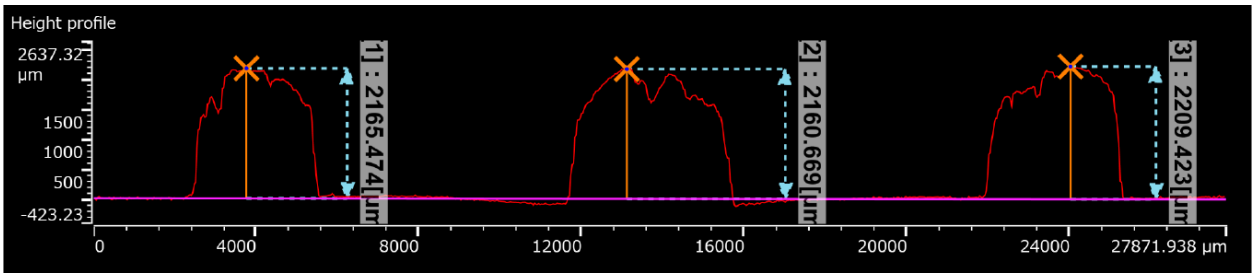

(b)

Figure 105: Plots showing height profiles of deposited Ti H slurry tracks (a) and SS L tracks (b) obtained from 3D profiles acquired using LEXT laser confocal microscope.

As explained in Section 3.5.5, the initial track width measurements were obtained from 2D analysis of images taken using the software Fiji as this provided a quick means of gathering track width data. As previously highlighted, the track width values themselves are not particularly important provided the tracks are stable and consistent, however the measured height of the deposited tracks must match the programmed *layer height* parameter value as this value determines the z-movement of the nozzle between the deposition of successive layers of material. If the true height of each layer is less than the programmed parameter value, then the nozzle will move further away from the material at each layer which would cause deposition issues. Conversely, if the true height is greater than the parameter value, the nozzle will not step far enough in the z-direction and as such will be moving through the previously extruded material which would again cause issues with deposition. This presents a particular problem when depositing multiple layers as this error will be cumulative as more layers are deposited.

As highlighted in Section 3.5.3, the *path width* and *layer height* parameter values were set as 2 mm and 1 mm respectively due to the assumptions around the nozzle diameter and track geometry. Initially these values were kept constant throughout the *print speed* and *thickness* parameter value experiments for all slurries. Upon measuring the average heights of the tracks deposited for each slurry composition with the optimal extrusion parameters, it was discovered that the true height of the tracks in all cases was approximately double the *layer height* parameter value, as presented in Table 14. Therefore if multiple layers were deposited with these parameter values and track dimensions, the nozzle would not move far enough in the z-direction between each layer resulting in the nozzle dragging through the previous layer.

		Track Height (mm)		**Track Width (mm)**	
Slurry Composition	**Key Extrusion Parameters**	**Mean**	**Standard Deviation**	**Mean**	**Standard Deviation**
Ti H	***W=2mm*** ***H=1mm*** $E = 5mm/s$ $T = 45$ %	2.1	0.37	3.5	0.68
Ti H	***W=1mm*** ***H=2mm*** $E = 5mm/s$ $T = 45$ %	1.88	0.25	3.17	0.65
SS L	***W=1mm*** ***H=2mm*** $E = 5mm/s$ $T = 50$ %	2.11	0.13	3.65	0.44

Table 14: Table presenting track height and width measurements obtained using LEXT laser confocal microscope for key slurry compositions, and values for key extrusion parameters used to deposit the tracks including *path width* (W), *layer height* (H), *print speed* (E) and *thickness* (T).

In order to find a solution to this problem, some basic experimentation was conducted whereby the *path width* and *layer height* values were modified. As the measured height of all the track sets was around 2 mm, the aim was to change the *layer height* value to match this and then tweak the *path width* value so that the overall geometry of the extruded tracks remained the same as previously measured. A simple solution was discovered, which was to decrease the *path width* parameter from 2 mm to 1 mm whilst increasing the *layer height* from 1 mm to 2 mm, resulting in the same

overall volumetric flow of material and resulting track geometry as with the previous parameter selection, as presented in Table 14. As described in Section 3.5.5, the track height measurements were all obtained from analysis of 3D profiles captured using a laser confocal microscope. Due to the accuracy of this measurement technique compared with the width measurements obtained through 2D imaging and analysis within Fiji, the measurements obtained are much more reliable. As such, at this stage track width measurements were also obtained using the laser confocal microscope as presented in Table 14, to provide the most accurate values which were then applied when setting up the .dxf files for single-layer depositions as discussed in Section 6.2.

6.2 Extruding Multiple Adjacent Tracks of Foamed Metal Powder Slurries

Having selected the optimal extrusion parameters for depositing individual tracks using the ZMorph thick paste extruder toolhead and syringe, as well as measuring the average track height and width values, the next important phase of the development was use this information to be able to deposit multiple adjacent tracks that would form a full continuous layer of material.

6.2.1 Multiple Adjacent Track Depositions using Ti H Slurry

Initially a full layer of Ti H foamed slurry was deposited by generating a .dxf file containing 4 adjacent lines spaced at the mean track width (3.17 mm) measured for Ti H slurry using the selected extrusion parameters as presented in Table 14. However, upon inspection of the deposited 4-track layer displayed in Figure 106, it was clear that spacing the tracks in this way was not suitable for producing a continuous layer due to a lack of merging between adjacent tracks causing observable breaks.

The image presented in Figure 106 shows that the adjacent tracks have not merged to form a continuous layer as clear gaps are visible between them. This is in part caused by the high viscosity of the slurry preventing adjacent tracks from flowing/spreading when deposited. However, highlighted in the cross-sectional profile in Figure 106b, there are points within the layer where adjacent tracks do appear to have merged successfully. Therefore it was also possible that the general lack of merging was a result of the spacing between the track paths within the .dxf file. Setting the spacing between adjacent tracks to be equal to the average track width doesn't account for the deviation in track width, and as such there are points within the layer where two adjacent

tracks are both under the average width which results in a visible gap between them.

(a)

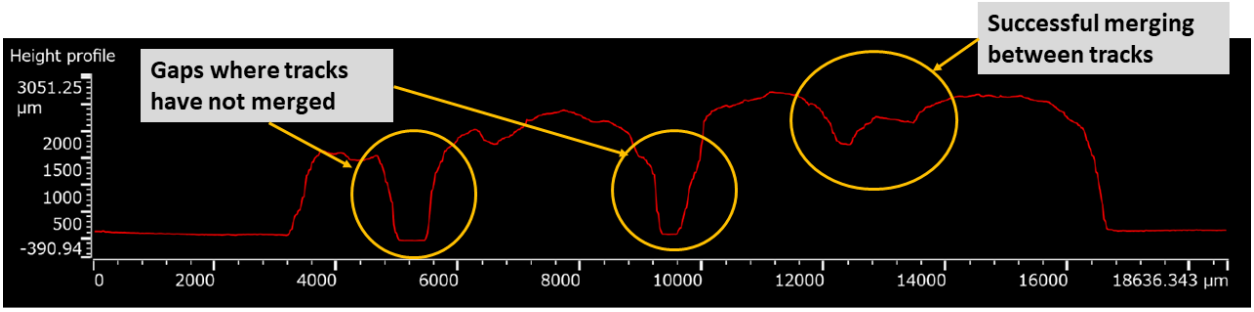

(b)

Figure 106: Image (a) and LEXT microscope height profile (b) showing the profile of a full layer consisting of 4 deposited Ti H slurry tracks using the mean track width as the track spacing value.

6.2.2 Adjacent Track Overlap Experiments using Key Slurry Compositions

The initial single-layer extrusion test presented in Section 6.2.1 demonstrated that there is a need for a degree of overlap between adjacent tracks in order to ensure merging between them to form one continuous layer. Within other material extrusion processes such as FDM there is an understanding that track overlap is required in order to ensure contact between adjacent hatch tracks, but also that excessive overlap can disrupt the printing process [290, 291], therefore there is a need to experimentally optimise the level of overlap between adjacent tracks when printing by material extrusion. As such, a set of simple experiments was conducted using the Ti H slurry as described in Sections 3.5.6 whereby single-layers consisting of sets of adjacent tracks were deposited with varying levels of overlap between $0 - 50$ %. Each full layer was visually inspected, as well as being scanned using the laser confocal microscope in order to obtain a detailed picture of how the tracks

had combined to form a layer, as displayed in Figures 107 & 109.

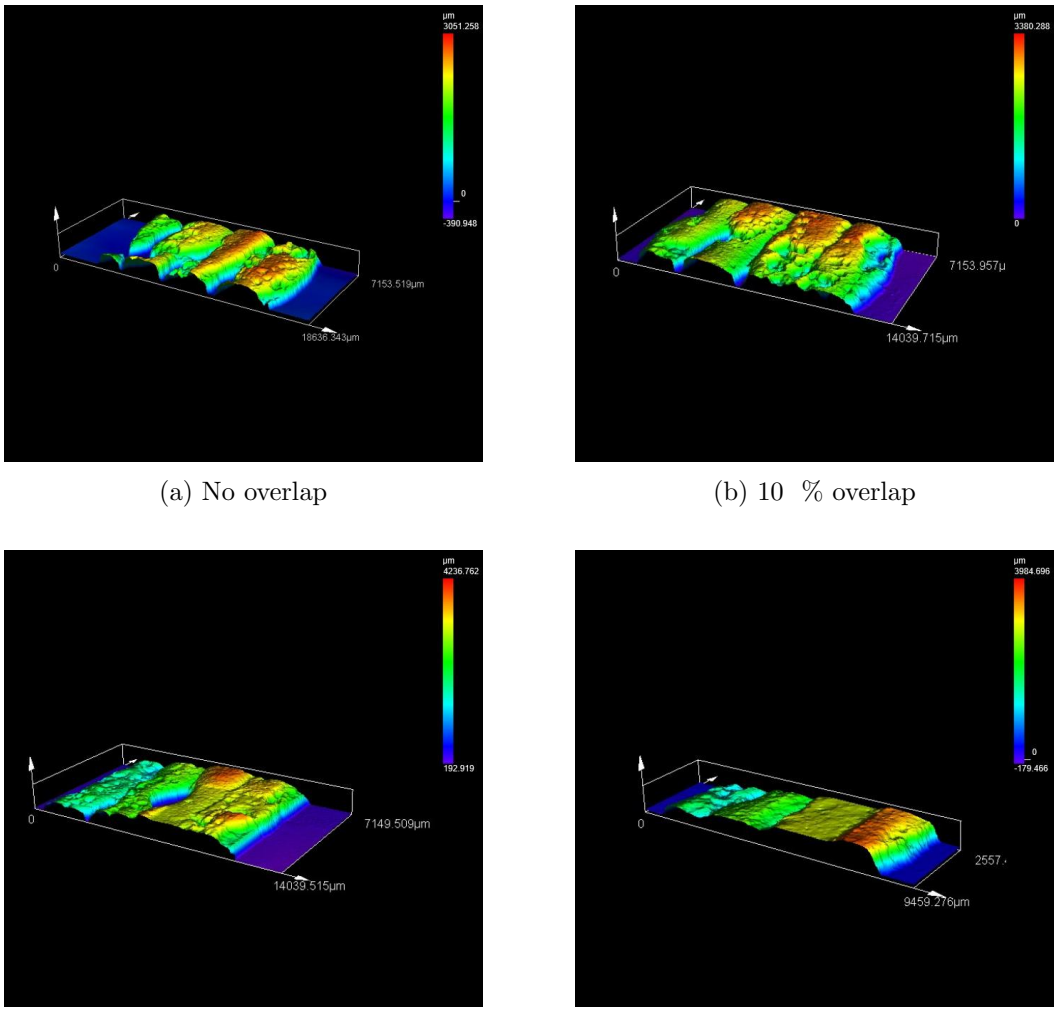

(a) No overlap

(b) 10 % overlap

(c) 25 % overlap

(d) 50 % overlap

Figure 107: Scanned 3D profiles of full layers produced by depositing 4 adjacent tracks of Ti H foamed slurry with various overlap percentages, obtained using LEXT laser confocal microscope.

The 3D profile images in Figure 107 and the 2D cross-sectional height profiles in Figure 109 clearly demonstrate that introducing any degree of overlap between the deposited tracks resulted in an improvement in merging between tracks. The 25 % and 50 % overlap height profiles in Figures 109d & 109c suggest that these levels of overlap are excessive because the height of the profile is seen to increase as each adjacent track is deposited (in order left to right). This is a result of the degree of overlap causing each track to being deposited slightly on top of the previous track, resulting in an increase in the track height with every new track deposited. It can be observed that the layer height increases to almost double the expected layer height of 2 mm where the 3^{rd} and 4^{th} tracks

were deposited, which results in an overall uneven layer height. The profile of the tracks deposited with 10 % overlap (Figure 109b) shows that this degree of overlap produced a more consistent layer height close to the expected height, whilst also improving the merging between adjacent tracks. However, from examining the whole layer shown in Figure 108 it is clear that there is still an issue with overall insufficient merging between tracks as various gaps are still visible. This highlights the difficulties around using this slurry composition for the purpose of building 3D structures through material extrusion because of its high viscosity, as previously discussed in Section 5. Because of its high viscosity, it is not possible to increase the track overlap to a sufficient level to ensure merging of adjacent tracks without causing an increase in track height and uneven overall layer height. If the viscosity was lower the track overlap could be increased beyond 10 % but the material would flow slightly and settle into a layer with an even height, which is in fact what was observed during the track overlap experiments for the Ti L and SS L slurries with lower viscosities.

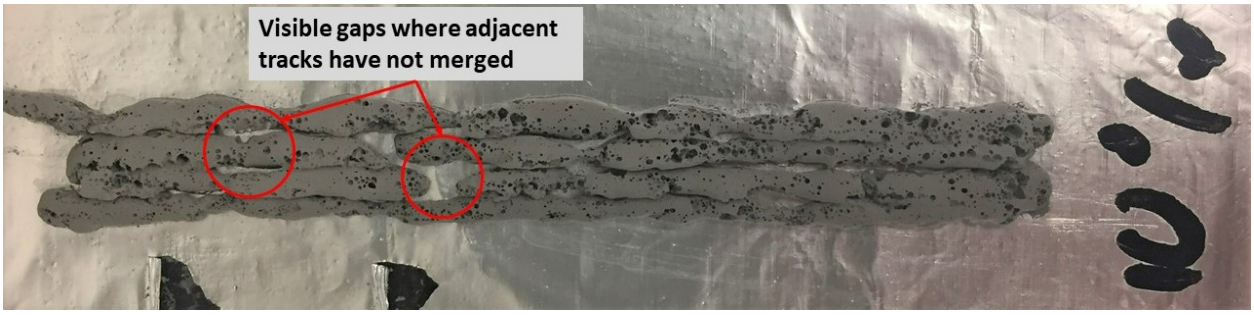

Figure 108: Image showing a full layer of adjacent tracks deposited with Ti H slurry using 10 % overlap between tracks.

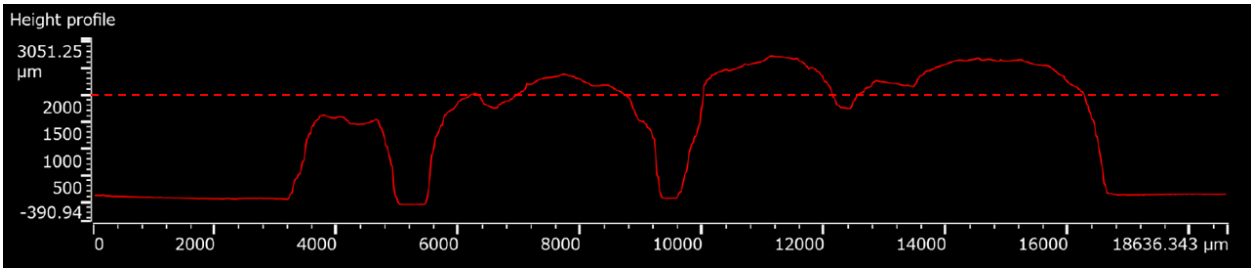

(a) No overlap

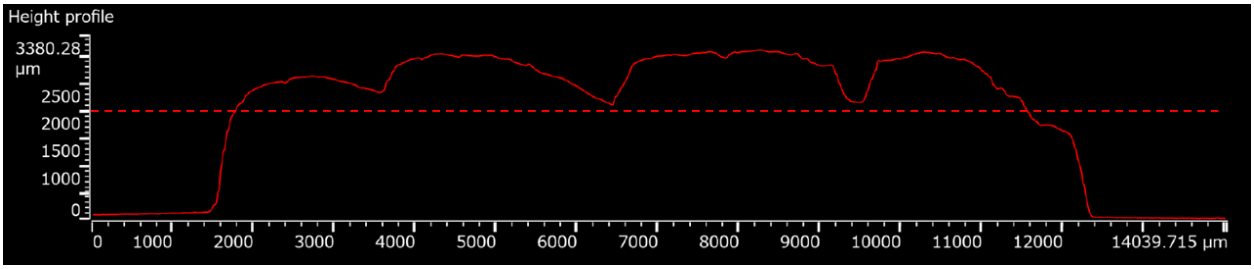

(b) 10 % overlap

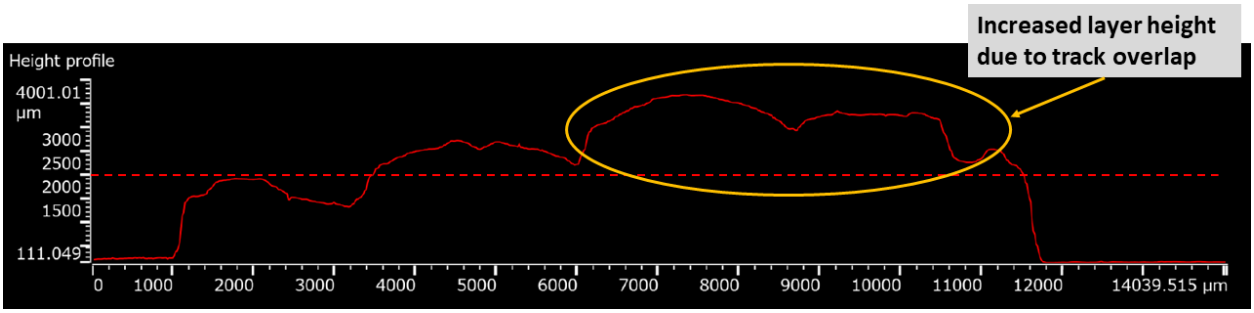

(c) 25 % overlap

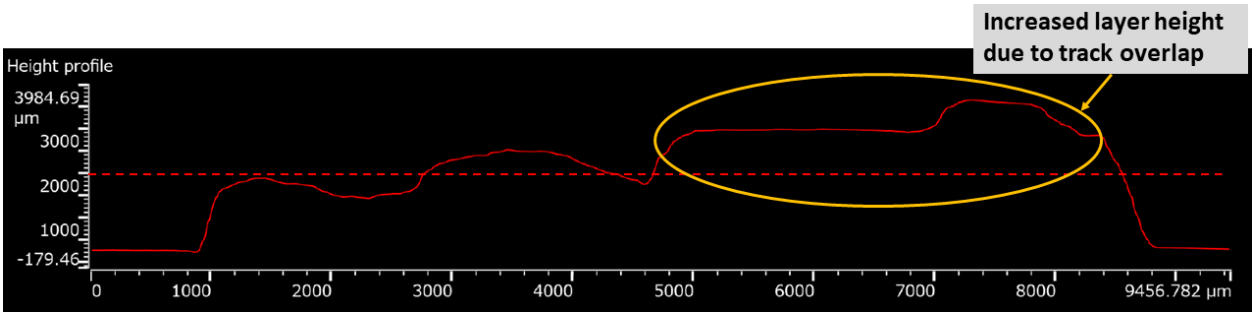

(d) 50 % overlap

Figure 109: Height profiles of full layers produced by depositing 4 adjacent tracks of Ti H foamed slurry with various overlap percentages, obtained using LEXT laser confocal microscope. The expected layer height of 2 *mm* is highlighted on each profile.

From the observations discussed regarding Ti H slurry track overlap, it was identified that an overlap within the range of $10-25$ % was required in order to ensure sufficient merging of adjacent tracks. The specific optimal overlap percentages for the other key slurry compositions were then also investigated. For the Ti L and SS L slurry track overlap experiments, overlaps of $10, 15$ and 20 % were investigated, and the images of the resulting single-layers for Ti L and SS L are presented in Figures 110 & 111 respectively.

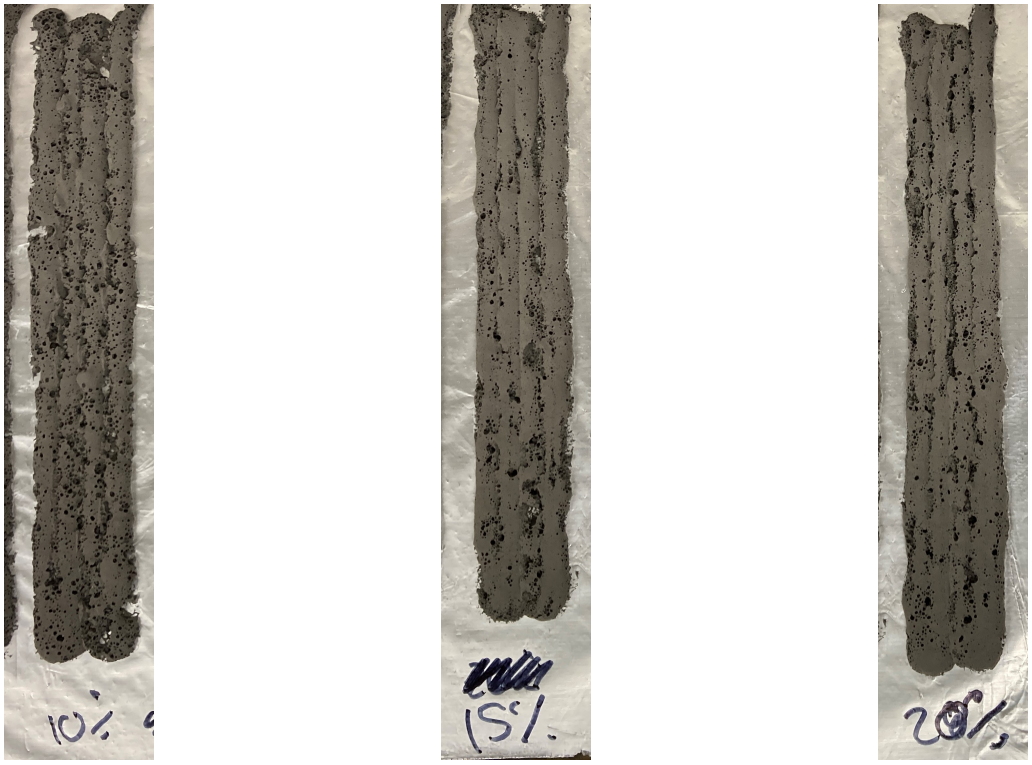

(a) (b) (c)

Figure 110: Images showing track overlap experiments for extruded Ti L foamed slurry at 10 % (a), 15 % (b) and 20 % (c) overlap.

As can be seen for both slurry compositions, an overlap of just 10 % was sufficient to prevent any visible gaps emerging between the adjacent tracks within each layer, and also upon examination of the single-layers it could be seen that even at 20 % overlap the layer heights were consistent for both slurries. Therefore, overlap within the range $10-20$ % for the Ti L and SS L was deemed suitable at this stage, and the effect of the level of overlap within the range when building multi-layer structures is discussed further in Sections 6.3.2 & 6.3.3. Figure 112 shows the cross-sectional height profile of a single layer of SS L slurry produced by depositing four adjacent tracks with an

overlap of 10 %. As can be seen, in contrast to the Ti H layers in Figure 109, the tracks have merged together whilst still producing an even overall layer height, as highlighted by the height measurements. The layer height fluctuates slightly but is always close to the expected layer height of 2 mm, which, as previously discussed, is vital for developing multi-layer extrusions. Due to the parabola profile of the tracks, when an overlap is applied, the edges of parabola where the height of each of the individual track is less than half the maximum height at the centre of the track combine to produce an overall height similar to the maximum height. This can only occur provided the tracks can flow and merge together as with the SS L slurry, which is evident in Figure 112.

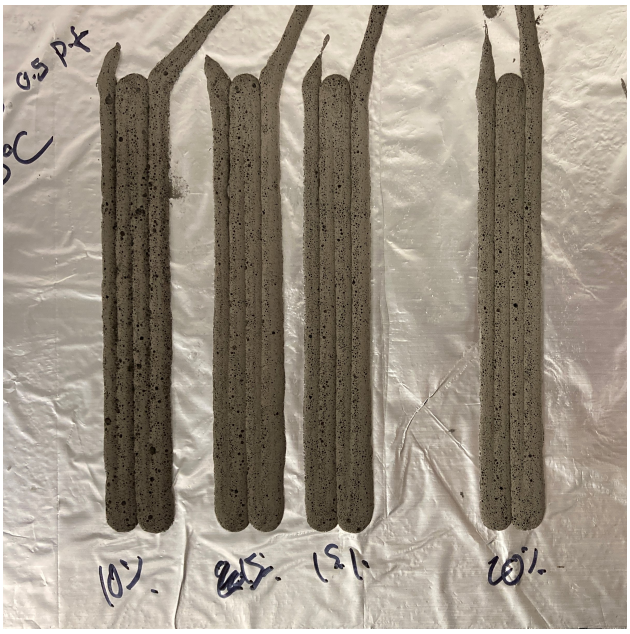

Figure 111: Image showing track overlap experiments for extruded SS L foamed slurry at 10 %, 15 % and 20 % overlap.

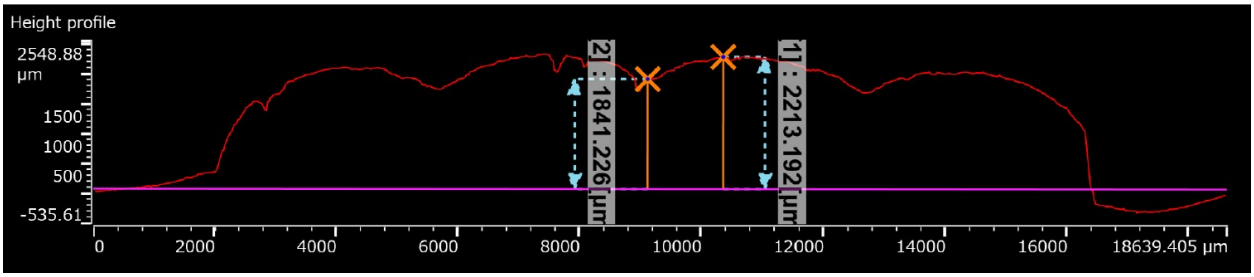

Figure 112: Height profile of full layer produced by depositing 4 adjacent tracks of SS L foamed slurry with 10 % overlap, obtained using LEXT laser confocal microscope.

For the Ti H slurry, due to the issues around uneven layer heights when overlap was increased, 10 % overlap was set as the limit. This 10 % overlap coincides with the minimum recommended overlap for FDM processes in literature [290], however it has been shown for FDM that increasing overlap beyond this leads to improved mechanical properties of the final part, which suggests that for this extrusion process a 10 % overlap may not produce the best quality structures when extruding multiple successive layers. Again, the effect of this on the ability to build multi-layer structures is discussed further in Sections 6.3.1 - 6.3.3.

6.3 Extruding Multi-Layer Structures using Foamed Metal Powder Slurries

6.3.1 Multi-Layer Depositions using Ti H Slurry Composition

Having found optimal extrusion parameter values for the various key slurry compositions that produced tracks with a measured height equal or very close to the *layer height* parameter value, as well as obtaining an idea of the required overlap between adjacent tracks, the next stage of development was to build full 3D structures by depositing multiple layers of slurry, each consisting of a series of individual tracks. These 3D structures consisted of either three or four square layers of approximately 40 mm (depending on the track spacing for each slurry composition) which were extruded following the pattern displayed in Figure 68a. As mentioned in Section 3.5.2, due to the limitations of the Voxelizer software it was not possible to change the extrusion pattern between layers as it only offers the option to repeat a single layer a set number of times, therefore this extrusion pattern was repeated in each layer. This was attempted with the original optimised AM-grade Ti64 powder slurry (Ti H), and then also with the other key slurry compositions.

For the Ti H slurry composition, the tracks were spaced in order to create an overlap of 10 % between adjacent tracks, and the *layer count* was set to 3 with a *layer height* of 2 mm. The Ti H slurry was extruded following this deposition pattern on an aluminium foil layer directly on the heated platform. When the build was complete, the structure was left on the heated platform to fully dry before removing and analysing. Figure 114a shows an image of the final build after removal from the build platform, Figure 114b shows an image of a cross section of the structure and Figure 113 shows the height profile and measurements of the build obtained by scanning with the LEXT laser confocal microscope. The mean measured height of the overall build was 6.1 mm.

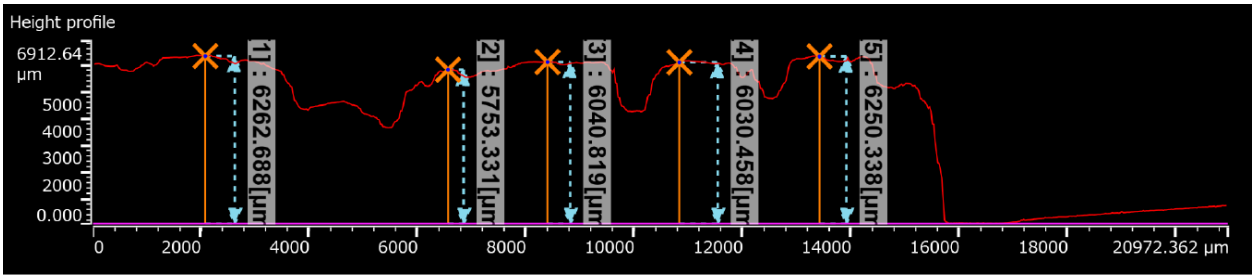

Figure 113: Height profile and height measurements of 3-layer deposition of Ti H foamed slurry, obtained by scanning with LEXT laser confocal microscope.

(a) (b)

Figure 114: Image (a) and cross-section (b) of full 3-layer extrusion of Ti H foamed slurry.

The image and cross-sectional image of the full 3-layer extrusion of TiH slurry (Figures 114a & 114b) show significant visible defects within the structure. As already discussed, the viscosity of this slurry composition means that the extruded tracks are inconsistent in their geometry, and also the tracks are not able to merge together to form a continuous structure. The cross-sectional image shows that even successive layers have not merged and as such each individual track can be identified within the structure. As a result, the structure was incredibly brittle and fell apart when handled because the tracks had very little adhesion to each other. These results demonstrate, as highlighted early on in the extrusion development process, that this slurry composition is not suitable for the extrusion of porous 3D structures. For the process to produce one continuous interconnected

porous structure as outlined in the research brief (Section 2.9), the individual tracks and layers must merge together into one continuous structure, which is evidently not achievable with this slurry composition due to the issues caused by its high viscosity. The only real positive observation from this multi-layer extrusion is that the overall average height of the structure measured from the height profile scan (Figure 113) was calculated to be 6.1 mm, which is approximately as would be expected from depositing three layers when the average height of the single tracks were originally measured to be 1.88 mm with a standard deviation of 0.25 mm (Table 14. This demonstrates the feasibility of the process as a layer-by-layer additive manufacturing process, if the viscosity of the slurry can be reduced whilst maintaining its optimal properties in terms of porosity, pore geometry and stability.

6.3.2 Multi-Layer Depositions using Ti L Slurry Composition

As highlighted in Section 6.2.2, the track overlap experiments concluded that an overlap of 20 % is optimal for Ti L slurry extrusion in order to allow adjacent tracks to merge. However, in order to examine the impact of track overlap on the multi-layer scale, full 3D builds were completed using both 15 % and 20 % overlapped tracks. The builds were set up in the same way as the Ti H 3-layer build, the only difference being that each layer was set up as a perimeter square which was then in-filled with parallel hatching (similar to Figure 62) and the *layer count* was set to 4. Again, the structures were allowed to fully dry on the heated platform before removal and analysis. Figure 115 shows images of both of the 4-layer builds, as well as optical micrographs of the cross sections showing the internal structures.

The optimal track overlap for the Ti L slurry was not necessarily evident from the single-layer experiments. The external images of the resulting extruded structure (Figure 115a) appears to show that 15 % overlap produced a stable structure where tracks combined effectively to build up continuous layers. However, the cross-sectional micrograph (Figure 115c) provides further insight by showing that there are a number of regions where the internal tracks have not merged. Some adjacent tracks have merged together to form continuous material, however throughout the structure the divide between successive layers is clearly visible. Therefore, 20 % overlap was applied in an attempt to mitigate these issues, and the micrograph of the internal cross section of the resulting structure (Figure 115d) shows that the tracks have effectively merged to form continuous material,

and the successive layers have merged together in some places. However, the separation between each layer is still visible in most cases. From the total track length deposited in each layer, and knowing the *print speed* value (5 mm/s) the time taken to deposit each layer was calculated to be 36 seconds, and there was no pause between layers so this time is equal to the period of drying for each layer before being deposited on. From the data collected and discussed later in Chapter 7, it is known that this time is very early within the drying profile for this material, therefore it can

(a) 15% track overlap

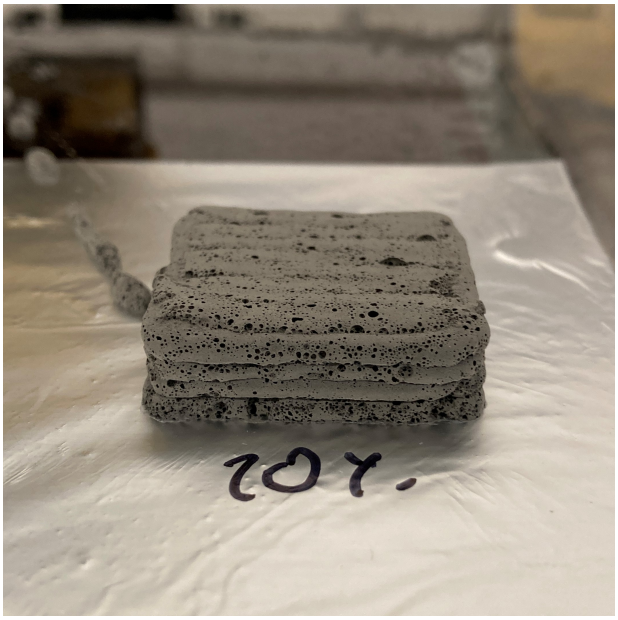

(b) 20% track overlap

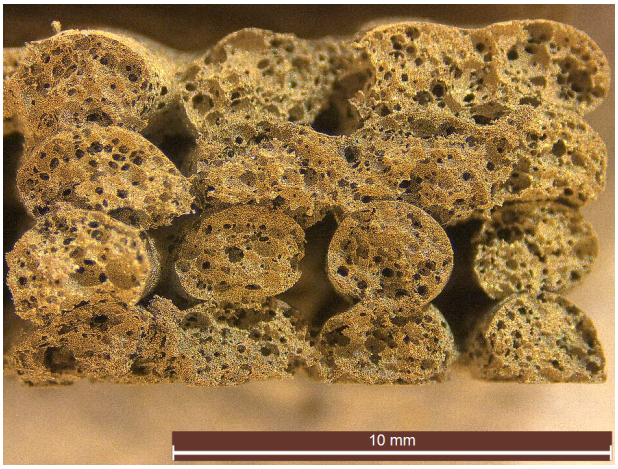

(c) 15% track overlap

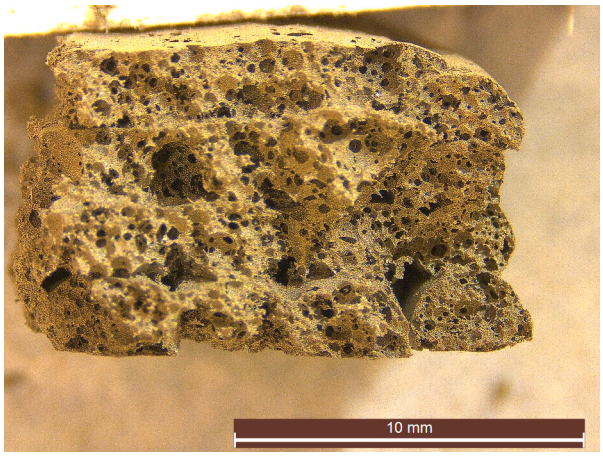

(d) 20% track overlap

Figure 115: Images and cross sectional micrographs showing 4-layer depositions of Ti L foamed slurry with track overlaps of 15 % and 20 %.

be stated that the lack of merging between successive layers is not a result of each layer becoming too dry before the next is deposited, as demonstrated in the layer deposition timing experiments in Section 7.1.2. Therefore it can be concluded that the viscosity of this slurry is responsible for the lack of merging between layers.

Overall, the structure generated using 20 % overlap (115b & 115d) is the best out of all the extruded Ti64 powder foamed slurry structures presented in this work, and provides a very clear demonstration of the promising feasibility of this method of foamed slurry 3D extrusion for producing highly interconnected porous titanium structures using readily available and affordable equipment. By analysing the cross-sectional micrographs using the software Fiji, average height measurements were obtained for both the structures to be 7.97 mm and 8.7 mm for 15 % and 20 % overlap respectively. These are both around the value that would be expected based off the extrusion parameters and initial track dimensions, however it appears that the increase in overlap to 20 % did result in a slight increase in overall height of the structure, however this does not appear to have caused any deposition issues, although if the number of layers extruded was increased beyond four this may start to cause issues as described in Section 6.1.3. It can be suggested that the overall tolerance for the error in total height of the structure should be kept below 1 mm in order to ensure the extrusion process is not disrupted. Again, these figures show that, providing the extrusion parameters are optimised and the track geometry data is available and used to inform the setting up of the .gcode files for 3D extrusion, this process is a feasible method of manufacturing porous Ti64 structures through extruding foamed powder based slurry through a layer-by-layer additive approach.

6.3.3 Multi-Layer Depositions using SS L Slurry Composition

A final 4-layer build was extruded using the SS L foamed slurry composition, with 15 % overlap between tracks and following the same hatching strategy as the Ti L 4-layer build as outlined in Section 6.3.2. The slurry layers were extruded onto a layer of aluminium foil on the pre-heated ZMorph build platform, and the full build was allowed to dry on the platform before being removed for analysis. Figure 116 presents images of the final structure, along with a micrograph of a cross section showing the full height of the build. This 4-layer build was also scanned using the confocal microscope to obtain a height profile and measurements, which is presented in Figure 117.

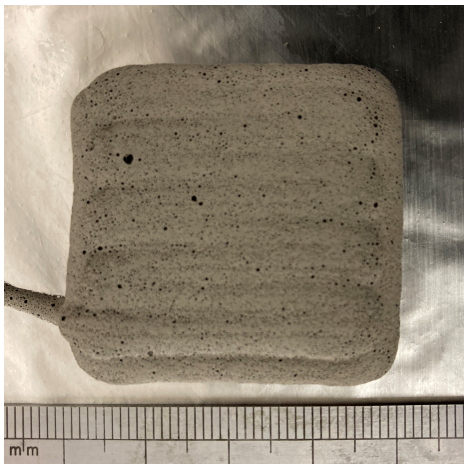

(a)

(b)

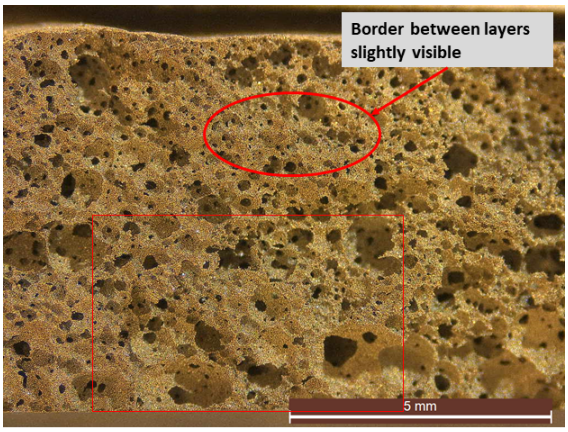

(c)

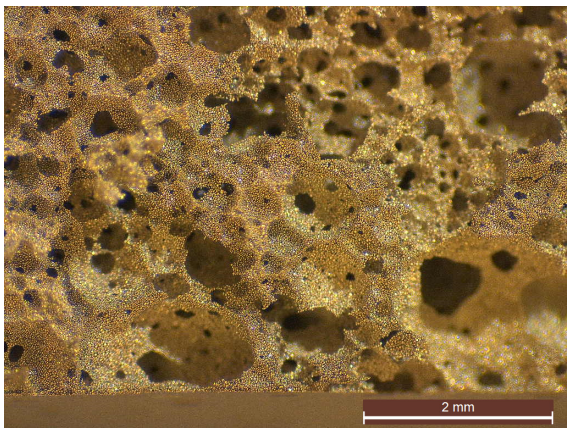

(d)

Figure 116: Images (a & b) and cross sectional micrographs (c & d) showing 4-layer deposition of SS L foamed slurry with track overlap of 15 %.

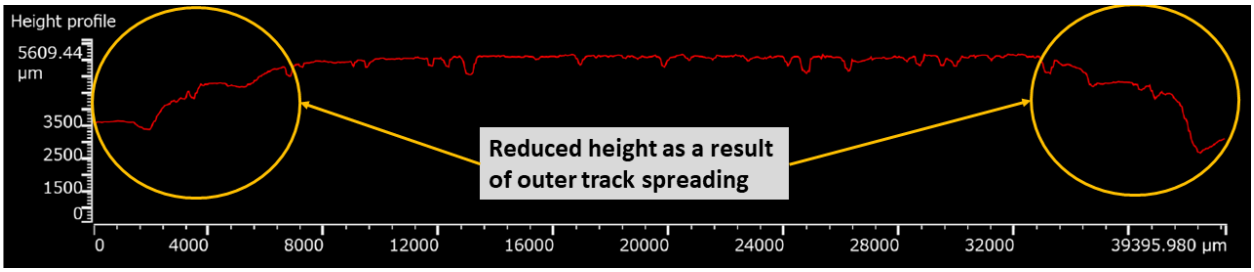

Figure 117: Surface profile of 4-layer deposition of SS L foamed slurry, obtained by scanning with LEXT laser confocal microscope.

The images of the final multi-layer structure extruded using SS L slurry (Figures 116a & 116b) show that the structure is well formed when compared to the original Ti H slurry multi-layer extrusion (Figure 114a), and that the structure is continuous with no visible gaps between tracks

or layers when examined externally. The cross-sectional micrographs (Figure 116c & 116d) show that the tracks and layers have all merged to form a continuous, interconnected porous structure, with the border between successive layers only being faintly visible in a small number of locations as highlighted.

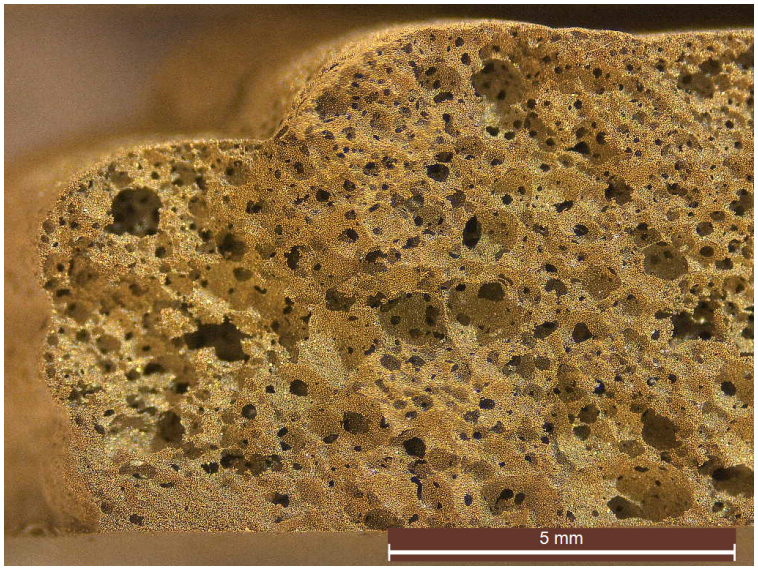

Figure 118: Cross-sectional micrograph showing the change in overall height at the outer edge of 4-layer deposition of SS L foamed slurry.

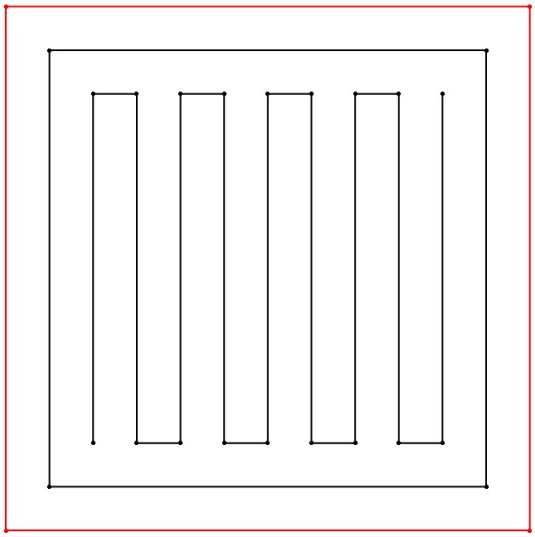

Figure 119: Image showing the extrusion pattern for a single layer of slurry (black) with support material (red) around the outer border track to prevent spreading.

The top surface of the structure is mostly flat apart from the outer edges where it slopes downwards, as can be seen in the height profile shown in Figure 117. An additional cross-sectional micrograph showing the edge of the structure is presented in Figure 118 which highlights this issue. This change in height of the structure is a result of the slurry's ability to flow, and because each layer was extruded following the path presented in Figure 62 where the outer border track was deposited first followed by the internal hatching. Within each layer, this border track is deposited without any adjacent track in place to provide support and prevent the track from spreading, which has resulted in the observed reduction in height. It is likely that this is more pronounced after the first deposited layer, as each successive border track was then deposited on a convex surface produced by the geometry of the previous track which caused the slurry to spread. The average height of the structure at this point obtained by analysing Figure 118 within the Fiji software was 5.55 mm, compared with the average height within the internal region of the structure of 7.1 mm. This deviation in height would have to be rectified in order to build structures with uniform geometry, which could be achieved in various ways. If the software provided the functionality to do so, an additional layer consisting of just the outer border track could be deposited every four or five layers in order to even out the height, however this would require the overall height of the structure both internally and around the border to be consistent in every build which would need further detailed testing and measurements to be taken to provide reliable data which could then be used when setting up the build files. Alternatively, the use of a support material could be employed if the printer had duel-extruder technology, which could be deposited to form an outer casing in order to prevent the border track from spreading, as presented in Figure 119. However, this would present other challenges as the dried powder slurry structure would be bonded to this support material, and therefore it would have to be a material that could be easily burnt out at a low temperature prior to sintering the components.

The average measured height of the internal region of this multi-layer extruded structure is slightly lower than expected, which is again likely to be a result of the flow of the slurry caused by its comparatively low viscosity. This does not present a major issue, as the four layers have still been successfully deposited, however if a greater number of layers were to be extruded it may cause problems as the syringe nozzle would be moving slightly further away from the top surface with each layer. The *layer height* and *path width* parameters could be easily tweaked to resolve

this error, however this would first require a series of multi-layer test extrusions with different layer counts that could be measured to clarify whether the variation in height is consistent. Overall, the SS L multi-layer extrusion presents an optimal internal structure for this application which contains continuous interconnected porosity, as well as well-defined overall geometry especially considering a 2 mm nozzle was used. Considering the simplicity of the process and the use of basic equipment for both mixing the slurry and extruding, this structure demonstrates that foamed slurry extrusion can be used to build 3D porous components.

6.3.4 SS L Builds with Alternative Geometries and Hatching

Having identified the slurry viscosity range that is able to produce stable continuous porous structures through a track-by-track extrusion process, it was important to examine the influence that the extrusion hatching patterns have on the resulting multi-layer structures. In order to do this, multi-layer SS L slurry structures were extruded using an alternative hatching strategy. Previously all layers had been extruded following the hatching pattern shown in Figure 68a, which involves an external contour extrusion followed by parallel internal hatched tracks. The alternative hatching strategy was to extrude concentric contours starting with the outer contour and working towards the centre of each layer, which can be observed in Figures 120a & 120c for square and circular structures respectively.

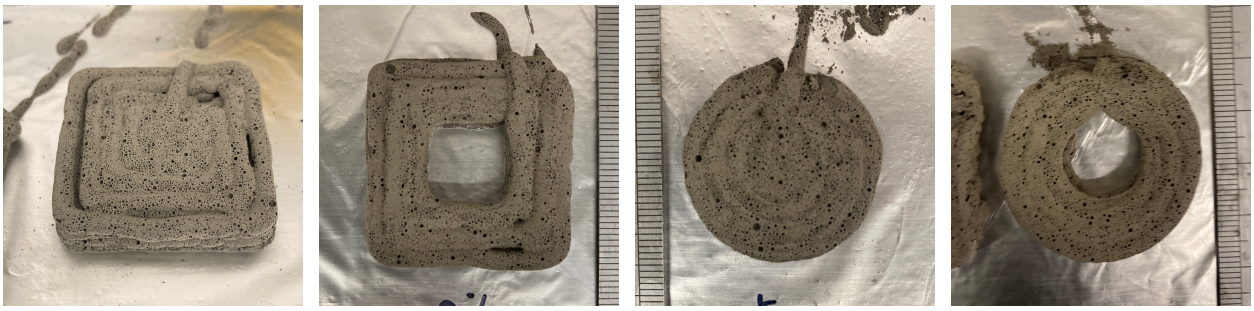

(a) (b) (c) (d)

Figure 120: Images showing 4-layer depositions of SS L slurry using a variety of geometries and alternative hatching strategies.

The 4-layer structure extruded using concentric square hatching was of particular interest as this serves as a direct comparison against the 4-layer SS L structures extruded using parallel hatching presented in Figure 6.3.3. Figure 120a presents an image of this structure, and it can

be clearly observed even from this external image that there is separation between some of the tracks, in particular the outer contour and the second concentric square. The cross-sectional height profile of the structure presented in Figure 121a shows that the height of the structure varies, with the maximum height observed in the centre and a gradual reduction in height towards the outer edges. The same observation can be made of the concentric circular hatched structure, as seen in Figure 121b. As discussed in Section 6.3.3, the cross-sectional height profile of the multi-layer SS L structure extruded using parallel hatching showed that the height of the structure was consistent throughout, apart from at the outer contour where the tracks within each layer had spread to cause an overall drop in height around the outer edge. Therefore, it seems that the concentric hatching strategy caused this continuous variation in height that can be observed. This would have been caused by the fact that each concentric track had more time to spread before the adjacent track was deposited, compared with the parallel line hatching. As the extrusion moved closed to the centre, the time between each concentric square track decreased and so the spreading reduced, resulting in the observed gradual increase in overall height towards the centre of the structure.

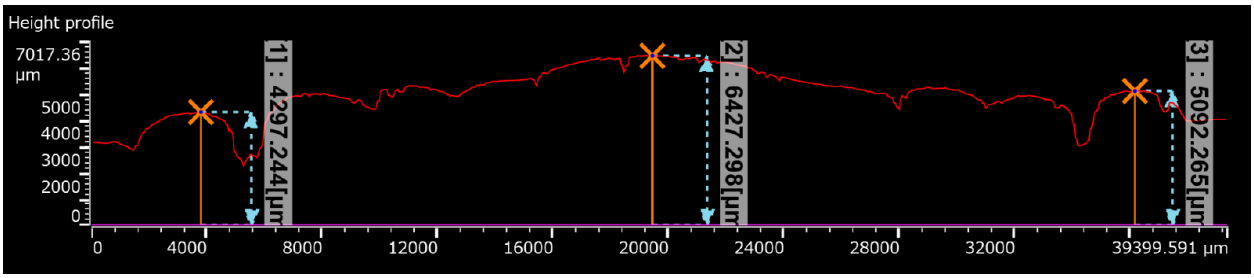

(a)

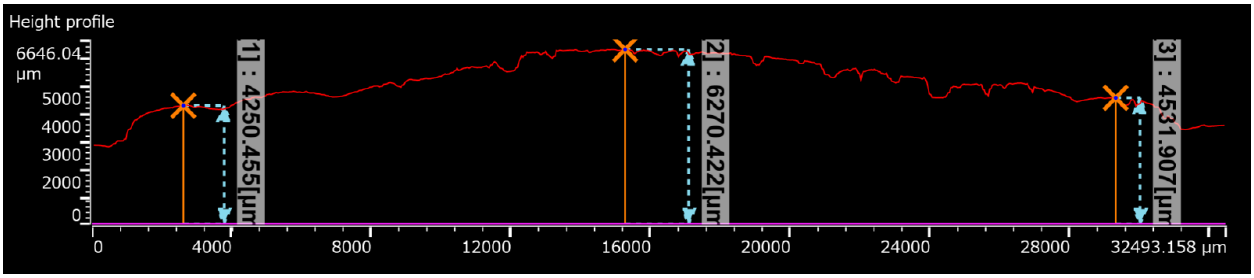

(b)

Figure 121: Height profiles of 4-layer builds consisting of concentric square layers (a) and concentric circle layers (b).

A cross-sectional micrograph of the 4-layer concentric square hatched structure is presented in Figure 122. It can be seen in this micrograph that there are clear gaps between adjacent tracks, as

can also be observed from the external image in Figure 120a. Again, these are likely to be a result of the increased time between the deposition of adjacent tracks due to the concentric hatching strategy compared with parallel hatching, which means that each track has a reduced moisture content when the adjacent track is deposited and therefore do not merge as effectively. Overall, the issues observed with this hatching strategy make it clear that the parallel hatching pattern produces the best results in terms of tracks and layers merging to form a continuous structure with a uniform geometry, providing the issues with the collapsing/spreading of the outer contour can be mitigated as discussed in Section 6.3.3.

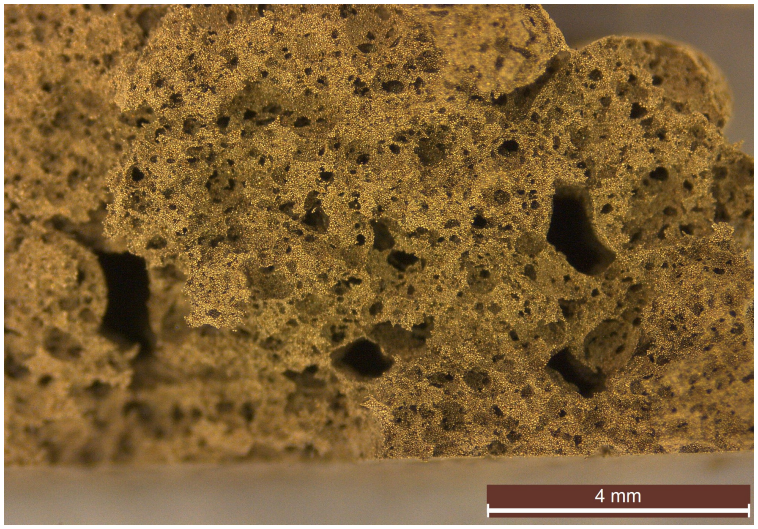

Figure 122: Cross-sectional optical micrograph showing the internal structure of a 4-layer extrusion of SS L slurry using a concentric hatching pattern.

6.4 Summary of 3D Extrusion Process Development and Final Multi-Layer Extrusions

This chapter presents the development of the 3D material extrusion process through the systematic extrusion and analysis of single tracks, single layers and building up to the extrusion of multi-layer structures with each of the three selected key slurry compositions. The structures produced through extruding the three different foamed powder-based slurries provide a broad insight into the potential scope of the process, as well as the challenges associated with this manufacturing technique. The observable differences in quality between the structures demonstrate the degree to which the viscosity of the slurry has an impact on its suitability for this process. These differences

are observed right through from single-track to multi-layer extrusions. The high viscosity of the Ti H slurry resulted in tracks which were irregular and inconsistent in geometry, concurring with the the scattered movement in syringe plunger force shown on the graph presented in Figure 96 (Chapter 6), which suggested that the slurry would not extrude in a steady continuous manner as discussed in Section 5.2.4. The result of these irregularities in track geometry, combined with the lack of fluidity of this slurry composition, resulted in poor quality multi-layer structures where individual tracks and layers did not merge to form continuous material. In contrast, the plunger force graph for SS L slurry controlled extrusions shows that there was no build up of pressure or scattered movement of the plunger during extrusion, which suggested that there was a regular steady flow of material being extruded. This was confirmed by the single-track extrusions which produced tracks that were continuous and regular in geometry, which then combined successfully within the single-layer and multi-layer extrusions by merging to form a continuous interconnected porous structure. The quality of the extruded structure using the SS L slurry clearly demonstrates the feasibility of this process for titanium powder slurries, providing further work can be done to identify suitable means of creating stable foamed slurries with suitable viscosity.

The fluidity of the SS L slurry resulted in the issue relating to the height of the structure around the outer edge, which suggests that the viscosity of this slurry may in fact be too low. Whilst it has clearly been shown that it is important for the slurry to be able to flow to allow adjacent tracks and layers to merge effectively, this issue also highlights that the tracks need to have enough stability to maintain their profile whilst gelation occurs. In general for all slurry compositions, but Ti L and SS L in particular, there was a variation in overall structure height of the multi-layer depositions compared to the expected height based on the number of layers and *layer height* parameter value. For the number of layers deposited in this work (up to a maximum of four) this did not present any real complications, however it has been highlighted that if more layers were deposited this error would compound and eventually cause issues with deposition as the nozzle either moves too far away from the extruded layers or begins to drag through the already deposited material. This issue could be resolved with in-process monitoring of the overall height of the structure, so that the offset between the top layer and the nozzle could be reset during the build process.

The Ti L slurry presented properties between the extremes of the Ti H and SS L slurries. The individual tracks were much more regular than the Ti H tracks and extruded continuously without

any breaks, and the tracks/layers were stable enough to build multi-layer structures with uniform geometry. However, the tracks and layers did not merge as effectively as within the SS L structure. There is a significant range in viscosity between these slurry compositions ($123,357$ and $31,360$ cP for Ti L and SS L respectively), and the observations from the multi-layer extrusions demonstrate that the Ti L slurry is too viscous whilst the SS L slurry is potentially too fluid. As such there is a clear viscosity range within which further developmental research could be conducted in order to find a slurry composition which provides a balance between flow and stability, with the viscosity values of these two slurries as the extreme limits of this range.

The hatching strategy experiments presented in Section 6.3.4 demonstrate that the hatching pattern displayed in Figure 68a which consists of an outer contour which is in-filled with linear parallel hatches produces the most optimal extruded structures in terms of the individual tracks and layers merging to form a continuous porous structure, as well as producing the most accurate overall geometry. Therefore this hatching pattern is recommended for this process, providing the issues with the spreading of the outer contour track can be addressed as discussed in Section 6.3.3.

Whilst the SS L slurry was demonstrated to be the most suitable for 3D material extrusion, and as such has been beneficial for demonstrating the feasibility of the manufacturing process, the primary material of interest in this work is Ti64. Therefore, the Ti L slurry composition was selected for the experiments investigating the drying behaviour of layers of slurry, and the data gathered for developing the thin-layer drying models, as presented in Chapter 7.

7 Chapter 7: Results & Discussion Part IV - Drying Behaviour of Foamed Metal Powder Slurries

Having developed the 3D material extrusion process for the deposition of multi-layer structures using foamed metal powder slurries, and identified the properties of such slurries that produce the most optimal structures through this manufacturing method, the final important area of understanding in need of development was around the drying behaviour of these slurries after deposition. As previously outlined, the slurry is mixed using a thermally activated gelling agent and the slurry is extruded onto a pre-heated platform which provides the thermal energy for gelation and drying to occur. Therefore, understanding the drying behaviour of each layer of deposited slurry and how these properties are affected by the layer thickness, layer count and platform temperature, is vital for identifying the capabilities and limitations of this manufacturing process. This chapter presents the results and discussions around this area of work, both through examining experimentally gathered data, as well as the development of semi-empirical models built upon these data.

7.1 Foamed Slurry Drying Experiments

A range of experiments were designed and conducted in order to gather an understand the drying behaviour of foamed slurry deposited on a pre-heated platform, as described in Section 3.6.1. The results from these experiments are presented and discussed in this section.

7.1.1 Thermal Camera Emissivity Calibration Temperature Profiles

Temperature profiles for foamed titanium slurry deposited on the pre-heated ZMorph build platform were acquired using both a thermocouple and a Flir thermal camera in conjunction with the Flir Tools + software, as described in Section 3.6.2. Figure 123 presents a selection of the emissivity calibration curves comparing temperature profiles obtained using the camera and thermocouple. The data for each of these graphs was captured from a different sample of deposited slurry, each with different thicknesses hence the variation in temperature and time between each plot. For each of the samples represented by the plots in Figure 123 the emissivity value was also varied within the software at 1 % intervals and the resulting temperature plots were compared against

the thermocouple data. The final result of all the emissivity calibration work was that 70 % was selected as the value which provided the most accurate temperature reading over the full range of the plots.

The calibration graphs presented in Figure 123 demonstrate the importance of setting the correct emissivity value for the material being measured. Varying the emissivity between $67 - 75$ % produces a clear difference in the temperature profiles measured by the camera compared against the temperature profile plotted from the thermocouple data. The emissivity value could only be altered at 1 % intervals, and as such it was straightforward to find the value (70 %) that produced a temperature plot with the closest match to the thermocouple data plot (Figure 123b). It is worth noting that the thermal camera temperature profile crosses over the thermocouple profile at around 700 s, which means that before this point the camera is slightly under-estimating the slurry temperature, and beyond this point it is slightly over-estimating. This change is due to the fact that the surface of the deposited slurry visually changes during the drying process, and it transitions from being a glossy surface to a matt surface which will affect the emissivity of the material and in turn the temperature measured by the camera. Also, the thermal camera reading is not particularly accurate during the initial heating prior to the plateau, which again is due to change in appearance of the slurry within this region as it is heated above the gelation temperature and gels. Despite these variations, within the main region of the temperature profile the thermal camera reading is within $\pm 2°C$ when emissivity was set to 70 %.

Having calibrated emissivity for the slurry drying process, it was then possible to use a thermal camera to record continuous temperature data of slurry deposited on the heated platform. This provided a much more efficient method of gathering this data compared with trying to position a thermocouple within the slurry, which would not be feasible if actually extruding the material from the syringe rather than manually depositing it. Also, the position of the thermocouple within the syringe in terms of proximity to the heated platform would affect temperature data recorded, so using a thermal camera to record to top surface of the slurry whilst drying is a more repeatable means of gathering this data.

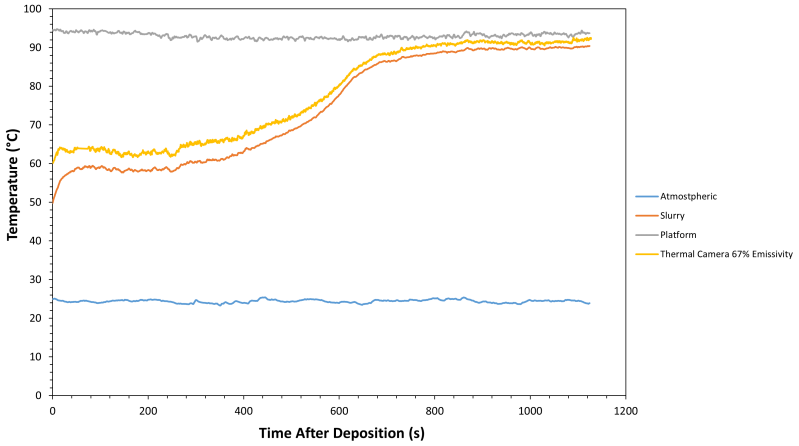

(a) 67% Emissivity

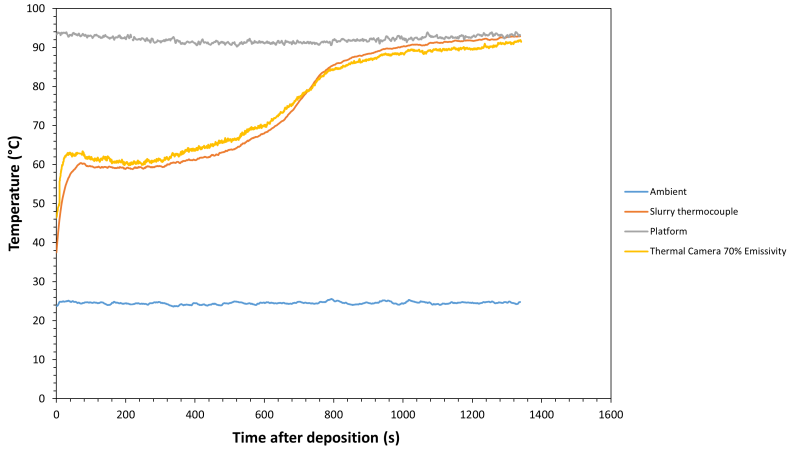

(b) 70% Emissivity

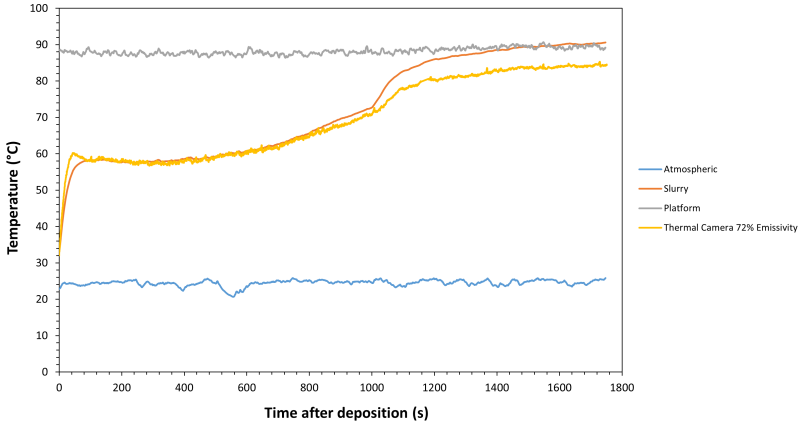

(c) 72% Emissivity

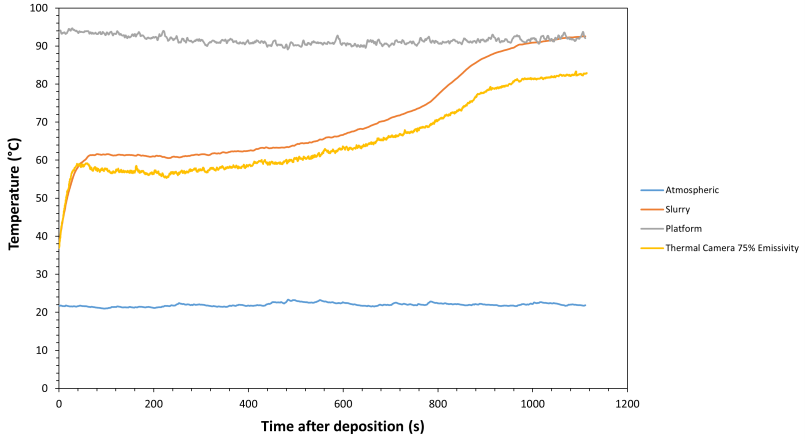

(d) 75% Emissivity

Figure 123: Graphs showing temperature profiles of foamed titanium slurry deposited on the pre-heated platform captured using thermocouples and thermal imaging with various emissivity values.

7.1.2 Layer Deposition Timing Experiment using SS L Slurry Composition

All of the multi-layer extrusions presented in Chapter 6 had been printed without any programmed pause time between layer deposition, meaning that the time that each layer had to dry was simply the length of time it took to deposit a full layer before the next layer was then deposited on top. In order to further understand the impact of the drying time for each layer on the quality of the build, and the bonding between layers, a deposition timing experiment was designed and conducted using SS L foamed slurry. This slurry was selected for further development work as it produced the highest quality extruded structure, as presented in Section 6.3.3, and so provides the best demonstration of the feasibility of this manufacturing process.

Following the method described in Section 3.5.7, a 2-layer extrusion was deposited such that the second layer was extruded in the reverse order to the first. This resulted in a structure where the time between deposition of the two successive layers varied between $0 - 600\ s$ throughout the structure, as highlighted in Figure 124. Once the 2-layer build had fully dried, it was fractured in multiple places and the cross sections were examined using an optical microscope. Figure 124 shows an image of the full extrusion after drying. The top-left of the build is the point where extrusion began/ended meaning the time between deposition of the 2 layers at this point was $\sim 600s$, and the top-right is where the first layer extrusion ended and the second layer began meaning there was no time between. Figure 125 shows cross-sectional micrographs of 3 key regions within the 2-layer deposition corresponding to $\sim 600s$, $\sim 300s$ and $0s$ intervals between layer deposition.

As highlighted in Figure 124, at the left side of the structure there are visible gaps between the tracks, starting from the track which corresponds to a time of $440s$ between deposition of the first and second layers. The cross-sectional micrograph taken of the two tracks at the far left of the two-layer structure with a deposition time interval of $\sim 600s$ (Figure 125a), shows that even where the adjacent tracks appear to be merged there are gaps present within the structure and the border between layers is clearly visible demonstrating that the layers have not effectively merged to form a continuous material. The cross-sectional micrograph presented in Figure 125c shows that for the track with the minimum deposition interval between the two layers ($0 - 20s$), there is a clear reduction in height of the overall structure which demonstrates that the bottom layer has not gelled sufficiently to support the deposition of the next layer and as a result the second layer has sunk

into it. The second track (left side of Figure 125c), which had a deposition time interval of over $20s$, appears to be more structurally stable suggesting that this time interval is enough to allow the first layer to sufficiently gel. The cross-sectional micrograph showing the centre of the two-layer structure with a deposition time interval of $\sim 300s$ (Figure 125b) shows that the tracks and layers at this point have effectively merged to form a continuous material, whilst also remaining structurally stable. It can be seen from this micrograph that pores are interconnected even across the boundary between what was initially separate layers, demonstrating that the extruded tracks have formed a continuous interconnected porous structure which is a key requirement of orthopaedic implant material.

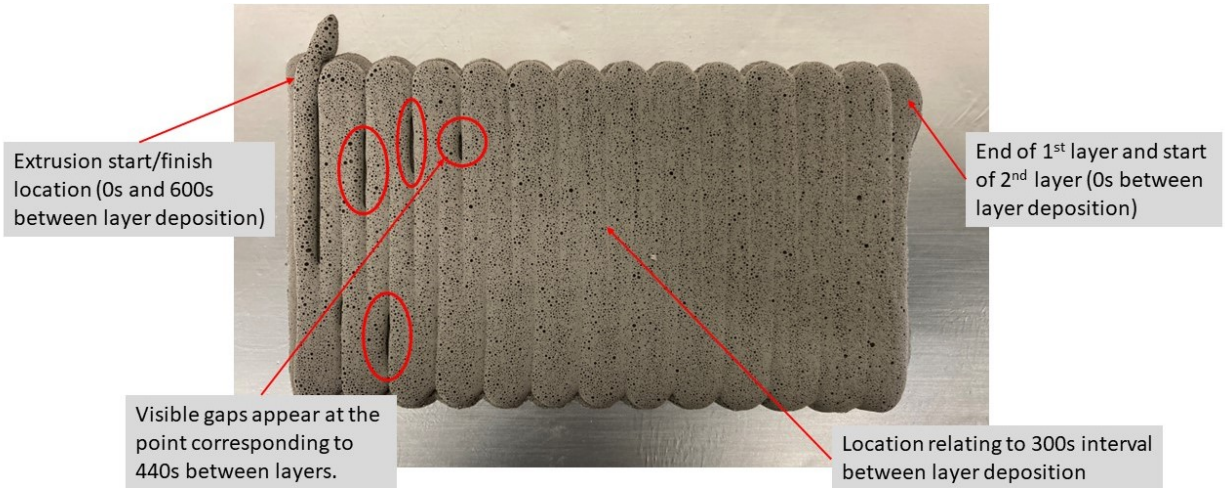

Figure 124: Image showing the final 2-layer structure deposited for layer deposition timing experiment.

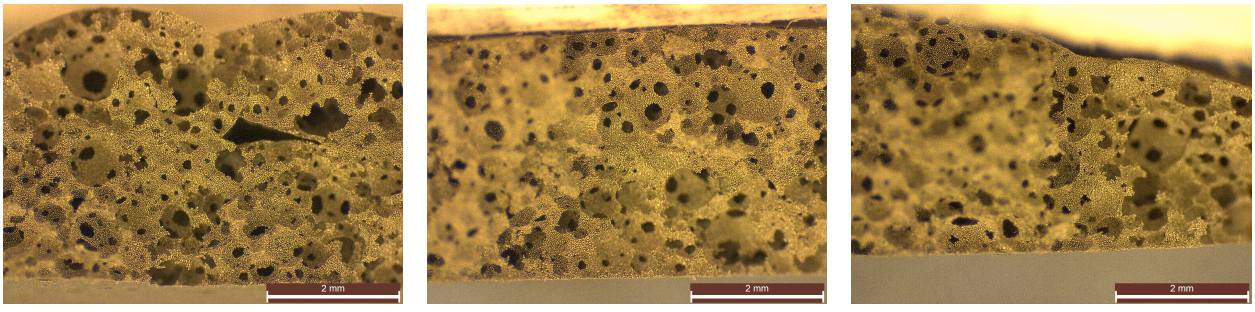

(a) (b) (c)

Figure 125: Cross-sectional micrographs of 2-layer SS L layer deposition timing build with $\sim 600s$ (a), $\sim 300s$ (b) and $0s$ (c) time interval between layer deposition.

From the micrographs presented in Figure 125 the height of the two-layer structure was mea-

sured at the various deposition intervals. For $600s$ and $300s$ the height was measured to be 3.92 mm and 3.69 mm respectively, confirming the observations made in Section 6.3.3 regarding the overall height of the multi-layer structure being less than expected and how this is related to the fluidity of the slurry. For the maximum deposition interval, the height of the two-layer structure was as would be expected based on the height of the individual tracks, however this resulted in issues around merging of tracks and layers. Some flow and spreading of the slurry is necessary to avoid these issues, which inevitably leads to some reduction in the overall height of the structure when depositing multiple layers. The observations from this experiment demonstrate that allowing a slurry layer to dry for too long prevents the next layer from merging properly, which suggests that a certain degree of residual moisture in the initial layer is required to allow the layers to merge together.

Figure 126 presents the surface temperature profile of a single $\sim$ 2 mm layer of foamed SS L slurry, obtained using thermal imaging as described in Section 3.6.3. The drying time can be approximated from the temperature profile plot as highlighted in Section 7.2. As discussed in detail later in Section 7.1.4, for all slurry layer depositions at different thicknesses the end of the 'drying plateau' on the temperature profile plot represents the point at which the slurry is at least 80 % dry (containing $<$ 20 % moisture), which for the SS L $\sim$ 2 mm layer profile in Figure 126 corresponds to $240s$. The moisture content beyond this point continues to decrease at a significantly reduced rate. The moisture content at $300s$ can be estimated to be $\sim$ 10 %, and beyond $440s$ where separation between tracks and layers begins to be observed it is likely that the moisture content is $<$ 5 %. Correlating these moisture levels with the observations from the layer deposition timing experiment, it can be recommended that 5 % should be the minimum moisture content required in the previous layer to allow successful merging of the next layer when deposited, which can be applied to layers of different thicknesses and platform temperatures combined with the mathematical thermal models discussed in Section 7.2 to inform extrusion parameters and deposition timing for specific slurries and conditions.

The height of the two-layer structure within the track with the $0 - 20s$ deposition interval was measured to be 2.72 mm, clearly showing, as already discussed, that the initial layer was not able to support the deposition of the next layer due to lack of gelation. At $24s$ on the slurry temperature profile (Figure 126) the slurry temperature has reached $76°C$ which is greater than the gelation

temperature of the methylcellulose solution ($\sim 48°C$). The height of second set of tracks within the structure in Figure 125c where the deposition interval was over $20s$ was measured to be 3.54 mm, which is very similar to the height measured at the $300s$ interval point, showing that as long as the initial layer has gelled it provides sufficient structural support for the next layer to be deposited.

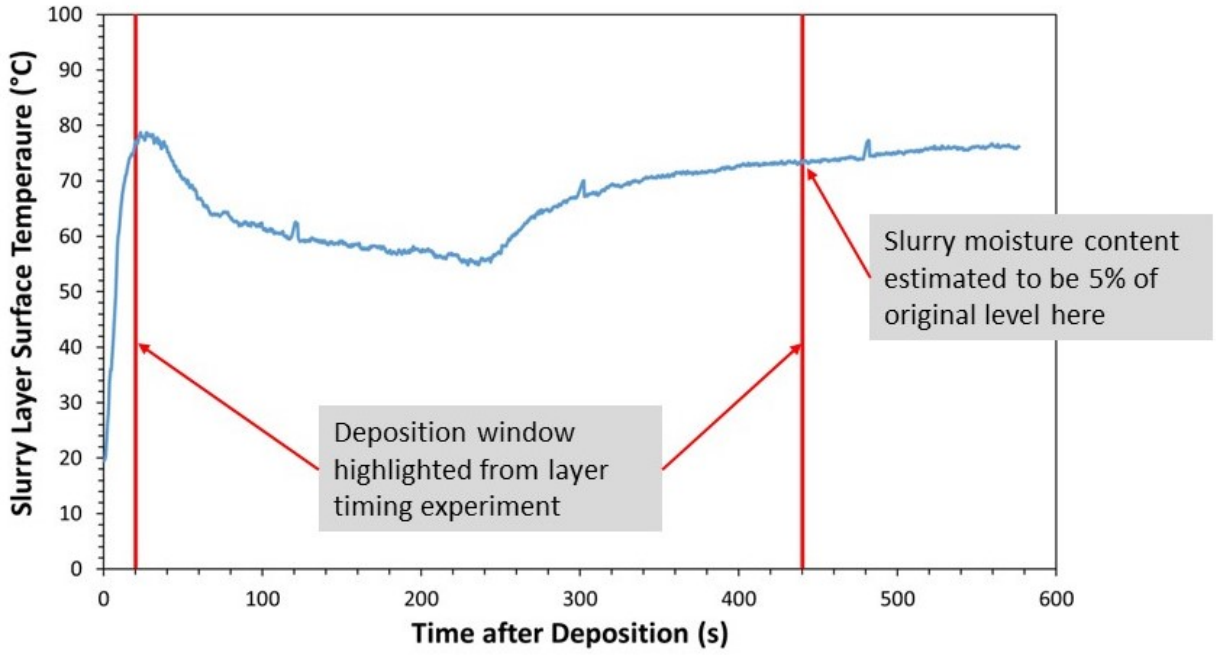

Figure 126: Temperature profiles for top surface of foamed SS L ~ 2 mm layer deposited on ZMorph build platform pre-heated to 100°C, with highlighted deposition time interval for second layer.

From these observations it can be recommended that the ideal range for timing between layer deposition is $20 - 440s$, which is visualised on the slurry temperature profile in Figure 126. Whilst this provides a wide range for deposition time, it may restrict the maximum geometry of an individual layer when extruding with a linear speed of 5 mm/s as in these experiments. However, little work has been done to optimise the extrusion parameters in order to print with greater linear speeds for the SS L slurry. With the properties of this slurry being much more optimal for extruding than the Ti H slurry, it is highly likely that the *print speed* could be increased to 10 mm/s which would double the maximum layer size that can be extruded within this time frame.

7.1.3 Slurry Temperature Profiles for Various Platform Temperature and Layer Thickness Combinations

As described in Section 3.6.3, temperature profiles were captured using the thermal camera of the top surface of a layer of foamed titanium slurry. Figures 127 - 129 present the temperature profiles plotted using the data from the from thermal camera recordings for slurry layer thicknesses of 2, 4 and 6 mm deposited on the platform pre-heated to 80, 90 and 100$°C$. The regular small spikes observed in each of the temperature plots are caused by the periodic self calibration of the camera which results in a blank image for a single frame and then interferes with the temperature reading during that frame. The true platform temperature values for each pre-set temperature were recorded separately with a thermocouple by logging the platform temperature for 60s at 1s intervals and then calculating an average, and are provided in Table 15. Also, for the samples used to gather the temperature profile data presented this section, as well as various samples from the mass loss drying experiments described in Section 7.1.4, true layer thickness values were obtained by removing the samples from the platform once then had fully dried and measuring the thickness of each sample using vernier calipers. As described in Section 3.6.3, the thickness of each sample layer was produced by depositing a mass of slurry on the platform and then levelling it to a certain height using the levelling tool. However, this method does not guarantee that the sample will remain at this specified thickness as there is likely to be some settling after the sample is deposited and levelled, hence the importance of gathering true measurements for sample thickness. Table 15 provides the average measured sample thickness values for each combination of platform temperature and leveller tool aperture size used to level the sample.

Platform Temperature ($°C$)		**Nominal Sample Layer Thickness (mm)**		
Pre-set	Measured	2	4	6
70	72	1.83	3.54	5.34
80	81	1.84	3.44	5.58
90	92	1.6	3.2	5.26
100	101	1.8	3.03	5.48

Table 15: Table presenting the true average measured sample thicknesses for each combination of platform temperature and nominal thickness (aperture size of levelling tool used when depositing sample), as well as the true average measured platform temperatures.

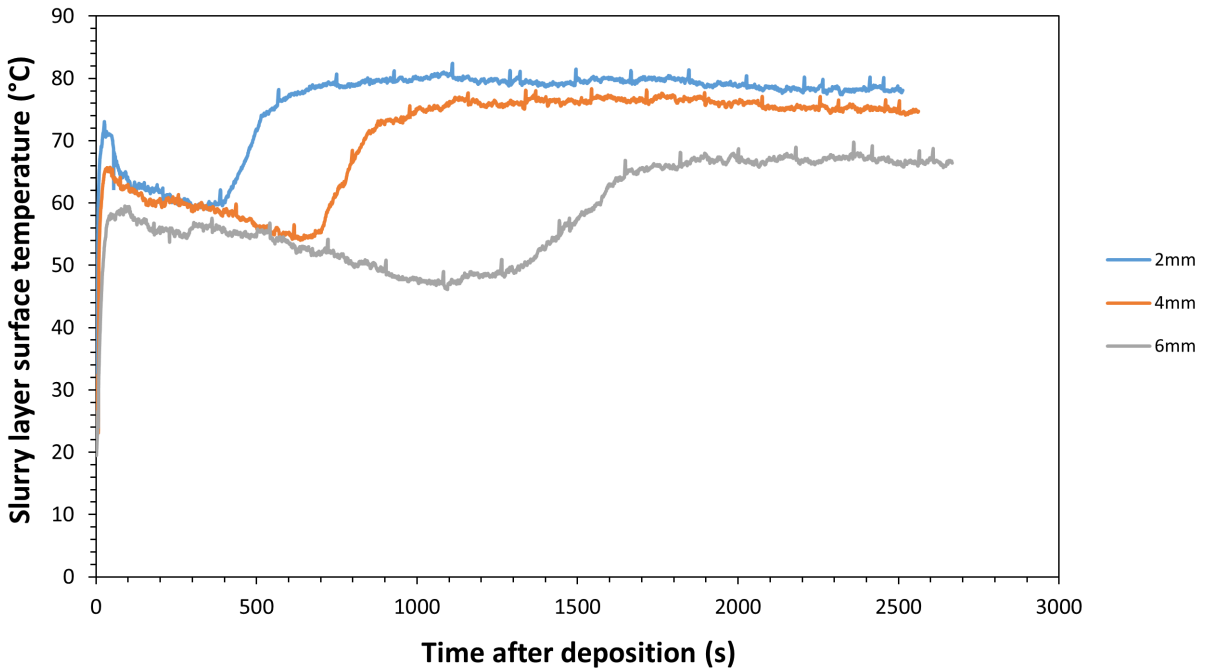

Figure 127: Temperature profiles for top surface of foamed titanium slurry layers deposited on ZMorph build platform pre-heated to 80°C with various thicknesses.

All the profiles presented in Figures 127 - 129 follow similar trends, with an initial spike in temperature during which gelation of the slurry occurs as it moves above the gelation temperature of the MC solution ($48°C$), followed by a plateau in temperature or a steady decease in temperature before increasing again up to the final steady state temperature. As would be expected, increasing the layer thickness results in an increased time for the slurry to reach the final steady state temperature. Also, the final temperature reached for all layer thicknesses is below the platform temperature, with the 2 mm layers reaching temperatures close to this and as the layer thickness increases the steady state temperature decreases further away from the platform temperature. It is worth highlighting that the thickness values stated on the graphs are the nominal thicknesses, meaning they were levelled using the slot on the levelling tool with that dimension (Figure 71c), however the true layer thicknesses were different due to spreading of the slurry after deposition. These true values are presented in Table 15.

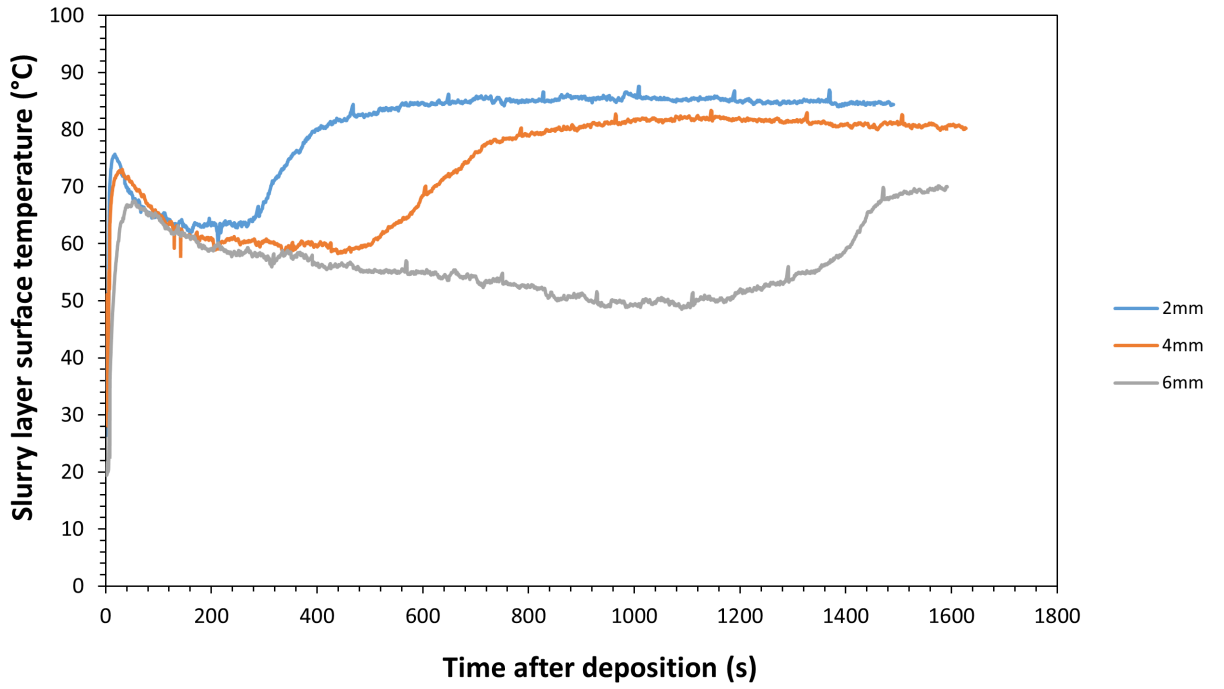

Figure 128: Temperature profiles for top surface of foamed titanium slurry layers deposited on ZMorph build platform pre-heated to 90°C with various thicknesses.

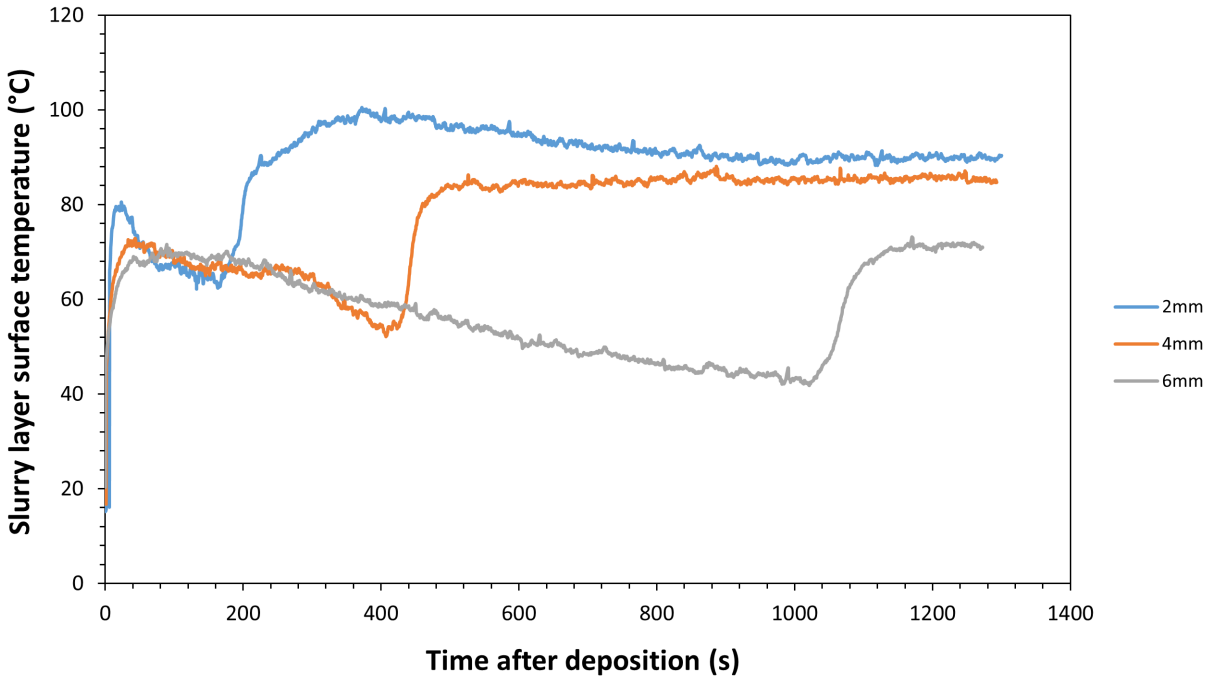

Figure 129: Temperature profiles for top surface of foamed titanium slurry layers deposited on ZMorph build platform pre-heated to 100°C with various thicknesses.

7.1.4 Slurry Drying Mass Loss Data

Whilst the temperature profiles obtained using thermal imaging provide an interesting insight in to the behaviour of the slurry once deposited on the heated platform, in order to gain a deeper insight it is important to understand the drying behaviour of the slurry during these profiles. Drying rates for foamed slurry layer samples deposited on the pre-heated platform were obtained by gathering mass loss data following the methods outlined in Section 3.6.4. This data was gathered for $4mm$ thick layers and platform temperatures of $70, 80, 90$ and $100°C$, as well as 2 and $6mm$ layers at 80 and $90°C$ in order to provide an array of data that could be used to develop the *drying time model* as described in Section 7.2.2. The mass loss measurements for $100°C$ and $4mm$ layer thickness are presented in Figure 130a alongside the surface temperature profile captured previously. Also, the final surface temperature of each individual sample was acquired prior to removal for weighing using the thermal camera recording, and these final temperature readings are plotted alongside the surface temperature profile in Figure 130b. Only the data for this temperature and thickness are presented here to provide an example for the purpose of discussion, however the rest of the mass loss data and final sample temperature recordings for the other platform temperature and layer thickness combinations are provided in Appendix D.

Analysis of the mass loss plots in Figure 130b and Appendix D demonstrates that evaporation of water from the slurry begins to occur during the initial temperature spike, and that during the near-constant temperature plateau region, the majority of the moisture content is evaporated, and hence this region of each of the plots is referred to as the 'drying plateau'. The drying rate extracted from the mass % trendline for the example plot displayed in Figure 130b was approximately $1\%/20s$. There appears to be some drying that still occurs beyond the end of this region after the temperature has increased up to the final steady state temperature, however it is at a reduced rate (approximately $1\%/120s$ for the example data shown). It is well understood that evaporation is an endothermic process, as the energy required to gasify a liquid is drawn from the surrounding environment which results in a cooling effect [292]. This explains why the temperature of the slurry either remains constant or steadily decreases whilst the majority of the evaporation of water is occurring, before increasing up to the final steady state temperature. The slurry composition consists of an initial water content of 29 % of the overall mass of the slurry.

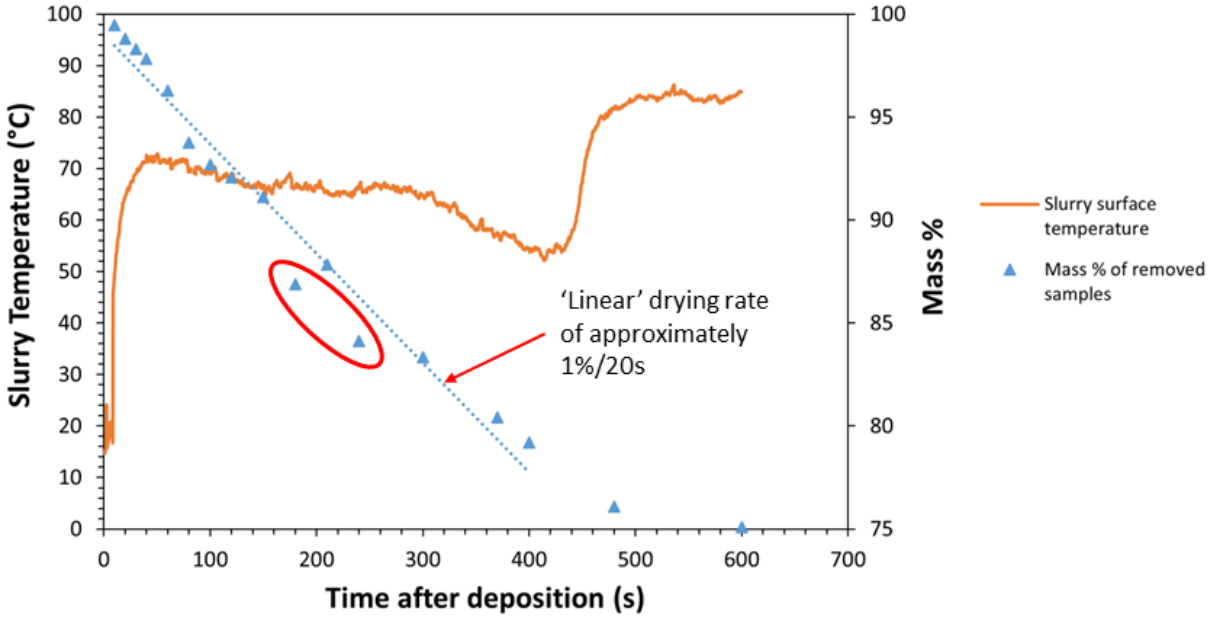

(a)

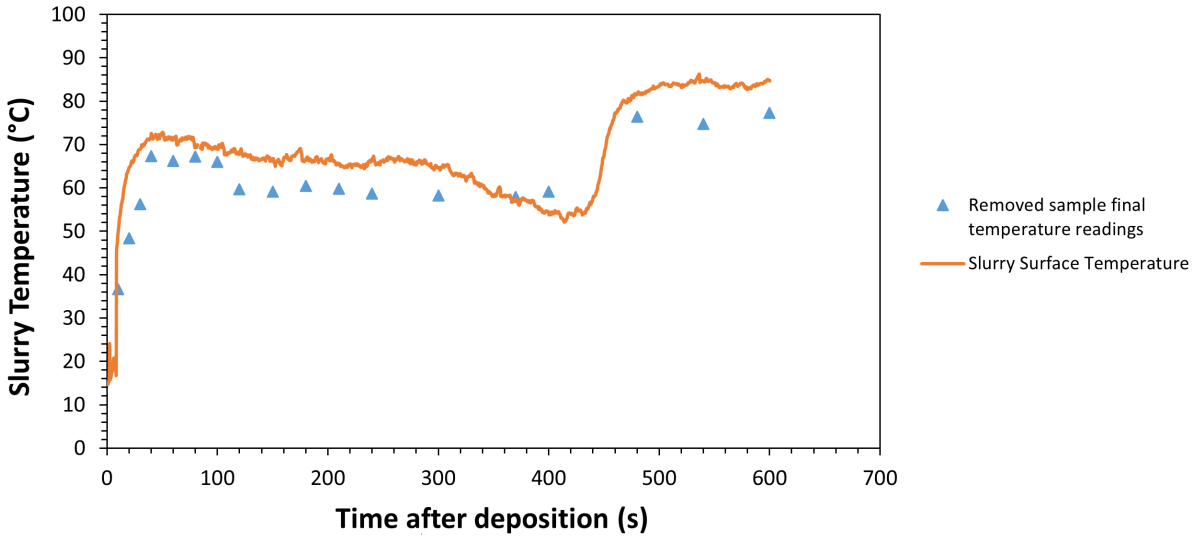

(b)

Figure 130: Graphs showing sample mass loss data against baseline temperature profile (a) and final sample temperature recordings against baseline temperature profile (b) for 4mm sample layers of foamed slurry deposited on 100°C platform.

As can be seen in Figure 130a, the percentage mass of the deposited slurry has reduced by around $24-25$ % by the end of the drying plateau, meaning that by this point at least 80 % of the water within the slurry has evaporated, and as such it follows that the remaining water evaporates at a reduced rate at the steady state temperature. Figure 130b shows the temperature of each

sample which was removed for mass measurement compared against the continuous temperature profile obtained from the control sample. The temperature readings for each sample closely follow the continuous profile which demonstrates that the data is reliable. There are some anomalies in the mass percentage data points as highlighted in Figure 130a, which is to be expected when each measurement corresponds to an individual sample that was removed and weighed and therefore will have slightly different thicknesses that impact the drying rate. Overall, however, the data fits well and provides a valuable insight into the drying behaviour. The data gathered from these experiments show that the majority of slurry drying (~ 80 %) has occurred by the end of the drying plateau region on the temperature profile, which means that the drying rate can be estimated from the temperature profile for all slurry temperature profiles even if mass loss measurements haven't been obtained, simply by extracting the time corresponding to the end of the drying plateau. This provides important data required for the development of the thermal models as described in Section 7.2.

7.2 Development of Semi-Empirical Drying Models for Titanium Powder Slurry

As previously highlighted, the thermal behaviour of each layer of deposited slurry on the heated platform is fundamentally important to the successful development of the deposition process in terms of the gelling and drying of each layer of the slurry. In order to build a thorough understanding of the thermal behaviour, three specific semi-empirical thermal models were developed using data collected as described in Section 3.6.1 and presented and discussed in Section 7.1, that could then be used to predict further information beyond the collected data which provides insight into the scope and limitations of this process. The development of these models is presented in this section, and the output data generated from them are presented and discussed.

The models are each built on slightly different variations of the model derived from Newton's law of cooling. The moisture ratio model was based on the *Modified Page-I* model, because this could be rearranged to allow the available moisture ratio data at various times during drying to be used in order to acquire the necessary empirical constants required in order to build the model. Similarly the original *Lewis* model was selected for developing the drying time model, because this could be rearranged to allow drying time and sample thickness data to be used to acquire values for the empirical constants required to build the model. As highlighted in Sections 2.7.1 2.7.2,

there are over twenty adapted versions of the models based on Newton's law of cooling, which have been developed for various thin-layer drying applications, and there is no single identifiable model that consistently provides the best universal prediction of drying behaviour. Therefore, it is simply recommended that a suitable model should be selected for the specific application based on the experimental data. As such, selecting different variations of the models in order to build the semi-empirical models presented in this work was deemed to be a suitable approach.

7.2.1 Moisture Ratio Model Development

The moisture ratio model is a model that, for a given layer thickness, can be used to predict the remaining moisture content of the deposited slurry at a given time after deposition. This model was developed using the *Modified Page-I model* for moisture ratio (Equation 18), which is based on the model derived by Lewis [256] for the drying of thin-layer materials.

$$MR = exp(-(kt)^n) \tag{18}$$

Where MR is the moisture ratio (the ratio of the mass of water present within the sample at any specific time to the initial mass of water within it), k is a drying constant, t is the time in seconds and n is a dimensionless empirical constant. Taking the natural log of both sides of the equation gives:

$$ln(MR) = -(kt)^n = -k^n t^n \tag{19}$$

Which can also be written:

$$-ln(MR) = k^n t^n \tag{20}$$

By taking the natural log of both sides of the equation again and then applying the laws of logarithms the following can be derived:

$$ln(-ln(MR)) = ln(k^n t^n) \tag{21}$$

$$ln(-ln(MR)) = nln(t) + nln(k) \tag{22}$$

When comparing Equation 22 to the equation of a straight line, it is clear that plotting $ln(-ln(MR))$ against $ln(t)$ gives n as the gradient and $nln(k)$ as the intercept. This was applied to the mass loss data collected as described in Section 3.6.4 for each platform temperature in order to develop a series of models predicting the moisture ratio of a single layer of slurry at any given time after being deposited on a pre-heated platform. These models are based upon the thickness of slurry layer being constant, and therefore require mass loss data at multiple platform temperatures for the same layer thickness. Mass loss data had been gathered for $4mm$ layer thickness at $70, 80, 90$ and $100°C$ platform temperatures, and therefore the moisture ratio models were developed using this data. The moisture ratio, as defined previously, refers to the ratio of the mass of water remaining within the sample to the initial mass of water within it. Using the gathered mass loss data the experimental moisture ratio (MR) values were calculated for each sample, so that $ln(-ln(MR))$ could be plotted against $ln(t)$ for each platform temperature in order to obtain values for the constants n and k from the equations of the straight lines produced from the data. These plots, along with the equations of the straight lines, are provided in Appendix E with the plot for $100°C$ provided in Figure 131 as an example, and the values for the empirical constants extracted from these plots are summarised in Table 16.

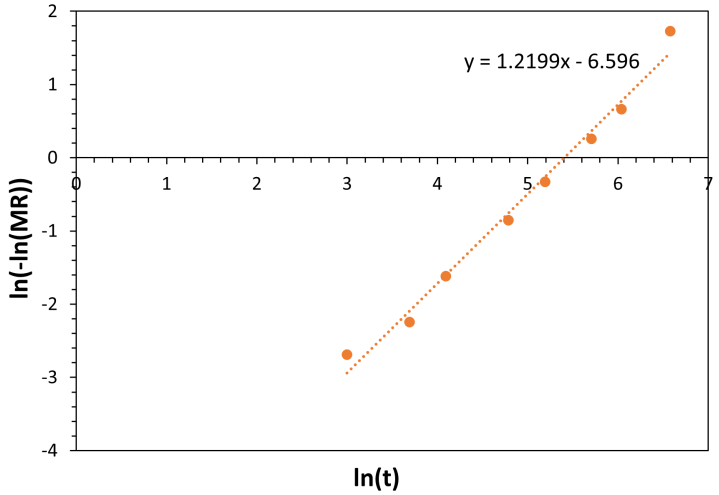

Figure 131: Graph showing straight line plot of ln(MR) against ln(t) for moisture ratio data gathered from samples deposited on the platform at $100°C$, along with the equation of the straigt line used to extract the empirical constants for this temperature.

As previously stated, the drying constant k is specific to the platform temperature upon which

the samples were dried, however the empirical constant n is the same across all platform temperatures. Taking an average of the n values obtained from the plots and presented in Table 16, gives a value of $n = 1.23$. Applying this average value and the k values specific to each platform temperature to Equation 30, produced the initial basic moisture ratio models for each temperature. From these models the plots in Figure 132 were produced which provide the theoretical moisture ratio for a $4mm$ thick layer of slurry deposited on a platform pre-heated to the specific temperatures at any given time after deposition.

	Platform Temperature (°C)			
	70	80	90	100
n (gradient)	1.2192	1.251	1.2386	1.2199
$nln(k)$ (intercept)	-7.5749	-7.5498	-6.9304	-6.596
k	0.0020032	0.0023935	0.0037151	0.0044851

Table 16: Table summarising key values obtained from the equations of straight lines plotted in Figure 160.

This simple initial model was used to predict moisture ratio for each platform temperature, with the constant k being a function of temperature but n the same for all temperatures. Whilst this model provides useful data, it is restricted by only providing output data for the platform temperatures at which data was gathered. It can, however, be developed further to be able to predict the moisture ratio for any platform temperature, by defining k using an Arrhenius-type relationship as developed by Crisp and Woods [293] by applying Equation 23 [294].

$$D_{eff} = D_0 exp\left(-\frac{E_a}{RT}\right) \tag{23}$$

Where D_{eff} is the effective moisture diffusivity ($m^2 s^{-1}$), D_0 is the Arrhenius pre-exponential factor, E_a is the activation energy ($Jmol^{-1}$), R is the universal gas constant and T is the platform temperature in degrees Kelvin. By combining Equation 23 with the linear relationship between the drying constant k and the effective moisture diffusivity described by Dadali et al. [295] (Equation 24), Equation 25 can be derived.

$$k = \lambda D_{eff} \tag{24}$$

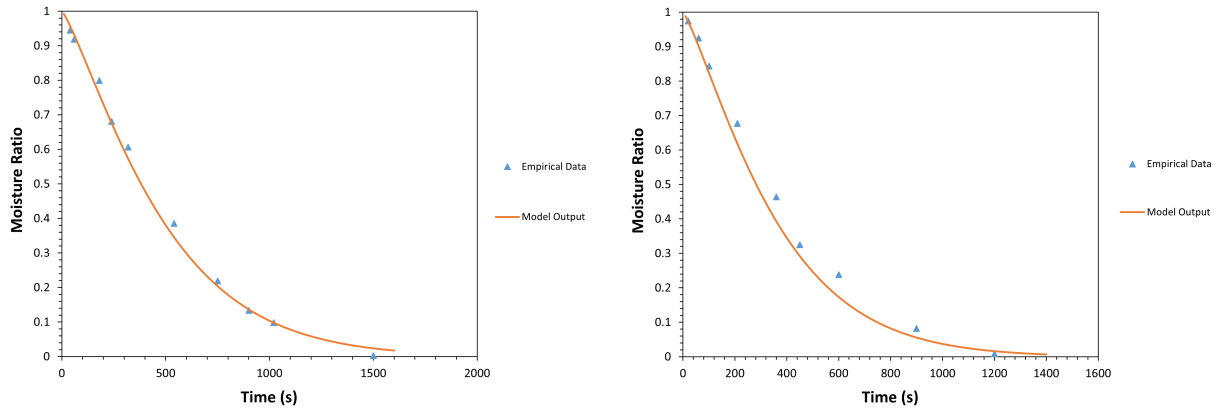

(a) 70 °C

(b) 80 °C

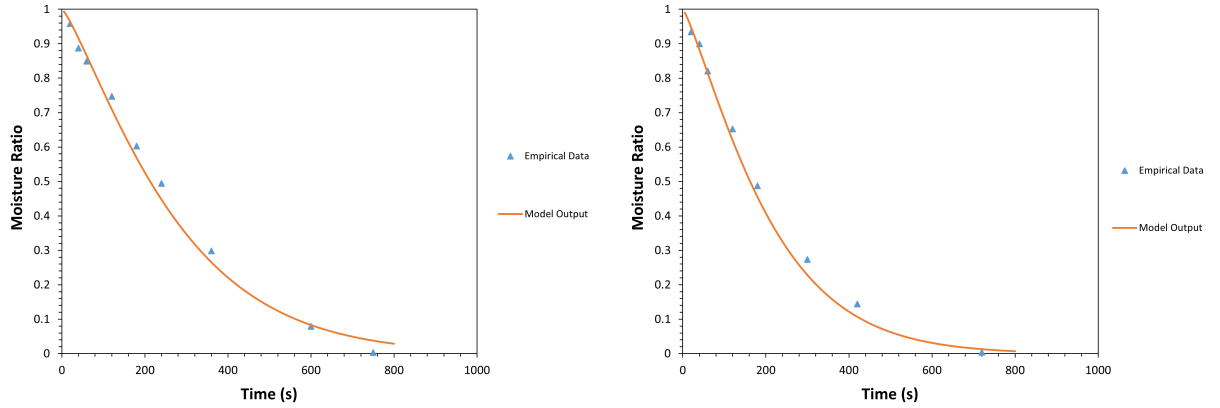

(c) 90 °C

(d) 100 °C

Figure 132: Graphs presenting empirical data and temperature specific model outputs for MR plotted against time after deposition on the ZMorph platform pre-heated to various temperatures.

$$k = \lambda D_0 exp\left(-\frac{E_a}{RT}\right) \tag{25}$$

Where λ is an empirical constant. By taking the natural log of both sides of Equation 25 and applying the laws of logarithms, the following can be derived:

$$ln(k) = ln\left(\lambda D_0 exp\left(-\frac{E_a}{RT}\right)\right) \tag{26}$$

$$ln(k) = ln(\lambda D_0) - \frac{E_a}{RT} \tag{27}$$

And finally by introducing the pseudo pre-exponential factor $k_0 = \lambda D_0$:

$$ln(k) = ln(k_0) - \frac{E_a}{RT} \tag{28}$$

Again, by comparing Equation 28 with the equation of a straight line it can be seen that plotting $ln(k)$ against $1/T$ gives $-E_a/R$ as the gradient and $ln(k_0)$ as the intercept. This was plotted for the k values derived using Equation 22 for each platform temperature that data had been collected for, as presented in Figure 133.

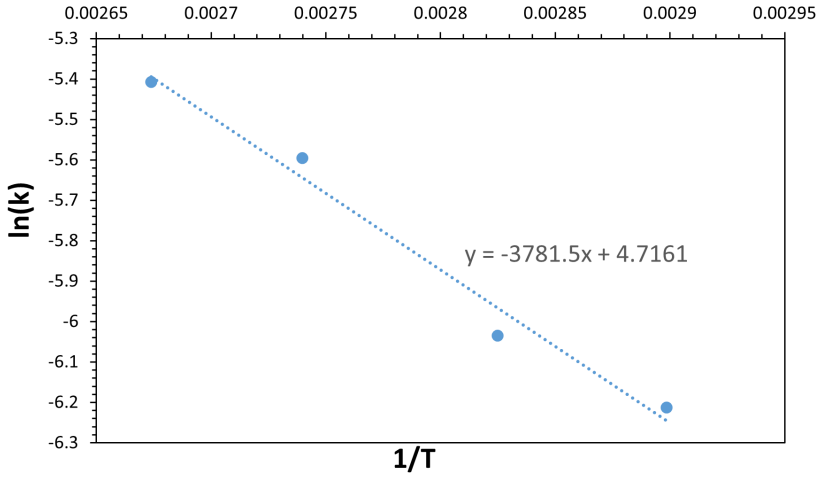

Figure 133: Graph showing $ln(k)$ plotted against $1/T$ for each platform temperature at which mass loss drying data was gathered for $4mm$ thick samples.

Extracting and processing the information from the equation of the straight line in Figure 133 gives $k_0 = 111.73$ and $E_a/R = 3781.5$. These values were then substituted into the following adapted version of the *Modified Page-I model*:

$$MR = exp\left(-tk_0 exp\left(-\frac{E_a}{RT}\right)\right)^n \tag{29}$$

This produced a MR model that can predict theoretical MR values for any platform temperature at any given time after deposition. The model outputs are presented in Figure 134 plotted alongside the gathered experimental data for each platform temperature for comparison. The model output MR values were also plotted directly against the experimentally gathered values, so that the accuracy of the model could be further analysed, and these plots are presented in Figure 135.

Figure 132 presents the output data from the moisture ratio model (Equation 18) using the

temperature specific empirical constants, plotted alongside the experimental data. The plots show a close fit between the experimental data and model output data for each of the platform temperatures. However, this model is restricted due to being temperature specific, meaning that it requires experimental data for each platform temperature in order to calculate the values of the empirical constants specific to that temperature. When depositing multiple successive layers during the foam gel extrusion process, the 'platform temperature' will change with each layer, as the final steady state temperature of a layer will provide the temperature upon which the next layer is deposited, as demonstrated by the slurry temperature profiles in Figures 127 - 129. As such, experimental data would have to been obtained for all possible platform temperatures in order to apply this model to predict the moisture ratio for successive layers of deposited slurry, which is infeasible. Therefore the adapted version of the model that can predict the moisture ratio over time for any given platform temperature was developed in order to overcome this limitation (Equation 29). Developing this model required mass loss data at multiple temperatures for a given layer thickness in order to extract the values for the empirical constants (as shown in Figure 160). This data was only available for 4 mm layer thickness (at $70 - 100°C$) and hence this model was only developed for this layer thickness.

The output data from this model plotted alongside the experimental data gathered as the corresponding platform temperature value provides an impressive level of accuracy for all temperatures presented (Figure 134), similar to that of the temperature specific models. In order to evaluate the accuracy of the model output data further it was plotted directly against the experimental data in Figure 135. The model data was generated by inputting the time corresponding to each experimental data point into the model to produce comparable moisture ratio values. These plots present a very close fit between the data sets, with an R-squared value of over 0.99 across all temperatures, which demonstrates the model's capability to accurately predict the moisture ratio of the slurry for any platform temperature at any given time after deposition. This strength of fit between experimental and model output data is comparable to the values presented in literature for the modelling of the moisture content within thin-layer fruits and vegetables [281, 296, 297], demonstrating that these types of models are suitable for this application.

As outlined in Section 2.7, the primary focus of thin-layer drying models for a range of applications has been modelling the moisture content over time of a given material throughout the drying

process. Whilst this has typically been applied to the thin-layer drying of fruits and vegetables [255], it is of significance for this work because the moisture content of a layer of slurry influences the deposition of the next successive layer, as discussed in Section 7.1.2. A moisture content too high results in insufficient structural strength of the initial layer and results in collapsing of the deposited tracks, whereas a moisture content too low results in poor merging between successive layers. Therefore being able to predict the moisture content over time for a given layer is important for understanding how to design the process to ensure it produces an optimal overall structure.

This model can be used to predict the optimal deposition time window for each layer during a multi-layer deposition, or specifically to ensure that the moisture content of the previous layer does not drop below the recommended 5 % minimum as discussed in Section 7.1.2 to allow sufficient merging between layers. Once the model has been developed for a specific layer thickness (4 mm in this case), all that is required is the steady state temperature for each layer that can be inputted into the model, which can be obtained either using thermal imaging during the deposition process or predicted using the final steady state temperature model as described in Section 7.2.3.

Ideally more data points would have been used for plotting Figure 133 in order to obtain the values for the empirical constants used to build the model, which would require mass loss data for a wider range of profile temperatures at a given layer thickness, in order to ensure the most accurate values for the empirical constants extracted from the plot. Also, it would have been valuable if this data was available for 2 mm and 6 mm, but particularly 2 mm as this is the layer thickness that represented the track/layer height for the process developed in this work. However, the accuracy output data from the model applied to the experimental data for 4 mm layer thickness demonstrates how accurately it can predict moisture content over time, providing sufficient experimental data is available to obtain values for the empirical constants and build the model. Whilst the data that this model is able to generate is valuable for the development of the layer-by-layer foamed slurry extrusion process, the data required to develop the model for each specific slurry layer thickness is extensive and laborious to gather. Multiple moisture ratio values (at least 8 per temperature in this work) throughout the drying process for each platform temperature are required in order to establish the values of the empirical constants. This data has to be gathered for at least 4 platform temperatures, however, as already discussed, ideally more than 4 temperatures would be applied in order to provide a more accurate values for the empirical constants extracted from Figure 133.

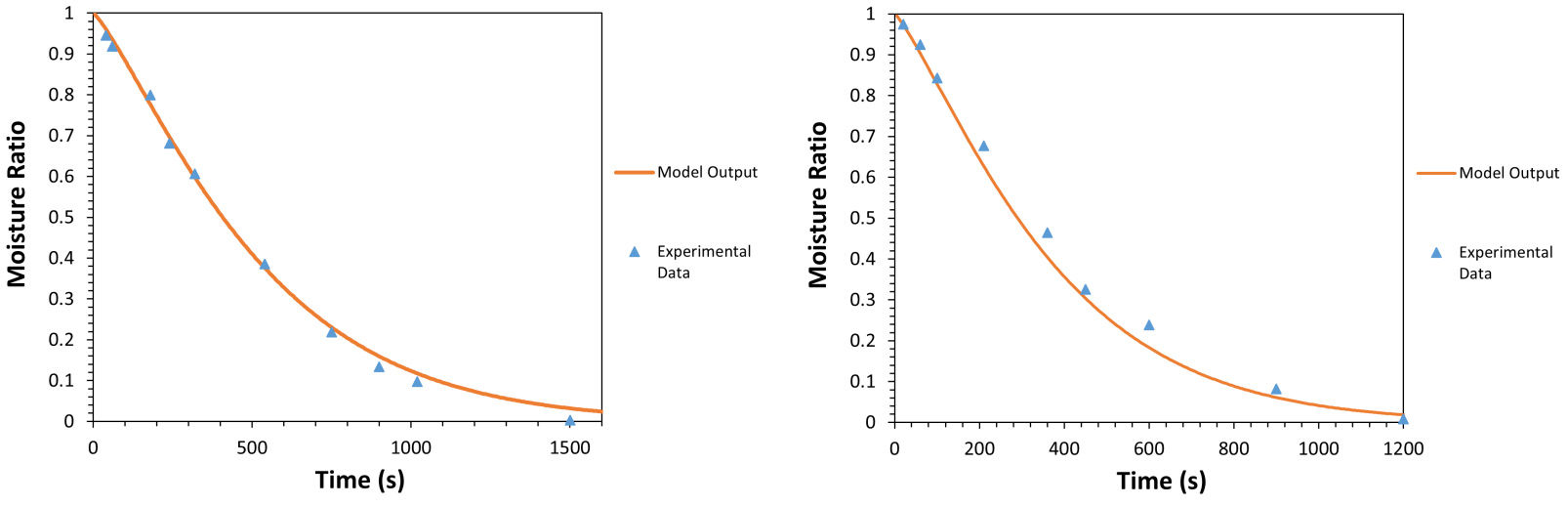

(a) 70 °C

(b) 80 °C

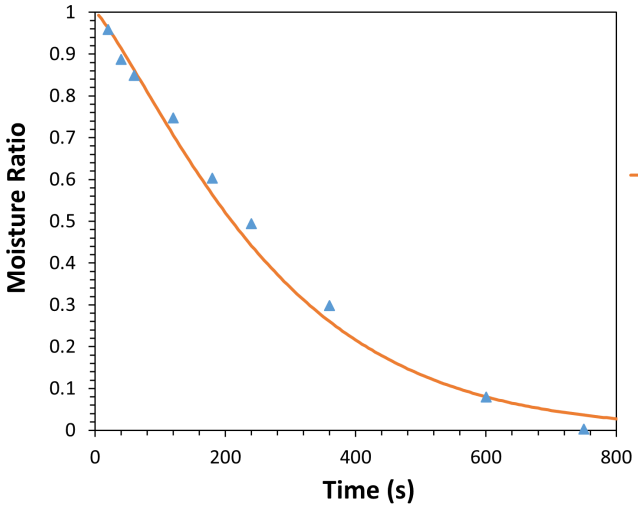

(c) 90 °C

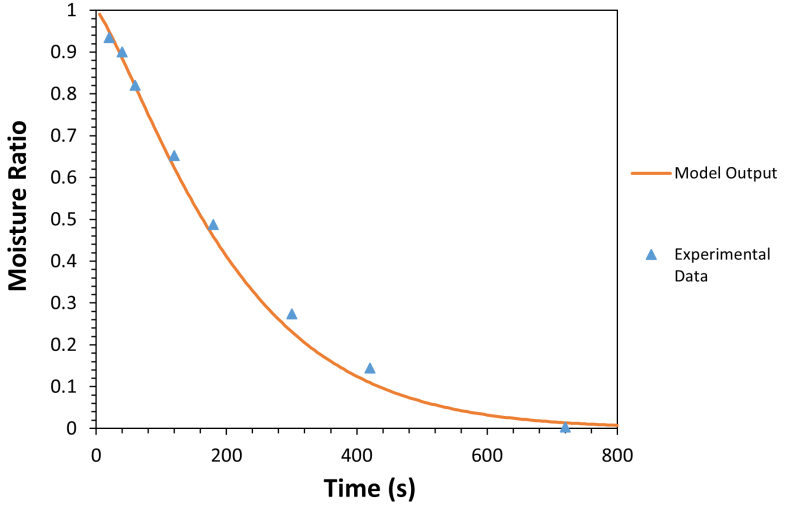

(d) 100 °C

Figure 134: Graphs showing empirical data and model outputs for MR plotted against time after deposition on the ZMorph platform, using the MR model that can be applied to any platform temperature.

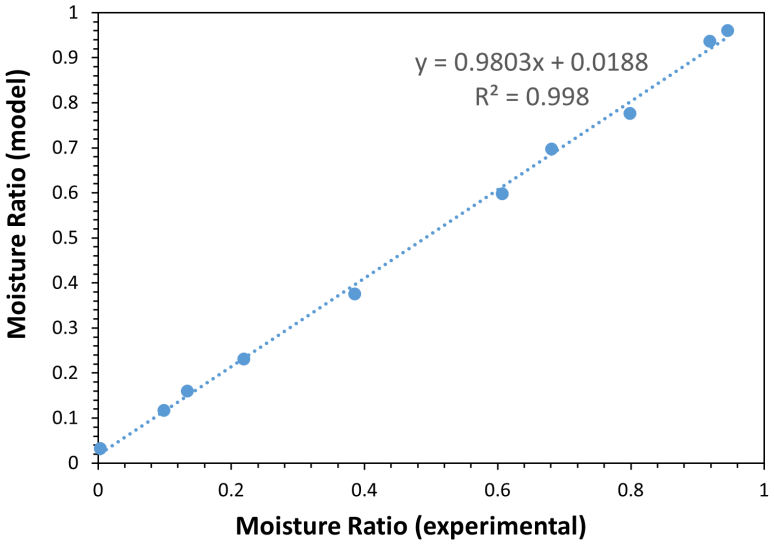

(a) 70 °C

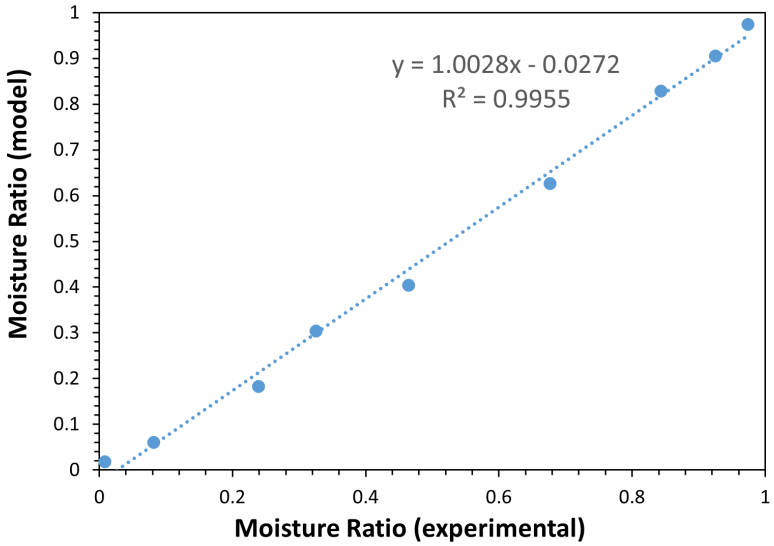

(b) 80 °C

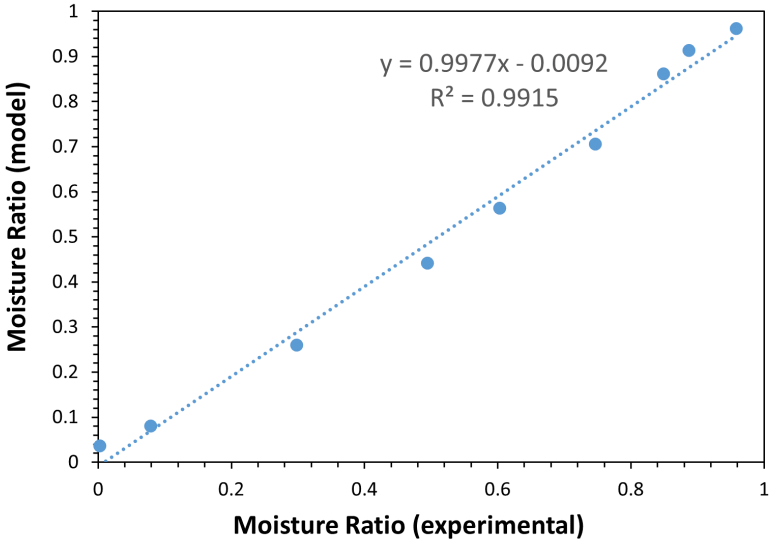

(c) 90 °C

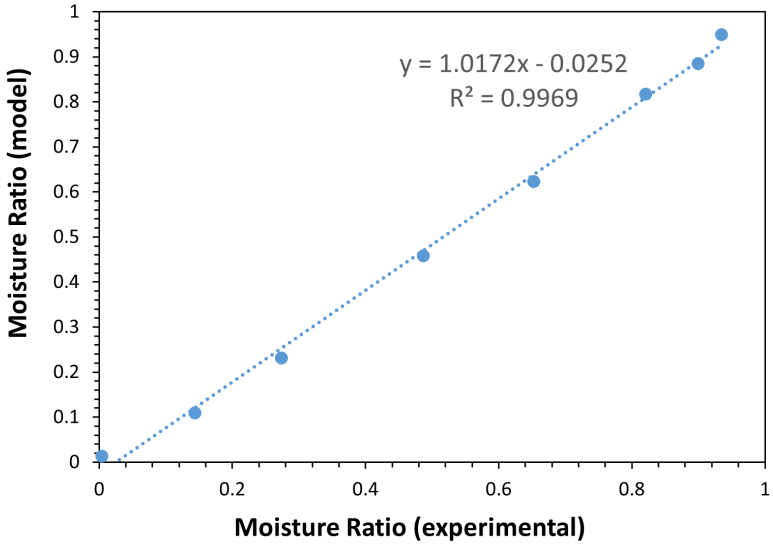

(d) 100 °C

Figure 135: Graphs showing model output values for MR plotted against empirical data values for each platform temperature.

7.2.2 Drying Time Model Development

The drying time model is a model that can be used to predict the time taken for a layer of slurry to dry when deposited on a heated platform, for any combination of layer thickness and platform temperature. Developing this model requires data for the drying times of layers of slurry at various thicknesses deposited on platforms at various temperatures. At least three different thicknesses and platform temperatures are required in order to extract relationships between drying time and these parameters. This data was available from the temperature profile and mass loss measurement experiments described in Section 3.6.1. As discussed in Section 7.1.4, the drying time can be approximately extracted from the temperature profile of a slurry layer deposited on the heated platform by reading the time at which the curve reaches the end of the 'drying plateau' and the temperature then begins to increase up towards the final steady state temperature. In reality, this point does not define the time at which the slurry has fully dried, as drying continues even as the slurry reaches its final steady state temperature, but at a greatly reduced rate. The mass loss data collected for various layer thicknesses and platform temperatures shows that, for all combinations, the slurries were at least 80 % dry at this point on the temperature profiles, as demonstrated in Figure 130a and Appendix D. Defining this point as the 'time to dry' provides a definitive and comparable cut-off where the majority of moisture has been removed from the slurry, which can be extracted from temperature profile data for any slurry layer even when mass loss data was not recorded.

The experimental values for drying time for each platform temperature and slurry layer thickness combination were extracted from the slurry temperature profiles acquired using continuous thermal image recordings. Table 17 presents the drying time data that was gathered from the captured temperature profiles for various temperature and thickness combinations, which was then used to develop the model.

The drying time model was developed from the initial moisture ratio model derived by Lewis [256] for the drying of thin-layer materials (Equation 30).

$$MR = exp(-(kt)) \tag{30}$$

Platform Temperature ($°C$)	**Measured Sample Thickness (mm)**	**Drying Time from Temperature Profile (s)**
$100°C$	1.8	166
	3.03	402
	5.48	1020
$90°C$	1.8	269
	3.2	438
	5.4	1186
$80°C$	1.84	347
	3.44	799
	5.32	1762
$70°C$	3.24	990

Table 17: Table of experimental data gathered for drying time and measured thicknesses of slurry samples deposited on ZMorph build platform pre-heated to various temperatures used to develop the drying time model.

This time the drying constant k was defined using an adaptation of the GAB (Guggenheim-Anderson-De Boer) relation [298]:

$$k = \frac{c \cdot exp(-Q/RT)}{x^n} \tag{31}$$

Where c and n are empirical constants, Q is the activation energy (J/mol), R is the molar gas constant and x is the sample thickness (mm). Applying Equation 31 relates the drying constant k to both the platform temperature as well as the thickness of material layer. Two instances can then be considered; constant temperature and constant thickness. By developing Equations 30 & 31 for these two instances, and applying them to the empirical data gathered, values for the empirical constants and other unknowns in Equation 31 can be acquired.

Equation 30 can be easily rearranged to give:

$$t = \frac{-ln(MR)}{k} \tag{32}$$

Then by treating temperature as a constant value Equation 31 can be re-written in the following way:

$$k = \frac{c'}{x^n} \tag{33}$$

Where

$$c' = c \cdot exp(-Q/RT) \tag{34}$$

Combining this with Equation 32 then gives:

$$t = \frac{-ln(MR)x^n}{c'} \tag{35}$$

By taking the natural log of both sides of Equation 35 and then applying the laws of logarithms, the following can be derived:

$$ln(t) = ln\left(\frac{-ln(MR)}{c'}\right) + nln(x) \tag{36}$$

Which now has the form of the equation of a straight line, therefore $ln(t)$ can be plotted against $ln(x)$ to give the gradient as the value of the empirical constant n and the intercept as the value of $ln\left(\frac{-ln(MR)}{c'}\right)$. Data was gathered as described in Section 3.6.3, from which time to dry values (s) were extracted for 3 different layer thicknesses of slurry at constant temperature values of $70, 80, 90$ and $100°C$. Values for the unknowns in Equation 36 were acquired by following the steps described here for each temperature value, and then an average across the temperatures was calculated for each.

A similar process was then followed, but with thickness being treated as a constant rather than temperature. If thickness is constant then Equation 31 can be written as:

$$k = c''exp(-Q/RT) \tag{37}$$

Where

$$c'' = \frac{c}{x^n} \tag{38}$$

Which, when combined with Equation 32 gives:

$$t = \frac{-ln(MR)exp(Q/RT)}{c''} \tag{39}$$

By taking the natural log of both sides of Equation 39 and then applying the laws of logarithms, the following can be derived:

$$ln(t) = ln\left(\frac{-ln(MR)}{c''}\right) + \frac{Q}{RT} \tag{40}$$

As with Equation 36, Equation 40 now has the form of the equation of a straight line, meaning that $ln(t)$ can be plotted against $1/T$ to give Q/R as the gradient and $ln\left(\frac{-ln(MR)}{c''}\right)$ as the intercept. Again, this was done using the data gathered as described in Section 3.6.3.

Following this method, the two instances were considered; constant temperature and constant thickness. By considering these two instances, it allowed one of the variables that influences drying time to be treated as a constant, which would then be combined with other empirical constants within the model which values could be obtained for by processing the experimental data. Initially temperature was treated as constant, and for each subset of data for drying time of samples of different thicknesses at the same platform temperatures ($80, 90$ and $100°C$), the natural log of the drying time ($ln(t)$) was plotted against the natural log the measured thickness of the sample ($ln(x)$). By comparing Equation 36 to the equation of a straight line, values for the empirical constant n and the combined empirical constant $ln\left(\frac{-ln(MR)}{c'}\right)$ were acquired from the linear trendlines of each data plot. These plots are provided in Figure 136, and the empirical values obtained from them are summarised in Table 18.

Similarly then for the constant thickness scenario, data was used from Table 17 for the drying time of samples of the same (or similar) thickness at different platform temperatures was used to plot the natural log of the drying time ($ln(t)$) against the inverse of the platform temperature ($1/T_p$) for 3 or more temperatures at each thickness. Again, by comparing Equation 40 with the equation of a straight line and extracting values from the linear trendlines of the plots, values for the combined empirical constants Q/R and $ln\left(\frac{-ln(MR)}{c''}\right)$ were obtained. These plots are provided in Figure 137, and the empirical values obtained are presented in Table 18 along with the empirical values obtained from the constant temperature scenario.

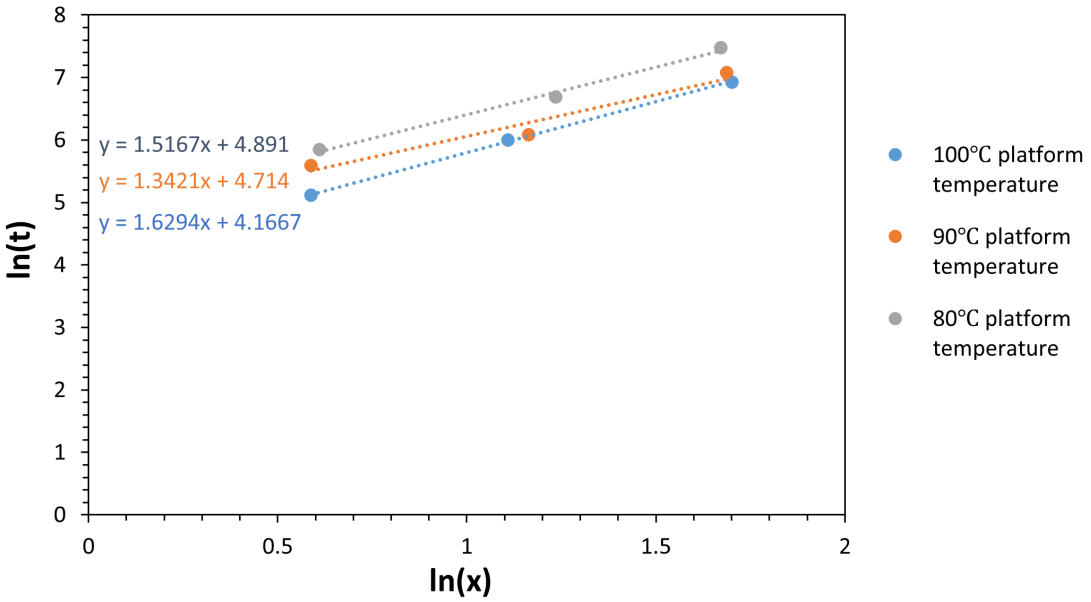

Figure 136: Graph showing the natural log of slurry sample drying time ($ln(t)$) plotted against the natural log of the sample thickness ($ln(x)$) for multiple platform temperatures, along with trendlines and linear equations used to acquire values for empirical constants.

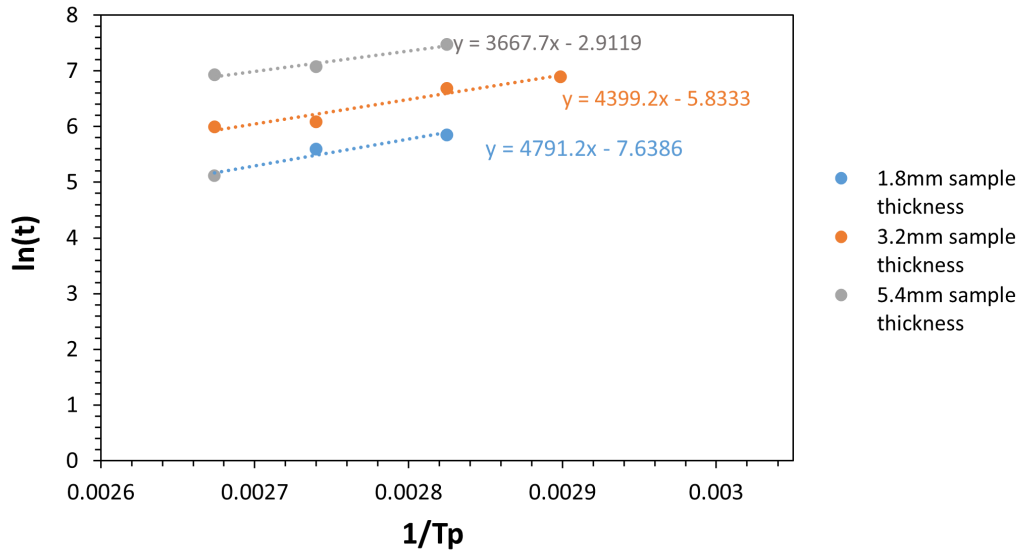

Figure 137: Graph showing natural log of slurry sample drying time ($ln(t)$) plotted against the inverse of the platform temperature ($1/T_p$) for multiple sample thicknesses, along with trendlines and linear equations used to acquire values for empirical constants.

Constant Temperature

Platform Temperature ($°C$)	Empirical Constant Values	
	$ln\left(\frac{-ln(MR)}{c'}\right)$	n
100	4.167	1.629
90	4.714	1.342
80	4.891	1.517
Mean	4.59	1.496

Constant Thickness

Sample Thickness (mm)	Empirical Constant Values	
	$ln\left(\frac{-ln(MR)}{c''}\right)$	Q/R
1.8	-7.639	4791.2
3.2	-5.833	4399.2
5.4	-2.912	3667.7
Mean	n/a	4286

Table 18: Table presenting drying time model empirical constant values obtained from trendline equations of experimental data plots provided in Figures 136 & 137.

Finally, to create a model for drying time that relates to both temperature and thickness, first Equations 34 and 35 were combined to give:

$$t = \frac{-ln(MR)}{c} exp(Q/RT) x^n \tag{41}$$

Equation 41 can also be derived by combining Equations 38 and 39 in a similar manner. The values for Q/R and n were acquired from plotting the experimental data in the way described earlier in this section, so in order to use Equation 41 to predict drying time a value needed to be calculated for $-ln(MR)/c$. This was done by using the values obtained for the combined constant $-ln(MR)/c'$ at each temperature as presented in Table 18, and applying Equation 34 which relates the constants c and c', to produce Equation 42.

$$\frac{-ln(MR)}{c} = exp\left(a + \frac{Q}{RT}\right) \tag{42}$$

Where a is the value of the combined empirical constant $ln\left(\frac{-ln(MR)}{c'}\right)$ for each platform temperature from Table 18. Using Equation 42, the values for the empirical constant $-ln(MR)/c$ at each platform temperature were calculated. From these, an average value was obtained which was then used along with Equation 41 and the other previously derived empirical constants to calculate theoretical values for drying time of a slurry sample of any thickness deposited on a platform pre-heated to any temperature. Figure 138 provides the final output plots from the drying time model applied for multiple sample layer thicknesses and a range of platform temperatures. Figure 139 shows the theoretical drying times from the model plotted against the experimental data for the same temperature and thickness value combinations, in order to provide a reference for analysing the accuracy of the model.

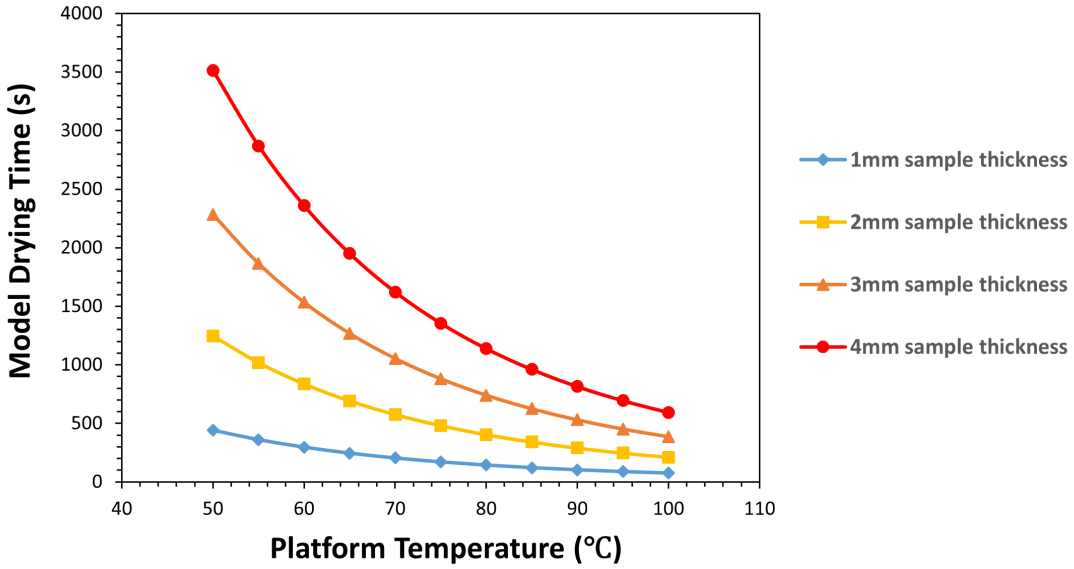

Figure 138: Graph of output data from drying time empirical model showing theoretical drying time for different layer thicknesses of slurry deposited on various temperatures.

The drying time model (Equation 41) was simply developed to predict the drying time of a layer of slurry of a given thickness deposited on a heated platform at a given temperature. As previously highlighted, the experimental values for drying time were extracted from the temperature profiles generated from the thermal imaging data for various temperature and layer thickness combinations.

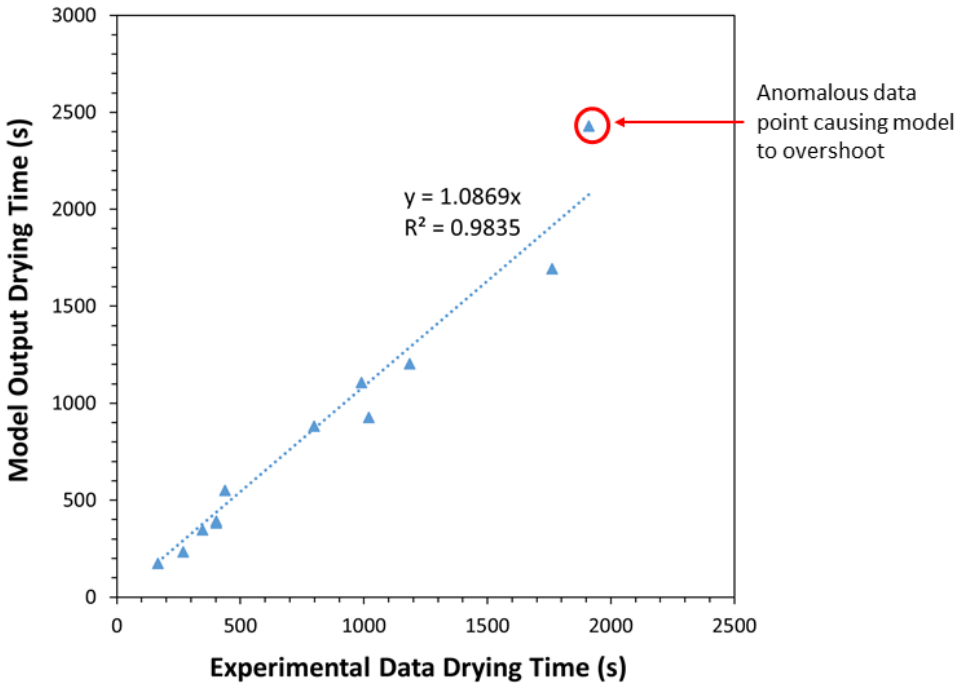

Figure 139: Graph of drying time model output data plotted against experimental data for the same combinations of layer thickness and platform temperature.

The end of the drying plateau region of each plot was defined as the point where the slurry had dried. In reality, as previously highlighted, this point represents the time at which at least 80 % of the moisture has been removed from the slurry, however the rate of drying beyond this point is significantly reduced. Extracting an exact time for when the moisture content reaches zero would be infeasible from the temperature profiles alone, whereas it is straightforward to identify the end of the drying plateau because it is an easily identifiable region on the profile.

Considering separate scenarios where temperature and thickness were each treated as constants rather than variables allowed these to be combined with other empirical constants to find values for the grouped empirical constants (Table 18). These grouped empirical constants were then inputted into Equation 41 to create the model which is able to predict drying time for any given combination of layer thickness and platform temperature. In order to calculate these grouped constants multiple data points were required at each platform temperature and layer thickness, however the plots used to extract the values (Figures 136 & 137) are based off only three or four data points because data was only gathered for three different layer thicknesses and four platform temperatures. There is a

reasonable degree of scatter within these plots, particularly the constant thickness plots in Figure 137, and therefore the accuracy of the values generated for these grouped empirical constants is questionable. Despite this, when the model output values for drying time at a given layer thickness and platform temperature were plotted against the corresponding experimental values (Figure 139), the result shows a reasonably strong fit between the data sets with an R-squared of 0.9835. However, with the gradient of the straight line fit being greater than 1, it is clear that the model is over-predicting the drying time values. This may be influenced by the anomalous data point highlighted in Figure 139, which corresponds to a 5.4 mm layer being dried on the platform at $70°C$. This model output presented the greatest error between model data and experimental data of 27 %. There was one other data point which had an error of 25 %, and the error for the rest of the output data ranged between $1 - 14$ %.

As well as the limited data used to generate the plots from which the empirical constants were extracted, output error for this model is likely to result from the fact that slurry layers will contain slightly different moisture contents at the end of the drying plateau region on the temperature profiles, and so using this time value to represent the experimental value for drying time does not necessarily provide a direct comparison. In general this model is of interest for this application, but doesn't actually provide information that is vital to the development of the process because as previously highlighted the layers don't need to be fully dry for successful deposition of the next layer, as highlighted in the layer deposition timing experiment (Section 7.1.2). However, the model is able to provide an estimate for the time corresponding to the end of the drying plateau with a reasonable degree of accuracy, which could be used to help identify the optimal deposition time for each layer within a multi-layer extrusion, as discussed further in Section 7.3. Also, once the model has been built for a specific slurry, provided the model is built on a wide enough range of data it can be used to predict the time for a layer of any thickness deposited on any platform temperature, without any further data gathering required.

7.2.3 Steady State Layer Temperature Model Development

The final steady state temperature model is built upon the simple conservation of energy principle as outlined in Equation 43, which states that the heat transferred through the slurry via conduction (Q_{slurry}) from the heated platform is equal to the heat transferred into the surrounding air via

convection (Q_{air}).

$$Q_{\text{slurry}} = Q_{\text{air}} \tag{43}$$

The heat transferred through the slurry can also be defined using the general heat conduction equation:

$$Q_{\text{slurry}} = kA\frac{\Delta T_1}{x} \tag{44}$$

Where k is the thermal conductivity of the slurry (W/mK), A is the area of the top surface of the slurry layer (mm^2), x is the slurry layer thickness (mm) and $\Delta T_1 = T_p - T_s$ where T_p is the platform temperature and T_s is the final steady state temperature of the slurry in Kelvin.

The convective heat transfer into the surrounding air can be defined using Newton's Law of Cooling:

$$Q_{\text{air}} = hA\Delta T_2 \tag{45}$$

Where h is the heat transfer coefficient (W/m^2K), $\Delta T_2 = T_s - T_a$ with T_a being the ambient temperature, also measured in degrees Kelvin.

Combining Equations 43, 44 and 45 gives:

$$\frac{kA}{x}(T_p - T_s) = hA(T_s - T_a) \tag{46}$$

Which by simplifying and rearranging gives:

$$\frac{T_p - T_s}{T_s - T_a} = \frac{h}{k}x \tag{47}$$

Equation 47 represents the equation of a straight line which passes through the origin, therefore the temperature ratio can be plotted against slurry layer thickness to give h/k as the gradient. This process was followed using the final steady state temperatures acquired from the slurry temperature profiles as described in Section 3.6.3, as well as the slurry layer thickness measurements and known ambient and platform temperatures. The final steady state temperature values for thin

layers of slurry deposited and dried on the pre-heated ZMorph platform were obtained from the thermal profiles captured using the thermal imaging camera for various combinations of platform temperature and layer thickness. Three different thicknesses of slurry were dried on the platform at $70 - 100°C$ at $10°C$ intervals, produced by passing the levelling tool over a deposited volume of slurry with the $2, 4$ and $6mm$ channels.

From this data, the temperature ratio was plotted against slurry layer thickness for each of the values obtained from the experimental data, as presented in Figure 140. The value for the empirical constant from the gradient was obtained as $h/k = 0.0828$ from the equation of the straight line.

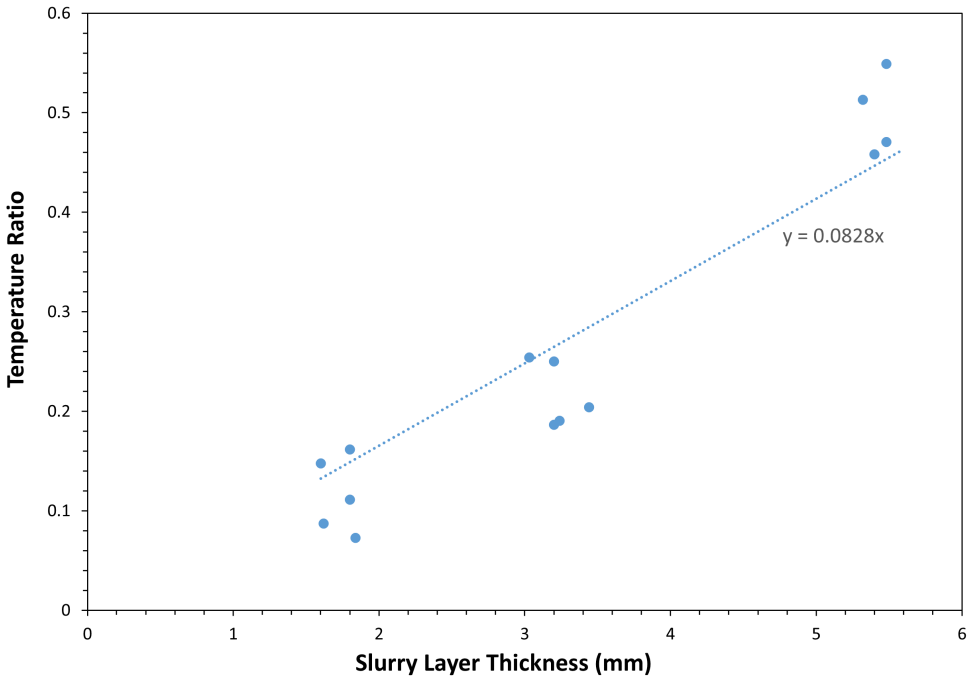

Figure 140: Graph showing the temperature ratio plotted against slurry layer thickness for final steady state temperature data along with equation of the linear trendline used to obtain a value for the empirical constant h/k, as outlined in Equation 47

Once the h/k value had been obtained, Equation 46 was then rearranged in the following way to provide an equation that can be used to model the final steady state temperature. Expanding the brackets on the RHS of Equation 46 and adding and subtracting terms gives:

$$T_p + T_a\frac{h}{k}x = T_s\frac{h}{k}x + T_s \tag{48}$$

Then by taking T_s as a factor:

$$T_p + T_a \frac{h}{k} x = T_s \left(\frac{h}{k} x + 1 \right) \tag{49}$$

Which can finally be rearranged to give:

$$T_s = \frac{T_p + T_a \frac{h}{k} x}{\frac{h}{k} x + 1} \tag{50}$$

Equation 50 outlines the final steady state temperature model which, providing the platform and ambient temperatures are known, can be used to predict the final steady state temperature of a slurry layer of a given thickness that is deposited on the heated platform. This model was applied using thickness and platform temperature values corresponding to the data already collected to produce theoretical steady state temperature values which were then plotted against the experimental values in order to assess the accuracy and reliability of the model, as presented in Figure 141. It was then also used to calculate steady state temperatures for layer thicknesses and platform temperatures for which experimental data had not been collected, as presented in Figure 142.

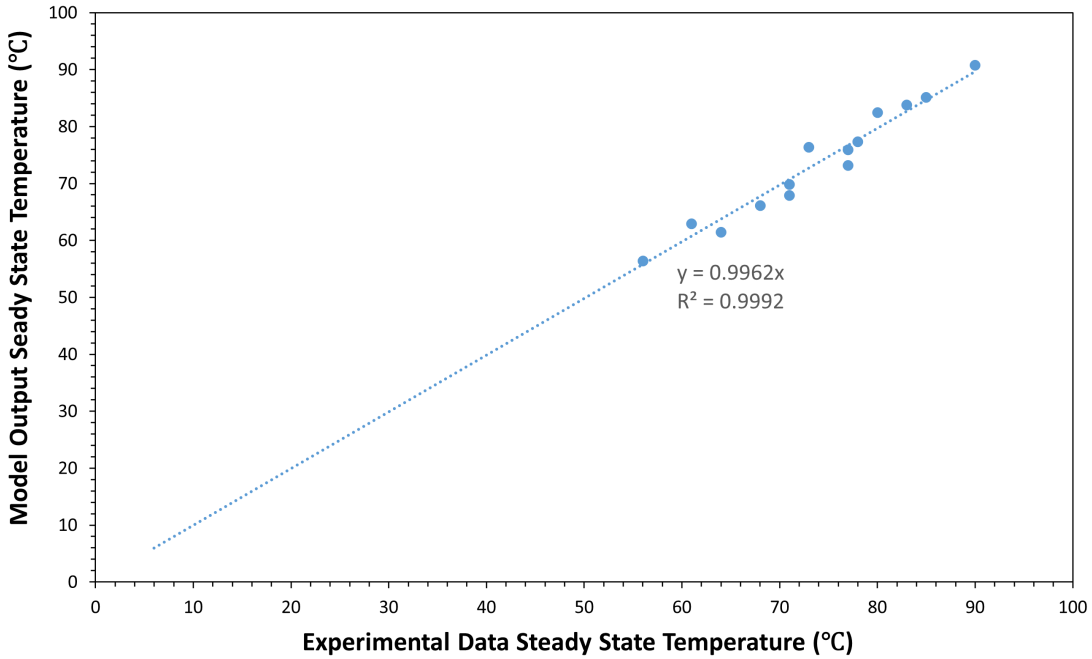

Figure 141: Graph showing steady state temperature model output values plotted against experimental data for the same platform temperature and slurry layer thickness values.

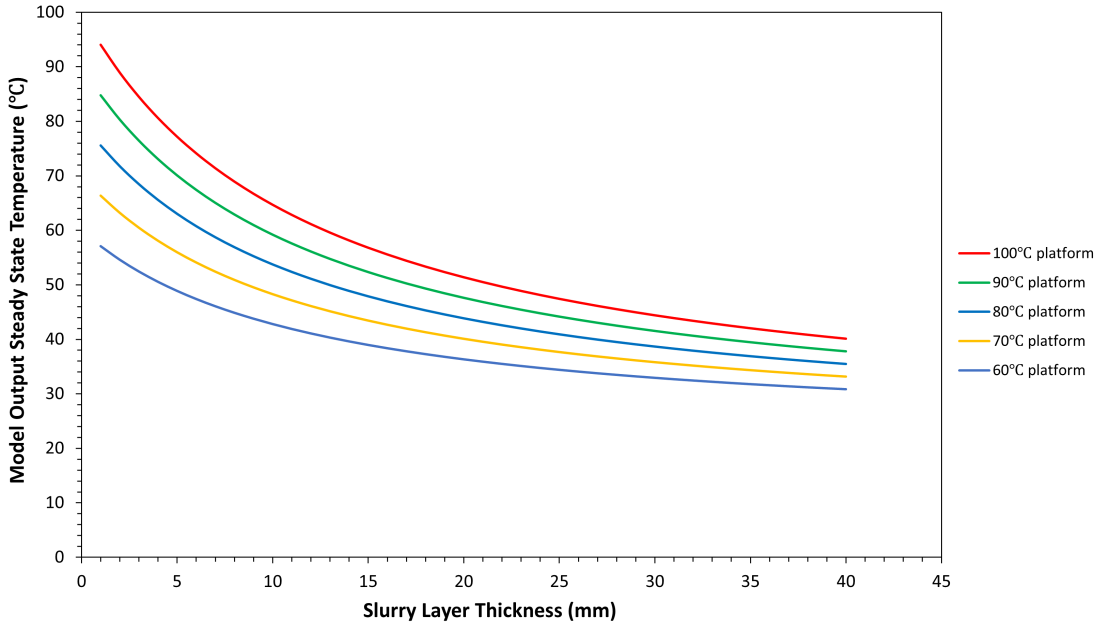

Figure 142: Graph showing steady state temperature model output plots for a range of slurry layer thicknesses deposited on specific platform temperatures.

The plot used to obtain the value of the empirical constant (Figure 140) combines the experimental data for all thickness and temperature values so there are sufficient data points in order to generate a trendline and extract the value of the empirical constant. However, a reasonable amount of scatter in the data can be observed in the plot. Figure 142 presents the output data of the model for layer thicknesses between $1-40\ mm$ and platform temperatures between $60-100°C$. The model output data values plotted against the experimental data (Figure 141) shows a strong fit between the data points with an R-squared of 0.999. This is somewhat surprising considering the scatter observed in the plot used to generate the empirical constant value, however once again demonstrates how accurately these semi-empirical models can predict drying/thermal behaviour of materials even within this application.

This model provides a number of key insights regarding the development of the foamed slurry extrusion process. Firstly, it can be applied in order to identify the layer count at which gelation of the foamed slurry will no longer occur because the steady state temperature of the previous layer no longer exceeds the gelation temperature of the MC, providing the layer thickness and starting platform temperature are known. This is demonstrated in Table 19 for 1.8 mm layer thickness deposited on an initial platform temperature of $100°C$. It can be concluded from the data presented

in the table that the absolute maximum layer count that could be reached is seven (as highlighted in Table 19), which corresponds to a total height of 12.6 mm suggesting that an alternative source of heating may be required in order to deposit more slurry beyond this point, as discussed further in Section 7.3. Even at the 7^{th} layer, with the low substrate temperature the drying time would be so long that it may be infeasible to dry through platform heating alone. The experiments in this work (Section 7.1) demonstrated that slurry layers can be dried at a platform/substrate temperature as low as $70°C$, so this serves as the minimum guaranteed temperature at which the process is feasible, which relates to the deposition of four layers at 1.8 mm layer thickness as highlighted in Table 19.

Layer Count	**Substrate Temperature ($°C$)**	**Model Output Final Steady State Temperature ($°C$)**
1	100	88.6
2	88.6	78.8
3	78.8	70.4
4	70.4	63.2
5	63.2	57.1
6	57.1	51.2
7	51.2	47.2
8	47.2	43.3

Table 19: Table showing steady state temperature model output data for 1.8 mm thick layers of Ti slurry deposited on an initial platform temperature of $100°C$.

The steady state layer temperature model highlights the importance of allowing each layer to reach its steady state temperature before depositing the next layer, in order to ensure that the number of extruded layers can be maximised whilst still being able to gel and dry. A wide deposition interval was highlighted from the layer deposition timing experiment as presented again in Figure 143, however the observations from this model output create a more narrow optimal deposition interval as highlighted on the same plot. Methods for identifying this optimal interval are discussed in Section 7.3.

This model links closely to the moisture ratio model because, as discussed in Section 7.2.1, it requires the temperature of the previous layer to be known in order to predict the moisture ratio over time of the next deposited layer. This final steady state temperature model can be used to predict this without requiring the deposition process to be monitored using thermal imaging.

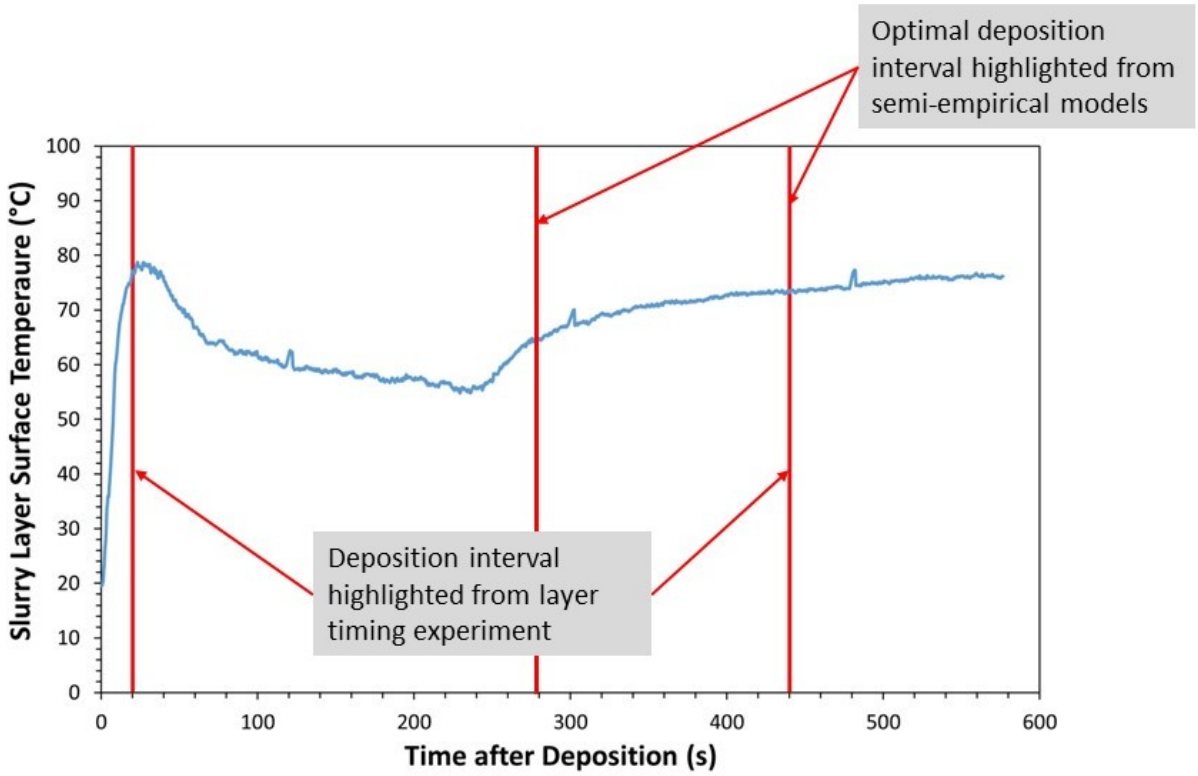

Figure 143: Temperature profile for SS L slurry $\sim 2\ mm$ layer deposited on ZMorph build platform pre-heated to 100°C, with highlighted deposition time interval from layer timing experiment and optimal deposition interval from semi-empirical models interval for second layer.

7.3 Summary of Drying Behaviour and Semi-Empirical Drying Models

This chapter presents the application of thin-layer drying models to the drying of individual layers of foamed metal powder-based slurry (for Ti64 powder). These models, combined with the understanding developed through the 3D material extrusion process development, provide an in-depth understanding of this manufacturing process and the parameters that influence quality of the extruded structures. The three semi-empirical models developed and applied to the novel AM process of foamed metal powder extrusion each predict different parameters for thin layers of slurry deposited on a heated substrate. When compared against the experimentally gathered data, the output data from all of the models presents a statistically good fit, particularly for the moisture ratio and steady state layer temperature models.

The moisture ratio model and final steady state temperature model provide vital information regarding the deposition timing of successive layers of slurry as well as the maximum layer count that

can be deposited for a given layer thickness and platform temperature. It has been highlighted that the drying time model does not provide a particularly useful insight because the same information can be extracted more accurately from the moisture ratio model, providing the final temperature of each layer is known, and this can be predicted using the steady state temperature model. However, the collection of moisture ratio data required to build the moisture ratio model is much more intensive than the drying time model, because it requires the drying of multiple samples for different durations, and recording mass both before and afterwards. The data required to build the drying time model can be gathered simply through recording slurry surface temperature using a thermal imaging camera and measuring the sample thicknesses after drying, therefore it is much more straightforward to gather data at multiple temperatures and layer thicknesses. Also, as previously highlighted, the moisture ratio model has to be developed for each specific layer thickness meaning that this data has to be gathered for each thickness, whereas once the drying time model has been developed it can predict the time for any temperature and thickness combination.

Overall, these models provide different valuable insights into the drying behaviour of the slurry and can provide useful information that can be used when designing the extrusion process, particularly with regards to the deposition timing of successive layers. The key outcome from this chapter is that, using the information developed through the thin-layer models along with the layer timing deposition experiment, an optimal deposition interval for each successive layer of slurry can be identified as presented in Figure 143. Depositing the next layer of slurry within this interval allows enough time for the previous layer to dry sufficiently and reach its final steady state temperature, whilst still containing enough moisture so that when the next layer is deposited the material will merge together to form a continuous structure. It is suggested that simple temperature monitoring of the multi-layer extrusion process could be used to inform the deposition timing. The optimal layer deposition timing interval can be identified from the temperature profile of the previous layer, and so an automated thermal imaging system could be developed to continually monitor slurry temperature and identify the start of this interval based on the expected temperature profile for a deposited layer.

The final steady state temperature model highlighted that the maximum height of structure that can be deposited using this method is limited, due to the only heat source being the heated platform and as such the gelation of each layer relies on this heat being conducted through the

previous layers. The model predicts the final temperature of each layer, which can then be fed back into the model as the 'substrate' temperature for the next layer to be deposited. With each layer the maximum temperature reached decreases and so the model can be used to highlight the layer number where this temperature drops below the gelation temperature of the MC solution. Beyond this, if further layers were deposited, the previous layers would not be gelled and as such the layers would completely merge into one-another (as observed in Section 7.1.2) and the porous structure would collapse. In order to remove this limitation, alternative heating methods would need to be explored, as it is not recommended that the platform temperature should be increased beyond $100°C$ due to potential issues that could be caused by rapid boiling of the water content within the slurry. A range of FDM machines available include a temperature controlled chamber in order to provide control over the temperature and cooling of the extruded filament to avoid issues around shrinkage or warping during cooling. This principle could be applied to provide an alternative heat source for this process of foamed slurry 3D extrusion, however the temperature of the syringe itself would need to be separately controlled to avoid gelation of the slurry within the syringe prior to extrusion.

As highlighted in the literature around the application of these models to the thin-layer drying of fruits and vegetables, these semi-empirical models provide more accurate predictions of drying behaviour than theoretical models because they rely heavily on experimental data and make fewer assumptions [255]. One of the concerns with applying these models to this AM process was that typically these models are applied to material samples with negligible thickness (up to three particles in thickness), whereas the average layer thickness for the process developed in this work is 1.8 mm. However, as outlined in Section 2.7.3, these models have been applied to the drying of whole fruits and were still able to provide an accurate prediction of drying behaviour [280].

As discussed in Section 2.7, the semi-empirical thin-layer drying models are built the assumption of isothermal drying conditions, or at least that initial time taken for the material to reach the drying temperature is negligible compared with the overall drying time. As such, the studies discussed from the existing literature typically involve long drying times from several hours to multiple days. It is clear from the temperature profiles obtained from the slurry samples deposited on the pre-heated platform that the drying process is not isothermal, as there is a clear initial period of heating (where gelation also occurs) prior to reaching the 'drying plateau' region (Section 7.1.3).

However, once the slurry has reached the initial drying temperature, the process can be assumed to be isothermal until the end of the drying plateau, as suggested by the near-constant temperature observed within this region on the temperature profile. In reality, the 3D material extrusion process is a track-by-track deposition process, whereas these models assume the temperature of each layer is uniform. Deposition of an adjacent track will have an influence on the temperature and drying behaviour of the previous track, however treating each layer as uniform allows these models to be applied. Because the hatching strategy for each layer is identical, the drying time for each track is the same throughout the layer before the next track is deposited on top, therefore treating the drying behaviour of each layer as uniform is a reasonable assumption.

Considering these limitations, as well as the previously highlighted issues caused by the scatter within the experimentally gathered data and limited available data points for defining linear trend-lines, the accuracy of the output data generated by the models developed in this work is somewhat impressive. This work confirms that these types of models are suitable for applications where material thickness is greater than a few particles, and even when isothermal conditions cannot strictly be assumed.

8 Chapter 8: Conclusions and Future Recommendations

This work has demonstrated the capabilities of a novel method of manufacturing for producing porous titanium (Ti64) with optimal properties for the application of artificial orthopaedic implant material. This method of manufacturing combines two processes; foam gel casting and AM, specifically material extrusion. Foam gel casting of Ti64 has received very little attention in existing research despite successful implementation with a wide range of ceramics and more recent development for stainless steel. Also, the foam gel casting process has not previously been combined with material extrusion.

8.1 Key Conclusions

In Chapter 4 of this work, a novel foam gel casting process was developed for Ti64 powder and optimised to produce porous structures with properties that have been highlighted in existing literature as being optimal for biocompatibility of orthopaedic implants, and that mimic those of human trabecular bone as summarised in Section 2.9. The application of the foam gel casting process using Ti64 powder has been almost entirely unexplored, and therefore this work provides an important novel contribution to this area of research. The stability of the optimised Ti64 powder slurry when foamed was demonstrated, particularly when stored within a syringe with the plunger inserted. Also, the ability to extrude this foamed slurry through a 2 mm nozzle without causing the foam to collapse was demonstrated, which is an application which has not previously been investigated for foamed powder-based slurries. The sintering stability of the resulting porous material was highlighted by burning out the MC binder that holds the powder particles together when the samples have been dried, which showed that these structures would be stable during sintering. In addition, the sintered mechanical properties of this highly porous Ti64 material were estimated by analysing data available within existing literature for porous SS 316L with comparable structure and porosity, and produced using the same process. These calculated estimates demonstrate that this material may, despite containing a high level of porosity as required for implant material, maintain mechanical properties close to those of human cortical bone, which is necessary in order to be applied in load-bearing applications.

Chapter 5 highlighted the high viscosity of the initial optimised Ti64 slurry, and identified

the challenges associated with reducing viscosity of this foamed slurry. The work in this chapter developed a clear understanding of how different slurry composition and mixing process parameters impact the viscosity and stability of the slurry and the green strength of the resulting dried samples. This chapter provides a summary of the parameters that can be used to reduce the slurry viscosity, and how these parameters impact the slurry stability and sample green strength. Whilst there is some scattered information in existing literature around altering the slurry viscosity for foam gel casting, it has not been thoroughly investigated and the information has not previously been presented in a clear manner as it has in this work. Reducing powder particle size was identified as a the most effective way to reduce slurry viscosity whilst maintaining stability and green sample strength, and the challenges this presents when working with Ti64 powder have been highlighted.

Chapter 6 presents the systematic development of the 3D extrusion process for the key foamed metal powder-based slurry compositions highlighted from Chapter 5, through the extrusion and analysis of single tracks, single layers containing multiple adjacent tracks, and 3D structures consisting of successive layers. This process has never previously been developed using foamed powder-based slurries in order to extrude material containing macro-scale porosity. As such, this work presents a key novel contribution to this area of research. The work in this chapter clearly demonstrates that this process is capable of extruding 3D scaffolds containing interconnected porosity, where the tracks and layers merge successfully to produce a continuous material.

The work in Chapter 7 developed a thorough understanding of the drying behaviour of the foamed Ti64 powder slurry when deposited on a heated platform in a layer-by-layer manner, which is key for the development of this process because gelling and drying of each extruded layer is vital. In addition to this, a number of thin-layer drying models were applied to this process and it was clearly demonstrated that these models can accurately predict the drying behaviour of foamed metal powder-based slurry, despite the assumptions that they are built on not being strictly true for this process. This work presents a novel application of these thin-layer drying models, which are typically applied to true thin-layer applications and have never been applied to the drying of powder-based slurries before. The work in this chapter demonstrated how these models can be used to highlight key information about the drying behaviour of the slurry, in particular identifying the optimal window for the deposition of successive layers, as well as the limitations of the process.

Overall, this work clearly demonstrates the feasibility of this innovative method of manufactur-

ing using a novel Ti64 foamed slurry composition, and its suitability for the application of producing porous Ti64 scaffolds for orthopaedic implant material, as well as a range of other applications for porous metals. This process is capable of producing titanium implants with optimal internal porous structures for bone in-growth that mimic that of human trabecular bone, whilst also potentially providing mechanical strength that is similar to that of cortical bone, which can be extruded in a layer-by-layer manner to readily produce bespoke geometries without the need for a mould. As highlighted in Section 2.8 and summarised in Table 4, there are no existing manufacturing processes able to achieve this without requiring complex computational resources, whereas the work presented here demonstrates the feasibility of this process using readily available equipment and simple processes. Whilst there are areas which require further important investigation, this body of work represents a fundamentally important foundation in the development of this process and provides key insights for its future development. The details of these areas which require further development are presented next.

8.2 Recommendations for Future Work

The work in Chapter 5 highlighted the importance of the viscosity of metal powder-based slurries for 3D material extrusion. It was demonstrated that the high viscosity of the original optimised Ti64 powder slurry had a significantly detrimental impact the quality of extruded tracks, layers and structures. Using SS 316L powders, it was clearly demonstrated that reducing powder size offers the most effective way of decreasing viscosity whilst maintaining stability and green strength. Whilst there are issues associated with handling very fine titanium powders, it was highlighted in this work that there is AM grade Ti64 powder available in smaller size ranges ($<$ 25 μm) than that used in this work ($23.2 - 44.9$ μm), that should be suitable for this process. This powder was not available for this work, and so presents an obvious opportunity for further developmental work in this area which has the potential to produce a foamed Ti64 slurry more suitable for the 3D extrusion process. This work in this chapter also highlighted that there is a significant gap in existing research around the suitability of specific dispersants for creating metal powder slurries, which presents an opportunity for valuable research to be conducted in the future.

The development of the 3D material extrusion process only included the extrusion of basic geometries, where each extruded layer followed the same extrusion pattern. More complex features

such as the ability to extrude overhangs, or the use of hatching strategies that vary with each layer, have not been explored in this work. Therefore, there is clear scope for further development of this process. Due to the nature of the material, it is unlikely that it would be possible to extrude overhangs between layers, and as such it is suggested that the use of a secondary sacrificial support material would be required, which was also suggested in Section 6.3.3 as being a possible means of preventing spreading of the outer track. As the slurry was mixed using MC solution as the gelling agent, it would be logical to use a MC based support material that could be loaded with a sacrificial powder that could be burned out during sintering. The development of this support material, as well as a multi-syringe system that would allow the extrusion of the slurry and support material in the same process, presents an important body of future work which could significantly enhance the capabilities of this process by enabling the extrusion of more complex geometries.

The thin-layer drying models, and the steady state layer temperature model in particular, highlight that if relying on a heated platform as the only heat source for this process, the number of layers that can be deposited is restricted because the maximum temperature that each layer reaches decreases, as outlined in Table 19. The maximum layer count is determined by the original platform temperature, as well as the thickness of the layers being deposited. After a certain number of layers, the temperature will no longer reach the gelling point of the MC solution within the slurry, and the layers will no longer be able to dry. Therefore, this highlights the need to develop systems with alternative heat sources, as discussed in Section 7.3, that can overcome this limitation. It should be noted that these thin-layer models would also be suitable for drying within a heated chamber, as their typical applications in literature are for drying of thin-layer materials within an oven.

It should be emphasised that all the structures and samples analysed and discussed in this work were green, meaning that they had not been sintered. The decision was made to analyse the samples without sintering because of a lack of access to a furnace capable of sintering Ti64 and SS 316 powders, and working with green samples allowed a significantly greater amount of samples to be analysed allowing the work to progress without delays related to accessing facilities for sintering samples. As a result, there still remains an important body of research to be completed following on from this work in order to understand the impact of the sintering process and conditions on the porous structures produced from both Ti64 and SS 316L powder slurries. The Ti64 structure

sintering stability test presented in Figure 4.1.5 demonstrated that the porous Ti64 samples produced by foam gel casting are able to maintain their structure even when the MC is burnt out, which shows that they can be sintered without collapsing providing the conditions are suitable. As discussed in Section 2.6.6, Lin and Kennedy reported a shrinkage of $15 - 25$ % as a result of sintering of their porous SS 316L samples produced by foam gel casting with a slurry of similar composition to the slurries developed in this work [243]. Currently there is no data available for the sintering of porous Ti64 samples produced through foam gel casting as this work presents a novel contribution in the development of this process for Ti64. However, the composition of the Ti64 powder slurries in this work is similar to those used by Lin and Kennedy, and therefore similar sintering behaviour in terms of shrinkage is to be expected. Section 2.3.1 presents details of the sintering conditions of Ti64 applied in various PM studies, and how the sintering conditions affect final density of Ti64 parts where the aim is to reduce the residual porosity that occurs as a result of the PM process. It has been demonstrated that both powder particle size and sintering temperature effect the shrinkage of parts during sintering, and as such have an impact on the final density [158]. Also sintering pressure has been shown to have a significant effect on the final density of sintered Ti64 powder parts [143], therefore all these conditions need to be considered and can be optimised for sintering the porous structures produced using the method developed in this work.

In addition, until the samples produced in this work have been sintered, the mechanical properties cannot be evaluated in order to determine whether they are suitable for the purpose. However, the graphs of Young's modulus and yield strength against porosity of Ti64 samples generated using data obtained from various literature sources, presented in Section 2.5, were generated to provide an estimate of the final mechanical properties of the structures produced from foamed Ti64 powder slurries. It is clear from these plots that the level of porosity in the samples produced in this work would result in a sufficient reduction in mechanical strength of the Ti64 in order to overcome the issues caused by stress-shielding, as outlined in Section 1.1. However, it is important to ensure that the material would still provide sufficient strength for load-bearing applications, and therefore there is a clear demand for mechanical testing of the sintered structures. Also, it was highlighted in the literature that the sintering conditions and heat treatment can have a significant impact on the properties of Ti, and as such there is scope for further investigation regarding the optimisation of these processes to enhance the mechanical properties of the structures for this application.

References

[1] A S Brydone, D Meek, and S Maclaine. "Bone grafting, orthopaedic biomaterials, and the clinical need for bone engineering". In: *Proceedings of the Institution of Mechanical Engineers, Part H: Journal of Engineering in Medicine* 224.12 (2010). PMID: 21287823, pp. 1329–1343. DOI: 10.1243/09544119JEIM770. eprint: https://doi.org/10.1243/09544119JEIM770. URL: https://doi.org/10.1243/09544119JEIM770.

[2] Lutz Claes et al. "Influence of size and stability of the osteotomy gap on the success of fracture healing". In: *Journal of Orthopaedic Research* 15.4 (1997), pp. 577–584. DOI: 10.1002/jor.1100150414. eprint: https://onlinelibrary.wiley.com/doi/pdf/10.1002/jor.1100150414. URL: https://onlinelibrary.wiley.com/doi/abs/10.1002/jor.1100150414.

[3] Peter V. Giannoudis, Haralambos Dinopoulos, and Eleftherios Tsiridis. "Bone substitutes: An update". In: *Injury* 36.3, Supplement (2005). Proceedings from the 1st European Clinical Symposium on Bone and Tissue Regeneration 27-28 November 2004, S20–S27. ISSN: 0020-1383. DOI: https://doi.org/10.1016/j.injury.2005.07.029. URL: http://www.sciencedirect.com/science/article/pii/S0020138305002871.

[4] C. Emmelmann et al. "Laser Additive Manufacturing of Modified Implant Surfaces with Osseointegrative Characteristics". In: *Physics Procedia* 12 (2011). Lasers in Manufacturing 2011 - Proceedings of the Sixth International WLT Conference on Lasers in Manufacturing, pp. 375–384. ISSN: 1875-3892. DOI: https://doi.org/10.1016/j.phpro.2011.03.048. URL: http://www.sciencedirect.com/science/article/pii/S1875389211001271.

[5] TW Bauer and GF Muschler. "Bone graft materials. An overview of the basic science". In: *Clinical orthopaedics and related research* 371 (Feb. 2000), pp. 10–27. ISSN: 0009-921X. URL: http://europepmc.org/abstract/MED/10693546.

[6] Yunpeng Li et al. "Clinical application of 3D-printed PEEK implants for repairing mandibular defects". In: *Journal of Cranio-Maxillofacial Surgery* 50.8 (2022), pp. 621–626.

[7] Krzysztof Pałka and Rafał Pokrowiecki. "Porous Titanium Implants: A Review". In: *Advanced Engineering Materials* 20.5 (), p. 1700648. DOI: 10.1002/adem.201700648. eprint: https://onlinelibrary.wiley.com/doi/pdf/10.1002/adem.201700648. URL: https://onlinelibrary.wiley.com/doi/abs/10.1002/adem.201700648.

[8] James A. Goulet et al. "Autogenous iliac crest bone graft: Complications and functional assessment". English (US). In: *Clinical Orthopaedics and Related Research* 339 (June 1997), pp. 76–81. ISSN: 0009-921X.

[9] Susmita Bose, Sahar Vahabzadeh, and Amit Bandyopadhyay. "Bone tissue engineering using 3D printing". In: *Materials Today* 16.12 (2013), pp. 496–504. ISSN: 1369-7021. DOI: https://doi.org/10.1016/j.mattod.2013.11.017. URL: http://www.sciencedirect.com/science/article/pii/S136970211300401X.

[10] Steve Lee et al. "Potential Bone Replacement Materials Prepared by Two Methods". In: *MRS Proceedings* 1418 (2012). DOI: 10.1557/opl.2012.671.

[11] Michaela Fousová et al. "Promising characteristics of gradient porosity Ti-6Al-4V alloy prepared by SLM process". In: *Journal of the Mechanical Behavior of Biomedical Materials* 69 (2017), pp. 368–376. ISSN: 1751-6161. DOI: https://doi.org/10.1016/j.jmbbm.2017.01.043. URL: http://www.sciencedirect.com/science/article/pii/S1751616117300541.

[12] Chunxu Li et al. “Advances in Medical Applications of Additive Manufacturing”. In: *Engineering* 6.11 (2020), pp. 1222–1231. ISSN: 2095-8099. DOI: https://doi.org/10.1016/j.eng.2020.02.018. URL: https://www.sciencedirect.com/science/article/pii/S2095809920302447.

[13] Donghua Yang et al. “Preparation and properties of biomedical porous titanium alloys by gelcasting”. In: *Biomedical Materials* 6.4 (2011), p. 045010. URL: http://stacks.iop.org/1748-605X/6/i=4/a=045010.

[14] A. Fukuda et al. “Osteoinduction of porous Ti implants with a channel structure fabricated by selective laser melting”. In: *Acta Biomaterialia* 7.5 (2011), pp. 2327–2336. ISSN: 1742-7061. DOI: https://doi.org/10.1016/j.actbio.2011.01.037. URL: http://www.sciencedirect.com/science/article/pii/S1742706111000584.

[15] Naoya Taniguchi et al. “Effect of pore size on bone ingrowth into porous titanium implants fabricated by additive manufacturing: An in vivo experiment”. In: *Materials Science and Engineering: C* 59 (2016), pp. 690–701. ISSN: 0928-4931. DOI: https://doi.org/10.1016/j.msec.2015.10.069. URL: http://www.sciencedirect.com/science/article/pii/S0928493115305002.

[16] S. Van Bael et al. “The effect of pore geometry on the in vitro biological behavior of human periosteum-derived cells seeded on selective laser-melted Ti6Al4V bone scaffolds”. In: *Acta Biomaterialia* 8.7 (2012), pp. 2824–2834. ISSN: 1742-7061. DOI: https://doi.org/10.1016/j.actbio.2012.04.001. URL: http://www.sciencedirect.com/science/article/pii/S1742706112001481.

[17] J. Knychala et al. “Pore Geometry Regulates Early Stage Human Bone Marrow Cell Tissue Formation and Organisation”. In: *Annals of Biomedical Engineering* 41.5 (May 2013), pp. 917–930. ISSN: 1573-9686. DOI: 10.1007/s10439-013-0748-z. URL: https://doi.org/10.1007/s10439-013-0748-z.

[18] Amir A. Zadpoor. “Bone tissue regeneration: the role of scaffold geometry”. In: *Biomater. Sci.* 3 (2 2015), pp. 231–245. DOI: 10.1039/C4BM00291A. URL: http://dx.doi.org/10.1039/C4BM00291A.

[19] Eichi Tsuruga et al. “Pore Size of Porous Hydroxyapatite as the Cell-Substratum Controls BMP-Induced Osteogenesis”. In: *The Journal of Biochemistry* 121.2 (1997), pp. 317–324.

[20] Vassilis Karageorgiou and David Kaplan. “Porosity of 3D biomaterial scaffolds and osteogenesis”. In: *Biomaterials* 26.27 (2005), pp. 5474–5491. ISSN: 0142-9612. DOI: https://doi.org/10.1016/j.biomaterials.2005.02.002. URL: http://www.sciencedirect.com/science/article/pii/S0142961205001511.

[21] Jia Ping Li et al. “Bone ingrowth in porous titanium implants produced by 3D fiber deposition”. In: *Biomaterials* 28.18 (2007), pp. 2810–2820. ISSN: 0142-9612. DOI: https://doi.org/10.1016/j.biomaterials.2007.02.020. URL: http://www.sciencedirect.com/science/article/pii/S014296120700172X.

[22] Lewis Mullen et al. “Selective Laser Melting: A regular unit cell approach for the manufacture of porous, titanium, bone in-growth constructs, suitable for orthopedic applications”. In: *Journal of Biomedical Materials Research Part B: Applied Biomaterials* 89B.2 (), pp. 325–334. DOI: 10.1002/jbm.b.31219. eprint: https://onlinelibrary.wiley.com/doi/pdf/10.1002/jbm.b.31219. URL: https://onlinelibrary.wiley.com/doi/abs/10.1002/jbm.b.31219.

[23] J. X. LU et al. “Role of interconnections in porous bioceramics on bone recolonization in vitro and in vivo”. In: *Journal of Materials Science: Materials in Medicine* 10.2 (Feb. 1999), pp. 111–120. ISSN: 1573-4838. DOI: 10.1023/A:1008973120918. URL: https://doi.org/10.1023/A:1008973120918.

[24] R. Stamp et al. “The development of a scanning strategy for the manufacture of porous biomaterials by selective laser melting”. In: *Journal of Materials Science: Materials in Medicine* 20.9 (June 2009), p. 1839. ISSN: 1573-4838. DOI: 10.1007/s10856-009-3763-8. URL: https://doi.org/10.1007/s10856-009-3763-8.

[25] Shunsuke Fujibayashi et al. “Osteoinduction of porous bioactive titanium metal”. In: *Biomaterials* 25.3 (2004), pp. 443–450. ISSN: 0142-9612. DOI: https://doi.org/10.1016/S0142-9612(03)00551-9. URL: http://www.sciencedirect.com/science/article/pii/S0142961203005519.

[26] Ruidi Li et al. “316L Stainless Steel with Gradient Porosity Fabricated by Selective Laser Melting”. In: *Journal of Materials Engineering and Performance* 19.5 (July 2010), pp. 666–671. ISSN: 1544-1024. DOI: 10.1007/s11665-009-9535-2. URL: https://doi.org/10.1007/s11665-009-9535-2.

[27] Claude O. Clerc et al. “Assessment of wrought ASTM F1058 cobalt alloy properties for permanent surgical implants”. In: *Journal of Biomedical Materials Research* 38.3 (1997), pp. 229–234. DOI: 10.1002/(SICI)1097-4636(199723)38:3<229::AID-JBM7>3.0.CO;2-R. eprint: https://onlinelibrary.wiley.com/doi/pdf/10.1002/\%28SICI\%291097-4636\%28199723\%2938\%3A3\%3C229\%3A\%3AAID-JBM7\%3E3.0.CO\%3B2-R. URL: https://onlinelibrary.wiley.com/doi/abs/10.1002/%5C%28SICI%5C%291097-4636%5C%28199723%5C%2938%5C%3A3%5C%3C229%5C%3A%5C%3AAID-JBM7%5C%3E3.0.CO%5C%3B2-R.

[28] Yahya Bozkurt and Elif Karayel. “3D printing technology; methods, biomedical applications, future opportunities and trends”. In: *Journal of Materials Research and Technology* 14 (2021), pp. 1430–1450. ISSN: 2238-7854. DOI: https://doi.org/10.1016/j.jmrt.2021.07.050. URL: https://www.sciencedirect.com/science/article/pii/S2238785421007134.

[29] R. Singh et al. “Titanium foams for biomedical applications: a review”. In: *Materials Technology* 25.3-4 (2010), pp. 127–136. DOI: 10.1179/175355510X12744412709403. eprint: https://doi.org/10.1179/175355510X12744412709403. URL: https://doi.org/10.1179/175355510X12744412709403.

[30] Ik-Hyun Oh et al. “Mechanical properties of porous titanium compacts prepared by powder sintering”. In: *Scripta Materialia* 49.12 (2003), pp. 1197–1202. ISSN: 1359-6462. DOI: https://doi.org/10.1016/j.scriptamat.2003.08.018. URL: http://www.sciencedirect.com/science/article/pii/S1359646203005244.

[31] Ying Long Zhou et al. “Corrosion resistance and biocompatibility of Ti–Ta alloys for biomedical applications”. In: *Materials Science and Engineering: A* 398.1 (2005), pp. 28–36. ISSN: 0921-5093. DOI: https://doi.org/10.1016/j.msea.2005.03.032. URL: http://www.sciencedirect.com/science/article/pii/S0921509305002133.

[32] S. Leuders et al. “On the mechanical behaviour of titanium alloy TiAl6V4 manufactured by selective laser melting: Fatigue resistance and crack growth performance”. In: *International Journal of Fatigue* 48 (2013), pp. 300–307. ISSN: 0142-1123. DOI: https://doi.org/10.1016/j.ijfatigue.2012.11.011. URL: http://www.sciencedirect.com/science/article/pii/S014211231200343X.

[33] Mitsuo Niinomi. "Mechanical biocompatibilities of titanium alloys for biomedical applications". In: *Journal of the Mechanical Behavior of Biomedical Materials* 1.1 (2008), pp. 30–42. ISSN: 1751-6161. DOI: https://doi.org/10.1016/j.jmbbm.2007.07.001. URL: http://www.sciencedirect.com/science/article/pii/S1751616107000148.

[34] Lai-Chang Zhang and Hooyar Attar. "Selective Laser Melting of Titanium Alloys and Titanium Matrix Composites for Biomedical Applications: A Review". In: *Advanced Engineering Materials* 18.4 (), pp. 463–475. DOI: 10.1002/adem.201500419. eprint: https://onlinelibrary.wiley.com/doi/pdf/10.1002/adem.201500419. URL: https://onlinelibrary.wiley.com/doi/abs/10.1002/adem.201500419.

[35] Harun H. Bayraktar et al. "Comparison of the elastic and yield properties of human femoral trabecular and cortical bone tissue". In: *Journal of Biomechanics* 37.1 (2004), pp. 27–35. ISSN: 0021-9290. DOI: https://doi.org/10.1016/S0021-9290(03)00257-4. URL: http://www.sciencedirect.com/science/article/pii/S0021929003002574.

[36] M Thieme et al. "Titanium powder sintering for preparation of a porous functionally graded material destined for orthopaedic implants". In: *Journal of materials science: materials in medicine* 12.3 (2001), pp. 225–231.

[37] BILL HUGHES and GREG WILSON. "3D/additive printing manufacturing: A BRIEF HISTORY AND PURCHASING GUIDE." In: *Technology & Engineering Teacher* 75.4 (2015), pp. 18–21. ISSN: 21580502. URL: http://search.ebscohost.com.ezproxy.lancs.ac.uk/login.aspx?direct=true&db=asn&AN=111216018&site=ehost-live&authtype=ip,shib&user=s1523151.

[38] H. Shipley et al. "Optimisation of process parameters to address fundamental challenges during selective laser melting of Ti-6Al-4V: A review". In: *International Journal of Machine Tools and Manufacture* 128 (2018), pp. 1–20. ISSN: 0890-6955. DOI: https://doi.org/10.1016/j.ijmachtools.2018.01.003. URL: http://www.sciencedirect.com/science/article/pii/S0890695518300233.

[39] Malte Gebler, Anton J.M. [Schoot Uiterkamp], and Cindy Visser. "A global sustainability perspective on 3D printing technologies". In: *Energy Policy* 74 (2014), pp. 158–167. ISSN: 0301-4215. DOI: https://doi.org/10.1016/j.enpol.2014.08.033. URL: http://www.sciencedirect.com/science/article/pii/S0301421514004868.

[40] Simon Ford and Mélanie Despeisse. "Additive manufacturing and sustainability: an exploratory study of the advantages and challenges". In: *Journal of Cleaner Production* 137 (2016), pp. 1573–1587. ISSN: 0959-6526. DOI: https://doi.org/10.1016/j.jclepro.2016.04.150.

[41] Thywill Dzogbewu. "ADDITIVE MANUFACTURING OF POROUS TI-BASED ALLOYS FOR BIOMEDICAL APPLICATIONS – A REVIEW". In: 15 (May 2017).

[42] Additive Manufacturing Platform. *Additive manufacturing roadmap*. Oct. 2018. URL: https://www.rm-platform.com/roadmaping-activities/additive-manufacturing-roadmap.

[43] Saquib Rouf et al. "Additive manufacturing technologies: industrial and medical applications". In: *Sustainable Operations and Computers* (2022).

[44] Aishwarya Bhargav et al. "Applications of additive manufacturing in dentistry: A review". In: *Journal of Biomedical Materials Research Part B: Applied Biomaterials* 106.5 (2018), pp. 2058–2064.

[45] Rakesh Kumar, Manoj Kumar, and Jasgurpreet Singh Chohan. "The role of additive manufacturing for biomedical applications: A critical review". In: *Journal of Manufacturing Processes* 64 (2021), pp. 828–850.

[46] WA Goodall, AC Greer, and N Martin. "Unilateral removable partial dentures". In: *British Dental Journal* 222.2 (2017), pp. 79–84.

[47] Khalid Ahmad Omar Arafa. "Comparing the effects of titanium alloy and chrome cobalt in removable partial denture connectors on tooth mobility, bone loss and tissue reaction". In: *The Saudi Journal for Dental Research* 7.2 (2016), pp. 112–117.

[48] Julia Magalhaes Costa Lima et al. "Removable partial dentures: use of rapid prototyping". In: *Journal of Prosthodontics* 23.7 (2014), pp. 588–591.

[49] RJ Williams et al. "Use of CAD/CAM technology to fabricate a removable partial denture framework". In: *The Journal of prosthetic dentistry* 96.2 (2006), pp. 96–99.

[50] Junning Chen et al. "Shape optimization for additive manufacturing of removable partial dentures-a new paradigm for prosthetic CAD/CAM". In: *PloS one* 10.7 (2015), e0132552.

[51] Jing Han, Yong Wang, and Peijun Lü. "A preliminary report of designing removable partial denture frameworks using a specifically developed software package." In: *International Journal of Prosthodontics* 23.4 (2010).

[52] Michael Molitch-Hou. *FDA approval 3D printed denture bases.* Aug. 2015. URL: `https://3dprintingindustry.com/news/dentures-get-3d-printed-boost-with-dentcas-fda-approval-55274/`.

[53] Jun Yue et al. "3D-printable antimicrobial composite resins". In: *Advanced functional materials* 25.43 (2015), pp. 6756–6767.

[54] Lucio Lo Russo et al. "Digital dentures: A protocol based on intraoral scans". In: *The Journal of Prosthetic Dentistry* 125.4 (2021), pp. 597–602.

[55] Lucio Lo Russo et al. "Accuracy of trial complete dentures fabricated by using fused deposition modeling 3-dimensional printing: An in vitro study". In: *The Journal of Prosthetic Dentistry* (2021).

[56] Fang Guo et al. "Evaluation of the mechanical properties and fit of 3D-printed polyetherether ketone removable partial dentures". In: *Dental Materials Journal* (2022).

[57] MM Shalabi et al. "Implant surface roughness and bone healing: a systematic review". In: *Journal of dental research* 85.6 (2006), pp. 496–500.

[58] Carlo Mangano et al. "Histological and synchrotron radiation-based computed microtomography study of 2 human-retrieved direct laser metal formed titanium implants". In: *Implant Dentistry* 22.2 (2013), pp. 175–181.

[59] Yaling Wang et al. "Studies on the performance of selective laser melting porous dental implant by finite element model simulation, fatigue testing and in vivo experiments". In: *Proceedings of the Institution of Mechanical Engineers, Part H: Journal of Engineering in Medicine* 233.2 (2019), pp. 170–180.

[60] Carlo Mangano et al. "A light and scanning electron microscopy study of human direct laser metal forming dental implants." In: *International Journal of Periodontics & Restorative Dentistry* 34.1 (2014).

[61] Jamil A Shibli et al. “Bone-to-implant contact around immediately loaded direct laser metal-forming transitional implants in human posterior maxilla”. In: *Journal of Periodontology* 84.6 (2013), pp. 732–737.

[62] Marta Revilla-León, Mehrad Sadeghpour, and Mutlu Özcan. “A review of the applications of additive manufacturing technologies used to fabricate metals in implant dentistry”. In: *Journal of Prosthodontics* 29.7 (2020), pp. 579–593.

[63] Samy Tunchel et al. “3D printing/additive manufacturing single titanium dental implants: a prospective multicenter study with 3 years of follow-up”. In: *International journal of dentistry* 2016 (2016).

[64] Carlo Mangano et al. “Prospective clinical evaluation of 201 direct laser metal forming implants: results from a 1-year multicenter study”. In: *Lasers in medical science* 27.1 (2012), pp. 181–189.

[65] Francesco Mangano et al. “Immediate restoration of fixed partial prostheses supported by one-piece narrow-diameter selective laser sintering implants: a 2-year prospective study in the posterior jaws of 16 patients”. In: *Implant Dentistry* 22.4 (2013), pp. 388–393.

[66] Marion Dehurtevent et al. “Stereolithography: a new method for processing dental ceramics by additive computer-aided manufacturing”. In: *Dental materials* 33.5 (2017), pp. 477–485.

[67] Keunbada Son, Jung-Ho Lee, and Kyu-Bok Lee. “Comparison of intaglio surface trueness of interim dental crowns fabricated with SLA 3D printing, DLP 3D printing, and milling technologies”. In: *Healthcare*. Vol. 9. 8. MDPI. 2021, p. 983.

[68] Mohammad Mujtaba Methani, Marta Revilla-León, and Amirali Zandinejad. “The potential of additive manufacturing technologies and their processing parameters for the fabrication of all-ceramic crowns: A review”. In: *Journal of Esthetic and Restorative Dentistry* 32.2 (2020), pp. 182–192.

[69] Yurdanur Uçar, İpek Aysan Meriç, and Orhun Ekren. “Layered manufacturing of dental ceramics: fracture mechanics, microstructure, and elemental composition of lithography-sintered ceramic”. In: *Journal of Prosthodontics* 28.1 (2019), e310–e318.

[70] Saori Muta et al. “Chairside fabrication of provisional crowns on FDM 3D-printed PVA model”. In: *Journal of Prosthodontic Research* 64.4 (2020), pp. 401–407. ISSN: 1883-1958. DOI: https://doi.org/10.1016/j.jpor.2019.11.004.

[71] Nabil Takahiro Moussa and Harry Dym. “Maxillofacial bone grafting materials”. In: *Dental Clinics* 64.2 (2020), pp. 473–490.

[72] Sekou Singare et al. “Design and fabrication of custom mandible titanium tray based on rapid prototyping”. In: *Medical engineering & physics* 26.8 (2004), pp. 671–676.

[73] Mohd. Javaid and Abid Haleem. “Additive manufacturing applications in medical cases: A literature based review”. In: *Alexandria Journal of Medicine* 54.4 (2018), pp. 411–422. ISSN: 2090-5068. DOI: https://doi.org/10.1016/j.ajme.2017.09.003. URL: https://www.sciencedirect.com/science/article/pii/S2090506817302282.

[74] Beth Stackpole. *3D-printed jaw used in Transplant*. Oct. 2016. URL: www.designnews.com/design-hardware-software/3d-printed-jaw-used-transplant.

[75] Hideto Saijo et al. “Maxillofacial reconstruction using custom-made artificial bones fabricated by inkjet printing technology”. In: *Journal of Artificial Organs* 12.3 (2009), pp. 200–205.

[76] Alberto J Ambard and Leonard Mueninghoff. "Calcium phosphate cement: review of mechanical and biological properties". In: *Journal of Prosthodontics* 15.5 (2006), pp. 321–328.

[77] Zhonghua Sun and L Shen-Yuan. "A systematic review of 3-D printing in cardiovascular and cerebrovascular diseases". In: *Anatolian journal of cardiology* 17.6 (2017), pp. 423–435.

[78] Kosuke Kondo et al. "A neurosurgical simulation of skull base tumors using a 3D printed rapid prototyping model containing mesh structures". In: *Acta neurochirurgica* 158.6 (2016), pp. 1213–1219.

[79] Nizar N. Zein et al. "Three-dimensional print of a liver for preoperative planning in living donor liver transplantation". In: *Liver Transplantation* 19.12 (2013), pp. 1304–1310. DOI: https://doi.org/10.1002/lt.23729. eprint: https://aasldpubs.onlinelibrary.wiley.com/doi/pdf/10.1002/lt.23729. URL: https://aasldpubs.onlinelibrary.wiley.com/doi/abs/10.1002/lt.23729.

[80] Jonathan L. Silberstein et al. "Physical Models of Renal Malignancies Using Standard Cross-sectional Imaging and 3-Dimensional Printers: A Pilot Study". In: *Urology* 84.2 (2014), pp. 268–273. ISSN: 0090-4295. DOI: https://doi.org/10.1016/j.urology.2014.03.042. URL: https://www.sciencedirect.com/science/article/pii/S0090429514004555.

[81] Jan Sylwester Witowski et al. "Cost-effective, personalized, 3D-printed liver model for preoperative planning before laparoscopic liver hemihepatectomy for colorectal cancer metastases". In: *International journal of computer assisted radiology and surgery* 12.12 (2017), pp. 2047–2054.

[82] Carling L Cheung et al. "Use of 3-dimensional printing technology and silicone modeling in surgical simulation: development and face validation in pediatric laparoscopic pyeloplasty". In: *Journal of surgical education* 71.5 (2014), pp. 762–767.

[83] Justin R Ryan et al. "A novel approach to neonatal management of tetralogy of Fallot, with pulmonary atresia, and multiple aortopulmonary collaterals". In: *JACC: Cardiovascular Imaging* 8.1 (2015), pp. 103–104.

[84] Israel Valverde. "Three-dimensional printed cardiac models: applications in the field of medical education, cardiovascular surgery, and structural heart interventions". In: *Revista Española de Cardiologıa (English Edition)* 70.4 (2017), pp. 282–291.

[85] Michael Di Giuseppe et al. "Mechanical behaviour of alginate-gelatin hydrogels for 3D bioprinting". In: *Journal of the mechanical behavior of biomedical materials* 79 (2018), pp. 150–157.

[86] Patrycja Szymczyk-Ziółkowska et al. "A review of fabrication polymer scaffolds for biomedical applications using additive manufacturing techniques". In: *Biocybernetics and Biomedical Engineering* 40.2 (2020), pp. 624–638.

[87] Jia Jia et al. "Engineering alginate as bioink for bioprinting". In: *Acta biomaterialia* 10.10 (2014), pp. 4323–4331.

[88] MyungGu Yeo et al. "An innovative collagen-based cell-printing method for obtaining human adipose stem cell-laden structures consisting of core–sheath structures for tissue engineering". In: *Biomacromolecules* 17.4 (2016), pp. 1365–1375.

[89] Haesun Park, Andrew Otte, and Kinam Park. "Evolution of drug delivery systems: From 1950 to 2020 and beyond". In: *Journal of Controlled Release* 342 (2022), pp. 53–65. ISSN: 0168-3659. DOI: https://doi.org/10.1016/j.jconrel.2021.12.030. URL: https://www.sciencedirect.com/science/article/pii/S0168365921006830.

[90] Ion-Bogdan Dumitrescu et al. “The age of pharmaceutical 3D printing. Technological and therapeutical implications of additive manufacturing”. In: *Farmacia* 66.3 (2018), pp. 365–389.

[91] Muzna Sadia et al. “Adaptation of pharmaceutical excipients to FDM 3D printing for the fabrication of patient-tailored immediate release tablets”. In: *International journal of pharmaceutics* 513.1-2 (2016), pp. 659–668.

[92] Jonathan Goole and Karim Amighi. “3D printing in pharmaceutics: A new tool for designing customized drug delivery systems”. In: *International journal of pharmaceutics* 499.1-2 (2016), pp. 376–394.

[93] Andrea Alice Konta, Marta Garcıa-Piña, and Dolores R Serrano. “Personalised 3D printed medicines: which techniques and polymers are more successful?” In: *Bioengineering* 4.4 (2017), p. 79.

[94] Eric Lepowsky and Savas Tasoglu. “3D printing for drug manufacturing: A perspective on the future of pharmaceuticals”. In: *International journal of bioprinting* 4.1 (2018).

[95] Jingjunjiao Long et al. “Application of fused deposition modelling (FDM) method of 3D printing in drug delivery”. In: *Current pharmaceutical design* 23.3 (2017), pp. 433–439.

[96] Leena Kumari Prasad and Hugh Smyth. “3D Printing technologies for drug delivery: a review”. In: *Drug development and industrial pharmacy* 42.7 (2016), pp. 1019–1031.

[97] Natalja Genina et al. “Ethylene vinyl acetate (EVA) as a new drug carrier for 3D printed medical drug delivery devices”. In: *European Journal of Pharmaceutical Sciences* 90 (2016), pp. 53–63.

[98] Tatsuaki Tagami et al. “3D printing factors important for the fabrication of polyvinylalcohol filament-based tablets”. In: *Biological and Pharmaceutical Bulletin* 40.3 (2017), pp. 357–364.

[99] Alvaro Goyanes et al. “Fused-filament 3D printing (3DP) for fabrication of tablets”. In: *International journal of pharmaceutics* 476.1-2 (2014), pp. 88–92.

[100] Justyna Skowyra, Katarzyna Pietrzak, and Mohamed A Alhnan. “Fabrication of extended-release patient-tailored prednisolone tablets via fused deposition modelling (FDM) 3D printing”. In: *European Journal of Pharmaceutical Sciences* 68 (2015), pp. 11–17.

[101] RCR Beck et al. “3D printed tablets loaded with polymeric nanocapsules: An innovative approach to produce customized drug delivery systems”. In: *International journal of pharmaceutics* 528.1-2 (2017), pp. 268–279.

[102] Tochukwu C Okwuosa et al. “A lower temperature FDM 3D printing for the manufacture of patient-specific immediate release tablets”. In: *Pharmaceutical research* 33.11 (2016), pp. 2704–2712.

[103] Mirja Palo et al. “3D printed drug delivery devices: perspectives and technical challenges”. In: *Expert review of medical devices* 14.9 (2017), pp. 685–696.

[104] Cristiane Patricia Pissinato Pere et al. “3D printed microneedles for insulin skin delivery”. In: *International journal of pharmaceutics* 544.2 (2018), pp. 425–432.

[105] Ahlam Zaid Alkilani, Maelıosa TC McCrudden, and Ryan F Donnelly. “Transdermal drug delivery: innovative pharmaceutical developments based on disruption of the barrier properties of the stratum corneum”. In: *Pharmaceutics* 7.4 (2015), pp. 438–470.

[106] Tao Han and Diganta Bhusan Das. "Potential of combined ultrasound and microneedles for enhanced transdermal drug permeation: a review". In: *European Journal of Pharmaceutics and Biopharmaceutics* 89 (2015), pp. 312–328.

[107] Ryan F Donnelly et al. "Microneedle-mediated transdermal and intradermal drug delivery". In: (2012).

[108] EV Mukerjee et al. "Microneedle array for transdermal biological fluid extraction and in situ analysis". In: *Sensors and Actuators A: Physical* 114.2-3 (2004), pp. 267–275.

[109] Gill HS Denson DD Burris and MR Prausnitz. "Effect of microneedle design on pain in human volunteers". In: *Clin J Pain* 24.7 (2008), pp. 585–94.

[110] Ryan D Boehm et al. "Inkjet printing of amphotericin B onto biodegradable microneedles using piezoelectric inkjet printing". In: *Jom* 65.4 (2013), pp. 525–533.

[111] Ryan D Boehm et al. "Inkjet printing for pharmaceutical applications". In: *Materials Today* 17.5 (2014), pp. 247–252.

[112] Sophia N Economidou, Dimitrios A Lamprou, and Dennis Douroumis. "3D printing applications for transdermal drug delivery". In: *International journal of pharmaceutics* 544.2 (2018), pp. 415–424.

[113] Cassie L Caudill et al. "Spatially controlled coating of continuous liquid interface production microneedles for transdermal protein delivery". In: *Journal of Controlled Release* 284 (2018), pp. 122–132.

[114] Michael A Luzuriaga et al. "Biodegradable 3D printed polymer microneedles for transdermal drug delivery". In: *Lab on a Chip* 18.8 (2018), pp. 1223–1230.

[115] Jorge M Zuniga et al. "Coactivation index of children with congenital upper limb reduction deficiencies before and after using a wrist-driven 3D printed partial hand prosthesis". In: *Journal of neuroengineering and rehabilitation* 15.1 (2018), pp. 1–11.

[116] Abby Megan Paterson et al. "Comparing additive manufacturing technologies for customised wrist splints". In: *Rapid Prototyping Journal* (2015).

[117] Rui Xu et al. "Effect of 3D printing individualized ankle-foot orthosis on plantar biomechanics and pain in patients with plantar fasciitis: a randomized controlled trial". In: *Medical science monitor: international medical journal of experimental and clinical research* 25 (2019), p. 1392.

[118] Zheng Ma et al. "Design and 3D printing of adjustable modulus porous structures for customized diabetic foot insoles". In: *International Journal of Lightweight Materials and Manufacture* 2.1 (2019), pp. 57–63.

[119] Gwen RJ Swennen, Lies Pottel, and Piet E Haers. "Custom-made 3D-printed face masks in case of pandemic crisis situations with a lack of commercially available FFP2/3 masks". In: *International Journal of Oral and Maxillofacial Surgery* 49.5 (2020), pp. 673–677.

[120] Ian Gibson et al. "Design for additive manufacturing". In: *Additive manufacturing technologies*. Springer, 2021, pp. 555–607.

[121] Sonova. *3D printing technology for improved hearing*. 2022. URL: `https://www.sonova.com/en/story/innovation/3d-printing-technology-improved-hearing`.

[122] Yu Ying Clarrisa Choong et al. "The global rise of 3D printing during the COVID-19 pandemic". In: *Nature Reviews Materials* 5.9 (2020), pp. 637–639.

[123] Stephanie Ishack and Shari R Lipner. "Applications of 3D printing technology to address COVID-19–related supply shortages". In: *The American journal of medicine* 133.7 (2020), p. 771.

[124] Sarah T Flanagan and David H Ballard. "3D printed face shields: a community response to the COVID-19 global pandemic". In: *Academic radiology* 27.6 (2020), pp. 905–906.

[125] Christian Wesemann et al. "3-D printed protective equipment during COVID-19 pandemic". In: *Materials* 13.8 (2020), p. 1997.

[126] Dina Amin et al. "3D printing of face shields during COVID-19 pandemic: a technical note". In: *Journal of Oral and Maxillofacial Surgery* 78.8 (2020), pp. 1275–1278.

[127] Lorenzo Dall'Ava et al. "Comparative analysis of current 3D printed acetabular titanium implants". In: *3D Printing in Medicine* 5 (2019), pp. 1–10.

[128] Lorenzo Dall'Ava et al. "3D printed acetabular cups for total hip arthroplasty: a review article". In: *Metals* 9.7 (2019), p. 729.

[129] Elyse J Berlinberg et al. "Minimum 2-Year Outcomes of a Novel 3D-printed Fully Porous Titanium Acetabular Shell in Revision Total Hip Arthroplasty". In: *Arthroplasty today* 18 (2022), pp. 39–44.

[130] Xiao Geng et al. "A new 3D printing porous trabecular titanium metal acetabular cup for primary total hip arthroplasty: a minimum 2-year follow-up of 92 consecutive patients". In: *Journal of Orthopaedic Surgery and Research* 15 (2020), pp. 1–8.

[131] Michael P Francis et al. *9. Additive Manufacturing for Biofabricated Medical Device Applications*. 2018. URL: https://app.knovel.com/hotlink/khtml/id:kt00CYJY7M/additive-manufacturing/additive-m-manufacturing-7.

[132] Robert B. Heimann, ed. *Materials for Medical Application*. Berlin, Boston: De Gruyter, 2020. ISBN: 9783110619249. DOI: doi:10.1515/9783110619249. URL: https://doi.org/10.1515/9783110619249.

[133] Properties, Material. *Ti-6Al-4V: Density, strength, hardness, melting point*. [Online; accessed 2-June-2022]. 2021. URL: https://material-properties.org/ti-6al-4v-density-strength-hardness-melting-point/.

[134] SL Semiatin et al. "Microstructure evolution during alpha-beta heat treatment of Ti-6Al-4V". In: *Metallurgical and Materials Transactions A* 34.10 (2003), pp. 2377–2386.

[135] U.S. Titanium Industry Inc. *Titanium alloys - TI6AL4V grade 5*. Sept. 2020. URL: https://www.azom.com/article.aspx?ArticleID=1547.

[136] Inc. ASM Aerospace Specification Metals. URL: https://asm.matweb.com/search/SpecificMaterial.asp?bassnum=MTP641.

[137] UL Prospector. *Titanium Alloy Ti-6Al-4V datasheet*. URL: https://metals.ulprospector.com/datasheet/e215837/titanium-alloy-ti-6al-4v.

[138] P.C. ANGELO and R. SUBRAMANIAN. *POWDER METALLURGY: SCIENCE, TECHNOLOGY AND APPLICATIONS*. Eastern economy edition. PHI Learning, 2008. ISBN: 9788120332812. URL: https://books.google.co.uk/books?id=7cmb7BgZtvIC.

[139] Yuankui Cao et al. "Characterization of fatigue properties of powder metallurgy titanium alloy". In: *Materials Science and Engineering: A* 654 (2016), pp. 418–425. ISSN: 0921-5093. DOI: https://doi.org/10.1016/j.msea.2015.12.058. URL: http://www.sciencedirect.com/science/article/pii/S0921509315307401.

[140] M. Qian and F.H. Froes. *Titanium Powder Metallurgy: Science, Technology and Applications*. Elsevier Science, 2015. ISBN: 9780128009109. URL: https://books.google.co.uk/books?id=pnSDBAAAQBAJ.

[141] James D Paramore et al. "A powder metallurgy method for manufacturing Ti-6Al-4V with wrought-like microstructures and mechanical properties via hydrogen sintering and phase transformation (HSPT)". In: *Scripta Materialia* 107 (2015), pp. 103–106.

[142] O. Ivasishin et al. "Synthesis of the Ti-6Al-4V alloy having low residual porosity by powder metallurgy method". In: (Jan. 2002), pp. 54–64.

[143] Wei Chen et al. "The investigation of die-pressing and sintering behavior of ITP CP-Ti and Ti-6Al-4V powders". In: *Journal of alloys and compounds* 541 (2012), pp. 440–447.

[144] Rezvan Abedini, Amir Abdullah, and Yunes Alizadeh. "Ultrasonic hot powder compaction of Ti-6Al-4V". In: *Ultrasonics Sonochemistry* 37 (2017), pp. 640–647.

[145] E Ergül, H Özkan Gülsoy, and V Günay. "Effect of sintering parameters on mechanical properties of injection moulded Ti–6Al–4V alloys". In: *Powder Metallurgy* 52.1 (2009), pp. 65–71.

[146] JJ Klawitter and Allan M Weinstein. "The status of porous materials to obtain direct skeletal attachment by tissue ingrowth." In: *Acta Orthopaedica Belgica* 40.5-6 (1974), pp. 755–765.

[147] AC Fraker et al. *Studies of Porous Metal Coated Surgical Implants*. 1985.

[148] John Charnley. "Anchorage of the femoral head prosthesis to the shaft of the femur". In: *The Journal of bone and joint surgery. British volume* 42.1 (1960), pp. 28–30.

[149] Myron Spector. "Historical review of porous-coated implants". In: *The Journal of Arthroplasty* 2.2 (1987), pp. 163–177.

[150] P Ducheyne et al. "Titanium implants with porous structures for bone ingrowth: a general approach". In: *Titanium alloys in surgical implants*. American Society for Testing and Materials Philadelphia, 1983, pp. 265–279.

[151] AJT Clemow et al. "Interface mechanics of porous titanium implants". In: *Journal of Biomedical Materials Research* 15.1 (1981), pp. 73–82.

[152] HM Kim et al. "Bioactive macroporous titanium surface layer on titanium substrate". In: *Journal of biomedical materials research* 52.3 (Dec. 2000), pp. 553–557. ISSN: 0021-9304. DOI: 10.1002/1097-4636(20001205)52:3<553::aid-jbm14>3.0.co;2-x. URL: https://doi.org/10.1002/1097-4636(20001205)52:3%3C553::AID-JBM14%3E3.0.CO;2-X.

[153] YZ Yang et al. "Preparation of graded porous titanium coatings on titanium implant materials by plasma spraying". In: *Journal of Biomedical Materials Research: An Official Journal of The Society for Biomaterials, The Japanese Society for Biomaterials, and The Australian Society for Biomaterials and the Korean Society for Biomaterials* 52.2 (2000), pp. 333–337.

[154] P Ducheyne et al. "Effect of hydroxyapatite impregnation on skeletal bonding of porous coated implants". In: *Journal of biomedical materials research* 14.3 (1980), pp. 225–237.

[155] Jaideep Adhikari, Prosenjit Saha, and Arijit Sinha. "Surface modification of metallic bone implants—Polymer and polymer-assisted coating for bone in-growth". In: *Fundamental Biomaterials: Metals*. Elsevier, 2018, pp. 299–321.

[156] S Yue, RM Pilliar, and GC Weatherly. "The fatigue strength of porous-coated Ti–6% Al–4% V implant alloy". In: *Journal of biomedical materials research* 18.9 (1984), pp. 1043–1058.

[157] John Banhart. "Manufacture, characterisation and application of cellular metals and metal foams". In: *Progress in Materials Science* 46.6 (2001), pp. 559–632. ISSN: 0079-6425. DOI: https://doi.org/10.1016/S0079-6425(00)00002-5. URL: http://www.sciencedirect.com/science/article/pii/S0079642500000025.

[158] José Luis Cabezas-Villa et al. "Sintering study of Ti6Al4V powders with different particle sizes and their mechanical properties". In: *INTERNATIONAL JOURNAL OF MINERALS METALLURGY AND MATERIALS* 25.12 (Dec. 2018), pp. 1389–1401. DOI: 10.1007/s12613-018-1693-5. URL: https://hal.archives-ouvertes.fr/hal-02071169.

[159] Luana Marotta Reis de Vasconcellos et al. "Porous titanium scaffolds produced by powder metallurgy for biomedical applications". en. In: *Materials Research* 11 (Sept. 2008), pp. 275–280. ISSN: 1516-1439. URL: http://www.scielo.br/scielo.php?script=sci_arttext&pid=S1516-14392008000300008&nrm=iso.

[160] Sandra M. Castillo et al. "Influence of the Compaction Pressure and Sintering Temperature on the Mechanical Properties of Porous Titanium for Biomedical Applications". In: *Metals* 9.12 (Nov. 2019), p. 1249. ISSN: 2075-4701. DOI: 10.3390/met9121249. URL: http://dx.doi.org/10.3390/met9121249.

[161] Ziya ESEN, Elif TARHAN BOR, and Şakir BOR. "Characterization of loose powder sintered porous titanium and Ti6Al4V alloy". In: *Turkish Journal of Engineering and Environmental Sciences* 33 (2009), pp. 207–219. ISSN: 1300-0160. DOI: 10.3906/sag-1208-45.

[162] Nidhi Jha et al. "Highly porous open cell Ti-foam using NaCl as temporary space holder through powder metallurgy route". In: *Materials & Design* 47 (2013), pp. 810–819. ISSN: 0261-3069. DOI: https://doi.org/10.1016/j.matdes.2013.01.005. URL: http://www.sciencedirect.com/science/article/pii/S0261306913000186.

[163] Y. Torres, J.J. Pavón, and J.A. Rodríguez. "Processing and characterization of porous titanium for implants by using NaCl as space holder". In: *Journal of Materials Processing Technology* 212.5 (2012), pp. 1061–1069. ISSN: 0924-0136. DOI: https://doi.org/10.1016/j.jmatprotec.2011.12.015. URL: http://www.sciencedirect.com/science/article/pii/S0924013611003724.

[164] Y. Boonyongmaneerat and D. C. Dunand. "Ni-Mo-Cr Foams Processed by Casting Replication of Sodium Aluminate Preforms". In: *Advanced Engineering Materials* 10.4 (), pp. 379–383. DOI: 10.1002/adem.200700300. eprint: https://onlinelibrary.wiley.com/doi/pdf/10.1002/adem.200700300. URL: https://onlinelibrary.wiley.com/doi/abs/10.1002/adem.200700300.

[165] Byounggab Lee et al. "Space-holder effect on designing pore structure and determining mechanical properties in porous titanium". In: *Materials & Design* 57 (2014), pp. 712–718. ISSN: 0261-3069. DOI: https://doi.org/10.1016/j.matdes.2013.12.078. URL: http://www.sciencedirect.com/science/article/pii/S0261306914000260.

[166] Yadir Torres et al. "Development of porous titanium for biomedical applications: A comparison between loose sintering and space-holder techniques". In: *Materials Science and Engineering: C* 37 (2014), pp. 148–155. ISSN: 0928-4931. DOI: https://doi.org/10.1016/j.msec.2013.11.036. URL: http://www.sciencedirect.com/science/article/pii/S0928493113006498.

[167] Güher KOTAN and A. Şakir BOR. "Production and Characterization of High Porosity Ti-6Al-4V Foam by Space Holder Technique in Powder Metallurgy". In: *Turkish Journal of Engineering and Environmental Sciences* 31 (2007), pp. 149–156. ISSN: 1300-0160. DOI: 10.3906/tar-1205-20.

[168] R. Goodall. "10 - Porous metals: foams and sponges". In: *Advances in Powder Metallurgy*. Ed. by Isaac Chang and Yuyuan Zhao. Woodhead Publishing Series in Metals and Surface Engineering. Woodhead Publishing, 2013, pp. 273–307. ISBN: 978-0-85709-420-9. DOI: https://doi.org/10.1533/9780857098900.2.273. URL: http://www.sciencedirect.com/science/article/pii/B9780857094209500106.

[169] Yunhui Chen et al. "Manufacturing of biocompatible porous titanium scaffolds using a novel spherical sugar pellet space holder". In: *Materials Letters* 195 (2017), pp. 92–95. ISSN: 0167-577X. DOI: https://doi.org/10.1016/j.matlet.2017.02.092. URL: http://www.sciencedirect.com/science/article/pii/S0167577X17302677.

[170] Jiangang Jia, Abdur R. Siddiq, and Andrew R. Kennedy. "Porous titanium manufactured by a novel powder tapping method using spherical salt bead space holders: Characterisation and mechanical properties". In: *Journal of the Mechanical Behavior of Biomedical Materials* 48 (2015), pp. 229–240. ISSN: 1751-6161. DOI: https://doi.org/10.1016/j.jmbbm.2015.04.018. URL: http://www.sciencedirect.com/science/article/pii/S1751616115001381.

[171] K. M. Hurysz et al. "Steel and Titanium Hollow Sphere Foams". In: *MRS Proceedings* 521 (1998), p. 191. DOI: 10.1557/PROC-521-191.

[172] CA) Torobin Leonard B. (Santa Monica. *Hollow porous microspheres made from dispersed particle compositions*. Mar. 1995. URL: https://www.freepatentsonline.com/5397759.html.

[173] O. Andersen et al. "Novel Metallic Hollow Sphere Structures". In: *Advanced Engineering Materials* 2.4 (2000), pp. 192–195. DOI: 10.1002/(SICI)1527-2648(200004)2:4<192::AID-ADEM192>3.0.CO;2-\#.

[174] P. Yu et al. "Microwave-assisted fabrication of titanium hollow spheres with tailored shell structures for various potential applications". In: *Materials Letters* 86 (2012), pp. 84–87. ISSN: 0167-577X. DOI: https://doi.org/10.1016/j.matlet.2012.07.022. URL: http://www.sciencedirect.com/science/article/pii/S0167577X12009822.

[175] C. Y. Yap et al. "Review of selective laser melting: Materials and applications". In: *Applied Physics Reviews* 2.4 (2015), p. 041101. DOI: 10.1063/1.4935926. eprint: https://doi.org/10.1063/1.4935926. URL: https://doi.org/10.1063/1.4935926.

[176] I. Yadroitsev et al. "Strategy of manufacturing components with designed internal structure by selective laser melting of metallic powder". In: *Applied Surface Science* 254.4 (2007). Laser synthesis and processing of advanced materials, pp. 980–983. ISSN: 0169-4332. DOI: https://doi.org/10.1016/j.apsusc.2007.08.046. URL: http://www.sciencedirect.com/science/article/pii/S0169433207012354.

[177] I. Yadroitsev and I. Smurov. "Selective laser melting technology: From the single laser melted track stability to 3D parts of complex shape". In: *Physics Procedia* 5 (2010). Laser Assisted Net Shape Engineering 6, Proceedings of the LANE 2010, Part 2, pp. 551–560. ISSN: 1875-3892. DOI: https://doi.org/10.1016/j.phpro.2010.08.083. URL: http://www.sciencedirect.com/science/article/pii/S1875389210005092.

[178] H. Attar et al. "Manufacture by selective laser melting and mechanical behavior of commercially pure titanium". In: *Materials Science and Engineering: A* 593 (2014), pp. 170–177. ISSN: 0921-5093. DOI: https://doi.org/10.1016/j.msea.2013.11.038. URL: http://www.sciencedirect.com/science/article/pii/S0921509313012665.

[179] Nesma T. Aboulkhair et al. "Reducing porosity in AlSi10Mg parts processed by selective laser melting". In: *Additive Manufacturing* 1-4 (2014). Inaugural Issue, pp. 77–86. ISSN: 2214-8604. DOI: https://doi.org/10.1016/j.addma.2014.08.001. URL: http://www.sciencedirect.com/science/article/pii/S2214860414000062.

[180] Umberto Scipioni Bertoli et al. "On the limitations of Volumetric Energy Density as a design parameter for Selective Laser Melting". In: *Materials & Design* 113 (2017), pp. 331–340. ISSN: 0264-1275. DOI: https://doi.org/10.1016/j.matdes.2016.10.037. URL: http://www.sciencedirect.com/science/article/pii/S0264127516313363.

[181] Wayne E. King et al. "Observation of keyhole-mode laser melting in laser powder-bed fusion additive manufacturing". In: *Journal of Materials Processing Technology* 214.12 (2014), pp. 2915–2925. ISSN: 0924-0136. DOI: https://doi.org/10.1016/j.jmatprotec.2014.06.005. URL: http://www.sciencedirect.com/science/article/pii/S0924013614002283.

[182] Galina Kasperovich et al. "Correlation between porosity and processing parameters in TiAl6V4 produced by selective laser melting". In: *Materials & Design* 105 (2016), pp. 160–170. ISSN: 0264-1275. DOI: https://doi.org/10.1016/j.matdes.2016.05.070. URL: http://www.sciencedirect.com/science/article/pii/S0264127516306761.

[183] I. Yadroitsev and I. Smurov. "Surface Morphology in Selective Laser Melting of Metal Powders". In: *Physics Procedia* 12 (2011). Lasers in Manufacturing 2011 - Proceedings of the Sixth International WLT Conference on Lasers in Manufacturing, pp. 264–270. ISSN: 1875-3892. DOI: https://doi.org/10.1016/j.phpro.2011.03.034. URL: http://www.sciencedirect.com/science/article/pii/S1875389211001131.

[184] Mingming Ma et al. "Layer thickness dependence of performance in high-power selective laser melting of 1Cr18Ni9Ti stainless steel". In: *Journal of Materials Processing Technology* 215 (2015), pp. 142–150. ISSN: 0924-0136. DOI: https://doi.org/10.1016/j.jmatprotec.2014.07.034. URL: http://www.sciencedirect.com/science/article/pii/S0924013614002933.

[185] E. Sallica-Leva, A.L. Jardini, and J.B. Fogagnolo. "Microstructure and mechanical behavior of porous Ti–6Al–4V parts obtained by selective laser melting". In: *Journal of the Mechanical Behavior of Biomedical Materials* 26 (2013), pp. 98–108. ISSN: 1751-6161. DOI: https://doi.org/10.1016/j.jmbbm.2013.05.011. URL: http://www.sciencedirect.com/science/article/pii/S1751616113001768.

[186] Sheng Zhang et al. "Effects of scan line spacing on pore characteristics and mechanical properties of porous Ti6Al4V implants fabricated by selective laser melting". In: *Materials & Design* 63 (2014), pp. 185–193. ISSN: 0261-3069. DOI: https://doi.org/10.1016/j.matdes.2014.05.021. URL: http://www.sciencedirect.com/science/article/pii/S0261306914003902.

[187] Di Wang et al. "Study on the designing rules and processability of porous structure based on selective laser melting (SLM)". In: *Journal of Materials Processing Technology* 213.10 (2013), pp. 1734–1742. ISSN: 0924-0136. DOI: https://doi.org/10.1016/j.jmatprotec.2013.05.001. URL: http://www.sciencedirect.com/science/article/pii/S0924013613001490.

[188] Hermann Karcher et al. "Construction of triply periodic minimal surfaces". In: *Philosophical Transactions of the Royal Society of London. Series A: Mathematical, Physical and Engineering Sciences* 354.1715 (1996), pp. 2077–2104. DOI: 10.1098/rsta.1996.0093. eprint: https://royalsocietypublishing.org/doi/pdf/10.1098/rsta.1996.0093. URL: https://royalsocietypublishing.org/doi/abs/10.1098/rsta.1996.0093.

[189] Sebastian C. Kapfer et al. "Minimal surface scaffold designs for tissue engineering". In: *Biomaterials* 32.29 (2011), pp. 6875–6882. ISSN: 0142-9612. DOI: https://doi.org/10.1016/j.biomaterials.2011.06.012. URL: http://www.sciencedirect.com/science/article/pii/S0142961211006776.

[190] F.S.L. Bobbert et al. "Additively manufactured metallic porous biomaterials based on minimal surfaces: A unique combination of topological, mechanical, and mass transport properties". In: *Acta Biomaterialia* 53 (2017), pp. 572–584. ISSN: 1742-7061. DOI: https://doi.org/10.1016/j.actbio.2017.02.024. URL: http://www.sciencedirect.com/science/article/pii/S1742706117301290.

[191] Deepak K. Pattanayak et al. "Bioactive Ti metal analogous to human cancellous bone: Fabrication by selective laser melting and chemical treatments". In: *Acta Biomaterialia* 7.3 (2011), pp. 1398–1406. ISSN: 1742-7061. DOI: https://doi.org/10.1016/j.actbio.2010.09.034. URL: http://www.sciencedirect.com/science/article/pii/S1742706110004447.

[192] Yan Wang et al. "Development of highly porous titanium scaffolds by selective laser melting". In: *Materials Letters* 64.6 (2010), pp. 674–676. ISSN: 0167-577X. DOI: https://doi.org/10.1016/j.matlet.2009.12.035. URL: http://www.sciencedirect.com/science/article/pii/S0167577X09009689.

[193] G. Zhao et al. "Salt-metal feedstocks for the creation of stochastic cellular structures with controlled relative density by powder bed fabrication". In: *Materials & Design* 149 (2018), pp. 63–72. ISSN: 0264-1275. DOI: https://doi.org/10.1016/j.matdes.2018.03.071. URL: http://www.sciencedirect.com/science/article/pii/S0264127518302624.

[194] P. Patnaik. *Handbook of Inorganic Chemicals*. McGraw-Hill handbooks. McGraw-Hill, 2003. ISBN: 9780070494398. URL: https://books.google.co.uk/books?id=Xqj-TTzkvTEC.

[195] A. Bansiddhi and D.C. Dunand. "Shape-memory NiTi foams produced by replication of NaCl space-holders". In: *Acta Biomaterialia* 4.6 (2008), pp. 1996–2007. ISSN: 1742-7061. DOI: https://doi.org/10.1016/j.actbio.2008.06.005. URL: http://www.sciencedirect.com/science/article/pii/S1742706108001773.

[196] Garrett E. Ryan, Abhay S. Pandit, and Dimitrios P. Apatsidis. "Porous titanium scaffolds fabricated using a rapid prototyping and powder metallurgy technique". In: *Biomaterials* 29.27 (2008), pp. 3625–3635. ISSN: 0142-9612. DOI: https://doi.org/10.1016/j.biomaterials.2008.05.032. URL: http://www.sciencedirect.com/science/article/pii/S0142961208003748.

[197] M. A. Lopez-Heredia et al. "Bone growth in rapid prototyped porous titanium implants". In: *Journal of Biomedical Materials Research Part A* 85A.3 (2008), pp. 664–673. DOI: 10.1002/jbm.a.31468. eprint: https://onlinelibrary.wiley.com/doi/pdf/10.1002/jbm.a.31468. URL: https://onlinelibrary.wiley.com/doi/abs/10.1002/jbm.a.31468.

[198] Jia Ping Li et al. "Porous Ti6Al4V scaffold directly fabricating by rapid prototyping: Preparation and in vitro experiment". In: *Biomaterials* 27.8 (2006), pp. 1223–1235. ISSN: 0142-9612. DOI: https://doi.org/10.1016/j.biomaterials.2005.08.033. URL: http://www.sciencedirect.com/science/article/pii/S0142961205007970.

[199] P. Trueba et al. “Development and implementation of a sequential compaction device to obtain radial graded porosity cylinders”. In: *Journal of Manufacturing Processes* 50 (2020), pp. 142–153. ISSN: 1526-6125. DOI: https://doi.org/10.1016/j.jmapro.2019.12.011. URL: http://www.sciencedirect.com/science/article/pii/S1526612519304311.

[200] Wei-Shao Lin et al. “Additive manufacturing technology (direct metal laser sintering) as a novel approach to fabricate functionally graded titanium implants: preliminary investigation of fabrication parameters”. In: *The International journal of oral & maxillofacial implants* 28.6 (2013), pp. 1490–1495. ISSN: 0882-2786. DOI: 10.11607/jomi.3164. URL: https://doi.org/10.11607/jomi.3164.

[201] Y. Li et al. “Additively manufactured functionally graded biodegradable porous iron”. In: *Acta Biomaterialia* (2019). ISSN: 1742-7061. DOI: https://doi.org/10.1016/j.actbio.2019.07.013. URL: http://www.sciencedirect.com/science/article/pii/S1742706119304933.

[202] Y. Torres et al. “Conventional Powder Metallurgy Process and Characterization of Porous Titanium for Biomedical Applications”. In: *Metallurgical and Materials Transactions B* 42.4 (Aug. 2011), pp. 891–900. DOI: 10.1007/s11663-011-9521-6.

[203] Haijun Gong et al. “Defect Morphology of Ti-6Al-4V Parts Fabricated by Selective Laser Melting and Electron Beam Melting”. In: (Aug. 2013).

[204] Johannes Schindelin et al. “Fiji: an open-source platform for biological-image analysis”. In: *Nature Methods* 9.7 (July 2012), pp. 676–682. DOI: 10.1038/nmeth.2019. URL: https://hal-pasteur.archives-ouvertes.fr/pasteur-02616466.

[205] Matteo Benedetti et al. “Study of the Compression Behaviour of Ti6Al4V Trabecular Structures Produced by Additive Laser Manufacturing”. In: *Materials* 12.9 (2019). ISSN: 1996-1944. DOI: 10.3390/ma12091471. URL: https://www.mdpi.com/1996-1944/12/9/1471.

[206] Ross Cunningham et al. “Synchrotron-Based X-ray Microtomography Characterization of the Effect of Processing Variables on Porosity Formation in Laser Power-Bed Additive Manufacturing of Ti-6Al-4V”. In: *JOM* 69.3 (Mar. 2017), pp. 479–484. ISSN: 1543-1851. DOI: 10.1007/s11837-016-2234-1. URL: https://doi.org/10.1007/s11837-016-2234-1.

[207] John A Slotwinski, Edward J Garboczi, and Keith M Hebenstreit. “Porosity Measurements and Analysis for Metal Additive Manufacturing Process Control”. In: *Journal of research of the National Institute of Standards and Technology* 119 (2014), pp. 494–528. ISSN: 1044-677X. DOI: 10.6028/jres.119.019. URL: http://europepmc.org/articles/PMC4487290.

[208] Sheila Lascano et al. “Porous Titanium for Biomedical Applications: Evaluation of the Conventional Powder Metallurgy Frontier and Space-Holder Technique”. In: *Applied Sciences* 9.5 (Mar. 2019), p. 982. ISSN: 2076-3417. DOI: 10.3390/app9050982. URL: http://dx.doi.org/10.3390/app9050982.

[209] IJ Gibson and Michael Farries Ashby. “The mechanics of three-dimensional cellular materials”. In: *Proceedings of the royal society of London. A. Mathematical and physical sciences* 382.1782 (1982), pp. 43–59.

[210] L.J. Gibson and M.F. Ashby. *Cellular Solids: Structure and Properties*. Cambridge Solid State Science Series. Cambridge University Press, 1999. ISBN: 9780521499118. URL: https://books.google.co.uk/books?id=IySUr5sn4N8C.

[211] Seyed Mohammad Ahmadi et al. "Additively Manufactured Open-Cell Porous Biomaterials Made from Six Different Space-Filling Unit Cells: The Mechanical and Morphological Properties". In: *Materials* 8.4 (2015), pp. 1871–1896. ISSN: 1996-1944. DOI: 10.3390/ma8041871. URL: http://www.mdpi.com/1996-1944/8/4/1871.

[212] Han Wang et al. "Comparison of 3D-printed porous tantalum and titanium scaffolds on osteointegration and osteogenesis". In: *Materials Science and Engineering: C* 104 (2019), p. 109908. ISSN: 0928-4931. DOI: https://doi.org/10.1016/j.msec.2019.109908. URL: http://www.sciencedirect.com/science/article/pii/S0928493119306575.

[213] J.K. Chen et al. "Continuous compression behaviors of selective laser melting Ti-6Al-4V alloy with cuboctahedron cellular structures". In: *Materials Science and Engineering: C* 100 (2019), pp. 781–788. ISSN: 0928-4931. DOI: https://doi.org/10.1016/j.msec.2019.03.054. URL: http://www.sciencedirect.com/science/article/pii/S0928493118330182.

[214] W. Pabst and E. Gregorová. "Critical Assessment 18: elastic and thermal properties of porous materials – rigorous bounds and cross-property relations". In: *Materials Science and Technology* 31.15 (2015), pp. 1801–1808. DOI: 10.1080/02670836.2015.1114697. eprint: https://doi.org/10.1080/02670836.2015.1114697. URL: https://doi.org/10.1080/02670836.2015.1114697.

[215] Tereza Uhlířová and Willi Pabst. "Conductivity and Young's modulus of porous metamaterials based on Gibson-Ashby cells". In: *Scripta Materialia* 159 (2019), pp. 1–4. ISSN: 1359-6462. DOI: https://doi.org/10.1016/j.scriptamat.2018.09.005. URL: http://www.sciencedirect.com/science/article/pii/S1359646218305463.

[216] A.H. Burstein, D.T. Reilly, and M. Martens. "Ageing of bone tissue: mechanical properties". In: *The Journal of Bone and Joint Surgery* 58.1 (Jan. 1976), pp. 82–88. ISSN: 0021-9355. URL: https://journals.lww.com/jbjsjournal/Abstract/1976/58010/Aging_of_bone_tissue__mechanical_properties.15.aspx.

[217] Donald T. Reilly and Albert H. Burstein. "The elastic and ultimate properties of compact bone tissue". In: *Journal of Biomechanics* 8.6 (1975), pp. 393–405. ISSN: 0021-9290. DOI: https://doi.org/10.1016/0021-9290(75)90075-5. URL: http://www.sciencedirect.com/science/article/pii/0021929075900755.

[218] Yan Li et al. "Gelcasting of metal powders in nontoxic cellulose ethers system". In: *Journal of Materials Processing Technology* 208.1 (2008), pp. 457–462. ISSN: 0924-0136. DOI: https://doi.org/10.1016/j.jmatprotec.2008.01.009. URL: http://www.sciencedirect.com/science/article/pii/S0924013608000666.

[219] Andrew Kennedy. "Porous Metals and Metal Foams Made from Powders". In: *Powder Metallurgy*. Ed. by Katsuyoshi Kondoh. Rijeka: IntechOpen, 2012. DOI: 10.5772/33060. URL: https://doi.org/10.5772/33060.

[220] A R Kennedy and X Lin. "Preparation and characterisation of metal powder slurries for use as precursors for metal foams made by gel casting". In: *Powder Metallurgy* 54.3 (2011), pp. 376–381. DOI: 10.1179/003258910X12707304454906. eprint: https://doi.org/10.1179/003258910X12707304454906.

[221] Mark A. Janney et al. "Development of Low-Toxicity Gelcasting Systems". In: *Journal of the American Ceramic Society* 81.3 (), pp. 581–591. DOI: 10.1111/j.1151-2916.1998.tb02377.x. eprint: https://onlinelibrary.wiley.com/doi/pdf/10.1111/j.1151-2916.1998.tb02377.x. URL: https://onlinelibrary.wiley.com/doi/abs/10.1111/j.1151-2916.1998.tb02377.x.

[222] Mehrdad Kokabi, Ali Akbar Babaluo, and Abolfazl Barati. "Gelation process in low-toxic gelcasting systems". In: *Journal of the European Ceramic Society* 26.15 (2006), pp. 3083–3090. ISSN: 0955-2219. DOI: https://doi.org/10.1016/j.jeurceramsoc.2005.08.020. URL: http://www.sciencedirect.com/science/article/pii/S0955221905008204.

[223] Jinlong Yang, Juanli Yu, and Yong Huang. "Recent developments in gelcasting of ceramics". In: *Journal of the European Ceramic Society* 31.14 (2011). Special Issue ICCPS 11: 11th International Conference of Ceramic Processing Science, pp. 2569–2591. ISSN: 0955-2219. DOI: https://doi.org/10.1016/j.jeurceramsoc.2010.12.035. URL: http://www.sciencedirect.com/science/article/pii/S0955221911000057.

[224] Marek Potoczek. "Gelcasting of alumina foams using agarose solutions". In: *Ceramics International* 34.3 (2008), pp. 661–667. ISSN: 0272-8842. DOI: https://doi.org/10.1016/j.ceramint.2007.02.001. URL: http://www.sciencedirect.com/science/article/pii/S0272884207000338.

[225] Ali Alem, Martin D Pugh, and Robin AL Drew. "Open-cell reaction bonded silicon nitride foams: fabrication and characterization". In: *Journal of the European Ceramic Society* 34.3 (2014), pp. 599–609.

[226] Lunlun Gong et al. "Porous mullite ceramics with low thermal conductivity prepared by foaming and starch consolidation". In: *Journal of Porous Materials* 21.1 (Feb. 2014), pp. 15–21. ISSN: 1573-4854. DOI: 10.1007/s10934-013-9741-z. URL: https://doi.org/10.1007/s10934-013-9741-z.

[227] K. Prabhakaran et al. "Effect of polymer concentration on porosity and pore size characteristics of alumina membrane substrates prepared by gelcasting". In: *Ceramics International* 35.5 (2009), pp. 2083–2085. ISSN: 0272-8842. DOI: https://doi.org/10.1016/j.ceramint.2008.10.001. URL: http://www.sciencedirect.com/science/article/pii/S0272884208003210.

[228] Juanli Yu et al. "Gelcasting preparation of porous silicon nitride ceramics by adjusting the content of monomers". In: *Journal of Sol-Gel Science and Technology* 53.3 (Mar. 2010), pp. 515–523. ISSN: 1573-4846. DOI: 10.1007/s10971-009-2125-9. URL: https://doi.org/10.1007/s10971-009-2125-9.

[229] Lina Wu et al. "Controlled fabrication of porous Al2O3 ceramic by N,N-dimethylformamide-based gel-casting". In: *Scripta Materialia* 62.8 (2010), pp. 602–605. ISSN: 1359-6462. DOI: https://doi.org/10.1016/j.scriptamat.2010.01.007.

[230] Hyunjung Kim et al. "Control of pore size in ceramic foams: Influence of surfactant concentration". In: *Materials Chemistry and Physics* 113.1 (2009), pp. 441–444. ISSN: 0254-0584. DOI: https://doi.org/10.1016/j.matchemphys.2008.07.099. URL: http://www.sciencedirect.com/science/article/pii/S0254058408005737.

[231] Xiaojian Mao, Shiwei Wang, and Shunzo Shimai. "Porous ceramics with tri-modal pores prepared by foaming and starch consolidation". In: *Ceramics International* 34.1 (2008), pp. 107–112. ISSN: 0272-8842. DOI: https://doi.org/10.1016/j.ceramint.2006.08.009. URL: http://www.sciencedirect.com/science/article/pii/S0272884206002665.

[232] Jean-Marc Tulliani et al. "Preparation and mechanical characterization of dense and porous zirconia produced by gel casting with gelatin as a gelling agent". In: *Ceramics International* 35.6 (2009), pp. 2481–2491. ISSN: 0272-8842. DOI: https://doi.org/10.1016/j.ceramint.2009.02.017. URL: http://www.sciencedirect.com/science/article/pii/S027288420900087X.

[233] Santanu Dhara and Parag Bhargava. "Influence of nature and amount of dispersant on rheology of aged aqueous alumina gelcasting slurries". In: *Journal of the American Ceramic Society* 88.3 (2005), pp. 547–552.

[234] LA Cyster et al. "The influence of dispersant concentration on the pore morphology of hydroxyapatite ceramics for bone tissue engineering". In: *Biomaterials* 26.7 (2005), pp. 697–702.

[235] Julian R Jones and Larry L Hench. "Regeneration of trabecular bone using porous ceramics". In: *Current Opinion in Solid State and Materials Science* 7.4 (2003), pp. 301–307. ISSN: 1359-0286. DOI: https://doi.org/10.1016/j.cossms.2003.09.012. URL: http://www.sciencedirect.com/science/article/pii/S1359028603000767.

[236] Dulal Chandra Jana, Govindan Sundararajan, and Kamanio Chattopadhyay. "Effect of porosity on structure, Young's modulus, and thermal conductivity of SiC foams by direct foaming and gelcasting". In: *Journal of the American Ceramic Society* 100.1 (2017), pp. 312–322.

[237] Xiangong Deng et al. "Preparation and characterization of porous mullite ceramics via foam-gelcasting". In: *Ceramics International* 41.7 (2015), pp. 9009–9017. ISSN: 0272-8842. DOI: https://doi.org/10.1016/j.ceramint.2015.03.237. URL: http://www.sciencedirect.com/science/article/pii/S0272884215006537.

[238] L Sharifi et al. "High porous alumina bodies: production and properties via gel-casting technique". In: *International Journal of Advanced Science and Technology* 65 (2014), pp. 59–70.

[239] S Dhara et al. "Shape forming of ceramics via gelcasting of aqueous particulate slurries". In: *Bulletin of Materials Science* 25.6 (2002), pp. 565–568.

[240] P Sepulveda et al. "Production of porous hydroxyapatite by the gel-casting of foams and cytotoxic evaluation". In: *Journal of Biomedical Materials Research: An Official Journal of The Society for Biomaterials and The Japanese Society for Biomaterials* 50.1 (2000), pp. 27–34.

[241] Rafael Barea et al. "Fabrication of Highly Porous Mullite Materials". In: *Journal of the American Ceramic Society* 88.3 (), pp. 777–779. DOI: 10.1111/j.1551-2916.2005.00092.x. eprint: https://onlinelibrary.wiley.com/doi/pdf/10.1111/j.1551-2916.2005.00092.x. URL: https://onlinelibrary.wiley.com/doi/abs/10.1111/j.1551-2916.2005.00092.x.

[242] Kendra A. Erk, David C. Dunand, and Kenneth R. Shull. "Titanium with controllable pore fractions by thermoreversible gelcasting of TiH2". In: *Acta Materialia* 56.18 (2008), pp. 5147–5157. ISSN: 1359-6454. DOI: https://doi.org/10.1016/j.actamat.2008.06.035. URL: http://www.sciencedirect.com/science/article/pii/S1359645408004643.

[243] Xi Lin and Andrew R. Kennedy. "Structure–Property–Processing Relationships for Stainless Steel Foams Made by Mechanical Aeration of Powder Slurries". In: *Advanced Engineering Materials* 17.6 (), pp. 839–845. DOI: 10.1002/adem.201400214. eprint: https://onlinelibrary.wiley.com/doi/pdf/10.1002/adem.201400214. URL: https://onlinelibrary.wiley.com/doi/abs/10.1002/adem.201400214.

[244] Marek Potoczek et al. "Manufacturing of highly porous calcium phosphate bioceramics via gel-casting using agarose". In: *Ceramics International* 35.6 (2009), pp. 2249–2254. ISSN: 0272-8842. DOI: https://doi.org/10.1016/j.ceramint.2008.12.006. URL: http://www.sciencedirect.com/science/article/pii/S0272884209000297.

[245] Hassna Rehman Ramay and Miqin Zhang. "Preparation of porous hydroxyapatite scaffolds by combination of the gel-casting and polymer sponge methods". In: *Biomaterials* 24.19 (2003), pp. 3293–3302. ISSN: 0142-9612. DOI: https://doi.org/10.1016/S0142-9612(03)00171-6. URL: http://www.sciencedirect.com/science/article/pii/S0142961203001716.

[246] Noriyuki Tamai et al. "Novel hydroxyapatite ceramics with an interconnective porous structure exhibit superior osteoconduction in vivo". In: *Journal of Biomedical Materials Research* 59.1 (), pp. 110–117. DOI: 10.1002/jbm.1222. eprint: https://onlinelibrary.wiley.com/doi/pdf/10.1002/jbm.1222. URL: https://onlinelibrary.wiley.com/doi/abs/10.1002/jbm.1222.

[247] Donghua Yang et al. "Mechanical Properties of Porous Ti-Mo and Ti-Nb Alloys for Biomedical Application by Gelcasting". In: *Procedia Engineering* 36 (2012). IUMRS International Conference in Asia 2011, pp. 160–167. ISSN: 1877-7058. DOI: https://doi.org/10.1016/j.proeng.2012.03.025. URL: http://www.sciencedirect.com/science/article/pii/S1877705812015524.

[248] Yan LI et al. "Porosity and mechanical properties of porous titanium fabricated by gelcasting". In: *Rare Metals* 27.3 (2008), pp. 282–286. ISSN: 1001-0521. DOI: https://doi.org/10.1016/S1001-0521(08)60130-8. URL: http://www.sciencedirect.com/science/article/pii/S1001052108601308.

[249] Andre R Studart et al. "Processing routes to macroporous ceramics: a review". In: *Journal of the American Ceramic Society* 89.6 (2006), pp. 1771–1789.

[250] Joseph T. Muth et al. "Architected cellular ceramics with tailored stiffness via direct foam writing". In: *Proceedings of the National Academy of Sciences* 114.8 (2017), pp. 1832–1837. ISSN: 0027-8424. DOI: 10.1073/pnas.1616769114. eprint: https://www.pnas.org/content/114/8/1832.full.pdf. URL: https://www.pnas.org/content/114/8/1832.

[251] Geoffrey Mulberry et al. "3D printing and milling a real-time PCR device for infectious disease diagnostics". In: *PloS one* 12.6 (2017), e0179133. ISSN: 1932-6203. DOI: 10.1371/journal.pone.0179133. URL: http://europepmc.org/articles/PMC5460903.

[252] Catalin Gheorghe Amza, Aurelian Zapciu, and Diana Popescu. "Paste extruder—hardware add-on for desktop 3D printers". In: *Technologies* 5.3 (2017), p. 50.

[253] ZMorph Support Team. *Guidelines for Printing with Thick Paste Extruder — ZMorph, ZMorph Knowledge Base*. [Online; accessed 8-October-2018]. 2018. URL: https://support.zmorph3d.com/hc/en-us/articles/115002218985-Guidelines-for-Printing-with-Thick-Paste-Extruder.

[254] N. Phatharapeetranun et al. "3D-printed barium titanate/poly-(vinylidene fluoride) nanohybrids with anisotropic dielectric properties". In: *J. Mater. Chem. C* 5 (47 2017), pp. 12430–12440. DOI: 10.1039/C7TC03697C. URL: http://dx.doi.org/10.1039/C7TC03697C.

[255] Daniel I Onwude et al. "Modeling the thin-layer drying of fruits and vegetables: A review". In: *Comprehensive reviews in food science and food safety* 15.3 (2016), pp. 599–618.

[256] W. K. Lewis. "The Rate of Drying of Solid Materials." In: *Journal of Industrial & Engineering Chemistry* 13.5 (1921), pp. 427–432. DOI: 10.1021/ie50137a021. eprint: https://doi.org/10.1021/ie50137a021. URL: https://doi.org/10.1021/ie50137a021.

[257] Chandan Kumar et al. “Modeling heat and mass transfer process during convection drying of fruit”. In: *Proceedings of the 4th International Conference on Computational Methods*. Queensland University of Technology. 2012, pp. 1–8.

[258] E Meisami-Asl et al. “Determination of suitable thin layer drying curve model for apple slices (variety-Golab)”. In: *Plant Omics* 3.3 (2010), pp. 103–108.

[259] H Pandey et al. *Experiments in food process engineering*. 2010.

[260] Uwem Ekwere Inyang, Innocent Oseribho Oboh, and Benjamin Reuben Etuk. “Kinetic models for drying techniques—food materials”. In: *Advances in Chemical Engineering and Science* 8 (2018), pp. 27–48.

[261] Thrupathihalli Pandurangapp Krishna Murthy and Balaraman Manohar. “Microwave drying of mango ginger (Curcuma amada Roxb): prediction of drying kinetics by mathematical modelling and artificial neural network”. In: *International Journal of Food Science & Technology* 47.6 (2012), pp. 1229–1236.

[262] Zafer Erbay and Filiz Icier. “A review of thin layer drying of foods: theory, modeling, and experimental results”. In: *Critical reviews in food science and nutrition* 50.5 (2010), pp. 441–464.

[263] Jie Chen et al. “Mathematical modeling of hot air drying kinetics of Momordica charantia slices and its color change”. In: *Advance Journal of Food Science and Technology* 5.9 (2013), pp. 1214–1219.

[264] H Darvishi and E Hazbavi. “Mathematical modeling of thin-layer drying behavior of date palm”. In: *Global Journal of Science Frontier Research Mathematics and Decision Sciences* 12.10 (2012), pp. 247–255.

[265] Osman Yaldyz and Can Ertekyn. “Thin layer solar drying of some vegetables”. In: *Drying Technology* 19.3-4 (2001), pp. 583–597.

[266] İbrahim Doymaz. “Drying behaviour of green beans”. In: *Journal of food Engineering* 69.2 (2005), pp. 161–165.

[267] S Simal et al. “Use of exponential, Page’s and diffusional models to simulate the drying kinetics of kiwi fruit”. In: *Journal of food engineering* 66.3 (2005), pp. 323–328.

[268] A Mohammadi et al. “Estimation of Thin-layer Drying Characteristics of Kiwifruit (cv. Hayward) with use of Page’s Model”. In: *American-Eurasian J. Agric. Environ. Sci* 3 (2008), pp. 802–805.

[269] EOM Akoy. “Experimental characterization and modeling of thin-layer drying of mango slices”. In: *International Food Research Journal* 21.5 (2014), p. 1911.

[270] Mwithiga Gikuru and Hany S El-Mesery. “The drying of onion slices in two types of hot-air convective dryers”. In: (2012).

[271] Raquel PF Guine, Susana Pinho, and Maria Joao Barroca. “Study of the convective drying of pumpkin (Cucurbita maxima)”. In: *Food and bioproducts processing* 89.4 (2011), pp. 422–428.

[272] CL Hii and JEREMIAH F Ogugo. “Effect of pre-treatment on the drying kinetics and product quality of star fruit slices”. In: *Journal of Engineering Science and Technology* 9.1 (2014), pp. 123–135.

[273] A El-Beltagy, GR Gamea, and AH Amer Essa. “Solar drying characteristics of strawberry”. In: *Journal of food engineering* 78.2 (2007), pp. 456–464.

[274] Mohammed Ayub Hossain, James Lyn Woods, and Bilash Kanti Bala. "Single-layer drying characteristics and colour kinetics of red chilli". In: *International journal of food science & technology* 42.11 (2007), pp. 1367–1375.

[275] TL Thompson, RM Peart, and GH Foster. "Matllematical simulation of corn drying a new model". In: *Transaction of the ASAE* 11.4 (1968), pp. 582–586.

[276] G. Y. Wang and R Paul Singh. "SINGLE LAYER DRYING EQUATION FOR ROUGH RICE." In: 1978.

[277] A Marabi et al. "Kinetics of solids leaching during rehydration of particulate dry vegetables". In: *Journal of Food Science* 69.3 (2004), pp. 91–96.

[278] Shaik Kaleemullah. "Studies on engineering properties and drying kinetics of chillies". PhD thesis. Tamil Nadu Agricultural University; Coimbatore, 2002.

[279] Wijitha Senadeera et al. "Influence of shapes of selected vegetable materials on drying kinetics during fluidized bed drying". In: *Journal of food engineering* 58.3 (2003), pp. 277–283.

[280] Wilton Pereira Da Silva et al. "Mathematical models to describe thin-layer drying and to determine drying rate of whole bananas". In: *Journal of the Saudi Society of Agricultural Sciences* 13.1 (2014), pp. 67–74.

[281] DG Praveen Kumar, H Umesh Hebbar, and MN Ramesh. "Suitability of thin layer models for infrared–hot air-drying of onion slices". In: *LWT-Food Science and Technology* 39.6 (2006), pp. 700–705.

[282] Sam Davies. *Ultimaker teams with BASF to offer metal expansion kit for S5 3D printer*. June 2022. URL: https://www.tctmagazine.com/additive-manufacturing-3d-printing-news/metal-additive-manufacturing-news/ultimaker-basf-metal-expansion-kit-s5-3d-printer/.

[283] P Sepulveda and JGP Binner. "Processing of cellular ceramics by foaming and in situ polymerisation of organic monomers". In: *Journal of the European Ceramic Society* 19.12 (1999), pp. 2059–2066.

[284] Vesna Middelkoop et al. "3D printed versus spherical adsorbents for gas sweetening". In: *Chemical Engineering Journal* 357 (2019), pp. 309–319. ISSN: 1385-8947. DOI: https://doi.org/10.1016/j.cej.2018.09.130. URL: https://www.sciencedirect.com/science/article/pii/S1385894718318497.

[285] ZMorph Support Team. *Introduction to Voxelizer 2*. [Online; accessed 27-July-2020]. 2019. URL: https://support.zmorph3d.com/hc/en-us/articles/.

[286] G D Scott and D M Kilgour. "The density of random close packing of spheres". In: *Journal of Physics D: Applied Physics* 2.6 (June 1969), p. 863. DOI: 10.1088/0022-3727/2/6/311. URL: https://dx.doi.org/10.1088/0022-3727/2/6/311.

[287] G. Marrucci. "A theory of coalescence". In: *Chemical Engineering Science* 24.6 (1969), pp. 975–985. ISSN: 0009-2509. DOI: https://doi.org/10.1016/0009-2509(69)87006-5. URL: https://www.sciencedirect.com/science/article/pii/0009250969870065.

[288] Rui Xie et al. "Gelcasting of alumina ceramics with improved green strength". In: *Ceramics International* 38.8 (2012), pp. 6923–6926.

[289] R Gilissen et al. "Gelcasting, a near net shape technique". In: *Materials & Design* 21.4 (2000), pp. 251–257.

[290] Xiaoyong Tian et al. “Interface and performance of 3D printed continuous carbon fiber reinforced PLA composites”. In: *Composites Part A: Applied Science and Manufacturing* 88 (2016), pp. 198–205.

[291] S Valvez et al. “3D printed continuous carbon fiber reinforced PLA composites: A short review”. In: *Procedia Structural Integrity* 25 (2020), pp. 394–399.

[292] Marisa Alviar-Agnew and Henry Agnew. *12.4: Evaporation and condensation*. July 2022. URL: https://batch.libretexts.org/print/url=https://chem.libretexts.org/Courses/Woodland_Community_College/WCC%3A_Chem_10_-_Concepts_of_Chemistry/Chapters/12%3A_Liquids_Solids_and_Intermolecular_Forces/12.4%3A_Evaporation_and_Condensation.pdf.

[293] J. Crisp and J. Lyn Woods. “The Drying Properties of Rapeseed”. In: *Journal of Agricultural Engineering Research* 57 (1994), pp. 89–97.

[294] P.C. Panchariya, D. Popovic, and A.L. Sharma. “Thin-layer modelling of black tea drying process”. In: *Journal of Food Engineering* 52.4 (2002), pp. 349–357. ISSN: 0260-8774. DOI: https://doi.org/10.1016/S0260-8774(01)00126-1. URL: https://www.sciencedirect.com/science/article/pii/S0260877401001261.

[295] Gökçe Dadali, Elçin Demirhan, and Belma Özbek. “Microwave Heat Treatment of Spinach: Drying Kinetics and Effective Moisture Diffusivity”. In: *Drying Technology* 25.10 (2007), pp. 1703–1712. DOI: 10.1080/07373930701590954. eprint: https://doi.org/10.1080/07373930701590954. URL: https://doi.org/10.1080/07373930701590954.

[296] Fateh Singh, VK Katiyar, and BP Singh. “Mathematical modeling to study drying characteristic of apple and potato”. In: *International Conference on Chemical, Environment & Biological Sciences (CEBS-2014), Kuala Lumpur (Malaysia)*. 2014.

[297] Gökçe Dadali and Belma Özbek. “Microwave heat treatment of leek: drying kinetic and effective moisture diffusivity”. In: *International journal of food science & technology* 43.8 (2008), pp. 1443–1451.

[298] Jan Hendrik DEBOER. *The dynamical character of adsorption*. Vol. 76. 2. LWW, 1953.

Appendices

A Methylcellulose Data Sheet

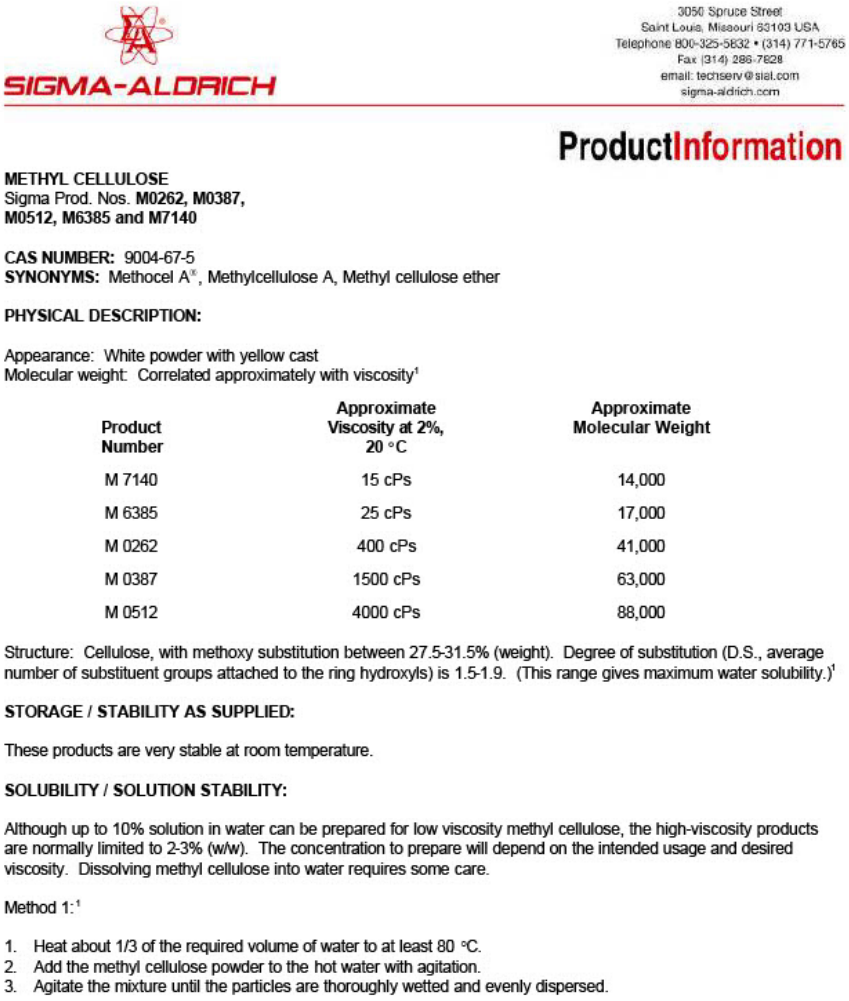

SIGMA-ALDRICH

3050 Spruce Street
Saint Louis, Missouri 63103 USA
Telephone 800-325-5832 • (314) 771-5765
Fax (314) 286-7828
email: techserv@sial.com
sigma-aldrich.com

ProductInformation

METHYL CELLULOSE
Sigma Prod. Nos. **M0262, M0387, M0512, M6385 and M7140**

CAS NUMBER: 9004-67-5
SYNONYMS: Methocel A®, Methylcellulose A, Methyl cellulose ether

PHYSICAL DESCRIPTION:

Appearance: White powder with yellow cast
Molecular weight: Correlated approximately with viscosity[1]

Product Number	Approximate Viscosity at 2%, 20 °C	Approximate Molecular Weight
M 7140	15 cPs	14,000
M 6385	25 cPs	17,000
M 0262	400 cPs	41,000
M 0387	1500 cPs	63,000
M 0512	4000 cPs	88,000

Structure: Cellulose, with methoxy substitution between 27.5-31.5% (weight). Degree of substitution (D.S., average number of substituent groups attached to the ring hydroxyls) is 1.5-1.9. (This range gives maximum water solubility.)[1]

STORAGE / STABILITY AS SUPPLIED:

These products are very stable at room temperature.

SOLUBILITY / SOLUTION STABILITY:

Although up to 10% solution in water can be prepared for low viscosity methyl cellulose, the high-viscosity products are normally limited to 2-3% (w/w). The concentration to prepare will depend on the intended usage and desired viscosity. Dissolving methyl cellulose into water requires some care.

Method 1:[1]

1. Heat about 1/3 of the required volume of water to at least 80 °C.
2. Add the methyl cellulose powder to the hot water with agitation.
3. Agitate the mixture until the particles are thoroughly wetted and evenly dispersed.

Figure 144: Technical data sheet for Methylcellulose M0262 (page 1).

METHYL CELLULOSE
Prod. Nos. **M0262, M0387,**
M0512, M6385 and M7140

SOLUBILITY / SOLUTION STABILITY: (continued)

Method 1:[1] (continued)

4. For complete solubilization, the remainder of the water is then added as cold water or ice to lower the temperature of the dispersion. Once the dispersion reaches the temperature at which that particular methyl cellulose product becomes water soluble, the powder begins to hydrate and the viscosity increases. Solution should be cooled to 0-5 °C for 20-40 min.
5. Continue agitation for at least 30 min. after the proper temperature is reached.

Method 2:[4]

Add 10 g methylcellulose to 1 liter of distilled water, and using a heating magnetic stirrer, slowly "bring to a boil for 5-10 minutes until small amorphous aggregates" of methylcellulose are formed. Immediately sterilize the solution for 16 minutes at 121 °C and 15 psi steam pressure. Allow solution to stand overnight at room temperature for complete dispersion. The solution will be cloudy, but uniform. The solution stored at room temperature can be used for one year.

Note: If a lumpy solution forms because of the methyl cellulose was not dispersed properly in cold water, then a high shear force is necessary to break the lumps, using a tissue homogenizer or blender.

A 0.5-1% solution of these products in water can be autoclaved under the usual conditions. However, higher concentrations may lead to chunks of methyl cellulose coming out of solution, so autoclaving these higher concentrations is not recommended. Heating a solution to the gel point results in thermogelation (see below). Upon cooling, the material rehydrates to the initial viscosity. If higher concentrations are autoclaved to thermogelation, then the rehydration may not take place sufficiently and big chunks will form. An alternative method to obtain a sterile solution of higher concentration would be to sterilize the water first, then add the material to the solvent.

GENERAL REMARKS:

Methylcelluloses have a wide range of uses in general industrial settings, depending on viscosity (related to molecular weight). They can be used for adhesives or thickening agents, viscosity control agents, or protection in paint formulations. Pharmaceutical grades have been used as thickeners, binders, emulsifiers, and stabilizers in a variety of cosmetic and food products. Biochemical applications are similar, as noted below.

Figure 145: Technical data sheet for Methylcellulose M0262 (page 2).

METHYL CELLULOSE
Prod. Nos. **M0262, M0387, M0512, M6385 and M7140**

GENERAL REMARKS: (continued)

Methylcelluose solutions when heated will reversibly form gels- at a temperature characteristic of the type and percentage. For these products, a 2% solution (w/w) has a gelation temperature of approximately 48 °C. The gelatin temperature drops linearly with increasing concentrations to about 30 °C for a 10% solution. Agitation affects the strength and apparent temperature of gelation; continued rapid agitation during gelation may break down gel structure. Additives (such as ordinary buffer salts or ethanol) can affect the gelation temperature, in either positive or negative direction. For maximum development of gel strength under quiescent conditions, the solution should be above the gelation temperature for about three hours.[1]

M 7140 (or cell culture tested M7027) is used at approximately 50 g/L in media to enhance viscosity characteristics.[2] Stewart et al. used methylcellulose (low viscosity, 0.2% solution) to restore the ability of human umbilical cord vein cells to adhere to fibronectin after they were removed from substrata. Methylcellulose also prevented human skin fibroblasts, human melanoma cells and mouse lung fibroblasts from losing adhesive properties. The authors concluded that the product can be a useful reagent for the preservation of cell function in suspension. They described methylcellulose as being non-toxic, enzyme-resistant, and not cell-permeable.[3]

M 0512 is recommended over glycerol for use in a cryopreservation medium; a higher percentage of viability was noted for each organism tested in a 1% methylcellulose solution compared to a 15% glycerol solution. The Sensitivity and resistance of the preserved organisms to various antibiotics did not change.[4] Methylcellulose of 4000 cps (M0512) was used in a semi-solid culture medium; plating cells in 1.2% methylcellulose with 10% fetal calf serum were plated over a layer of 0.9% agar.[5,6] Similar applications involved plating cells in an 0.8% solution.[7,8] Human neuroblastoma cells were cloned and cultured successfully in a 1% methylcellulose medium.[9] A standard protocol for plating in Methocel (M0512) using 1.6% final concentration in medium has been published.[10]

The graph that follows gives the correlation between concentration and viscosity for methyl cellulose of different molecular weights.

REFERENCES:

1. Supplier information.
2. Sigma Cell Culture Technical Service.
3. Stewart, G.J. et al., *Biotechniques*, 19, 598 (1995).
4. Reamer, R. et al, *Journal of AOAC International*, 78, 997-1001 (1995).
5. Freedman, V.H. and Shin, S., *Cell*, 3, 355-359 (1974).

Figure 146: Technical data sheet for Methylcellulose M0262 (page 3).

REFERENCES: (continued)

6. Risser, R. and Pollack, R., *Virology*, 59, 477-480 (1974).
7. Muller-Sieburg, C.E. et al., *J. Exp. Medicine*, 167, 1825-1840 (1988).
8. Rennick, D., Yang, G., Muller-Sieburg, C. et al., *Proc. Natl. Acad. Sci.* USA, 84, 6889-6983 (1987).
9. Ito, T. et al., *Cancer Research*, 47, 4146-4149 (1987).
10. *Gene Transfer and Expression: A Laboratory Manual*, M. Kriegler (Stockton Press, NY, 1990), pp 94-95.

Sigma warrants that its products conform to the information contained in this and other Sigma-Aldrich publications. Purchaser must determine the suitability of the product(s) for their particular use. Additional terms and conditions may apply. Please see reverse side of the invoice or packing slip.

Figure 147: Technical data sheet for Methylcellulose M0262 (page 4).

METHYL CELLULOSE
Sigma Prod. Nos. **M0262, M0387, M0512, M6385 and M7140**

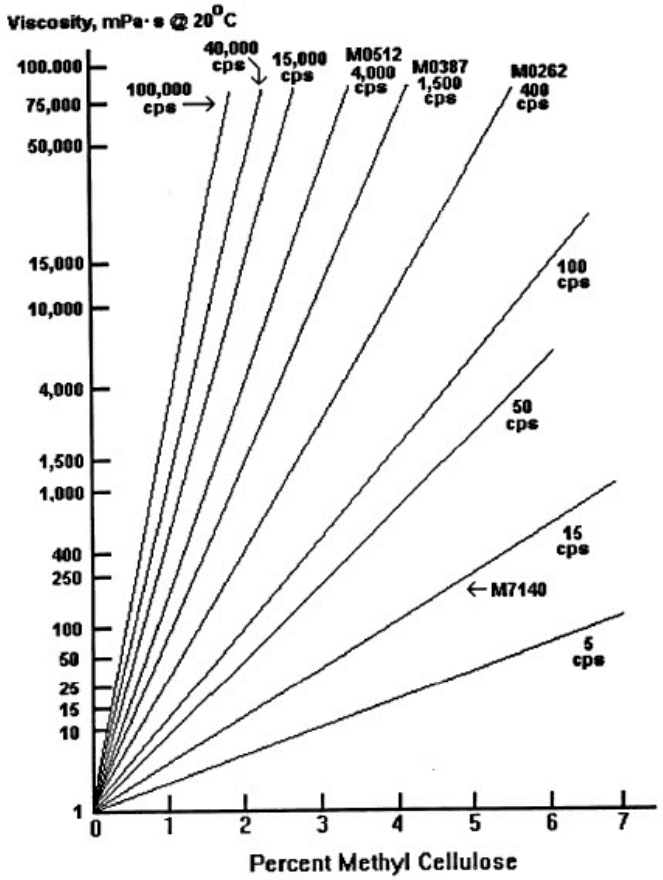

Figure 148: Technical data sheet for Methylcellulose M0262 (page 5).

B Darvan 7-N Dispersant Data Sheet

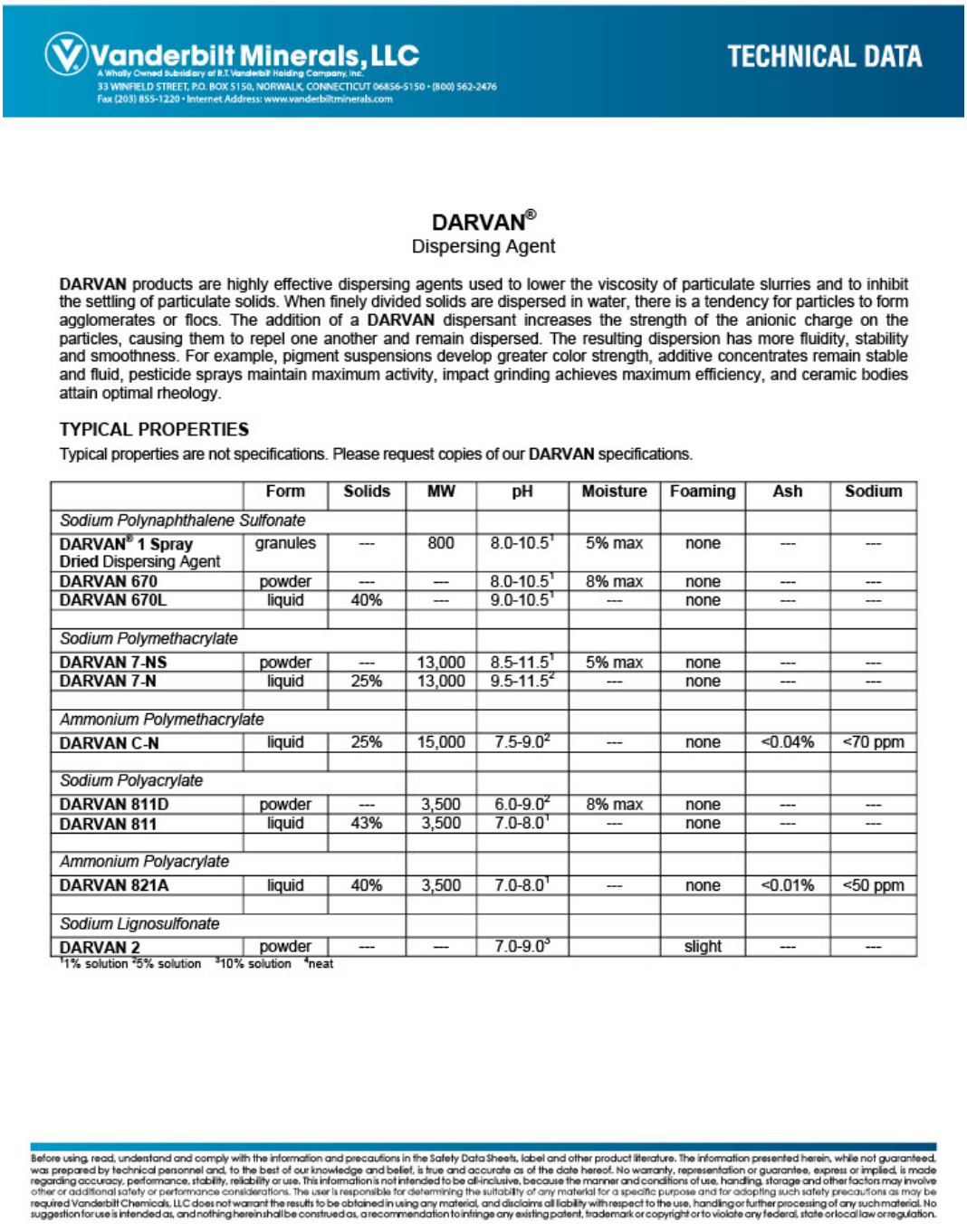

Vanderbilt Minerals, LLC
A Wholly Owned Subsidiary of R.T. Vanderbilt Holding Company, Inc.
33 WINFIELD STREET, P.O. BOX 5150, NORWALK, CONNECTICUT 06856-5150 • (800) 562-2476
Fax (203) 855-1220 • Internet Address: www.vanderbiltminerals.com

TECHNICAL DATA

DARVAN®
Dispersing Agent

DARVAN products are highly effective dispersing agents used to lower the viscosity of particulate slurries and to inhibit the settling of particulate solids. When finely divided solids are dispersed in water, there is a tendency for particles to form agglomerates or flocs. The addition of a **DARVAN** dispersant increases the strength of the anionic charge on the particles, causing them to repel one another and remain dispersed. The resulting dispersion has more fluidity, stability and smoothness. For example, pigment suspensions develop greater color strength, additive concentrates remain stable and fluid, pesticide sprays maintain maximum activity, impact grinding achieves maximum efficiency, and ceramic bodies attain optimal rheology.

TYPICAL PROPERTIES

Typical properties are not specifications. Please request copies of our **DARVAN** specifications.

	Form	Solids	MW	pH	Moisture	Foaming	Ash	Sodium
Sodium Polynaphthalene Sulfonate								
DARVAN® 1 Spray Dried Dispersing Agent	granules	---	800	8.0-10.5[1]	5% max	none	---	---
DARVAN 670	powder	---	---	8.0-10.5[1]	8% max	none	---	---
DARVAN 670L	liquid	40%	---	9.0-10.5[1]	---	none	---	---
Sodium Polymethacrylate								
DARVAN 7-NS	powder	---	13,000	8.5-11.5[1]	5% max	none	---	---
DARVAN 7-N	liquid	25%	13,000	9.5-11.5[2]	---	none	---	---
Ammonium Polymethacrylate								
DARVAN C-N	liquid	25%	15,000	7.5-9.0[2]	---	none	<0.04%	<70 ppm
Sodium Polyacrylate								
DARVAN 811D	powder	---	3,500	6.0-9.0[2]	8% max	none	---	---
DARVAN 811	liquid	43%	3,500	7.0-8.0[1]	---	none	---	---
Ammonium Polyacrylate								
DARVAN 821A	liquid	40%	3,500	7.0-8.0[1]	---	none	<0.01%	<50 ppm
Sodium Lignosulfonate								
DARVAN 2	powder	---	---	7.0-9.0[3]		slight	---	---

[1]1% solution [2]5% solution [3]10% solution [4]neat

Before using, read, understand and comply with the information and precautions in the Safety Data Sheets, label and other product literature. The information presented herein, while not guaranteed, was prepared by technical personnel and, to the best of our knowledge and belief, is true and accurate as of the date hereof. No warranty, representation or guarantee, express or implied, is made regarding accuracy, performance, stability, reliability or use. This information is not intended to be all-inclusive, because the manner and conditions of use, handling, storage and other factors may involve other or additional safety or performance considerations. The user is responsible for determining the suitability of any material for a specific purpose and for adopting such safety precautions as may be required. Vanderbilt Chemicals, LLC does not warrant the results to be obtained in using any material, and disclaims all liability with respect to the use, handling or further processing of any such material. No suggestion for use is intended as, and nothing herein shall be construed as, a recommendation to infringe any existing patent, trademark or copyright or to violate any federal, state or local law or regulation.

Figure 149: Technical data sheet for Darvan 7-N dispersant (page 1).

The amount of **DARVAN**® Dispersing Agent required for dispersant and stabilization applications will vary with the composition of the product. Simple experimentation will determine the proper amount for each specific use. Usually, the concentration required is between 0.25% and 5.0%, based on the weight of the ingredient being dispersed. The optimal amount of dispersant can be determined by the dispersant demand curve method. A copy of this method is available on request.

TYPICAL USES

See individual department data sheets for detailed use recommendations.

	DARVAN® Dispersing Agent						
	1 Spray Dried	670	2	7-N, 7-NS	811 811D	821A	C-N
Color pigment dispersions	X	X	X	X	X		
Mineral dispersions	X	X	X	X	X		
Particulate chemical dispersions	X	X	X	X	X		
Agricultural pesticide concentrates	X	X	X	X			
Agricultural sprays	X	X	X	X			
Pitch Control (pulp & paper)	X	X					
Whiteware bodies, glazes, refractories				X	X		
Specialty ceramics requiring low Na						X	X
Spray dried slurries				X	X	X	X
Rubber Latexes	X						

FDA STATUS

DARVAN® Dispersing Agent	FDA 21CFR	SUBJECT HEADING	LIMITATION
2, 7-N, 7-NS	173.310	Boiler water additives	None
1 Spray Dried, 670, 2, 7-N, 7-NS, 811, 811D, 821A	175.105	Adhesives	None
1 SPpray Dried 670	175.300	Resinous and polymeric coatings	≤0.6% by weight of cement solids in can end cements for containers having a capacity of not less than 5 gallons
1 Spray Dried, 670	176.170	Components of paper and paperboard in contact with aqueous and fatty foods	For use as an adjuvant to control pulp absorbency and pitch content prior to sheet-forming operations in paper manufacturing
2, 811, 811D	176.170	"	None
7-N, 7-NS	176.170	"	≤0.3% by weight of the coating for viscosity control
1 Spray Dried, 670, 2, 811, 811D	176.180	Components of paper and paperboard in contact with dry food	None
1 Spray Dried, 670, 2	176.210	Defoaming agents used in the manufacture of paper and paperboard	None
1 Spray Dried, 670	177.1200	Cellophane	0.1% for use as an emulsifier
1 Spray Dried, 670, 2	177.1210	Closures with sealing gaskets for food containers	≤0.2% by weight of closure sealing gasket compositions
1 Spray Dried 670	177.1650	Polysulfide polymer-polyepoxy resins	None
1 Spray Dried, 670, 2	182.99	Adjuvants for pesticides chemicals	Surfactant
7-N, 7-NS	182.99	"	pH control.
2	573.600	Lignin sulfonates (for animal feed)	≤4% of animal feed
	FDA 40CFR		
1 Spray Dried, 670, 2	180.910	Inert ingredients used pre- and post-harvest; exemptions from the requirement of a tolerance.	Surfactant, related adjuvants of surfactants
1 Spray Dried, 670	180.920	Inert ingredients used pre-harvest; exemptions from the requirement of a tolerance.	Dispersant
1 Spray Dried, 670, 2	180.930	Inert ingredients applied to animals; exemptions from the requirement of a tolerance.	Surfactant, related adjuvants of surfactants
1 Spray Dried, 670	180.940	Tolerance exemptions for active and inert ingredients for use in antimicrobial formulations (Food-contact surface sanitizing)	When ready for use, the sulfonate chemicals in the solution is not to exceed 332 ppm naphthalene sulfonates

Registered and pending trademarks appearing printed in bold in these materials are those of Vanderbilt Minerals, LLC. For a complete listing, please visit Trademark Listing.

rev01/28/2016

Figure 150: Technical data sheet for Darvan 7-N dispersant (page 2).

C Triton X100 Surfactant Data Sheet

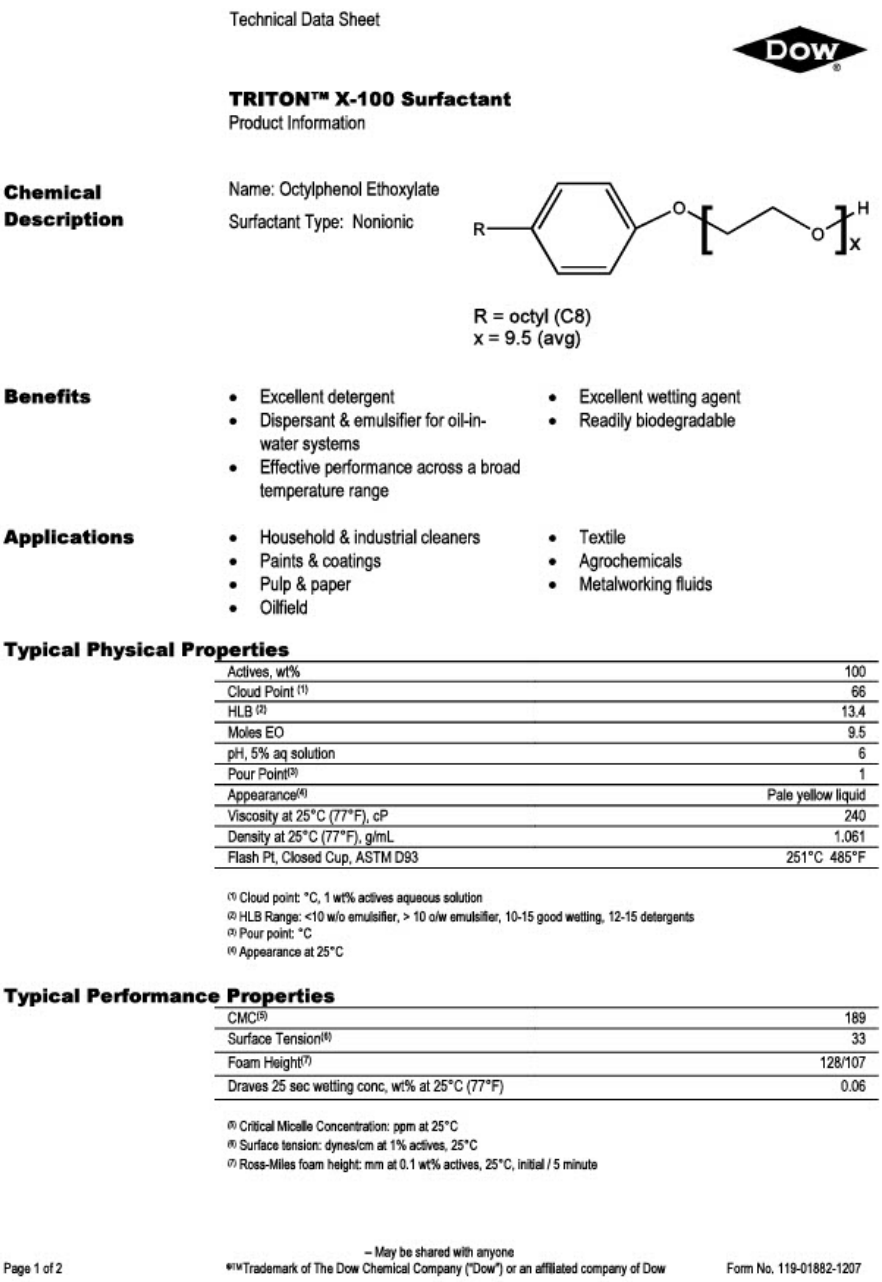

Technical Data Sheet

TRITON™ X-100 Surfactant
Product Information

Chemical Description

Name: Octylphenol Ethoxylate
Surfactant Type: Nonionic

R = octyl (C8)
x = 9.5 (avg)

Benefits

- Excellent detergent
- Dispersant & emulsifier for oil-in-water systems
- Effective performance across a broad temperature range
- Excellent wetting agent
- Readily biodegradable

Applications

- Household & industrial cleaners
- Paints & coatings
- Pulp & paper
- Oilfield
- Textile
- Agrochemicals
- Metalworking fluids

Typical Physical Properties

Actives, wt%	100
Cloud Point [1]	66
HLB [2]	13.4
Moles EO	9.5
pH, 5% aq solution	6
Pour Point[3]	1
Appearance[4]	Pale yellow liquid
Viscosity at 25°C (77°F), cP	240
Density at 25°C (77°F), g/mL	1.061
Flash Pt, Closed Cup, ASTM D93	251°C 485°F

[1] Cloud point: °C, 1 wt% actives aqueous solution
[2] HLB Range: <10 w/o emulsifier, > 10 o/w emulsifier, 10-15 good wetting, 12-15 detergents
[3] Pour point: °C
[4] Appearance at 25°C

Typical Performance Properties

CMC[5]	189
Surface Tension[6]	33
Foam Height[7]	128/107
Draves 25 sec wetting conc, wt% at 25°C (77°F)	0.06

[5] Critical Micelle Concentration: ppm at 25°C
[6] Surface tension: dynes/cm at 1% actives, 25°C
[7] Ross-Miles foam height: mm at 0.1 wt% actives, 25°C, initial / 5 minute

– May be shared with anyone
®™Trademark of The Dow Chemical Company ("Dow") or an affiliated company of Dow

Form No. 119-01882-1207

Figure 151: Technical data sheet for Triton X100 surfactant (page 1).

Solubility and Compatibility

- Soluble in water
- Miscible in most polar organic solvents & aromatic hydrocarbons
- Insoluble in aliphatic hydrocarbons
- Chemically stable in most acidic & alkaline solutions
- Compatible with anionic, cationic, and other nonionic surfactants

Contact information goes here:
North America: 1-800-447-4369
Europe: (+32) 3-450-2240
Asia/Pacific: (+852) 2879 7339
Other areas: 1-989-832-1556
http://www.dow.com/surfactants

NOTICE: No freedom from any patent owned by Seller or others is to be inferred. Because use conditions and applicable laws may differ from one location to another and may change with time, Customer is responsible for determining whether products and the information in this document are appropriate for Customer's use and for ensuring that Customer's workplace and disposal practices are in compliance with applicable laws and other governmental enactments. Seller assumes no obligation or liability for the information in this document. NO WARRANTIES ARE GIVEN; ALL IMPLIED WARRANTIES OF MERCHANTABILITY OR FITNESS FOR A PARTICULAR PURPOSE ARE EXPRESSLY EXCLUDED.

– May be shared with anyone
®™Trademark of The Dow Chemical Company ("Dow") or an affiliated company of Dow

Form No. 119-01882-1207

Figure 152: Technical data sheet for Triton X100 surfactant (page 2).

D Slurry mass loss and temperature plots

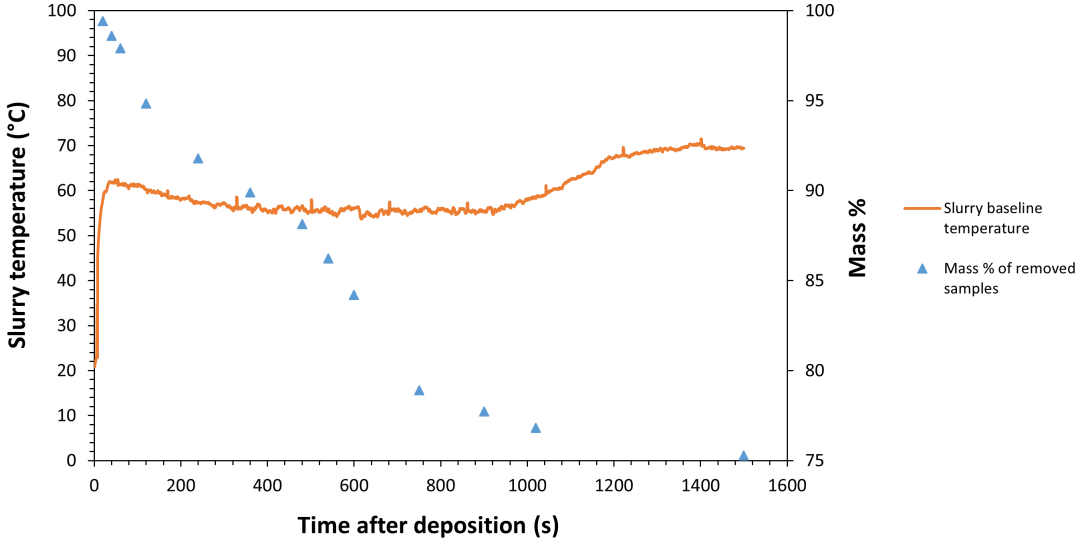

(a)

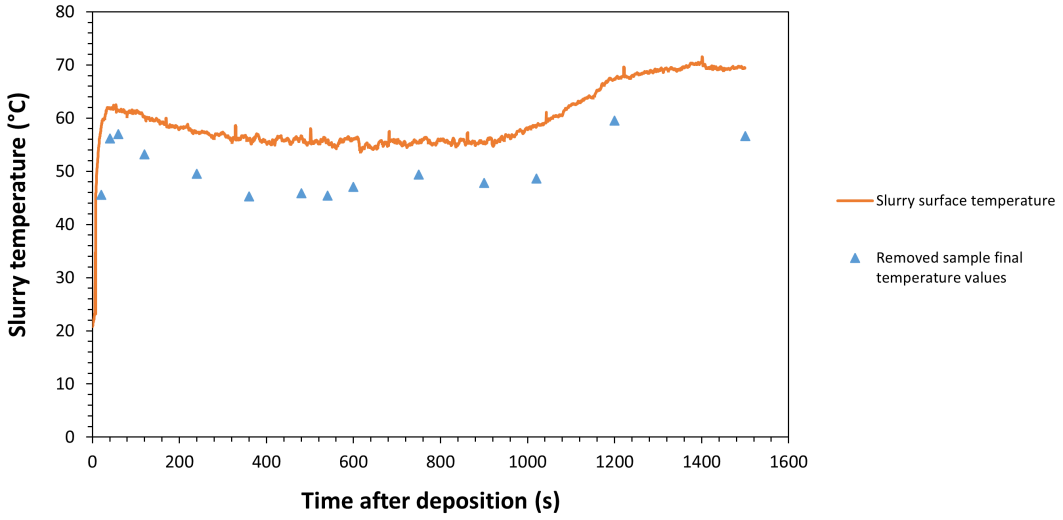

(b)

Figure 153: Graphs showing sample mass loss data against baseline temperature profile (a) and final sample temperature recordings against baseline temperature profile (b) for 4mm sample layers of foamed slurry deposited on 70°C platform.

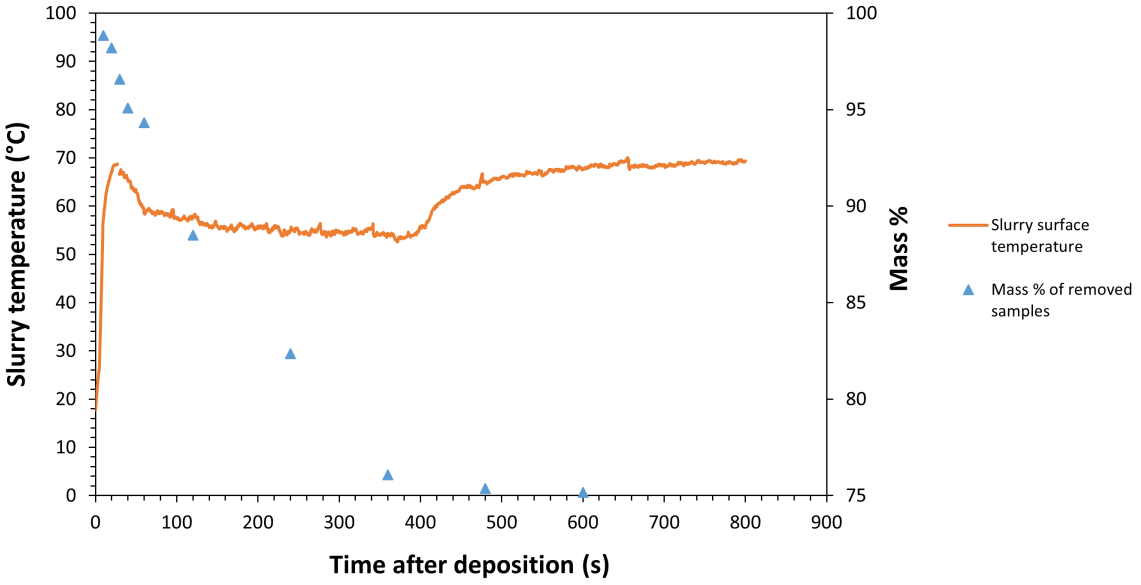

(a)

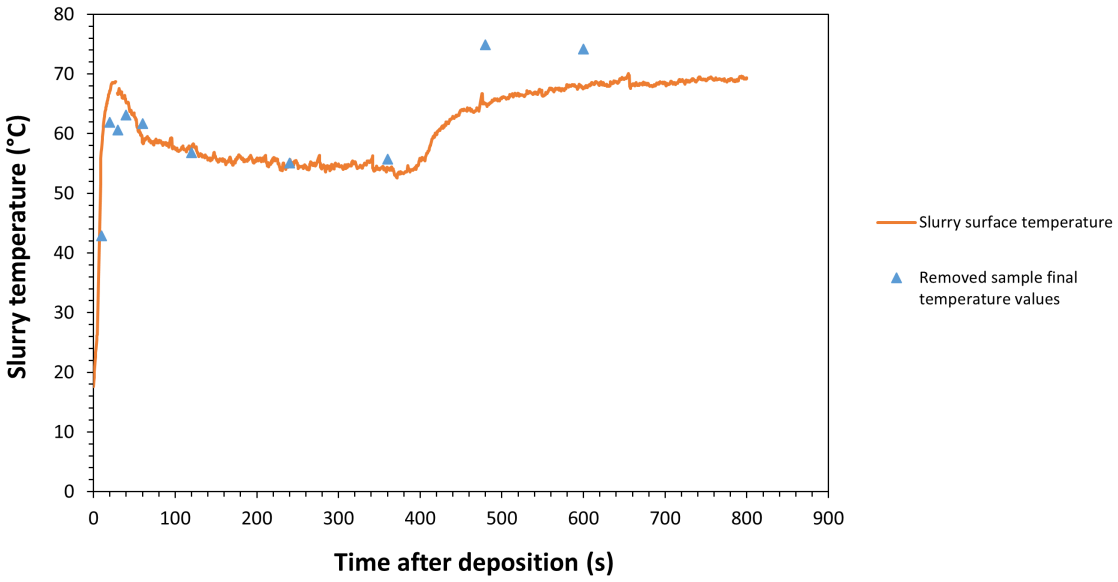

(b)

Figure 154: Graphs showing sample mass loss data against baseline temperature profile (a) and final sample temperature recordings against baseline temperature profile (b) for 2mm sample layers of foamed slurry deposited on 80°C platform.

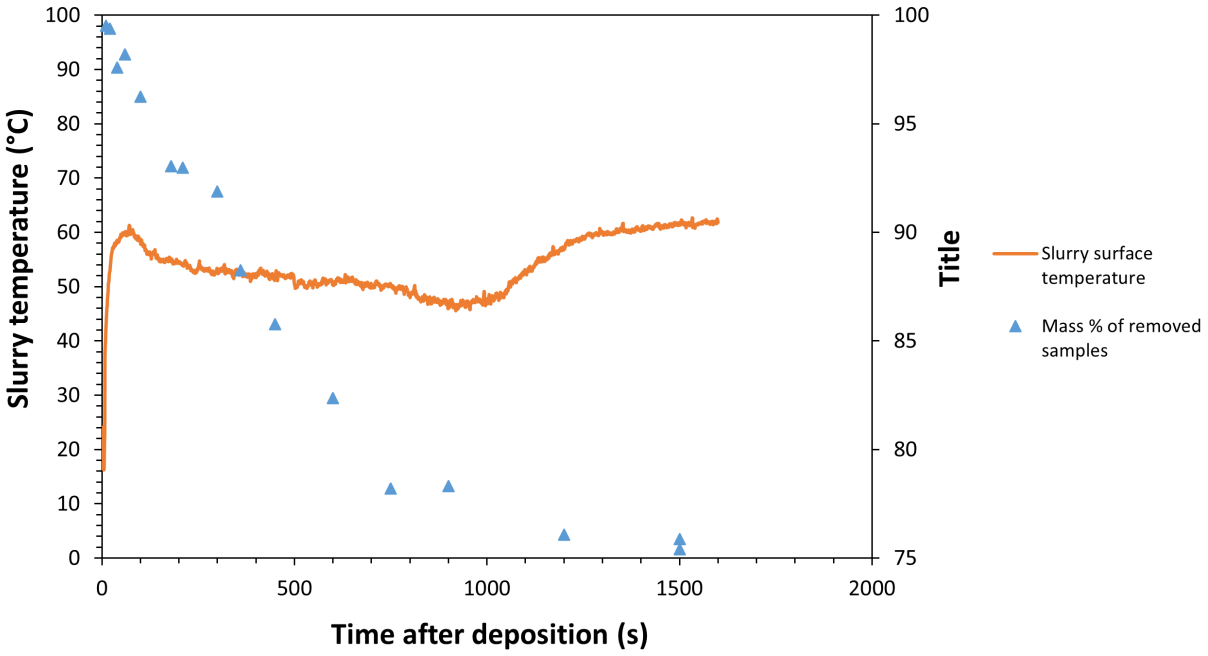

(a)

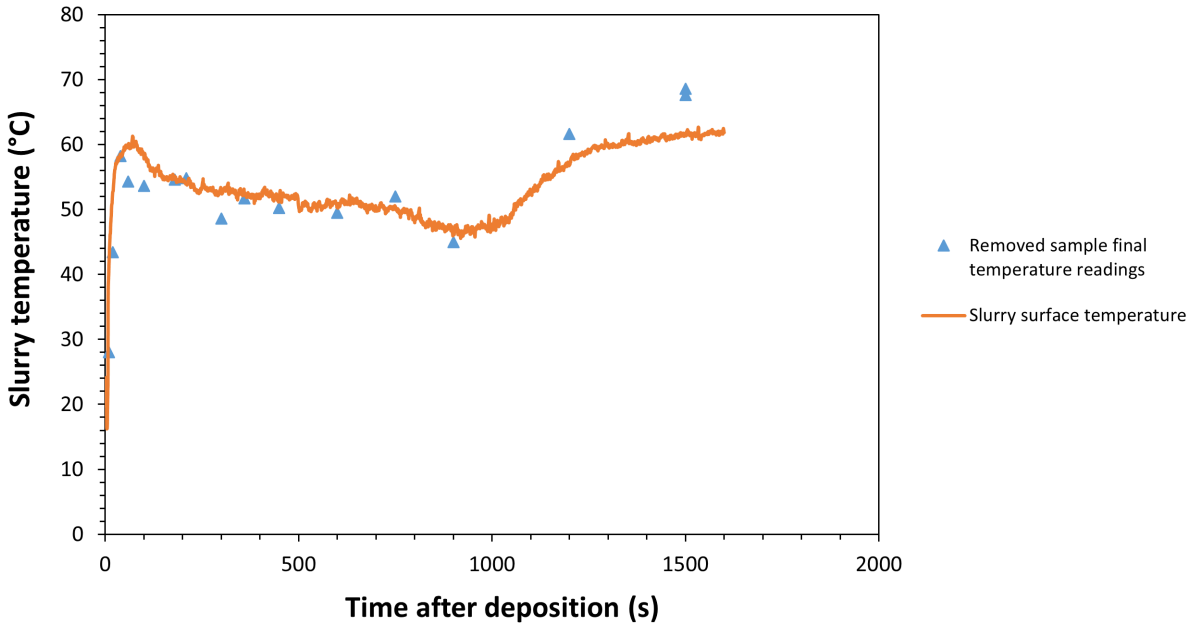

(b)

Figure 155: Graphs showing sample mass loss data against baseline temperature profile (a) and final sample temperature recordings against baseline temperature profile (b) for 4mm sample layers of foamed slurry deposited on 80°C platform.

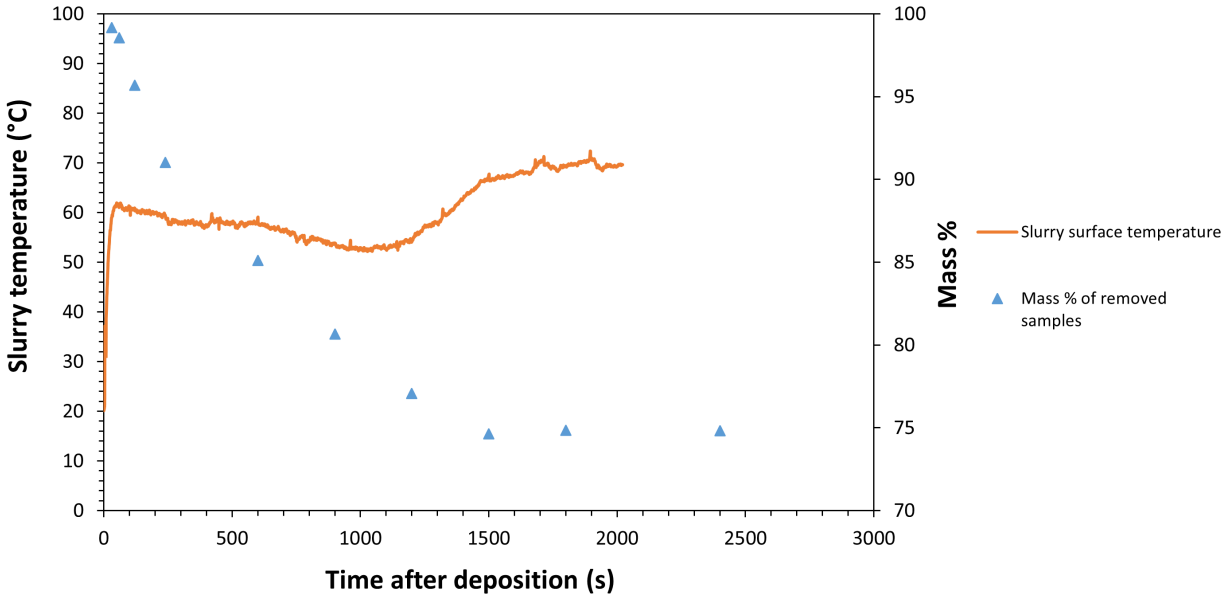

(a)

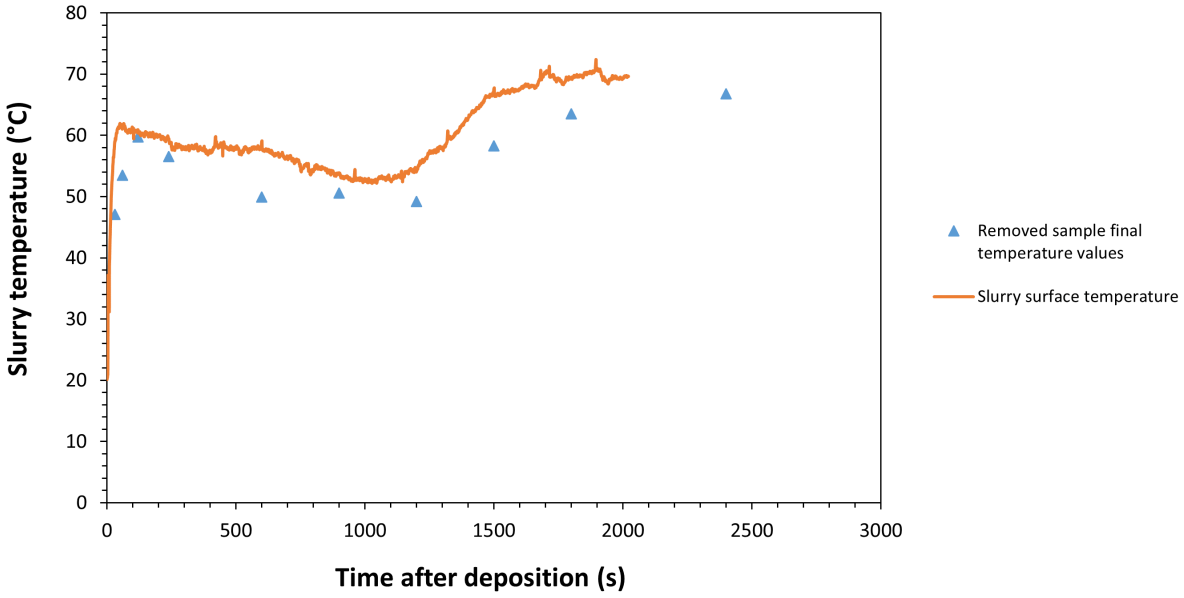

(b)

Figure 156: Graphs showing sample mass loss data against baseline temperature profile (a) and final sample temperature recordings against baseline temperature profile (b) for 6mm sample layers of foamed slurry deposited on 80°C platform.

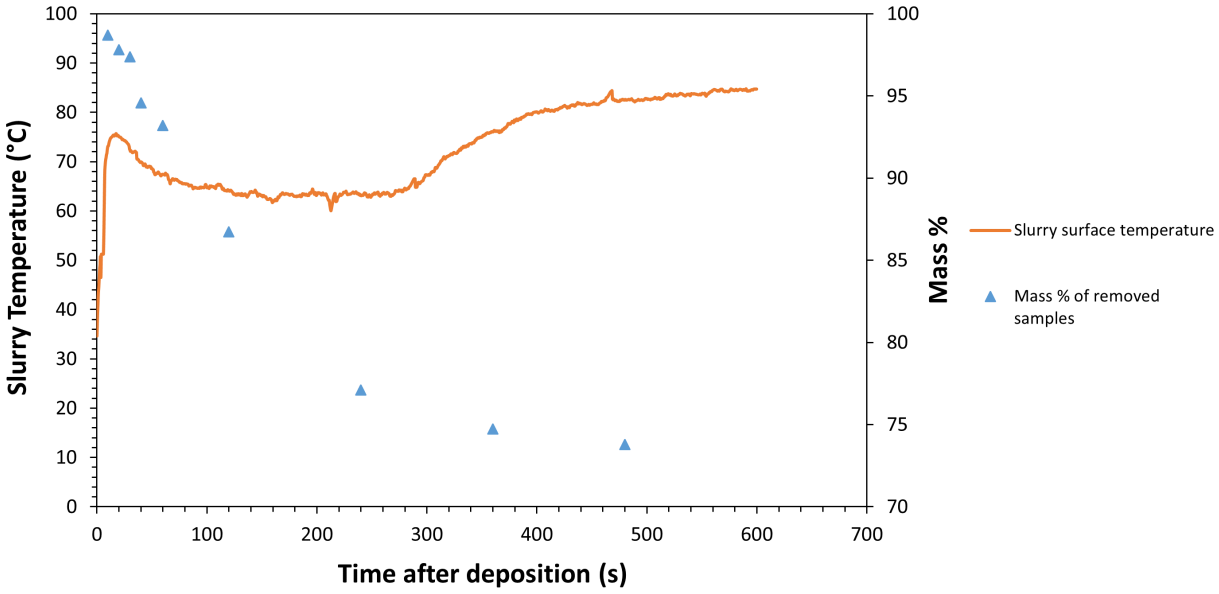

(a)

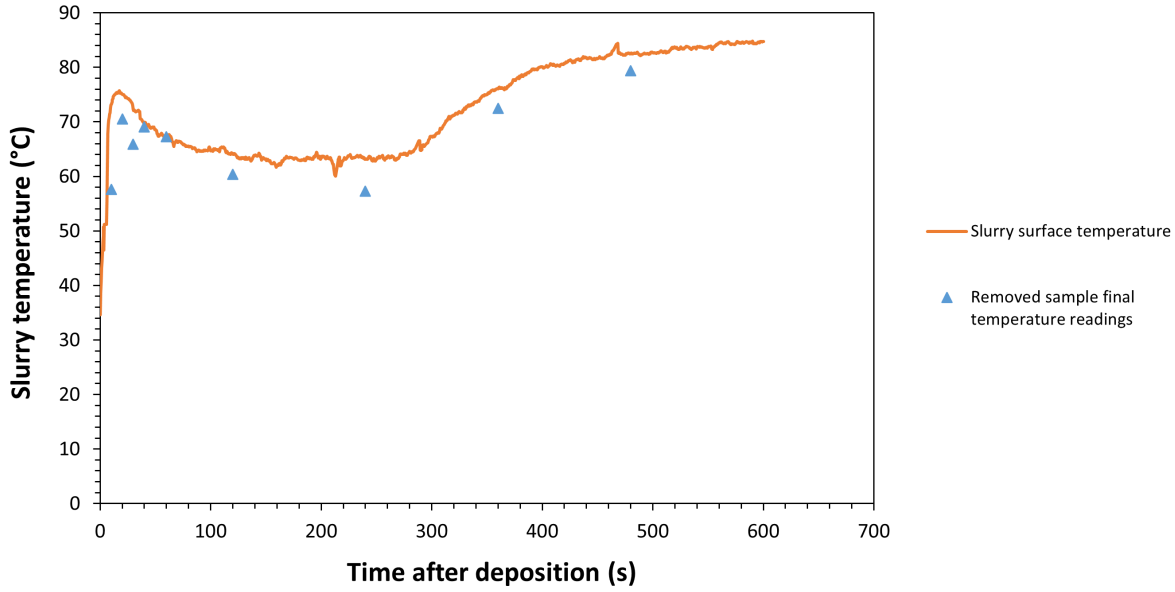

(b)

Figure 157: Graphs showing sample mass loss data against baseline temperature profile (a) and final sample temperature recordings against baseline temperature profile (b) for 2mm sample layers of foamed slurry deposited on 90°C platform.

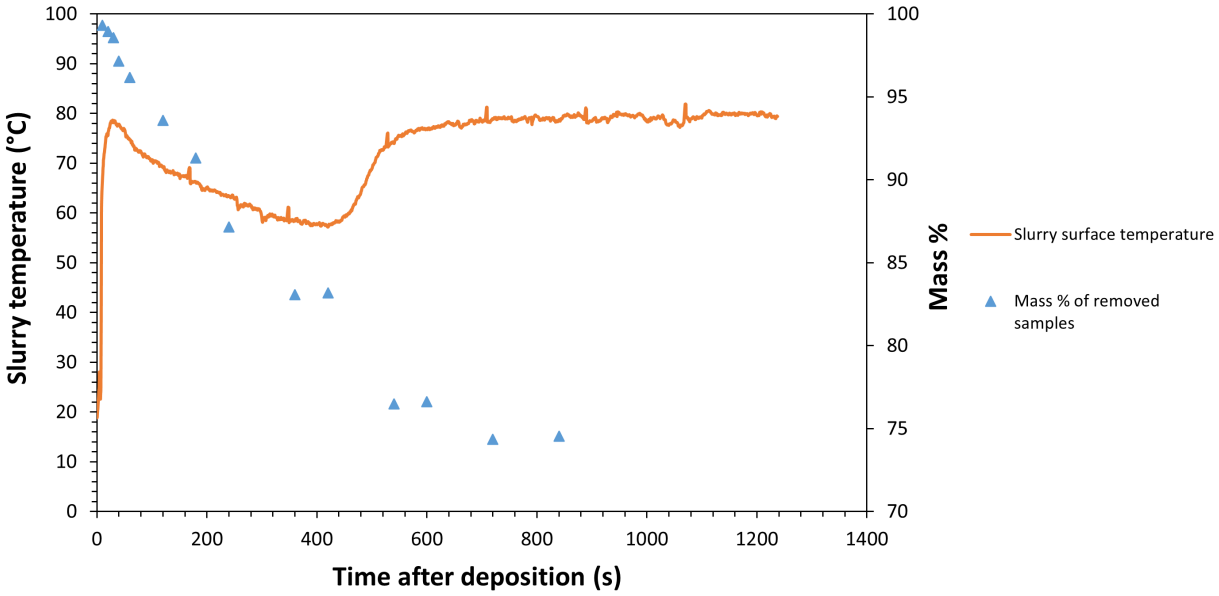

(a)

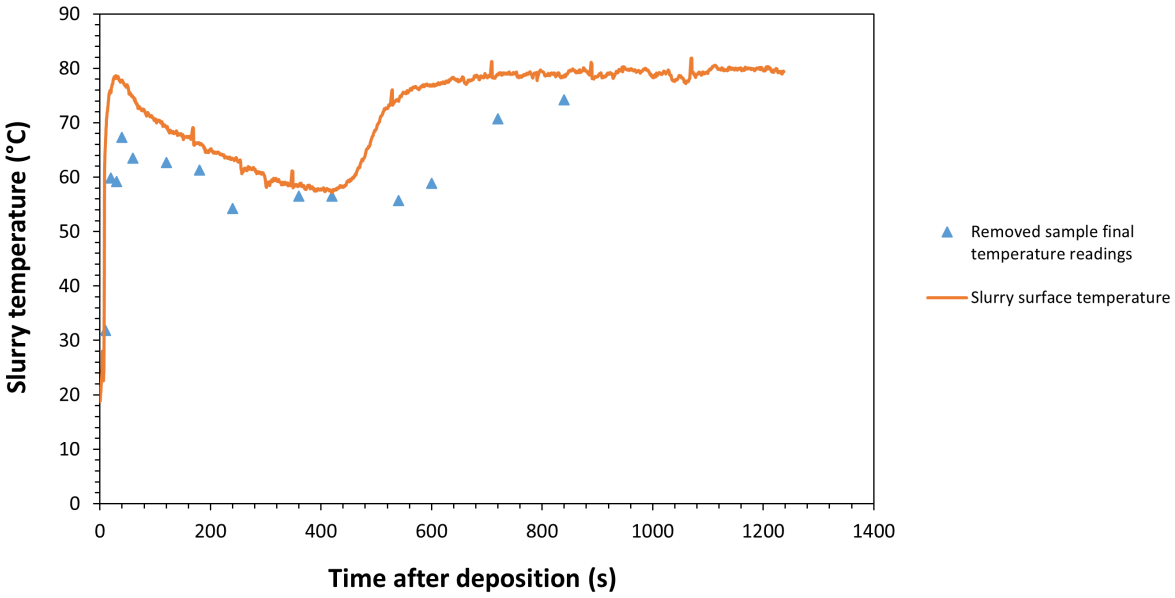

(b)

Figure 158: Graphs showing sample mass loss data against baseline temperature profile (a) and final sample temperature recordings against baseline temperature profile (b) for 4mm sample layers of foamed slurry deposited on 90°C platform.

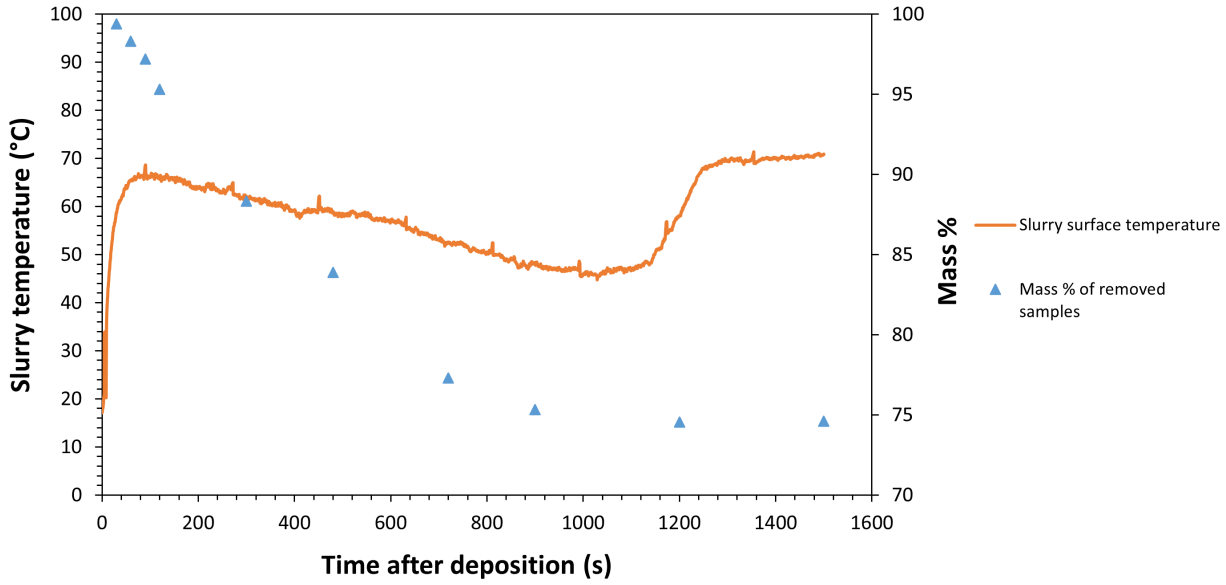

(a)

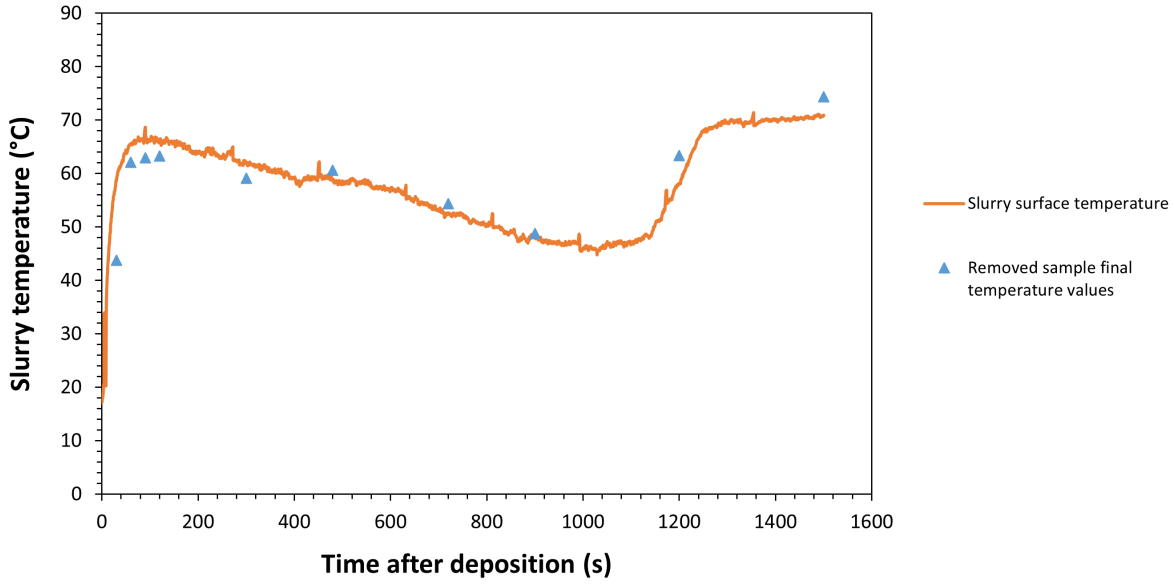

(b)

Figure 159: Graphs showing sample mass loss data against baseline temperature profile (a) and final sample temperature recordings against baseline temperature profile (b) for 6mm sample layers of foamed slurry deposited on 90°C platform.

E Plots from Moisture Ratio Model used to Calculate Empirical Constants

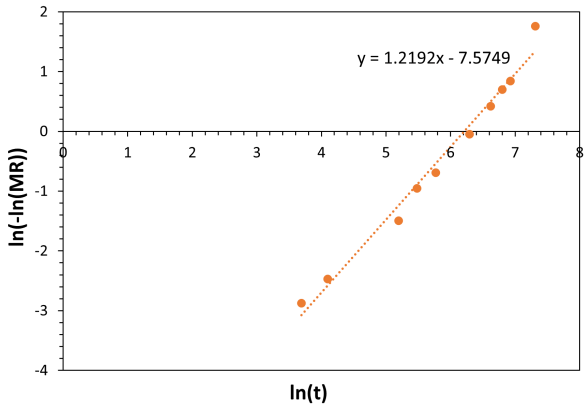

(a) 70 °C

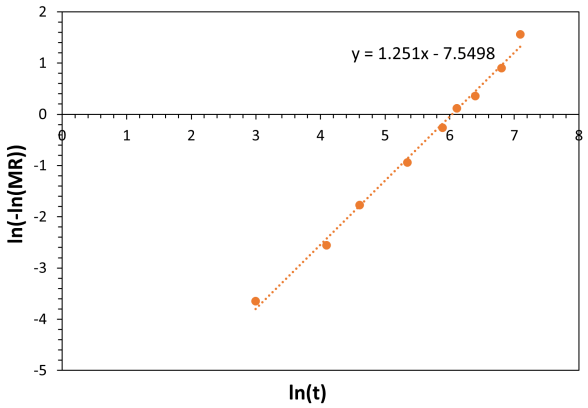

(b) 80 °C

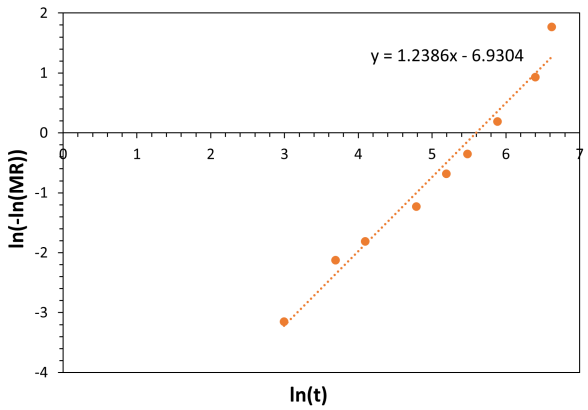

(c) 90 °C

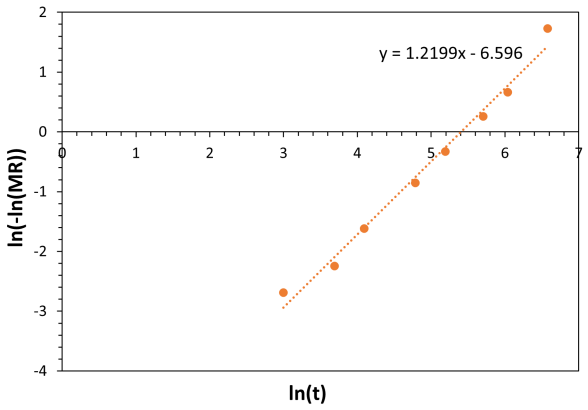

(d) 100 °C

Figure 160: Graphs showing $ln(-ln(MR))$ plotted against $(ln(t))$ for $4mm$ thick slurry layers drying on ZMorph platform pre-heated to various temperatures.